Assessment of Prostate Cancer Aggressiveness with Magnetic Resonance Spectroscopic Imaging and Diffusion-weighted Imaging

Thiele Kobus

Colofon

The research in this thesis was funded by the Dutch Cancer Society. The studies were performed at the Department of Radiology, Radboudumc, Nijmegen, The Netherlands and at the Erwin L. Hahn Institute for Magnetic Resonance Imaging, Essen, Germany.

Publication of this thesis was financially supported by Radboudumc and the Dutch Cancer Society

Design: Dennis Willems, Dezzign, Arnhem
Printed by: Off Page B.V. Amsterdam

ISBN: 978-94-6182-450-9

Assessment of Prostate Cancer Aggressiveness with Magnetic Resonance Spectroscopic Imaging and Diffusion-weighted Imaging

Proefschrift

ter verkrijging van de graad van doctor
aan de Radboud Universiteit Nijmegen
op gezag van de rector magnificus prof. mr. S.C.J.J. Kortmann,
volgens besluit van het college van decanen
in het openbaar te verdedigen op woensdag 25 juni 2014
om 12:30 uur precies

door

Thiele Kobus
geboren op 27 januari 1983
te Veghel

Promotor:

Prof. dr. A. Heerschap

Copromotor:

Dr. T.W.J. Scheenen

Manuscriptcommissie:

Prof. dr J. Schalken (voorzitter)

Prof dr. H. van Krieken

Dr. G. Strijkers (Academisch Medisch Centrum / Technische Universiteit Eindhoven)

Voor mijn opa's

Contents

1

CHAPTER ONE

Introduction

Prostate cancer

The prostate is a part of the male reproductive system and consists of tubular-alveolar glands surrounded by stroma. In the glands citrate, polyamines and several enzymes are stored that are secreted during ejaculation. The surrounding stroma is built up from smooth muscle cells and dense connective tissue. The prostate consists of different anatomical zones: the peripheral zone, central zone and transition zone. In the transition zone often at older age the nonmalignant condition benign prostatic hyperplasia (BPH) occurs (1). This is a benign enlargement of the prostate and can result in increasing pressure on the urethra. Other common diseases of the prostate are prostatitis, which is an inflammation of the prostate, and prostate cancer, which is the most common noncutaneus cancer in men. The estimated number of new prostate cancer diagnoses in the Netherlands is 10.390 (2). Recently, the disease has become the second leading cause of cancer-related death in men (3). Approximately 70% of the cancers arise in the peripheral zone, about 30% in the transition and central zone (4). Three generally recognized risk factors for prostate cancer are older age, ethnicity, and heredity; however, not all risk factors are known yet (5).

Due to the rising age of the population and the increasing number of prostate-specific antigen (PSA) blood tests, the incidence of prostate cancer is increasing. PSA is a protease produced by epithelial cells of the prostate and normally secreted into the glands. It is suggested that the disruption in the architecture of the glands in prostate cancer causes leakage of PSA in the capillary bed (6,7). As a consequence, an increased level of PSA in the blood stream can be an indication of prostate cancer (7). However, also with BPH often an increase in PSA level is observed, which limits the specificity of the blood test (7). An elevated PSA level and/or suspicious finding of a digital rectal examination, are reason to take biopsies of the prostate to assess the presence of prostate cancer. These biopsies are often obtained under transrectal ultrasound (TRUS) guidance. By means of histopathologic examination of biopsy tissues, the presence of prostate cancer can be confirmed, and, if cancer is present, the Gleason score will be determined. The Gleason score is the pathologic measure of prostate cancer aggressiveness (8-10).

In 1974, the pathologist Gleason and his colleagues published a grading system for prostate cancer based on the over-all pattern of growth (10). They graded the tumors from a scale 1 to 5 with increasing aggressiveness, corresponding to increased de-differentiation of tumor cells. During the 2005 International Society of Urological Pathology (ISUP) Consensus Conference, the ISUP modified Gleason grading system was initiated (Figure 1.1) (9). Because about half of the tumors consist of more than one grade, the Gleason score of a tumor consists of the primary and secondary Gleason grade (8,10). There is a difference in determining the Gleason score from a biopsy sample and radical prostatectomy specimen. The pathologist bases the primary and secondary Gleason grades in a prostatectomy sample on their prevalence. As biopsy tissue represents only a small part of the tumor, the primary and the highest grade determine the Gleason score. When a third grade occupies more than 5% of the tumor tissue in a prostatectomy sample, a tertiary grade can be included in the Gleason score (9). Tumors with a tertiary Gleason score of 5 have a higher risk of extraprostatic extension and PSA recurrence than tumors with the same score but without a tertiary pattern (11-13).

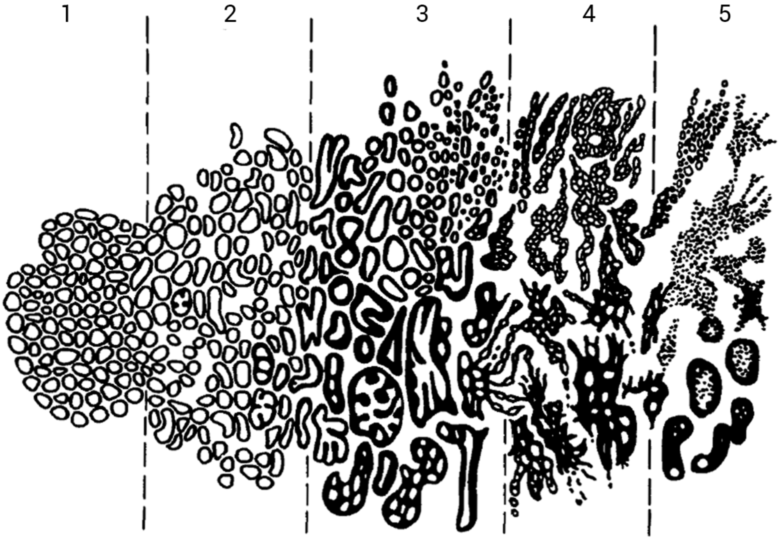

Figure 1.1. Schematic diagram of the ISUP modified Gleason grading system (9). While Gleason grade 1 and 2 consist of closely packed, but separate small glands that are in a circumscribed nodule, Gleason grade 3 can infiltrate between noncancerous glandular tissue and consists of smaller glands. Pattern 4 includes ill-defined and cribriform glands. Pattern 5 on the other hand has lost all glandular structure and sporadically necrosis can be seen.

Prostate cancers are often nonaggressive, which is illustrated by the much-heard expression that more men die with prostate cancer than from prostate cancer. A database study demonstrated that only a quarter of the diagnosed prostate cancers were of high aggressiveness (PSA > 20 ng/ml, Gleason score ≥ 8 and/or T2c-3a) in the 2004-2006 period (14). Furthermore, in autopsies, studying men who died of other causes than prostate cancer, often prostate cancer was found (15). The percentage of men having latent prostate cancer at autopsy increased with increasing age of the investigated men (15). It has been proposed to screen for prostate cancer by means of PSA testing. However, the high number of indolent prostate cancers raises the question whether this screening should be realized. A large European study showed that over an 11 year period in 37 men prostate cancer would need to be detected by PSA screening of 1055 men to prevent one death from prostate cancer (16). It is estimated that half of these diagnosed men would not have presented any clinical symptoms during the rest of their lives without the screening (17). They will probably experience more inconvenience from the treatment and its side effects than from the indolent tumor. In order to prevent overdiagnosis and overtreatment, there is a need for good methods to determine cancer aggressiveness.

There are several models (e.g. D'Amico classification and Partin tables (18,19)) based on clinical parameters that are used to classify prostate cancer and assist in the treatment planning. These models are based on the PSA level, biopsy Gleason score and the clinical stage determined by a digital rectal exam. However, prostate cancer is often multifocal and heterogeneous, which might lead to sampling errors with TRUS guided biopsy (Figure 1.2). Several studies have demonstrated discrepancies between the Gleason score of the biopsy tissue and the subsequent radical prostatectomy specimen (20,21). Better guidance of the biopsy needle to the most aggressive part of the tumor or alternative methods to assess tumor aggressiveness are therefore required.

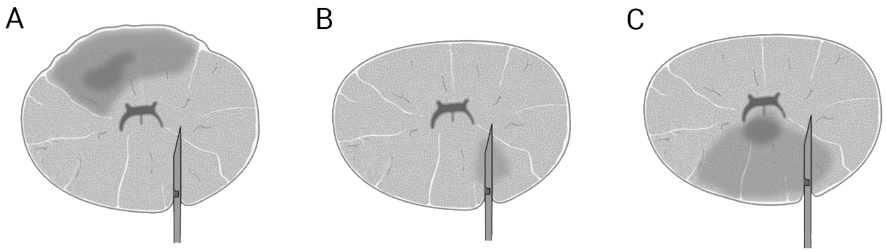

Figure 1.2. TRUS-guided biopsy has limitations, as the tumor can be missed (A), a clinically insignificant tumor can be found (B) or the biopsy underestimates the aggressiveness of the tumor (C).

Outline of the thesis

An important aspect in prostate cancer management is the assessment of its aggressiveness. As TRUS guided biopsies often miss the tumor or underestimate its Gleason score, other approaches are highly desired. One interesting approach is the use of magnetic resonance (MR) techniques. The technique is noninvasive and with MR imaging excellent soft tissue contrast can be obtained. Besides the use of MR to obtain anatomical images, MR offers also possibilities to obtain more functional information that could be related with cancer aggressiveness. In this thesis the performance of two MR techniques is studied for noninvasive assessment of aggressiveness. These techniques are: MR spectroscopic imaging (MRSI) and diffusion-weighted imaging (DWI).

Chapter 2 starts with the basic principles of MR, MR imaging (MRI) and MRSI. Then more detail about the role of MR(S)I for prostate cancer management is provided. Usually a multi-parametric approach is used for a prostate MR exam, which means that anatomical imaging is combined with one or more functional imaging methods such as DWI and MRSI. The focus will be on the hardware, acquisition methods, information content and applications of MRSI and DWI for prostate MR.

MRSI is a technique that enables spatial mapping of metabolites in a tissue that are present in high concentration. Using ^{1}H MRSI, the metabolites choline, polyamines, creatine and citrate can be studied. During MRSI acquisition, spectra are acquired from which the relative amounts of the metabolites can be derived and expressed in a metabolite ratio. The most used metabolite ratio for prostate cancer management is the choline plus creatine to citrate ratio since in prostate cancer an increase in choline and decrease in citrate is observed. In **chapter 3** the use of the metabolite ratio for prostate MRSI is discussed. All aspects that affect the metabolite ratio are described, from acquisition to post-processing, and recommendations for standardization of this ratio are provided.

Next, in **chapter 4**, this metabolite ratio is used to assess the aggressiveness of the tumor. The ratio is related to the Gleason score of the tumor to study whether a correlation exists. It is investigated how well indolent tumors can be separated from more aggressive tumors.

While MRSI is used to study metabolites, DWI provides information about the restriction of water motion in tissue. This restriction is expressed as the apparent diffusion coefficient (ADC). As the diffusion of water-molecules is different between healthy tissue and cancer tissue, different ADC values are obtained. In the study described in **chapter 5,** the ADC values are correlated with the Gleason score, as are the metabolite ratios. Furthermore, the metabolite ratios and ADC value are combined to study their complementary value to assess the aggressiveness. Distinction is made between the origin of the tumors, peripheral zone or transition zone, to study the zonal performance of the two techniques.

Important aspects that should be considered are the underlying mechanisms that cause the changes in metabolite concentrations or ADC value. A change in ADC value represents a change in compartmentalization, which is probably caused by a decrease in luminal space and increase in cell density. As citrate, the most important factor in the metabolite ratio, is stored in the luminal space, a decrease in citrate could also reflect the changed structure in cancer. However, another theory is that citrate decreases because cancer cells oxidize it. In **chapter 6** the structural changes in prostate cancer are studied in detail and correlated with the metabolite ratio and the ADC value. In this way, more insight is gained in the possible underlying mechanisms and potential complementary value of the two techniques.

While with ^{1}H MRSI of the prostate mainly choline, creatine and citrate are studied, the technique offers possibilities to study more metabolites. One of the metabolites that can be of importance for aggressiveness assessment and treatment selection is lactate. Lactate is an indicator for hypoxia and the Warburg effect. In **chapter 7** a sequence was developed for lactate detection in the prostate. With this sequence, MRSI was performed in 17 patients with highly aggressive tumors. In these patients the minimal detectable lactate concentration was calculated to obtain an impression about the lactate levels in prostate cancer.

Besides a decrease in citrate also an increase in choline is observed in prostate cancer. The choline signal represents the resonances from free choline, glycerophosphocholine and phosphocholine. These last two metabolites contain a phosphorus-atom, and can therefore be studied in more detail with ^{31}P MRSI. To study these and other phosphorus metabolites, the increased signal-to-noise ratio and spectral resolution of a high field strength are very beneficial. Therefore, dedicated coils were developed that enabled the implementation of ^{31}P MRSI for *in vivo* prostate measurements on a 7T system. In **chapter 8** an extensive safety validation is presented of this coil setup. The safety validation consists of simulations, phantom measurements and an *in vivo* temperature examination. In this chapter the first *in vivo* ^{31}P spectra of the human prostate at 7 T are presented, demonstrating the feasibility of our setup. This study paves the way for more clinical studies to investigate the use of ^{31}P MRSI for prostate cancer management in general, and more specific for assessing prostate cancer aggressiveness.

Finally **chapter 9** summarizes all chapters. The results of the different studies are discussed and put in perspective. An outlook to future directions is given.

References

1. Verhamme K, Dieleman J, Bleumink G, Van Der Lei J, Sturkenboom M, Artibani W, Begaud B, Berges R, Borkowski A, Chappel C. Incidence and prevalence of lower urinary tract symptoms suggestive of benign prostatic hyperplasia in primary care--the Triumph project. Eur Urol 2002;42(4):323.
2. http://kanker.kwfkankerbestrijding.nl/soorten-kanker/Pages/soorten-kanker-prostaatkanker.aspx. 2013.
3. Siegel R, Naishadham D, Jemal A. Cancer statistics, 2012. CA Cancer J Clin 2012;62(1):10-29.
4. McNeal JE, Redwine EA, Freiha FS, Stamey TA. Zonal distribution of prostatic adenocarcinoma. Correlation with histologic pattern and direction of spread. Am j surg pathol 1988;12(12):897.
5. Heidenreich A, Bellmunt J, Bolla M, Joniau S, Mason M, Matveev V, Mottet N, Schmid H-P, van der Kwast T, Wiegel T. EAU guidelines on prostate cancer. Part 1: screening, diagnosis, and treatment of clinically localised disease. Eur Urol 2011;59(1):61-71.
6. Brawer MK. How to use prostate-specific antigen in the early detection orscreening for prostatic carcinoma. CA Cancer J Clin 1995;45(3):148-164.
7. Stenman U-H, Leinonen J, Zhang W-M, Finne P. Prostate-specific antigen. 1999. Elsevier. p 83-93.
8. Gleason DF. Histologic grading of prostate cancer: a perspective. Hum pathol 1992;23(3):273-279.
9. Epstein JI, Allsbrook Jr WC, Amin MB and others. The 2005 International Society of Urological Pathology (ISUP) consensus conference on Gleason grading of prostatic carcinoma. Am J Surg Pathol 2005;29(9):1228-1242.
10. Gleason DF, Mellinger GT. Prediction of prognosis for prostatic adenocarcinoma by combined histological grading and clinical staging. J Urology 1974;111(1):58.
11. Hattab EM, Koch MO, Eble JN, Lin H, Cheng L. Tertiary Gleason Pattern 5 is a Powerful Predictor of Biochemical Relapse in Patients With Gleason Score 7 Prostatic Adenocarcinoma. J Urol 2006;175(5):1695-1699.
12. Mosse CA, Magi-Galluzzi C, Tsuzuki T, Epstein JI. The Prognostic Significance of Tertiary Gleason Pattern 5 in Radical Prostatectomy Specimens. Am J Surg Pathol 2004;28(3):394-398.
13. Pan CC, Potter SR, Partin AW, Epstein JI. The prognostic significance of tertiary Gleason patterns of higher grade in radical prostatectomy specimens: A proposal to modify the Gleason grading system. Am J Surg Pathol 2000;24(4):563-569.
14. Cooperberg MR, Broering JM, Kantoff PW, Carroll PR. Contemporary Trends in Low Risk Prostate Cancer: Risk Assessment and Treatment. J Urology 2007;178(3 SUPPL.):S14-S19.
15. Franks L. Latent carcinoma of the prostate. J Pathol Bacteriol 1954;68(2):603-616.
16. Schröder FH, Hugosson J, Roobol MJ and others. Prostate-cancer mortality at 11 years of follow-up. New Engl J Med 2012;366(11):981-990.
17. Draisma G, Boer R, Otto SJ, van der Cruijsen IW, Damhuis RAM, Schröder FH, de Koning HJ. Lead times and overdetection due to prostate-specific antigen screening: Estimates from the European randomized study of screening for prostate cancer. J Natl Cancer I 2003;95(12):868-878.
18. D'Amico AV, Cote K, Loffredo M, Renshaw AA, Schultz D. Determinants of prostate cancer–specific survival after radiation therapy for patients with clinically localized prostate cancer. Journal of Clinical Oncology 2002;20(23):4567-4573.
19. Eifler JB, Feng Z, Lin BM, Partin MT, Humphreys EB, Han M, Epstein JI, Walsh PC, Trock BJ, Partin AW. An updated prostate cancer staging nomogram (Partin tables) based on cases from 2006 to 2011. BJU International

2012.
20. Tomioka S, Nakatsu H, Suzuki N, Murakami S, Matsuzaki O, Shimazaki J. Comparison of Gleason grade and score between preoperative biopsy and prostatectomy specimens in prostate cancer. Int J Urol 2006;13(5):555-559.
21. Rajinikanth A, Manoharan M, Soloway CT, Civantos FJ, Soloway MS. Trends in Gleason Score: Concordance Between Biopsy and Prostatectomy over 15 Years. Urology 2008;72(1):177-182.

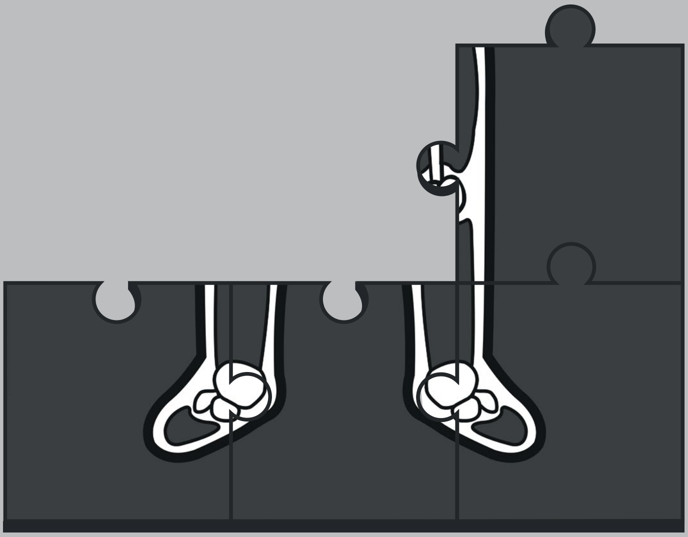

2

CHAPTER TWO

Magnetic Resonance Imaging and Spectroscopic Imaging of the Prostate

Part of the content of this chapter is based on the publication:
Mapping of prostate cancer by proton MR spectroscopic imaging
T. Kobus, A.J. Wright, T.W.J. Scheenen and Arend Heerschap
NMR in Biomedicine, 2013, Jan;27(1):39-52

Introduction

In the diagnostics of patients with clinical signs suspicious for prostate cancer transrectal ultrasound (TRUS) guided biopsy specimens, analyzed by histopathology, are the standard to confirm the presence of cancer and describe its further characterization. Magnetic resonance (MR) is a versatile modality with potential to aid the diagnostic workup of patients with prostate cancer, but currently its role is still limited (1). In oncology MR is commonly used to outline anatomical features, but also offers many possibilities to acquire more functional information, in particular of physiologic and metabolic nature, which may help to increase diagnostic specificity and sensitivity. For instance, dynamic contrast enhanced MR imaging (DCE-MRI) may be used to assess vascular functionality, diffusion-weighted imaging (DWI) to assess tissue characteristics associated with restrictions in water motion and MR spectroscopy (MRS) to assess tissue metabolism and physiology.

Magnetic resonance

MR makes use of the property that the magnetic moment of certain nuclei aligns with a magnetic field. In this external magnetic field the nuclei acquire magnetic energy. Nuclei with an odd mass number (spin-½-nuclei) have two energy levels and the energy difference (ΔE) between these states is given by:

$$\Delta E = \gamma h B_0 \qquad (2.1)$$

in which γ is the gyromagnetic ratio, *h* is Planck's constant and B_0 the external magnetic field (Figure 2.1A).

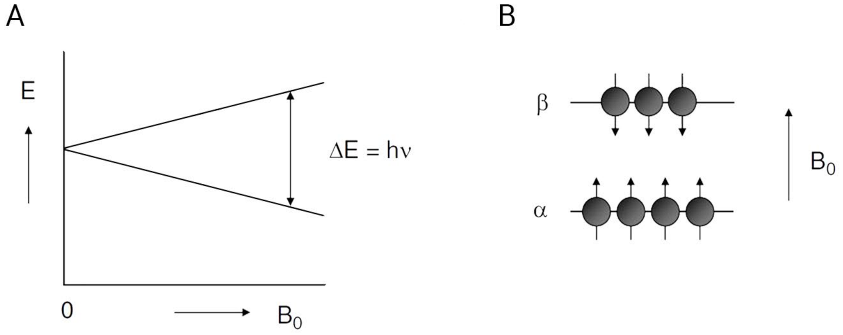

Figure 2.1. *A) The dependence of the magnetic energy of a spin-½-nucleus on the strength of the external magnetic field. B) The spin energy of nuclei aligns parallel (spin state α) or anti-parallel (spin state β) with the external magnetic field. Source: (2).*

When an oscillating electromagnetic wave is applied perpendicular to the main magnetic field, resonance will occur if the energy of the oscillating field equals the magnetic energy. The energy of the electromagnetic wave is given by:

$$\Delta E = h v_0 \qquad (2.2)$$

in which v_0 is the frequency of the electromagnetic wave. Combining equation 2.1 and 2.2 leads to:

$$v_0 = \gamma B_0 \qquad (2.3)$$

This equation is the Larmor equation and v_0 is better known as Larmor frequency.

The two energy levels of the spin-½-nuclei depend on the orientation of the spin energies: either parallel (low energy state) or anti-parallel (high energy state) to the main magnetic field (Figure 2.1B). The spins precess in the magnetic field at the Larmor frequency under an angle of 55.7° and have a magnetic moment of μ_z in the longitudinal direction (Figure 2.2A). In a sample, many spins are present and in thermal equilibrium slightly more spins align in the direction of the magnetic field. Using the Boltzmann equation, the population difference can be calculated:

$$\left(\frac{n_\alpha}{n_\beta}\right) = e^{hv/kT} \qquad (2.4)$$

In this formula is n_α the number of spins in the low energy state, n_β the number of spins in the high energy state, k is the Boltzmann constant and T is the absolute temperature.

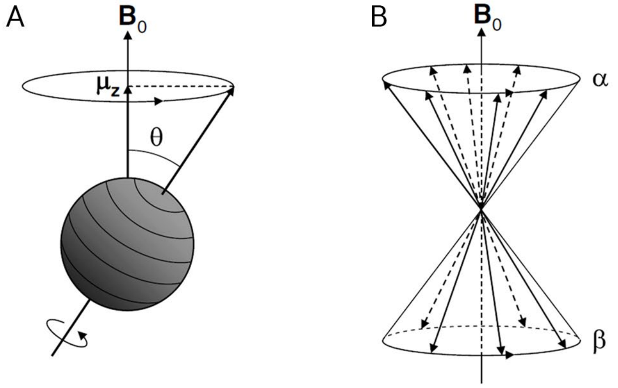

Figure 2.2. *A) In the external magnetic field, the nuclear spin precesses with an angle θ and amplitude μ_z in the longitudinal direction. B) The spins arrange in the two orientations (α and β) and distribute randomly over the cones, so there is no transverse magnetization. Adapted from (2).*

The longitudinal magnetization is the sum of μ_z of all spins in the sample. The spins do not have the same phase and their transversal vector components are randomly distributed (Figure 2.2B). Therefore, there is no transverse magnetization in thermal equilibrium and only the longitudinal magnetization vector remains. At thermal equilibrium, the longitudinal magnetization equals:

$$M_0 = (\gamma h)^2 \left(\frac{nB_0}{4kT} \right) \qquad (2.5)$$

which follows from an expansion and truncation of a Taylor series of equation 2.4, assuming that hν is much smaller than kT. In this equation is n the sum of n_α and n_β. For MR purposes, the most used nucleus with spin ½ is the proton (^{1}H), because it has a high natural abundance and high gyromagnetic ratio, which means it has a high sensitivity as can be derived from equation 2.5.

When a radiofrequency (RF) pulse is applied to the spins at the Larmor frequency, the spins will start to arrange more equally over the two energy states and will gain phase coherence. When the pulse is applied long enough, M_0 can be excited completely in the transverse plane (90° degree excitation). The magnetization can even be inverted to the –z-axis (inversion).

After the pulse, the spins will return to thermal equilibrium and lose phase coherence. This process is called relaxation and this process is measured during an MR experiment. The return of the longitudinal magnetization is called T1 relaxation. The loss of phase coherence in the transverse plane is called T2 relaxation. The T1 and T2 relaxation times are tissue dependent.

MR imaging

MRI makes use of the differences in T1 and T2 relaxation times between various tissues. An MRI sequence can be made sensitive to T1 or T2 relaxation to visualize these differences. There are many methods available to make MR images. It is beyond the scope of this thesis to discuss all methods; only the spin echo sequence will be discussed. This sequence starts with a 90° excitation pulse (along the –x axis) to transfer the magnetization to the transverse plane (Figure 2.3B). As the magnetic field has small inhomogeneities, not all spins will have the same Larmor frequency and this will result in dephasing of the spins (Figure 2.3C). After a certain time, defined as half the echo time (TE), a 180° inversion pulse is given along the y axis that will mirror the magnetization vectors with respect to this axis (Figure 2.3D). As the spins will experience the same field inhomogeneities, they will rephase. Complete rephasing will occur after the second delay of half TE and an echo will be formed (Figure 2.3E). There will be some decrease of signal intensity in the transverse plane due to T2 relaxation (microscopic dephasing).

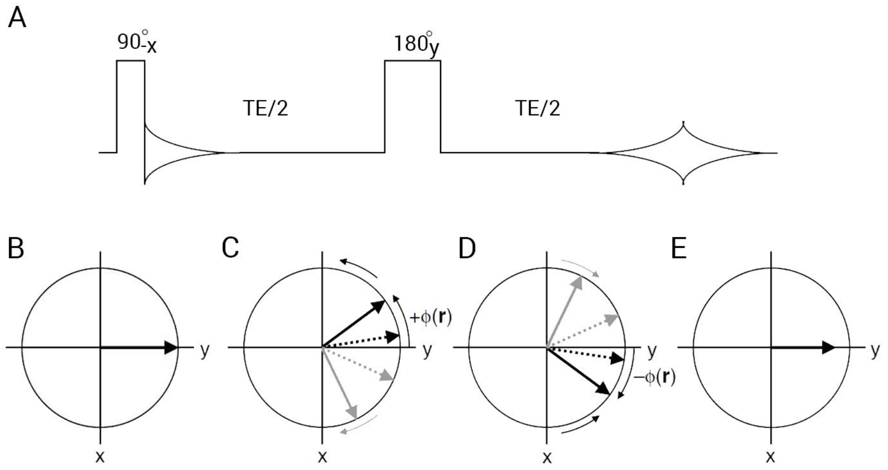

Figure 2.3. *A) The spin echo-experiment, in which a 90˚ excitation and 180˚ inversion pulse are followed by an echo. (B-E) show the orientation of the spins in the transvers plane during the experiment. B) Immediately after the 90˚ pulse there is full coherence of the spins in the transverse plane. C) The spins will lose their coherence dueto inhomogeneities in the magnetic field. D) The 180˚ inversion pulse mirrors all magnetization vectors and due to the same inhomogeneities the spins will rephase. E) At TE complete rephasing has occurred leading to an echo. Source: (2).*

A signal can be recorded during the echo, because the transverse magnetization induces a current in the receive coil. This received signal is transformed into an image. To obtain an image the spin echo sequence described above needs to be expanded with magnetic field gradients. When a magnetic field gradient is turned on, a spatial variation in the magnetic field strength is added to the main magnetic field. As a result, there is a spatial variation

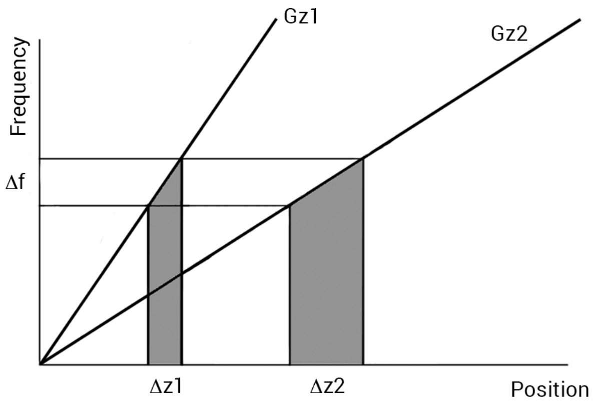

Figure 2.4. *In the presence of a gradient, only the spins with a Larmor frequency within the bandwidth (Δf) of the RF pulse will be excited. The thickness of the slice (Δz) depends on the gradient strength.*

in the Larmor frequency of the spins. When an RF pulse is played out in the presence of a gradient, only the spins with a Larmor frequency within the bandwidth of the pulse will be excited. This way, a slice can be excited of which the thickness can be varied by the strength of the gradient (Figure 2.4).

By applying a slice selection gradient during the excitation and refocusing pulse, the coil will only receive signal from this one slice during the echo. To obtain spatial information within the slice, frequency and phase encoding gradients can be used (Figure 2.5). The frequency encoding gradient is turned on during the acquisition of the echo. As a result, the spins will have a frequency that is dependent on their position along the direction of the gradient. The signal consists thus of a range of frequencies that are proportional to the gradient strength and this can be related to their position.

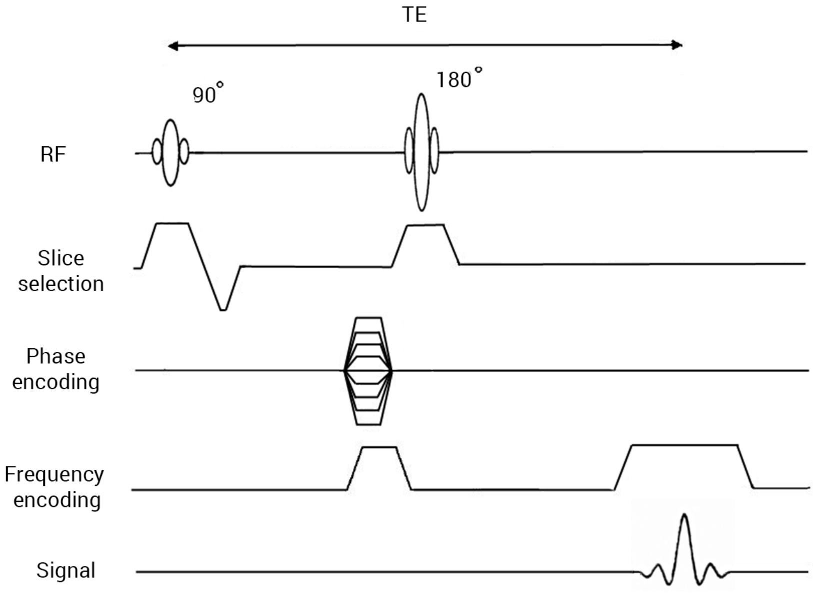

Figure 2.5. *A spin echo sequence consists of a 90° and 180° pulse during which a slice selection gradient is applied. During acquisition of the echo, a frequency encoding gradient is used and after each acquisition the phase encoding gradients are altered. This way, spatial information is obtained that is used to make an image.*

In the last direction phase encoding is used. To this end, a short gradient is applied before acquisition and during this gradient the frequency of the spins is altered. After the gradient, the spins return to their original frequency, but have gained a spatially determined phase shift. One acquisition with a phase shift contains not enough information to obtain all necessary spatial information in this direction. To this end, the gradient strength (and thus the phase shift) is slightly altered in each following acquisition. The number of phase encoding steps necessary depends on the desired resolution. The complete spin echo sequence with gradients in shown in Figure 2.5.

The coil receives signals during the echo and these are stored in a matrix called k-space. The MR image is obtained after Fourier transformation of k-space.

MR Spectroscopy

While MR imaging essentially uses the signal of only water and lipids, a broader range of molecules can be viewed by MRS, as it exploits the specific resonance frequencies (chemical shifts) that MR sensitive nuclei in different chemical groups possess, and which are sensitive to their chemical and physiological environment.

Electronic shielding causes the chemical shift. In a magnetic field, electrons surrounding a nucleus will rotate in such a way that they induce a small magnetic moment in the opposite direction of the spin's precession (Figure 2.6A). This small magnetic moment will reduce the effective magnetic field of the nucleus and in this way, its Larmor frequency.

The resonance frequency of the nucleus (v) is defined as:

$$v = \gamma(1-\sigma)B_0 \qquad (2.6)$$

where σ is the shielding constant. The amount of electronic shielding depends on the atoms close to the proton. Nearby electro-negative atoms will decrease the electronic shielding of the proton and in this way, increase the Larmor frequency (Figure 2.6B). Protons at different positions in a molecule and protons from different molecules will have specific resonance frequencies (Figure 2.6C).

This chemical shift (δ) is expressed in parts per million (ppm):

$$\delta = \frac{\nu - \nu_{ref}}{\nu_{ref}} \cdot 10^6 \qquad (2.7)$$

and v_{ref} is the resonance frequency of a reference compound.

An MR spectrum obtained from a location in the body contains signals of which the patterns and intensity reflect the identity, physiological state and amount of the compounds present at that location. In clinical applications of MRS the proton plays a dominant role, because it is present in most body compounds, and has a relatively high sensitivity. Since clinical MR machines are dedicated to detect protons in water and fat, the hardware is readily available, which simplifies implementation of ^{1}H MRS. However, as the tissue concentration

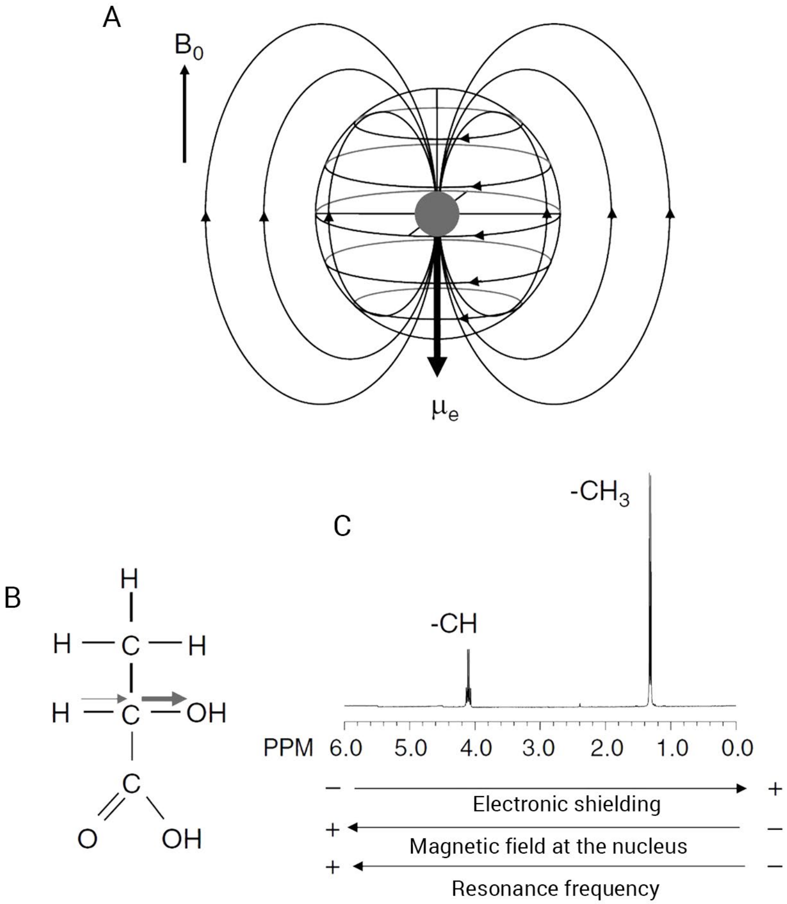

Figure 2.6. *A) Electronic shielding: a nucleus is surrounded by electrons that induce a small magnetic moment* μ_e*.* μ_e *has the opposite direction as the nuclear spin and this lowers the effective magnetic field of the nucleus and thus its Larmor frequency. B) The lactate molecule possesses an electro-negative oxygen atom that shifts electrons from the protons away from the nucleus and reduces its electronic shielding,which results in an increase in the Larmor frequency. The protons in the methylgroup experience a different electronic shielding than the other non-exchangeable proton and have thus a different Larmor frequency (chemical shift). C) Their differences in chemical shift (expressed in parts per million (ppm)) are visible in the spectrum. Source: (2).*

of biochemicals is much lower than that of water, their detection at sufficient signal-to-noise (SNR) is only possible at a relatively low spatial resolution and for metabolite levels above ~ 0.5 mM. This implies that MRS is not suited for detailed anatomical imaging, but rather for a coarse spatial mapping of metabolism and physiology.

Besides differences in chemical shift, there is another feature that can be used to distinguish between different biochemicals, that is, the splitting of resonances due to scalar coupling. This coupling comes from the electrons in the chemical bonds between two nuclei. In an isolated atom, the electron spin and nuclear spin prefer an anti-parallel arrangement. When there are two uncoupled protons with a different chemical shift, there are four different energy states possible, these are shown in Figure 2.7A. There are four permitted transitions and the energy differences for the two transitions of proton 1 are both equal (= hv_{H1}) and both transitions of proton 2 are hv_{H2}. Therefore, the corresponding spectrum will show two spectral lines (singlets) positioned at the chemical shifts of proton 1 and 2 (Figure 2.7C).

When the atoms are coupled, slight changes in the energy levels occur due to the Pauli exclusion principle. This principle demands that the electron spins in a bond are in anti-parallel orientation. This leads to less favorable energy states for the α-α and β-β spin states, where the nuclear spins cannot be both anti-parallel to the electron spins. As a consequence, the energy increases with an amount of J/4, where J is the scalar coupling constant, also known as J-coupling constant.

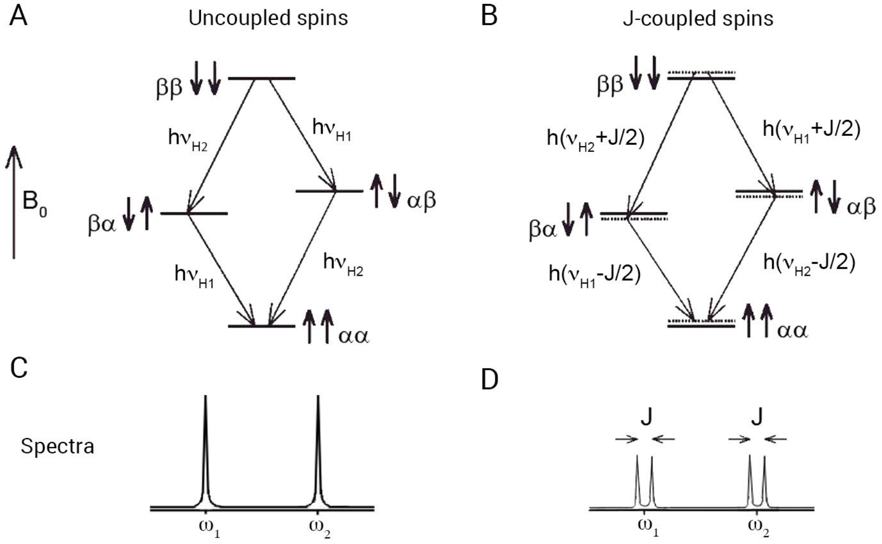

Figure 2.7. *The effect of J-coupling on the spectra. A and B show the energy levels for two spins with different chemical shifts and the possible transitions. There are four energy levels for these two spins; both spin state α (lowest energy state), one spin α and one spin β, and both spin β (highest energy state). A) For uncoupled spins are the energy differences for both transitions of proton 1 equal (=hv_{H1}), as are the energy differences for proton 2 (=hv_{H2}). As a result, there are two spectral lines in the corresponding spectrum in C. B) For coupled spins, the bonding electrons cannot be anti-parallel to the nuclear spins for the α-α and β-β spin states, leading to energetically less favorable states. This leads to slight changes in the energy differences. The energy differences for the two transitions of proton 1 are no longer equal: $h(v_{H1}+J/2) \neq h(v_{H1}-J/2)$. As a consequence, small changes in the frequencies occur and this results in a splitting of the resonances in the spectrum in D.*

In the α-β and β-α spins states, the nuclear spin and electron spins can be in anti-parallel directions, which leads to an energetically more favorable state and an energy decrease of J/4 (Figure 2.7B). The energy differences for the two transitions of proton 1 are no longer equal: $h(v_{H1}+J/2) \neq h(v_{H1}-J/2)$. This leads to small changes in the Larmor frequencies and results in a splitting of the resonances in the spectrum (Figure 2.7D). In principle scalar coupling constants are considered for one chemical bond; however, ^1H-^1H interactions stretch over three bonds.

MR Diffusion-weighted Imaging

Water molecules are in constant Brownian motion. When this random motion of the water molecules is unrestricted, the molecules can diffuse freely. The Einstein relation describes how the mean square displacement ($<\Delta r^2>$) of a particle over a certain time (Δt) depends on the diffusion coefficient (D):

$$< \Delta r^2 >= 6D\Delta t \qquad (2.8)$$

The diffusion coefficient depends on the mass of the molecules, the temperature and viscosity of the medium (3). Assuming a D in biological tissue of $1 \cdot 10^{-9}$ m^2/s (4) and a Δt of 50ms, an average displacement of water molecules of approximately 17 μm can be derived (equation 2.8). As a typical cell has a diameter of about 10 μm, this means that the water molecules will encounter cell membranes during the diffusion time. This will restrict the motion of the water molecules. As a result, in a diffusion-weighted MR experiment, not purely the true diffusion coefficient is measured. We speak therefore of the apparent diffusion coefficient (ADC).

The degree of movement can be visualized with MR by extending the spin echo sequence with diffusion-sensitizing gradients as described by Stejskal and Tanner (5). They placed two strong gradients around the 180° pulse. During the first diffusion gradient, all spins will gain a phase shift due to the imposed gradient. The 180° pulse mirrors the magnetization vectors. During the second gradient, the static spins will rephase and no signal loss due to the gradients has occurred. However, the water molecules that have moved between the two gradients will not completely be rephased and a signal loss will occur (Figure 2.8).

The signal attenuation is expressed as:

$$\frac{S}{S_0} = \exp\left(-bADC\right) \qquad (2.9)$$

in which S_0 is the signal intensity without diffusion weighting, S is the signal intensity with diffusion weighting and b is the diffusion-sensitizing factor (also known as b-value).

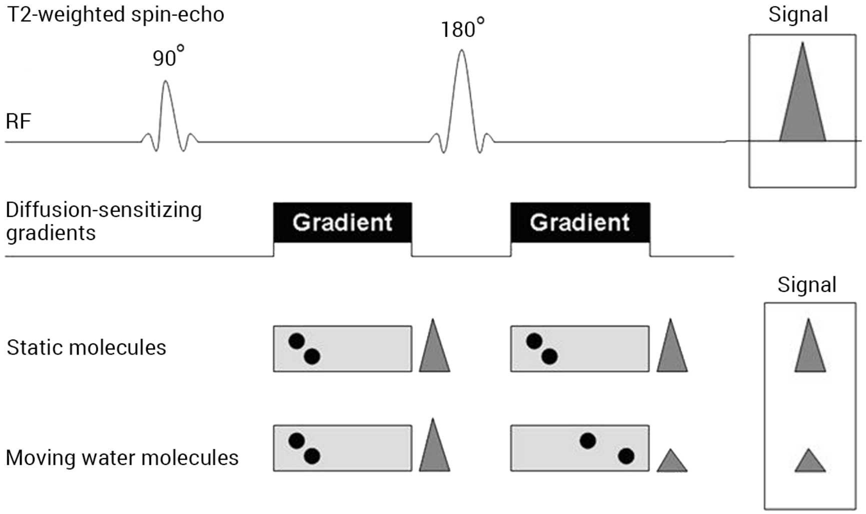

Figure 2.8. *Spin echo sequence expanded with diffusion-sensitizing gradients around the 180° pulse. During the first gradient, all molecules will gain a phase shift. This phase shift is rephased by the second gradient for static molecules and no signal loss due to the gradients will occur. The phase shift of moving water molecules will not be re-phased completely during the second gradient, leading to a signal loss. Source: (6).*

The b-value can be calculated in the following way:

$$b = \gamma^2 G^2 \delta^2 \left(\Delta - \frac{\delta}{3} \right) \qquad (2.10)$$

in which G is the strength of the gradient, δ is the duration of the gradient and Δ is the time between the gradients.

The chosen b-value determines what kind of diffusion is visible in the diffusion image. In a low b-value (50-100 s/mm^2) image, large diffusion distances are needed to evoke signal attenuation. This is mostly intravascular diffusion and these images show tissue perfusion. Higher b-values are used to study water molecules that move slower or are more restricted by the tissue. A limitation of b-value images is that T2 relaxation effects are also present in the image. To overcome this problem, ADC maps were introduced that are calculated using multiple b-value images. The ADC value is a quantitative measure that is obtained by plotting an exponential function through the plot of the signal intensity against the b-value (Figure 2.9). The higher the ADC value, the more freely the water molecules can move.

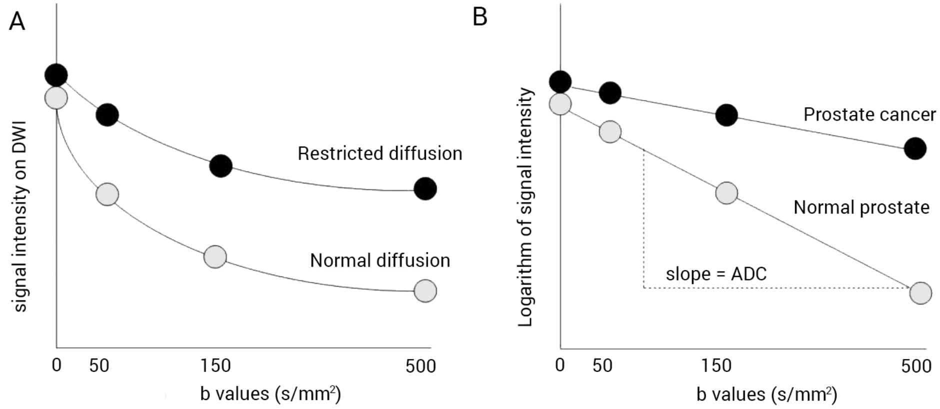

Figure 2.9. *Calculation of the ADC value. A) The signal intensity depends on the used b-value and type of tissue studied. B) To calculate the ADC value, the logarithm of the signal intensity is plotted against the b-value. The ADC value corresponds to the slope of the plotted line. Adaptedfrom: (7).*

Hardware for MR of the prostate

MR images and spectra of the prostate are commonly obtained with a body coil for excitation and a external phased array coils around the pelvic area for data acquisition. It is fortuitous, for MR purposes, that the prostate can also be approached with a local loop via the rectum. The addition of an endorectal coil for MR signal reception gives a substantial gain in local SNR, which can be exploited in MRS and DWI to obtain a better resolution with improved clinical performance. Disadvantages of the use of an endorectal coil are patient discomfort, additional costs and the need for proper placement of the coil, which requires some skill and is time-consuming. There are inflatable and rigid endorectal coils in use. Inflatable endorectal probes are commonly used with a coil placed within a double balloon of which, after insertion in the rectum, the inner one is filled to press the coil close to the prostate (Figure 2.10).

Inflatable coils can cause more compression of the prostate in the anterior/posterior direction than rigid coils (8). However, inflatable coils have a larger field of view and perhaps show less motion artifacts than rigid probes (9). Another advantage of inflatable coils is that the balloon can be filled with a tissue susceptibility matching fluid (e.g. perfluorcarbons) to avoid susceptibility problems due to air-tissue borders. This leads to better shim results than air-filled or rigid coils (9). The reception profile of the endorectal surface coil shows a spatial variation, which may be compensated for (10).

At 1.5 T the use of an endorectal coil for prostate MRSI is recommended if spatial resolutions below about 1 cm^3 are desired (11), as the SNR at such resolution will be relatively low with only external phased-array coils (12), which may result in poor quality data (13). Compared to 1.5 T, MRS at 3 T can have a better SNR and chemical shift dispersion. This better SNR may be used for MRSI without an endorectal coil depending on factors such as desired voxel size (11,14,15). A doubling in SNR was reported when moving from 1.5 T to 3 T for prostate MRS (16). A relative increase in SNR may also be caused by reduced intra-voxel dephasing if a higher spatial resolution is selected (16). At 3 T, a small but significant increase in the performance of MR spectroscopy for cancer localization was observed when an endorectal coil was compared to solely external phased-array coils (17). Thus the choice to perform MRSI at 3 T with or without endorectal coil mainly depends on the preference for best practicality or optimal spatial resolution. Also DWI can benefit from the gain in SNR. In several studies the endorectal coil is used for DWI of the prostate (e.g. (18-21)). The increase in SNR can be used for increased image quality of increased spatial resolution.

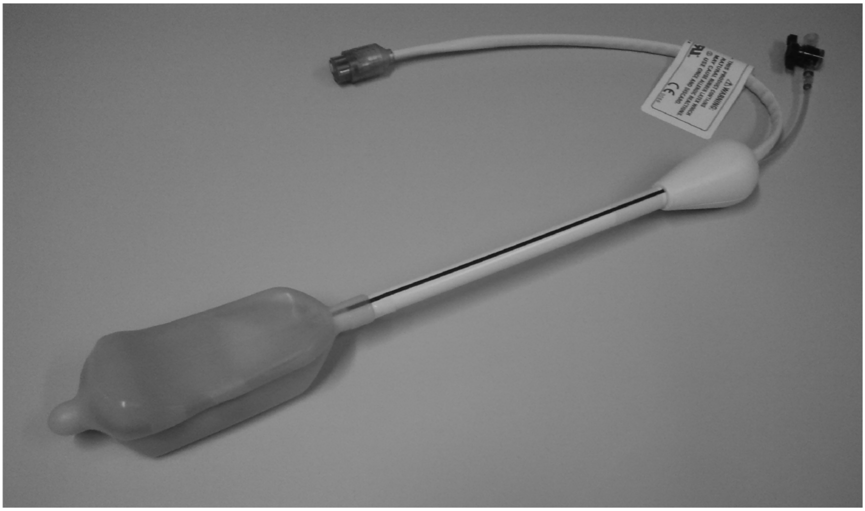

Figure 2.10. Endorectal coil for prostate MR imaging and spectroscopy.

MR spectroscopic imaging of the prostate

About 20 years ago it was demonstrated that ^{1}H MR spectra of extracts of prostate tissue showed a number of metabolite signals, including proton signals from citrate (Cit) and choline (Cho) compounds and that those of Cit were decreased and those of Cho compounds were increased in prostate cancer (22,23). After the introduction of endorectal coils it also became possible to obtain *in vivo* ^{1}H MR spectra of small volumes (down to approximately 0.3 cm^3) of the prostate with sufficient SNR (24-26). The dominant peaks observed in these spectra included those from protons in Cit (at 2.6 ppm) and Cho compounds (total cholines at about 3.2 ppm). Compared to healthy peripheral zone or BPH tissue the signals of Cit were reduced and those of Cho often increased in cancer tissue. Other prominent signals in prostate spectra are the methyl protons of creatine (at about 3 ppm) and usually also a set of signals for coupled polyamine protons in the same spectral region. Figure 2.11 shows a typical spectrum of healthy peripheral zone tissue obtained at 3 T with a point resolved spectroscopy (PRESS) sequence and TE of 145 ms.

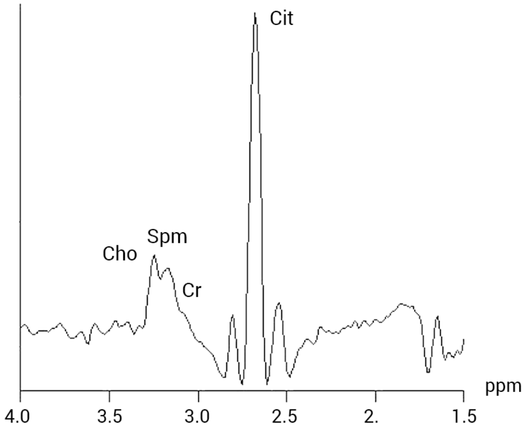

Figure 2.11. *Typical prostate spectrum of normal peripheral zone obtained with a PRESS sequence and a TE of 145 ms. The spectrum contains the metabolites Cho, spermine (Spm), creatine (Cr) and Cit.*

Because prostate cancer is often multifocal and tumor tissue can occur anywhere in the prostate it became clear that multi-voxel acquisition is preferable in clinical studies. As the prostate is relatively small and surrounded by adipose tissue, this required the implementation of advanced RF pulses and sequences to suppress interfering strong lipid signals. In this way 2 and 3-dimensional MR spectroscopic imaging sequences were realized (14,24,27,28) of which 3 dimensional (3D) variants are most favored as these can cover the whole prostate.

An important step in the ^{1}H MRSI acquisition protocol is the optimization (shimming) of the B_0 field homogeneity. Bad homogeneity spoils spectral quality as it broadens the spectral lines, due to a faster decay of the apparent transverse magnetization. This will complicate good separation of metabolite signals, especially in the Cho, polyamine and creatine region, and hampers a reliable recognition and quantification of the metabolites. Good homogeneity is also essential for effective water and lipid signal suppression, as broadened or shifted signals may escape the frequency selective pulses needed for this suppression.

Localization protocols

In 1990, the first publication on *in vivo* ^{1}H MR spectroscopy of the human prostate appeared (29). MR spectra were acquired with a spin echo sequence and the field of view of the rigid endorectal coil determined the localization (29). Later, localized single voxel spectra were obtained by point resolved spectroscopy (PRESS) (30) or stimulated echo acquisition mode (STEAM) (25). In the same period MRSI of the prostate was introduced (24,26,27). MRSI with PRESS localization is now the most common method in the clinic to acquire prostate MR spectra. Currently, 3D acquisitions at 1.5 – 3 T with sufficient SNR can be typically performed in 8 – 15 minutes at spatial resolutions down to ~ 0.3 cm^3, depending whether an endorectal coil is used or not. A certain spatial resolution is important as tumor foci of < 0.5 cm^3 are assumed to be clinically insignificant (31).

For localization, spectral-spatial selective pulses can be used that prevent excitation of peri-prostatic lipids and water (16,32-34), but not all vendors have implemented these pulses. A common alternative is to use dual frequency pulses, added to a PRESS sequence for selective lipid and water suppression (double band-selective inversion with gradient dephasing (BASING) (34,35) or Mescher-Garwood (MEGA) (36)). Dual frequency pulses, surrounded by crusher gradients, selectively invert and dephase the lipid and water signals. Furthermore, outer volume saturation (OVS) slabs are placed around the prostate to decrease lipid signals. In these slabs, all signals are spatially excited and crushed by a series of dephasing gradients. OVS pulses have been optimized to further improve lipid suppression (37). Placement of these slabs is a subjective and time-consuming process, and only a limited number of slabs can be placed (Figure 2.12). Therefore, automated placement of these saturations slabs around the prostate has been developed (38,39), in which the number of OVS slabs can be increased through temporal ordering of the saturation slabs and flip angle modifications (39). While these methods still segment prostate volumes manually, MR vendors are working on complete automation of this segmentation, volume of interest (VOI) and field of view (FOV) selection, matrix size determination and OVS placement. This automation is an important step to encourage routine clinical use.

In classical MRSI the limited number of steps in k-space acquisition causes signal contamination between neighboring voxels due to the side-lobes of the spatial response function (SRF). This contamination may be substantial if peri-prostatic areas with high lipids are included in the VOI. Optimization of the SRF helps to minimize contamination of these peri-prostatic lipid signals. One can smooth the SRF by applying an apodization filter in k-space, at the cost of some sensitivity loss and reduced spatial localization due to an increased voxel size (40). A Hanning window is a good compromise between sensitivity loss and improved SRF (40,41). As the whole k-space is sampled equally, this is a time inefficient approach. When k-space is sampled with a scheme similar to a Hanning function, the sensitivity can be preserved while improving the SRF (14,41).

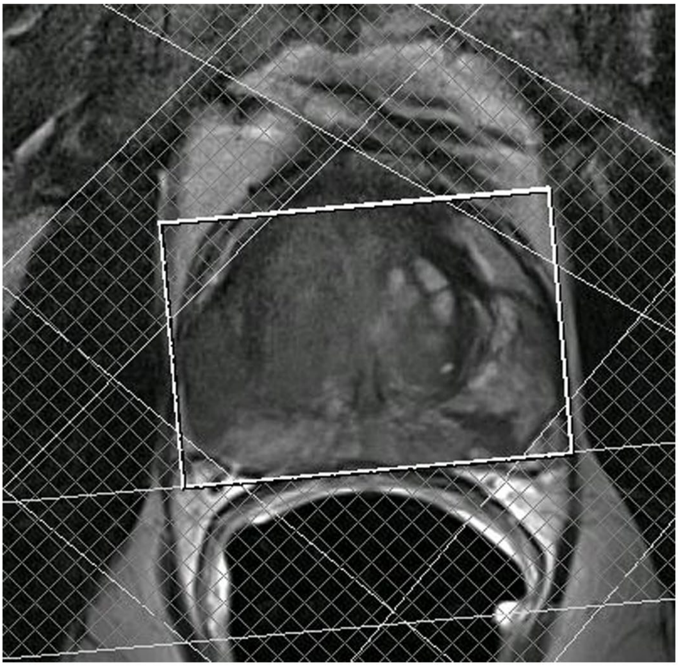

Figure 2.12. *T2-weigthed image of the prostate of a 54-year-old man with biopsy-proven prostate cancer. The white box indicates the volume of interest and outer volume saturation slabs for lipid suppression surround the prostate.*

Another approach to prevent lipid contamination is the use of very accurate localization techniques, such as selective adiabatic refocusing (LASER). When combined with positioning of the VOI completely within the prostate, LASER or semi-LASER volume selection is precise enough not to excite or refocus peri-prostatic lipids (42,43). However, as 70% of the prostate tumors occur in the peripheral zone, the usability of this approach is limited. A more practical approach would be the use of parallel transmit systems that enables the use of spatially customized RF pulses to excite only the prostate, although the demanded accuracy could be a challenge. These techniques were developed for higher field systems (44,45), but will probably find their way to the clinic, as 3T-systems nowadays can be equipped with multi-channel transmit arrays.

Prostate MR spectroscopy is prone to movement artifacts, due to the location of the prostate near the bowels and the relatively long acquisition times. To limit bowel movement, patients often receive an injection with anti-peristaltic drugs (e.g. glucagon or butylscopolamine bromide (Buscupan)). The use of a navigator has been proposed to reduce motion artifacts (46). The examination time can be reduced by weighted k-space sampling as described above. Implementation of spiral readout gradients could be used for acceleration as well as for correction of motion-induced phase variations, as each spiral starts in the center of k-space (47). Methods proposed to further decrease the acquisition time of prostate MRSI are e.g. flyback echo-planar encoding (48) and compressed sensing (49); however, these approaches come at an SNR cost, and will only be of use in a non-SNR-limited regime.

Origin of the signals in prostate MR spectra

In particular for Cit it is of interest to consider its origin. It is well known that the normal human prostate accumulates Cit at high levels, in particular in the peripheral zone (50,51), mainly because in epithelial cells the oxidation of Cit is inhibited by the interaction of zinc ions with the mitochondrial enzyme m-aconitase (52). Although this results in an increased Cit level in epithelial cells (e.g. estimated between 1 and 2 mM in epithelial cells of the rat ventral prostate (50)), the majority of Cit is excreted into the luminal space. Cit levels in prostatic fluid between about 50 – 150 mM have been reported (50,52,53). As the volume percentage of the luminal space in the normal peripheral zone is approximately 30% (54) this means that in a spectroscopic voxel the average Cit level in the peripheral zone should be between about 15 and 50 mM. This is confirmed by absolute Cit levels estimated from MRS measurement which revealed mean peripheral zone levels of about 40 mM (55,56); a similar concentration for glandular tissue was calculated from high-resolution magic-angle spectroscopy (HRMAS) spectra (57). Interestingly in glandular BPH tissue Cit levels are increased (52,55,56). This may differentiate it from stromal BPH, which has a lower Cit level (57).

Polyamines, of which 50% - 95% is spermine (58,59), are secreted by specialized ductal cells in the prostate (60). In accordance with accumulation in the luminal space a linear relationship is observed between the content of polyamines and Cit (57,61,62). It has been suggested that such a relationship exists because of the association between spermine and Cit, which have opposite polarity (61). The tissue concentration of polyamines in the normal prostate has been reported to be about 12 mM (53). HRMAS studies have estimated their tissue content between 3 – 20 mmol/kg, with a low content for stromal tissue and high content for glandular tissue (57).

Prostatic fluid contains relatively little Cho and creatine (61,63), thus the signals from these compounds come essentially from within prostate cells, which could be epithelial or stromal cells (mostly smooth muscle cells and fibroblasts). E.g. it may be expected that the coinciding signals of creatine and phosphocreatine at about 3.0 ppm largely arise from smooth muscles, which are the dominating component in the stromal fraction (64). From *in vivo* MRS measurements it was estimated that in normal prostate the average total Cho levels were 3.1 mM and total creatine 4.4 mM (24). HRMAS studies estimated total Cho to be about 7 mmol/kg and total creatine about 8 mmol/kg (57).

Cancer MR spectroscopy biomarkers

Already in 1964 it was reported that Cit levels are decreased in prostate cancer (65). Later this was attributed to a decreased zinc build up in the process towards malignancy with consequent Cit oxidation in the Krebs cycle, leading to less Cit in malignant epithelial cells (52). Indeed, a relationship between the expression of the enzymes m-aconitase and acetyl citrate lyase and prostate Cit levels has been observed (66). However, it is also known that cancer growth decreases the luminal space and this inevitably causes lower tissue levels of Cit, even if Cit production would not diminish. For instance, it has been reported that in Gleason 6 and 7 cancers the luminal space fraction in the peripheral zone decreases from 30% to about 13% (54). Thus it is most likely that the decrease in Cit signal seen in voxels with prostate cancer is largely due to a decrease of luminal space; and thus reports a morphological change (Figure 2.13). As alterations in Cit metabolism have been proposed to occur in a premalignant stage before major histopathological changes are apparent (51), it would be of interest if lower Cit levels could be identified in this stage by *in vivo* MRS. Indeed, in premalignant lesions (high-grade prostatic intraepithelial neoplasia) a metabolic profile between normal peripheral zone and cancer tissue was seen, but it was unclear if this involved a lower Cit amount as only relative metabolite levels were assessed (67). It was concluded that this would not confuse cancer detection by MRSI as these nodules occur infrequently and generally are small compared to the MRSI voxel size. In this respect ^{1}H HRMAS of representative biopsy tissue may be more informative (66,68,69).

It is well established that polyamine signals decline in prostate cancer tissue (57,59,62,68,70). This goes together with the decline in Cit signals, which is in line with a reduction of the ductal space due to cancer growth. Despite the difficult quantification of the polyamine signals it is increasingly more used as an additional biomarker to assess the presence of prostate cancer *in vivo* (71).

A metabolic hallmark of malignant transformation is a change in Cho metabolism (72), which commonly results in an increase in the methyl proton signal of Cho compounds at 3.2 ppm in MR spectra. For the prostate this makes the ratio of the signals of Cho compounds over Cit signals an attractive index for the presence of prostate malignancy. From *in vitro* nuclear magnetic resonance studies of biopsy extracts the peak of “choline compounds” at 3.2 ppm turned out to be mainly composed of the resonances originating from protons in methyl groups of choline, phosphocholine and glycerophophocholine. The ^{1}H chemical shift dispersion of the methyl protons is too small to be resolved in the *in vivo* spectrum and therefore the composite peak at about 3.2 ppm is commonly referred to as the total Cho peak, although it may also contain (smaller) contributions from other compounds (e.g. taurine, ethanolamine and myo-inositol (73)).

The Cho compounds are involved in the biosynthesis and degradation of phospholipids

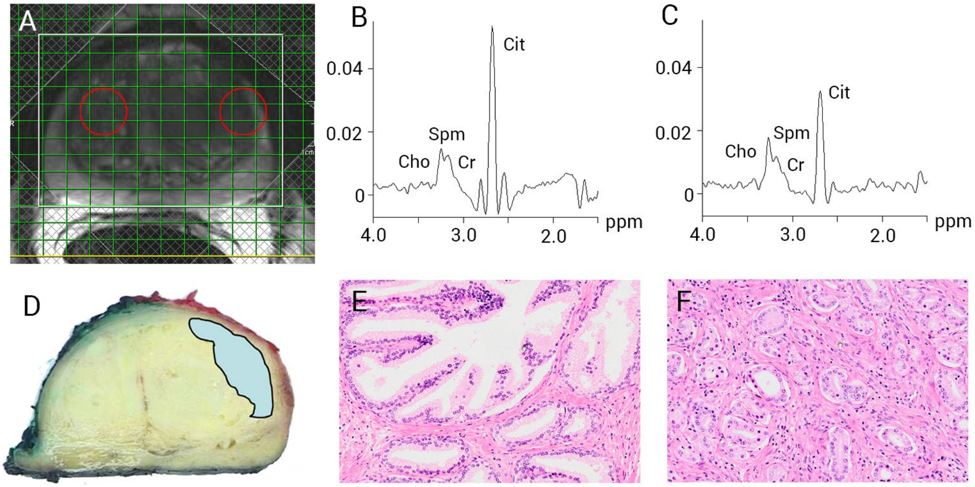

Figure 2.13. *A) T2-weigthed image of the prostate of a 53-year-old man with biopsy-proven prostate cancer in the left transition zone. B) Spectrum of normal peripheral zone tissue (left sphere in A) containing Cho, creatine (Cr), spermine (Spm) and Cit resonances.C) Spectrum of tumor tissue (right sphere in A) showing increased Cho and decreased Cit levels compared to B. D) Corresponding slice of the excised prostate indicating the tumor. E) Hematoxylin and eosin stained tissue of normal tissue and tumor tissue (F) of this patient.*

such as phosphatidylcholine, which is required for the build-up and maintenance of cell membranes. More specifically the signals of phosphocholine and glycerophosphocholine increase in tumors (72,73). The exact reason behind this increase is still a matter of research, but may be caused by increased Cho transport into tumor cells, increased choline kinase

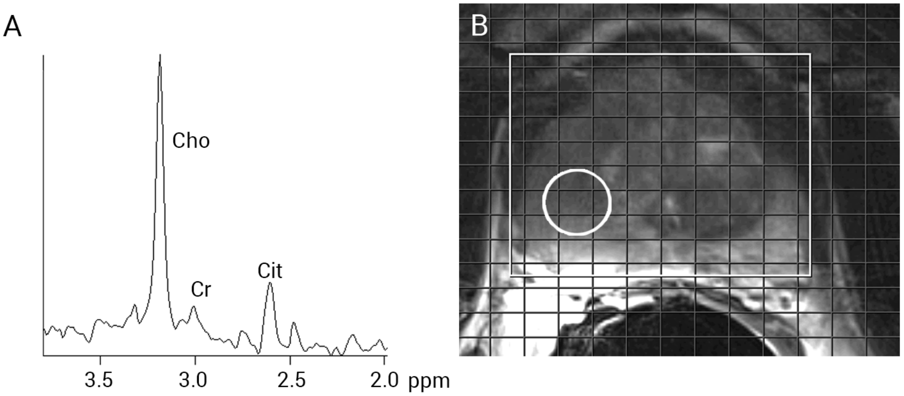

Figure 2.14. *A) Spectrum of tumor tissue showing high Cho and low creatine (Cr) and Cit resonances. B) T2-weighted image of a 71-year-old patient with a Gleason 9 tumor in the peripheral zone. The white circle indicates the location and true voxel size (after filtering and zero-filling) of the spectrum in A.*

activity and increased phospholipase expression and activity in tumors. Increases in the total Cho peak have also been associated with increased cell density and tumor hypoxia (74). For high grades of prostate cancer sometimes a very high Cho to creatine ratio can be observed (Figure 2.14), which also may reflect replacement of smooth muscle tissue by tumor cells.

Potentially confounding spectral features in prostate cancer identification

Obviously, the dominant luminal origin of Cit and polyamine signals *in vivo* implies that any prostate condition, which substantially reduces the luminal space, may also lower these signals. For instance this could happen with inflammation of the prostate, but in a 2D MRSI study of patients clinically diagnosed to suffer from chronic prostatitis, we did not see a change in relative Cit levels (75). However, in other studies some, but not all, prostatitis lesions occurring in prostates next to cancer tissue did mimic the *in vivo* MRS profile of prostate cancer tissue (76,77). The differentiation of prostatitis from prostate cancer is also difficult for other MR approaches (78).

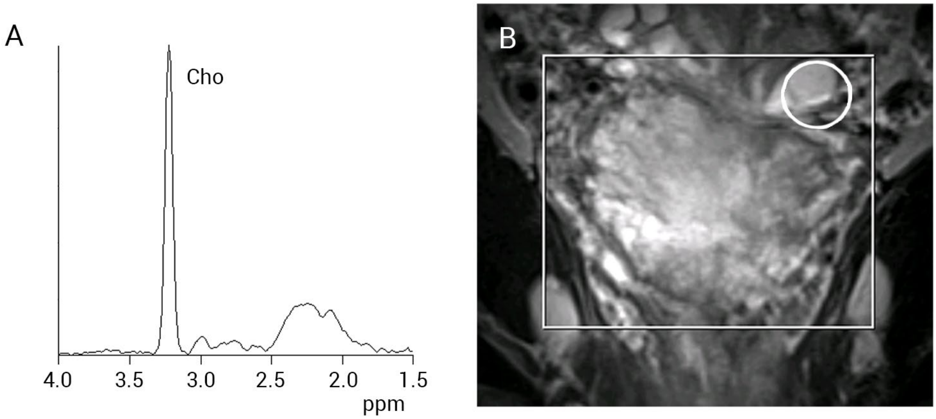

Figure 2.15. *A) Spectrum of the seminal vesicles showing a high total Cho content. B) T2-weighted image of a 63-year-old patient with small cancer lesions in the peripheral zone. The white circle indicated the location and true voxel size (after filtering and zero-filling) of the spectrum in A.*

In the analysis of patient data it should also be taken into account that different regions of the healthy prostate such as peripheral zone, transition zone, and areas close to the urethra, the seminal vesicles and anterior fibromuscular stroma may have a different metabolite composition. For instance, seminal fluid contains relative high levels of cholines (79), which may affect spectra of voxels close to or overlapping the seminal vesicles (Figure 2.15). Cit levels are highest in the normal peripheral zone and lower in areas close to the urethra. If BPH is mainly of stromal origin this can result in relative low Cit levels (57).

In addition, post-biopsy changes may affect spectral appearances. MRS has to be performed sufficiently delayed with respect to the time of biopsy to avoid a possible deleterious effect of a hemorrhage on spectral quality, due to magnetic field or morphological distortions (80). The presence of hemorrhages is best detected on T1-weighted MRI (81).

Diffusion-weighted imaging of the prostate

The use of DWI for prostate MR examinations was introduced almost a decade later than MR spectroscopic imaging (82). Nevertheless, at this moment, DWI is more routinely used in clinical MR exams of the prostate. The technique is simple, fast and, in contrast to MRSI, readily available on clinical MR systems.

Acquisition protocols

DWI of the prostate is often based on a spin echo sequence with diffusion gradients and an echo planar imaging read-out. As DWI is very sensitive to motion artifacts, fast acquisition is required. This was enabled by the introduction of echo planar imaging read-out and the use of parallel imaging. The administration of anti-peristaltic drugs is also advisable for prostate DWI to minimize motion artifacts. Usually, diffusion weighting gradients in three orthogonal directions are used. The European Society of Urogenital Radiology (ESUR) recommends the use of at least 3 b-values: 0, 100 and 800–1000 s/mm^2. They recommend to make an ADC map by excluding the b-0 image and not to use b-values higher than 1000 s/mm^2 for the ADC

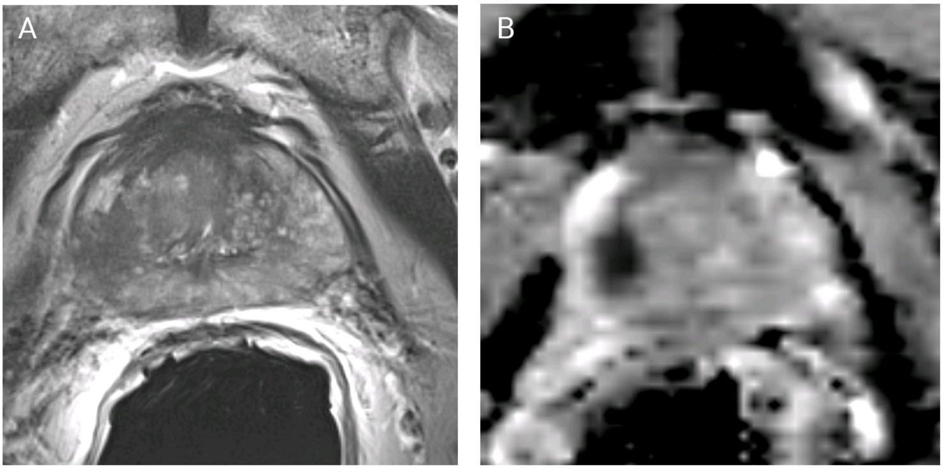

Figure 2.16. *A) T2 weighted image of the prostate of a 68 year-old patient with proven prostate cancer. A tumor with Gleason score 3+4 is present in the right peripheral zone. B) Corresponding apparent diffusion coefficient map showing a hypointense region at the tumor location, indicative for reduced diffusion. For this map b-values of 50 and 800 s/mm^2 were used.*

calculation (11). In literature many different settings are used for DWI of the prostate and determination of the ADC map e.g. (20,83-85). The ADC maps can be generated automatically by the MR system. An example of an ADC map of the prostate is shown in Figure 2.16.

To obtain a certain b-value, either the gradient strength, time between the gradients or duration of the gradient can be adapted (equation 2.10). As there is a limit to the gradient strength that can be used, long diffusion times are required to get high b-values. A diffusion interval between 40 to 80 ms is often used on clinical systems (86). The diffusion measurement is thus limited by SNR and T2 relaxation time. Therefore, it is recommended to use a TE as short as achievable (typically <90 ms) (11).

As the SNR has to be high enough for DWI, the technique can benefit from the use of an endorectal coil and a higher field strength. This allows for higher image quality and increased spatial resolution. However, at higher field strength also larger susceptibility artifacts have to be overcome. When an endorectal coil is used for signal reception, more signal will come from the prostate area close to the endorectal coil. Since this coil profile is present in all b-value images, this effect is eliminated in the ADC map. At 1.5 T, axial slices of 5 mm thick and an in-plane resolution of 1.5×1.5 mm to 2.0×2.0 mm are used, while at 3 T, we can go to 4 mm thick slices with a resolution of 1.0×1.0 mm to 1.5×1.5 mm (11).

Features and information content of DWI of the prostate

The information that is obtained in a DWI experiment depends on the chosen settings. When a short diffusion time is chosen (and the gradient strength is increased to obtain a certain b-value), the average displacement of water molecules is smaller than the cell dimensions. This measured ADC value will be more a reflection of the true diffusion coefficient of the tissue (87). However, at longer diffusion times the water molecules will encounter barriers like cell membranes. Cell membranes are not impermeable for water molecules, but passing the cell membrane takes time. This hinders the water molecules and the ADC value reflects therefore more the compartmentalization of the tissue. In the prostate, there is a lot of glandular tissue. The size of the acini is much larger than cells, 0.3-0.5 mm on average in healthy tissue (88). The healthy peripheral zone contains approximately 30% of luminal space (54), in which the water molecules feel less restriction. As a consequence, healthy peripheral zone has a low signal intensity on high b-value images (figure 2.17) and a high signal intensity on the ADC map (18,82,89).

In the transition zone often BPH occurs. BPH can have different appearances: it can be more glandular, more stromal, but often it is a mix between these glandular and stromal. The different compositions of the transition zone give rise to contrast differences in T2 weighted images (90) and ADC maps (83). The ADC value in glandular hyperplasia is higher than in stromal hyperplasia (83), which can be explained by the larger degree of freedom of the

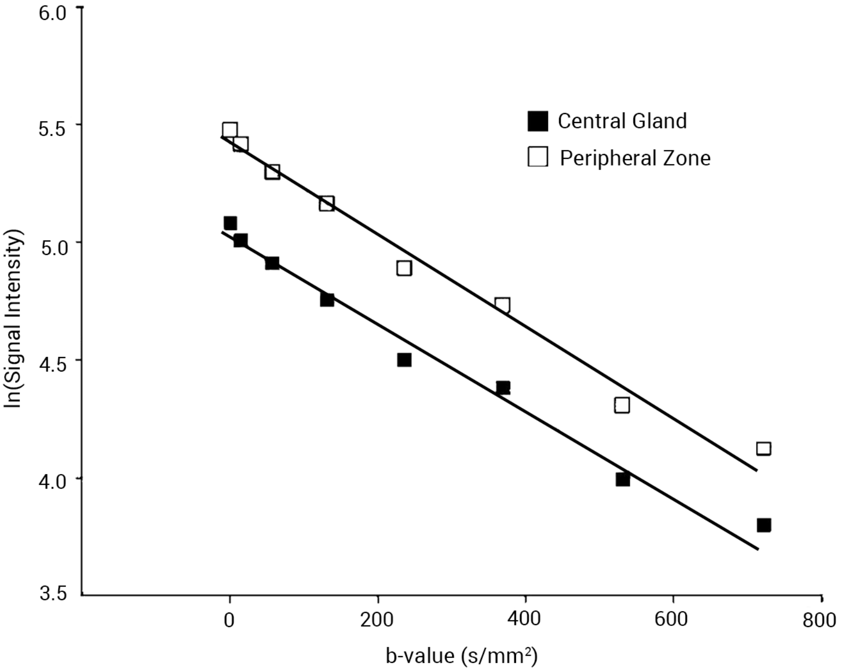

Figure 2.17. The logarithm of the signal intensity on normal appearing central gland and peripheral zone tissue for several b-values (82).

water molecules to diffuse in the glandular tissue.

In tumor tissue, there is a loss of glandular structure and an increased cellularity. This leads to lower ADC values than for the healthy peripheral zone (54,82,89). A correlation was reported between the ADC value and the histological grades of prostate cancer (well, moderately or poorly differentiated cells) (91). Furthermore, significant correlations between the ADC value and the cellularity and the area of luminal space are reported (54).

References

1. Hoeks CMA, Barentsz JO, Hambrock T and others. Prostate cancer: Multiparametric MR imaging for detection, localization, and staging. Radiology 2011;261(1):46-66.
2. De Graaf RA. In Vivo NMR Spectroscopy - 2nd Edition Principles and Techniques: John Wiley & Sons Ltd; 2007.
3. Le Bihan D. Looking into the functional architecture of the brain with diffusion MRI. Nat Rev Neurosci 2003;4(6):469-480.
4. Sukstanskii A, Yablonskiy D, Ackerman J. Effects of permeable boundaries on the diffusion-attenuated MR signal: insights from a one-dimensional model. J Magn Reson 2004;170(1):56-66.
5. Stejskal EO, Tanner J. Spin diffusion measurements: Spin echoes in the presence of a time dependent field gradient. J Chem Phys 1965;42:288.
6. Koh D-M, Collins DJ. Diffusion-weighted MRI in the body: applications and challenges in oncology. Am J Roentgenol 2007;188(6):1622-1635.
7. Qayyum A. Diffusion-weighted imaging in the abdomen and pelvis: concepts and applications. Radiographics 2009;29(6):1797-1810.
8. Kim Y, Hsu ICJ, Pouliot J, Noworolski SM, Vigneron DB, Kurhanewicz J. Expandable and rigid endorectal coils for prostate MRI: Impact on prostate distortion and rigid image registration. Medical Physics 2005;32(12):3569-3578.
9. Noworolski SM, Crane JC, Vigneron DB, Kurhanewicz J. A clinical comparison of rigid and inflatable endorectal-coil probes for MRI and 3D MR Spectroscopic Imaging (MRSI) of the prostate. Journal of Magnetic Resonance Imaging 2008;27(5):1077-1082.
10. Noworolski SM, Reed GD, Kurhanewicz J, Vigneron DB. Post-processing correction of the endorectal coil reception effects in MR spectroscopic imaging of the prostate. J Magn Reson Imaging 2010;32(3):654-662.
11. Barentsz JO, Richenberg J, Clements R, Choyke P, Verma S, Villeirs G, Rouviere O, Logager V, Fütterer JJ. ESUR prostate MR guidelines 2012. Eur Radiol 2012;22(4):746-757.
12. Kaji Y, Wada A, Imaoka I, Matsuo M, Terachi T, Kobashi Y, Sugimura K, Fujii M, Maruyama K, Takizawa O. Proton two-dimensional chemical shift imaging for evaluation of prostate cancer: external surface coil vs. endorectal surface coil. J Magn Reson Imaging 2002;16(6):697-706.
13. Lichy MP, Pintaske J, Kottke R and others. 3D proton MR spectroscopic imaging of prostate cancer using a standard spine coil at 1.5 T in clinical routine: a feasibility study. Eur Radiol 2005;15(4):653-660.
14. Scheenen TW, Klomp DW, Roll SA, Futterer JJ, Barentsz JO, Heerschap A. Fast acquisition-weighted three-dimensional proton MR spectroscopic imaging of the human prostate. Magn Reson Med 2004;52(1):80-88.
15. Futterer JJ, Scheenen TW, Huisman HJ, Klomp DW, van Dorsten FA, Hulsbergen-van de Kaa CA, Witjes JA, Heerschap A, Barentsz JO. Initial Experience of 3 Tesla Endorectal Coil Magnetic Resonance Imaging and 1H-Spectroscopic Imaging of the Prostate. Invest Radiol 2004;39(11):671-680.
16. Chen AP, Cunningham CH, Kurhanewicz J, Xu D, Hurd RE, Pauly JM, Carvajal L, Karpodinis K, Vigneron DB. High-resolution 3D MR spectroscopic imaging of the prostate at 3 T with the MLEV-PRESS sequence. Magn Reson Imaging 2006;24(7):825-832.
17. Yakar D, Heijmink SWTPJ, Hulsbergen-Van De Kaa CA, Huisman H, Barentsz JO, Fütterer JJ, Scheenen TWJ. Initial results of 3-dimensional 1H-magnetic resonance spectroscopic imaging in the localization of prostate cancer at 3 tesla: Should we use an endorectal coil? Invest Radiol 2011;46(5):301-306.
18. Hosseinzadeh K, Schwarz SD. Endorectal diffusion weighted imaging in prostate cancer to differentiate malignant and benign peripheral zone tissue. J Magn Reson Imaging

2004;20(4):654-661.
19. Haider MA, van der Kwast TH, Tanguay J, Evans AJ, Hashmi A-T, Lockwood G, Trachtenberg J. Combined T2-weighted and diffusion-weighted MRI for localization of prostate cancer. Am J Roentgenol 2007;189(2):323-328.
20. Hambrock T, Somford DM, Huisman HJ, van Oort IM, Witjes JA, Hulsbergen-van de Kaa CA, Scheenen TJW, Barentsz JO. Relationship between Apparent Diffusion Coefficients at 3.0-T MR Imaging and Gleason Grade in Peripheral Zone Prostate Cancer. Radiology 2011;259(2):459-461.
21. Vargas HA, Akin O, Franiel T, Mazaheri Y, Zheng J, Moskowitz C, Udo K, Eastham J, Hricak H. Diffusion-weighted endorectal MR imaging at 3 T for prostate cancer: tumor detection and assessment of aggressiveness. Radiology 2011;259(3):775-784.
22. Cornel EB, Smits GA, Oosterhof GO, Karthaus HF, Deburyne FM, Schalken JA, Heerschap A. Characterization of human prostate cancer, benign prostatic hyperplasia and normal prostate by in vitro 1H and 31P magnetic resonance spectroscopy. J Urol 1993;150(6):2019-2024.
23. Kurhanewicz J, Dahiya R, Macdonald JM, Chang LH, James TL, Narayan P. Citrate alterations in primary and metastatic human prostatic adenocarcinomas: 1H magnetic resonance spectroscopy and biochemical study. Magn Reson Med 1993;29(2):149-157.
24. Heerschap A, Jager GJ, Van Der Graaf M, Barentsz JO, Ruijs SHJ. Proton MR spectroscopy of the normal human prostate with an endorectal coil and a double spin-echo pulse sequence. Magn Reson Med 1997;37(2):204-213.
25. Kurhanewicz J, Vigneron DB, Nelson SJ, Hricak H, MacDonald JM, Konety B, Narayan P. Citrate as an in vivo marker to discriminate prostate cancer from benign prostatic hyperplasia and normal prostate peripheral zone: detection via localized proton spectroscopy. Urology 1995;45(3):459-466.
26. Heerschap A, Jager GJ, Van Der Graaf M, Barentsz JO, De La Rosette JJMCH, Oosterhof GON, Ruijter ETG, Ruijs SHJ. In vivo proton MR spectroscopy reveals altered metabolite content in malignant prostate tissue. Anticancer Res 1997;17(3 A):1455-1460.
27. Kurhanewicz J, Vigneron DB, Hricak H, Narayan P, Carroll P, Nelson SJ. Three-dimensional H-1 MR spectroscopic imaging of the in situ human prostate with high (0.24-0.7-cm3) spatial resolution. Radiology 1996;198(3):795-805.
28. Van Der Graaf M, Van Den Boogert HJ, Jager GJ, Barentsz JO, Heerschap A. Human prostate: Multisection proton MR spectroscopic imaging with a single spin-echo sequence - Preliminary experience. Radiology 1999;213(3):919-925.
29. Thomas MA, Narayan P, Kurhanewicz J, Jajodia P, Weiner MW. 1H MR spectroscopy of normal and malignant human prostates in Vivo. J Magn Reson B 1990;87(3):610-619.
30. Schick F, Bongers H, Kurz S, Jung WI, Pfeffer M, Lutz O. Localized proton MR spectroscopy of citrate in vitro and of the human prostate in vivo at 1.5 T. Magn Reson Med 1993;29(1):38-43.
31. Sandhu GS, Andriole GL. Overdiagnosis of Prostate Cancer. J Natl Cancer Inst Monogr 2012;2012(45):146-151.
32. Schricker AA, Pauly JM, Kurhanewicz J, Swanson MG, Vigneron DB. Dualband spectral-spatial RF pulses for prostate MR spectroscopic imaging. Magn Reson Med 2001;46(6):1079-1087.
33. Cunningham CH, Vigneron DB, Chen AP, Xu D, Hurd RE, Sailasuta N, Pauly JM. Design of symmetric-sweep spectral-spatial RF pulses for spectral editing. Magn Reson Med 2004;52(1):147-153.
34. Males RG, Vigneron DB, Star Lack O, Falbo SC, Nelson SJ, Hricak H, Kurhanewicz J. Clinical application of BASING and spectral/spatial water and lipid suppression pulses for prostate cancer staging and localization by in vivo 3D H-1 magnetic resonance spectroscopic imaging. Magn Reson Med 2000;43(1):17-22.
35. Star-Lack J, Nelson SJ, Kurhanewicz J, Huang

LR, Vigneron DB. Improved water and lipid suppression for 3D PRESS CSI using RF band selective inversion with gradient dephasing (BASING). Magn Reson Med 1997;38(2):311-321.

36. Mescher M, Tannus A, Johnson MO, Garwood M. Solvent suppression using selective echo dephasing. J Magn reson A 1996;123(2):226-229.

37. Tran TKC, Vigneron DB, Sailasuta N, Tropp J, Le Roux P, Kurhanewicz J, Nelson S, Hurd R. Very selective suppression pulses for clinical MRSI studies of brain and prostate cancer. Magnet Reson Med 2000;43(1):23-33.

38. Venugopal N, McCurdy B, Al Mehairi S, Alamri A, Sandhu GS, Sivalingam S, Drachenberg D, Ryner L. Short echo time in vivo prostate 1H-MRSI. Magn Reson Imaging 2012;30(2):195-204.

39. Venugopal N, McCurdy B, Hovdebo J, Al Mehairi S, Alamri A, Sandhu GS, Sivalingam S, Drachenberg D, Ryner L. Automatic conformal prescription of very selective saturation bands for in vivo 1H-MRSI of the prostate. NMR in Biomedicine 2012;25(4):643-653.

40. Mareci TH, Brooker HR. Essential considerations for spectral localization using indirect gradient encoding of spatial information. Journal of Magnetic Resonance (1969) 1991;92(2):229-246.

41. Pohmann R, von Kienlin M. Accurate phosphorus metabolite images of the human heart by 3D acquisition-weighted CSI. Magn Reson Med 2001;45(5):817-826.

42. Near J, Romagnoli C, Curtis AT, Klassen LM, Izawa J, Chin J, Bartha R. High-field MRSI of the prostate using a transmit/receive endorectal coil and gradient modulated adiabatic localization. Journal of Magnetic Resonance Imaging 2009;30(2):335-343.

43. Kobus T, Wright AJ, Asten JJ, Heerschap A, Scheenen TW. In vivo 1H MR spectroscopic imaging of aggressive prostate cancer: Can we detect lactate? Magn Reson Med 2013;DOI: 10.1002/mrm.24635.

44. Katscher U, Börnert P, Leussler C, Van den Brink JS. Transmit SENSE. Magn Reson Med 2003;49(1):144-150.

45. Zhu Y. Parallel Excitation with an Array of Transmit Coils. Magn Reson Med 2004;51(4):775-784.

46. Thiel T, Czisch M, Elbel GK, Hennig J. Phase coherent averaging in magnetic resonance spectroscopy using interleaved navigator scans: Compensation of motion artifacts and magnetic field instabilities. Magn Reson Med 2002;47(6):1077-1082.

47. Kim DH, Adalsteinsson E, Spielman DM. Spiral Readout Gradients for the Reduction of Motion Artifacts in Chemical Shift Imaging. Magn Reson Med 2004;51(3):458-463.

48. Chen AP, Cunningham CH, Ozturk-Isik E, Xu D, Hurd RE, Kelley DAC, Pauly JM, Kurhanewicz J, Nelson SJ, Vigneron DB. High-speed 3T MR spectroscopic imaging of prostate with flyback echo-planar encoding. J Magn Reson Imaging 2007;25(6):1288-1292.

49. Geethanath S, Baek HM, Ganji SK, Ding Y, Maher EA, Sims RD, Choi C, Lewis MA, Kodibagkar VD. Compressive sensing could accelerate 1H MR metabolic imaging in the clinic. Radiology 2012;262(3):985-994.

50. Costello LC, Franklin RB. Concepts of citrate production and secretion by prostate. 1. Metabolic relationships. Prostate 1991;18(1):25-46.

51. Costello LC, Franklin RB. Citrate metabolism of normal and malignant prostate epithelial cells. Urology 1997;50(1):3-12.

52. Costello LC, Franklin RB. Novel role of zinc in the regulation of prostate citrate metabolism and its implications in prostate cancer. Prostate 1998;35(4):285-296.

53. Kavanagh JP. Sodium, potassium, calcium, magnesium, zinc, citrate and chloride content of human prostatic and seminal fluid. J Reprod Fertil 1985;75(1):35-41.

54. Langer DL, Van Der Kwast TH, Evans AJ, Plotkin A, Trachtenberg J, Wilson BC, Haider MA. Prostate tissue composition and MR measurements: Investigating the relationships between ADC, T2, Ktrans, Ve, and corresponding histologic features. Radiology 2010;255(2):485-494.

55. Liney GP, Turnbull LW, Lowry M, Turnbull LS, Knowles AJ, Horsman A. In vivo quantification of citrate concentration and water T2 relaxation time of the pathologic prostate gland using 1H MRS and MRI. Magn Reson Imaging 1997;15(10):1177-1186.
56. Lowry M, Liney GP, Turnbull LW, Manton DJ, Blackband SJ, Horsman A. Quantification of citrate concentration in the prostate by proton magnetic resonance spectroscopy: zonal and age-related differences. Magn Reson Med 1996;36(3):352-358.
57. Swanson MG, Zektzer AS, Tabatabai ZL and others. Quantitative analysis of prostate metabolites using 1H HR-MAS spectroscopy. Magn Reson Med 2006;55(6):1257-1264.
58. Dunzendorfer U, Russell DH. Altered polyamine profiles in prostatic hyperplasia and in kidney tumors. Cancer Res 1978;38(8):2321-2324.
59. Van der Graaf M, Schipper RG, Oosterhof GO, Schalken JA, Verhofstad AA, Heerschap A. Proton MR spectroscopy of prostatic tissue focused on the detection of spermine, a possible biomarker of malignant behavior in prostate cancer. Magma (New York, NY 2000;10(3):153-159.
60. Cohen RJ, Fujiwara K, Holland JW, McNeal JE. Polyamines in prostatic epithelial cells and adenocarcinoma; the effects of androgen blockade. Prostate 2001;49(4):278-284.
61. Lynch MJ, Nicholson JK. Proton MRS of human prostatic fluid: Correlations between citrate, spermine, and myo-inositol levels and changes with disease. Prostate 1997;30(4):248-255.
62. Cheng LL, Wu CL, Smith MR, Gonzalez RG. Non-destructive quantitation of spermine in human prostate tissue samples using HRMAS H-1 NMR spectroscopy at 9.4 T. FEBS Lett 2001;494(1-2):112-116.
63. Lynch MJ, Masters J, Pryor JP, Lindon JC, Spraul M, Foxall PJ, Nicholson JK. Ultra high field NMR spectroscopic studies on human seminal fluid, seminal vesicle and prostatic secretions. J Pharm Biomed 1994;12(1):5-19.
64. Kassen A, Sutkowski DM, Ahn H, Sensibar JA, Kozlowski JM, Lee C. Stromal cells of the human prostate: initial isolation and characterization. Prostate 1998;28(2):89-97.
65. Cooper JF, Farid I. Role of citric acid in physiology of prostate. 3. Lactate/citrate ratios in benign and malignant prostatic homogenates as index of prostatic malignancy. Journal of Urology 1964;92(5):533-&.
66. Bertilsson H, Tessem MB, Flatberg A, Viset T, Gribbestad I, Angelsen A, Halgunset J. Changes in gene transcription underlying the aberrant citrate and choline metabolism in human prostate cancer samples. Clinical Cancer Research 2012;18(12):3261-3269.
67. Hom JJ, Coakley FV, Simko JP, Lu Y, Qayyum A, Westphalen ACA, Schmitt LD, Carroll PR, Kurhanewicz J. High-grade prostatic intraepithelial neoplasia in patients with prostate cancer: MR and MR spectroscopic imaging features - Initial experience. Radiology 2007;242(2):483-489.
68. Van Asten JJA, Cuijpers V, Hulsbergen-Van De Kaa C, Soede-Huijbregts C, Witjes JA, Verhofstad A, Heerschap A. High resolution magic angle spinning NMR spectroscopy for metabolic assessment of cancer presence and Gleason score in human prostate needle biopsies. Magn Reson Mater Phy 2008;21(6):435-442.
69. Cheng LL, Burns MA, Taylor JL, He W, Halpern EF, McDougal WS, Wu CL. Metabolic characterization of human prostate cancer with tissue magnetic resonance spectroscopy. Cancer Research 2005;65(8):3030-3034.
70. Swanson MG, Vigneron DB, Tabatabai ZL, Males RG, Schmitt L, Carroll PR, James JK, Hurd RE, Kurhanewicz J. Proton HR-MAS Spectroscopy and Quantitative Pathologic Analysis of MRI/3D-MRSI-Targeted Postsurgical Prostate Tissues. Magn Reson Med 2003;50(5):944-954.
71. Shukla-Dave A, Hricak H, Moskowitz C and others. Detection of prostate cancer with MR spectroscopic imaging: An expanded paradigm incorporating polyamines. Radiology 2007;245(2):499-506.
72. Ackerstaff E, Pflug BR, Nelson JB, Bhujwalla ZM. Detection of increased choline

compounds with proton nuclear magnetic resonance spectroscopy subsequent to malignant transformation of human prostatic epithelial cells. Cancer Res 2001;61(9):3599-3603.

73. Swanson MG, Keshari KR, Tabatabai ZL, Simko JP, Shinohara K, Carroll PR, Zektzer AS, Kurhanewicz J. Quantification of choline- and ethanolamine-containing metabolites in human prostate tissues using 1H HR-MAS total correlation spectroscopy. Magn Reson Med 2008;60(1):33-40.
74. Glunde K, Bhujwalla ZM, Ronen SM. Choline metabolism in malignant transformation. Nat Rev Cancer 2011;11(12):835-848.
75. Dorsten F, Engelbrecht M, Van der Graaf M, De La Rosette J, Barentsz JO, Heerschap A. Differentiation of Prostatitis from Prostate Carcinoma Using 1H MR Spectroscopic Imaging and Dynamic Contrast-Enhanced MRI. 2001; Glasgow, Scotland, UK.
76. Shukla-Dave A, Hricak H, Eberhardt SC, Olgac S, Muruganandham M, Scardino PT, Reuter VE, Koutcher JA, Zakian KL. Chronic prostatitis: MR imaging and 1H MR spectroscopic imaging findings--initial observations. Radiology 2004;231(3):717-724.
77. Testa C, Schiavina R, Lodi R, Salizzoni E, Tonon C, D'Errico A, Corti B, Morselli Labate AM, Franceschelli A, Bertaccini A. Accuracy of MRI/MRSI based transrectal ultrasound biopsy in peripheral and transition zones of the prostate gland in patients with prior negative biopsy. NMR in Biomed 2010;23(9):1017-1026.
78. Nagel KN, Schouten MG, Hambrock T, Litjens GJ, Hoeks CM, ten Haken B, Barentsz JO, Fütterer JJ. Differentiation of Prostatitis and Prostate Cancer by Using Diffusion-weighted MR Imaging and MR-guided Biopsy at 3 T. Radiology 2013.
79. Tomlins AM, Foxall PJD, Lynch MJ, Parkinson J, Everett JR, Nicholson JK. High resolution (1)H NMR spectroscopic studies on dynamic biochemical processes in incubated human seminal fluid samples. BBA -Gen Subjects 1998;1379(3):367-380.
80. Qayyum A, Coakley FV, Lu Y, Olpin JD, Wu L, Yeh BM, Carroll PR, Kurhanewicz J. Organ-confined prostate cancer: effect of prior transrectal biopsy on endorectal MRI and MR spectroscopic imaging. AJR Am J Roentgenol 2004;183(4):1079-1083.
81. Barrett T, Vargas HA, Akin O, Goldman DA, Hricak H. Value of the hemorrhage exclusion sign on T1-weighted prostate MR images for the detection of prostate cancer. Radiology 2012;263(3):751-757.
82. Gibbs P, Tozer DJ, Liney GP, Turnbull LW. Comparison of quantitative T2 mapping and diffusion-weighted imaging in the normal and pathologic prostate. Magn Reson Med 2001;46(6):1054-1058.
83. Oto A, Kayhan A, Jiang Y, Tretiakova M, Yang C, Antic T, Dahi F, Shalhav AL, Karczmar G, Stadler WM. Prostate cancer: differentiation of central gland cancer from benign prostatic hyperplasia by using diffusion-weighted and dynamic contrast-enhanced MR imaging. Radiology 2010;257(3):715-723.
84. Tamada T, Sone T, Jo Y, Toshimitsu S, Yamashita T, Yamamoto A, Tanimoto D, Ito K. Apparent diffusion coefficient values in peripheral and transition zones of the prostate: Comparison between normal and malignant prostatic tissues and correlation with histologic grade. J Magn Reson Imaging 2008;28(3):720-726.
85. Turkbey B, Shah VP, Pang Y and others. Is apparent diffusion coefficient associated with clinical risk scores for prostate cancers that are visible on 3-T MR images? Radiology 2011;258(2):488-495.
86. Padhani AR, Liu G, Mu-Koh D and others. Diffusion-weighted magnetic resonance imaging as a cancer biomarker: Consensus and recommendations. Neoplasia 2009;11(2):102-125.
87. Neil JJ. Measurement of water motion (apparent diffusion) in biological systems. Concept Magnetic Res 1997;9(6):385-401.
88. Ahmed R, Ara S, Nurunnabi ASM, Mahbub S, Alim A, Shahriah S. Histological Study on the Diameter of the Acini of the Human Prostate

Gland–A Postmortem Study. Bangladesh J Anat 2010;8(2):52-55.

89. Issa B. In vivo measurement of the apparent diffusion coefficient in normal and malignant prostatic tissues using echo-planar imaging. J Magn Reson Imaging 2002;16(2):196-200.

90. Schiebler ML, Tomaszewski JE, Bezzi M, Pollack HM, Kressel HY, Cohen EK, Altman HG, Gefter WB, Wein AJ, Axel L. Prostatic carcinoma and benign prostatic hyperplasia: Correlation of high-resolution MR and histopathologic findings. Radiology 1989;172(1):131-137.

91. Yoshimitsu K, Kiyoshima K, Irie H, Tajima T, Asayama Y, Hirakawa M, Ishigami K, Naito S, Honda H. Usefulness of apparent diffusion coefficient map in diagnosing prostate carcinoma: Correlation with stepwise histopathology. J Magn Reson Imaging 2008;27(1):132-139.

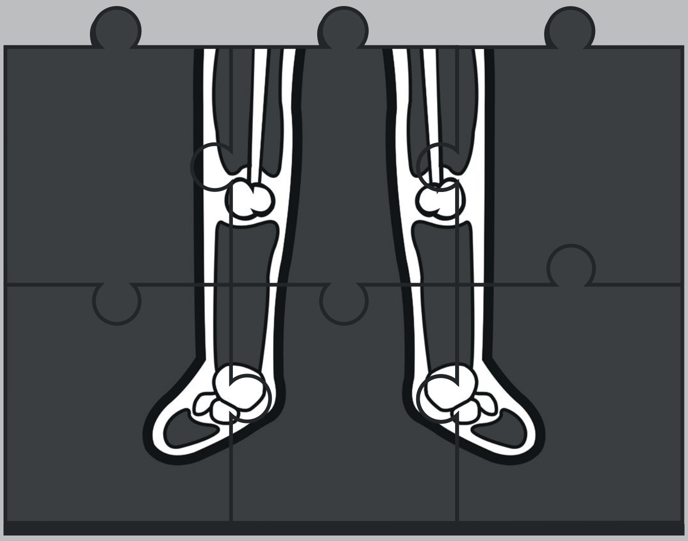

3

CHAPTER THREE

Metabolite Ratios in ^{1}H MR Spectroscopic Imaging of the Prostate

This chapter is based on:
Metabolite ratios in ^{1}H MR spectroscopic imaging of the prostate
T. Kobus, A.J. Wright, E. Weiland, A. Heerschap and T.W.J. Scheenen
Magnetic Resonance in Medicine, 2014

Introduction

Prostate cancer is the most prevalent non-cutaneous cancer in men and the second leading cause of cancer related death in western countries (1). The use of MR in prostate cancer management is emerging, and the demand from patients and clinicians is increasing as a result of the growing number of men suspected of having prostate cancer due to the uptake of blood tests for prostate specific antigen. In clinical practice MR is used for its anatomical details in the detection, localization and characterization of the disease, but the technique also offers possibilities to obtain more functional information, for example by diffusion weighted imaging (DWI), dynamic contrast enhanced imaging (DCE-MRI) and MR spectroscopic imaging (MRSI) (2).

Proton MR spectroscopy (^{1}H MRS) enables one to study a range of (bio-)molecules, by making use of the signals of ^{1}H nuclei in these molecules. *In vivo*, the detection of molecules is limited to those present at tissue levels of more than 0.5-1 mM. The first metabolite studied with *in vivo* ^{1}H MRS of the prostate was citrate and a decrease in its resonances' amplitude was observed in prostate cancer patients compared to healthy controls (3). Next, the choline methyl resonance gained attention as an increase in this signal in prostate cancer was observed (4,5). Due to frequency-selective water and lipid suppression, only signals of major metabolites between approximately 2.2 and 3.8 ppm remain in prostate spectra, which also includes those of creatine and polyamines. Because the choline and creatine methyl signals are only separated by a relatively small chemical shift difference, a non-optimal B_0 homogeneity, causing line broadening, will lead to signal overlap. The presence of polyamine signals between these two metabolite signals further complicates their separation. This potential overlap led to the introduction of the signal ratio of choline plus creatine divided by citrate [(Cho+Cr)/Cit] (4,6) and its inverted counterpart (citrate over choline plus creatine ratio (5)) as a marker for prostate cancer.

In this paper the major variables that can influence the (Cho+Cr)/Cit ratio are discussed. An overview of the main metabolites detectable in the commonly obtained MR spectra of the prostate, their function and the acquisition parameters that influence their appearance in the spectrum will be provided. These metabolites form the basis for the (Cho+Cr)/Cit ratio, of which the intensity not only depends on the underlying physiology, metabolism and anatomy, but also on the acquisition parameters. This latter aspect is particularly relevant for the citrate and polyamine signals.

Although ^{1}H MRSI has great potential in prostate cancer management, its use in routine clinical practice is limited. A major hurdle towards clinical use is that several acquisition and processing steps still rely on manual procedures, in particular post-processing of the data, including quality control, and displaying easily visualized and interpretable results

(7). As is the case for DWI and DCE-MRI of the prostate, a more widespread consensus in the acquisition and fitting of data would also promote clinical translation. A generalized classification scheme for prostate MR spectroscopy to assist in prostate cancer management is not available. The second part of this article discusses the use of a protocol dependent classification scheme that could increase the clinical usability of the metabolite ratio for prostate cancer management.

Prostate metabolites

The main metabolite signals in commonly obtained ^{1}H MRSI spectra of the prostate are choline, creatine, polyamines and citrate (Figure 3.1).

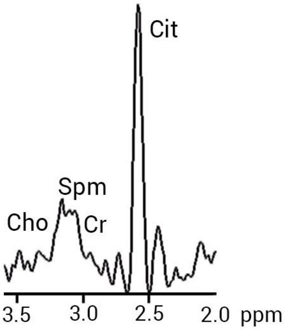

Figure 3.1. *^{1}H MR spectrum of the peripheral zone of the prostate of a healthy male containing signals of choline (Cho), spermine (Spm), creatine (Cr) and citrate (Cit). The spectrum is acquired at 3 T using a PRESS sequence with a TE of 145 ms and MEGA pulses for water and lipid suppression.*

Choline

Different compounds containing a choline moiety can contribute to the main peak at about 3.2 ppm in *in vivo* ^{1}H MR spectra. These are free choline, glycerophosphocholine and phosphocholine, but also contributions from protons in taurine, ethanolamines and myo-inositol may be present at this spectral position (8). As a convenient shorthand we refer to this composite resonance as the “choline” signal. Choline-containing metabolites are precursors and breakdown products of the phospholipid phosphatidylcholine, a major cell membrane compound (9). In prostate cancer cell lines an increase in choline is observed, due to an altered phospholipid metabolism (10). This alteration is probably due to an increased expression and activity of choline-kinase, a higher rate of choline transport and an increased phospholipase activity (9,10).

The choline moiety has nine chemically equivalent protons of three methyl groups resonating as a singlet around 3.19 ppm and two methylene groups, resulting in two multiplets at 4.05

and 3.50 ppm (11). As the intensity of these multiplets is very low in *in vivo* MR spectra of the prostate it is common to only evaluate the nine-proton singlet at 3.19 ppm. Estimates of the T1 and T2 relaxation times of the choline methyl protons (Table 3.1) are valuable to determine the effect of the chosen TE and TR on the choline signal intensity.

		T1		***T2***	
		1.5 T	*3 T*	*1.5 T*	*3 T*
Heerschap et al. 1997 (6)	*Choline*	*0.84±0.09 s*		*0.23 ±0.06 s*	
	Creatine	*0.86 ±0.1 s*		*0.21±0.1 s*	
	Citrate	*0.34 ± 0.04 s*			
Heerschap et al. (62)	*Citrate*			*0.18± 0.1 s*	
Lowry et al. (45)	*Citrate*	*0.84 ± 0.08 s*		*0.14 ± 0.02 s (PZ)* *0.12 ± 0.03 s (TZ)*	
Scheenen et al. (22)	*Choline*		*1.1 ± 0.4 s*		*0.22±0.09 s*
	Citrate		*0.47 ± 0.14 s*		*0.17 ± 0.05 s*
Chen et al. (63)	*Choline*		*0.96±0.25 s*		
	Citrate		*0.54±0.14 s*		

Table 3.1. T1 and T2 relaxation times of the prostate metabolites choline, creatine and citrate. Unless indicated, no distinction was made between the peripheral zone (PZ) and transition zone (TZ).

Creatine

Both creatine and phosphocreatine contribute to the methyl resonance observed at about 3.0 ppm in ^{1}H MRS of the prostate (referred to, in combination, as the creatine signal in this paper). Creatine plays a crucial role in the energy metabolism of tissues (12), as phosphocreatine acts as a spatial and temporal buffer to maintain constant adenosine triphosphate (ATP) levels in tissue through the creatine-kinase reaction. The stromal cells consist predominantly of smooth muscle cells (13), which are expected to contribute most to the creatine and phosphocreatine signals.

Creatine has five non-exchanging protons: a methyl group resonating at 3.03 ppm and the methylene group at 3.93 ppm. The protons in each group are chemically equivalent and uncoupled, resulting in two singlets with a ratio of 3:2. The relaxation times of the methyl protons of creatine are given in Table 3.1. The concentration of creatine was estimated with *in vivo* MRS at 4.4 ±0.8 mM (6) and with *ex vivo* high-resolution magic angle spinning (HR-MAS) spectroscopy as being between 7.6 ± 2.7 and 9.7 ± 4.4 mmol/kg for normal and cancer tissue (no significant differences) (14).

Citrate

The production and storage of citrate is one of the main functions of the prostate. Citrate is an intermediate in the tricarboxylic acid cycle (TCA cycle). In most organs citrate is quickly oxidized in the TCA cycle and is therefore only present in low concentrations. In contrast, prostate epithelial cells actively produce citrate and store it in the luminal space, where it is one of the main components of the prostatic fluid (15). Prostate tissue has high levels of zinc, which inhibits mitochondrial (m-)aconitase activity. This leads to the buildup of a high concentration of citrate (16). In prostate cancer a decrease in zinc levels is observed which leads to activation of m-aconitase and the consequential oxidation of citrate (16). At the same time, the morphology of the prostate gland changes, leading to a loss of luminal space, which might also cause a decrease in the observed (or total) citrate levels.

Citrate contains two methylene groups that are magnetically equivalent (Figure 3.2A). The four protons of these groups form a strongly coupled AB spin system. The difference in chemical shifts (Δ), the midpoint of the chemical shifts (δ), and the scalar coupling (J) of this spin system depend on pH (17,18) and cation concentration (18) and are approximately 0.15 ppm, 2.61 ppm, and 16.3Hz, respectively (Figure 3.2B). Because citrate is a strongly coupled spin system, its shape depends on inter-pulse timing, pulse shape, TE, and field strength (17-23). In Table 3.1, the relaxation times for citrate at 1.5 and 3 T are given. The determination of the T2 relaxation time of citrate is less straightforward than for singlets. By increasing the TE in such an experiment, there is not just attenuation of the signal intensity due to T2 relaxation, but also shape and intensity variation due to J-modulation.

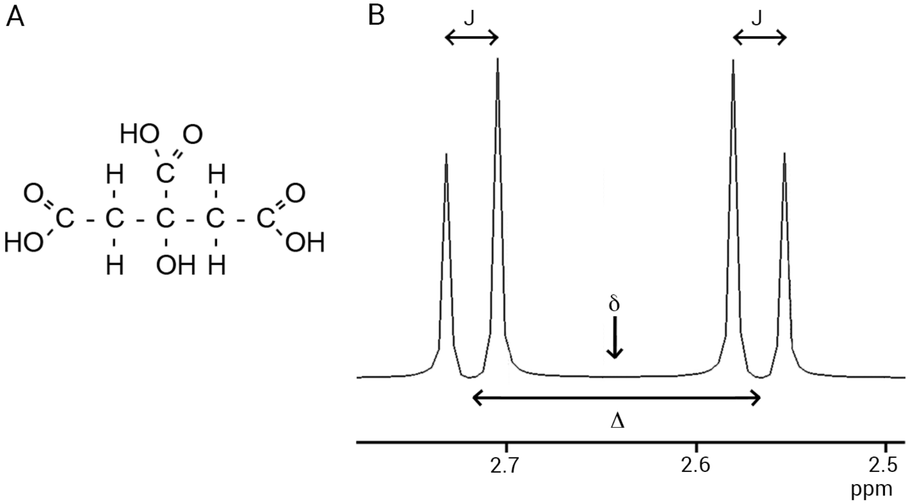

Figure 3.2. A) Schematic chemical structure of citrate. B) The simulated spectral shape of citrate at 600 MHz. Indicated are the scalar coupling constant (J), the chemical shift difference (Δ) and the midpoint of the chemical shifts of the second and third peak (δ).

In the first *in vivo* prostate ^{1}H MRS studies at 1.5T, stimulated echo acquisition mode (STEAM) and point resolved spectroscopy (PRESS) techniques were used for volume localization (4,24). One advantage of the STEAM for these data is its ability to use a very short TE (at the expense of the general loss of half of the signal in a stimulated echo). In this way, the strongly coupled protons of citrate will have limited phase evolution, which will result in an almost completely in-phase citrate signal. Integration of the area of the citrate peak(s) will then result in maximal signal intensity. For the PRESS sequence generally longer TEs are used for prostate MRS and dispersive parts can be present in the spectrum that affect the peak area by cancellation with absorptive parts in simple integration. Several studies have been performed to determine the PRESS pulse timing with maximum absorptive signal at the central lines of the citrate signal. Van der Graaf et al. used a delay of 7.5 ms between excitation and the first refocusing pulse, and varied the TE. Their optimal TE was 130 ms at 1.5 T (25). One sequence optimization procedure at 3 T led to an optimal TE of 75 ms (negative absorptive shape) and 145 ms (positive absorptive shape) with a delay of 25 ms between excitation and refocusing (22). However, other researchers found an optimal TE of 85 ms (26) and there are more possibilities that result in a favorable citrate signal (19). It is therefore not surprising that prostate MRSI acquisition software packages of three MR vendors at 3 T are equipped with quite different TEs, varying from 85 to 145 ms (27). The differences in the spectral shape of citrate in different pulse sequences will lead to variations in the integral of citrate signal at a constant citrate concentration. The influence of inter-pulse timing is also evident from matrix density simulations (19,22) illustrated in Figure 3.3, which shows simulated and *in vivo* spectra of one patient, using a PRESS sequence at 3 T with a TE of 145 ms and a semi-LASER sequence (Localization by Adiabatic Selective Refocusing) at nearly the same TE of 144 ms (28). In the semi-LASER sequence the excitation pulse is followed by four adiabatic refocusing pulses.

The optimal TR for citrate detection can be quite short, because of its relatively short T1 (Table 3.1). It was calculated that the use of a TR of 750 ms, instead of 1500 ms, would lead to an increase in SNR per unit time of 17% for citrate and a decrease of 6% for choline for 3T data (22). When a weighted averaged acquisition scheme is used for MRSI, the use of a short TR allows for more averages in the centre of k-space in the same amount of measurement time. In this way, the acquisition of the phase encoding steps in k-space can be done following the shape of a Hanning filter. Apodization in k-spacewith a Hanning filter produces a point spread function with widened full-width-at-half-maximum, but strongly decreased signal contamination form more spatially distant signals (22). The effective voxel size increases, but extra-prostatic lipid signal contamination is strongly decreased.

In the physiological range of pH (6.8-7.4), variations in Δ of 3.2 Hz and variations in δ of 0.025 ppm were observed using a 400MHz magnet (17). The changes in J are minimal in this pH range (17,18), but the concentrations of zinc, calcium and magnesium also influence

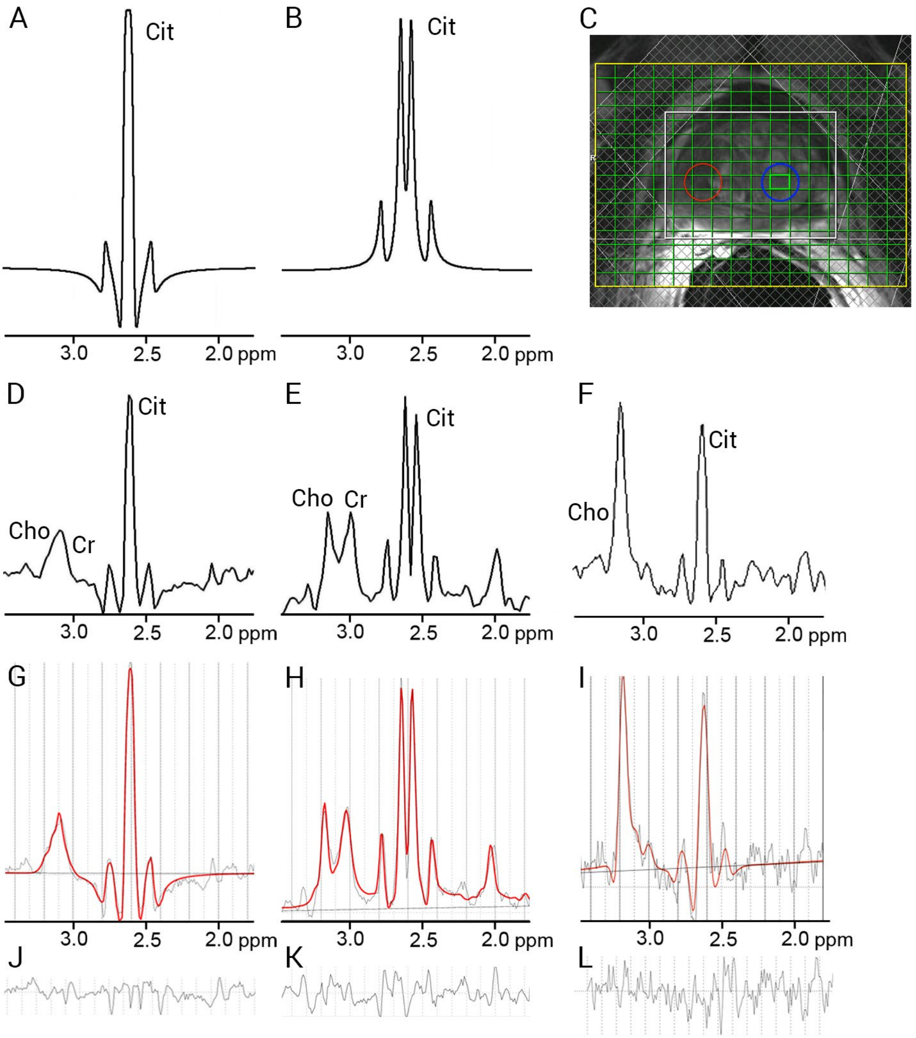

Figure 3.3. *A) The simulated spectral shape of citrate (Cit) using the PRESS sequence with an optimized pulse timing (90˚ – 25ms – 180˚ – 72.5 ms – 180˚ - 47.5 ms – echo) at a TE of 145ms at 3T (22). B) The simulated Cit shape using an optimized semi-LASER sequence at a TE of 144ms (90˚ - 11 ms - 180˚ - 21 ms - 180˚ - 29 ms - 180˚ - 51 ms - 180˚ - 32 ms - echo) (28). C) T2 weighted image of the prostate of a 71 year old man with biopsy proven prostate cancer (Gleason score 9). D) In vivo spectrum of the PRESS (TR=750 ms) of normal tissue and (E) spectrum of corresponding region with the semi-LASER sequence (TR= 2070 ms). The region is indicated in C with a blue circle. F) In vivo spectrum of tumor tissue (red circle in C) with the PRESS. G, H and I) The corresponding fits of LCModel using the simulated citrate shape of A and B show minimal residuals (J, K and L). Each spectrum is scaled to maximum intensity.*

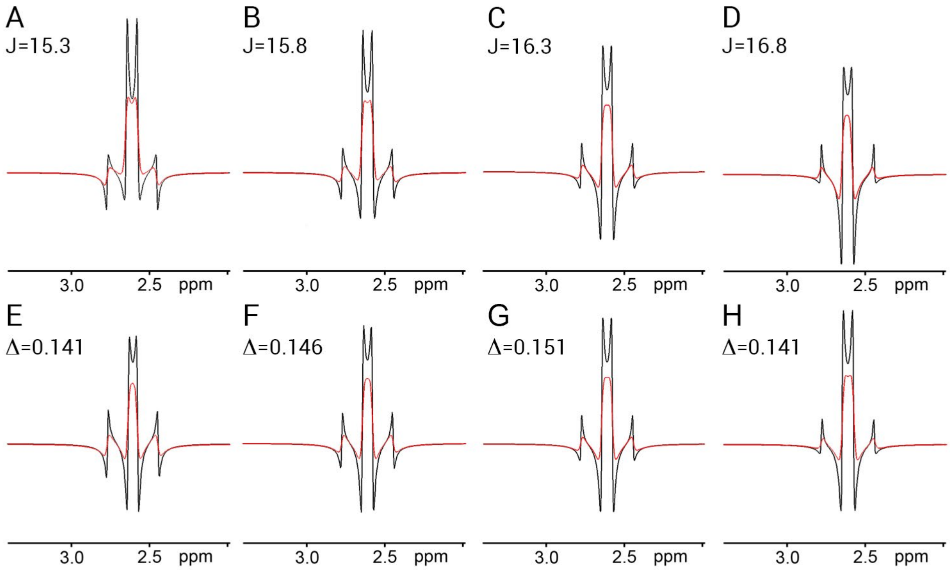

Figure 3.4. *Simulations with NMRSIM (part of Topspin, Bruker BioSpin Corporation, Billerica, MA) show the influence of small differences in the scalar coupling and chemical shifts on the citrate shape at a field strength of 3T with an optimized pulse sequence (TE 145 ms) (22). Line broadening of 1 Hz (black spectra) and 4 Hz (red spectra) were used. Δ was 2.6105 ppm for all spectra. For A-D, Δ was kept constant at 0.151 and the scalar coupling was varied between 15.3Hz and 16.8Hz. For E-H, J was kept constant at 16.3 Hz and Δ was varied between 0.141ppm and 0.156ppm. The amplitudes of all spectra are scaled to a reference signal.*

the value of this coupling (18) which may have significant effects on the *in vivo* resonances. Figure 3.4 shows that small changes in Δ and J can have substantial influences on the spectral shape of citrate. Although *in vitro* a relation was found between the spectral shape of citrate and the ion concentration or pH, variations in the spectral citrate shape *in vivo* are difficult to relate to ion concentrations or pH, as these are hard to measure. For a good fitting, it is necessary to use a model signal that is based on J, δ, and Δ values that closely resemble those present *in vivo*. At our institution we use J=-16.2, δ=2.625, Δ=0.154 as this led to the smallest residuals for the citrate resonance using LCModel fitting (unpublished data). Using these parameters, the *in vivo* citrate shape closely resembles the simulated spectrum (see Figure 3.3). This was the case for both the PRESS spectrum and that obtained with the semi-LASER sequence, indicating that these values are a good approximation of the *in vivo* coupling parameters.

The side lobes of the citrate resonance extend to the 3 ppm region and contain a mixture of absorption and dispersion shapes at a TE of 145 ms at 3 T (22), which can result in a negative effect on the total intensity in this region. When a model signal is used for the fitting, this effect can be taken into account; however, when simple peak integration is used, one cannot fully compensate for this effect. Negative components of the citrate signal will be excluded from citrate quantification and one might need to revert to severe baseline corrections to prevent an influence on other metabolite signals.

The RF pulses that are used to suppress the large lipid and water signals may adversely affect the citrate signals. Often dual frequency-selective pulses are used to suppress both these signals simultaneously, mainly by MEGA (Mescher-Garwood (29)) or double BASING (Band Selective Inversion with Gradient Dephasing (30,31)) pulses. These pulses selectively invert the lipid and water resonances and are surrounded by crusher gradients. Their bandwidth and position in the frequency domain should be sufficient to invert all lipid signals, but distant enough from the chemical shift of citrate. When the bandwidth of the lipid inversion pulse is too broad, this will cause a decreased signal intensity of citrate (see Figure 3.5). As a consequence, healthy spectra may get a 'cancerous' profile. Therefore, a

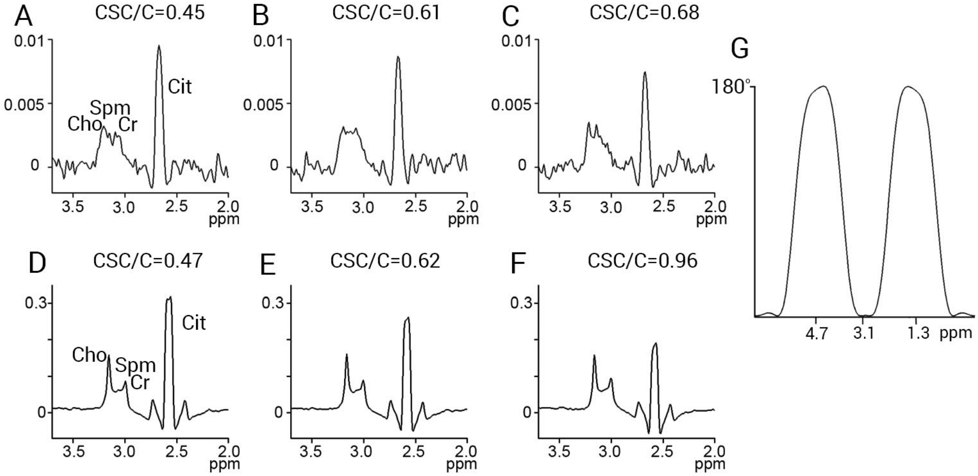

Figure 3.5. *A-C) In vivo prostate spectra of a healthy volunteer at 3T using PRESS with MEGA pulses for water and lipid suppression. The spectra are from the same location, but the width of the frequency selective inversion bands was 1.40 ppm in A, 1.45 ppm in B and 1.55 ppm in C, leading to a decrease in the citrate (Cit) intensity, while the intensities of choline (Cho), spermine (Spm) and creatine (Cr) remain unchanged. As a consequence the choline plus spermine plus creatine to citrate [(Cho+Spm+Cr)/Cit] ratio increases influencing the classification of the spectrum. D-F) shows the same effect in a phantom containing Cit, Cho, Spm and Cr using MEGA pulses with a width of the inversion bands of 1.35 ppm in D, 1.45 ppm in E and 1.55 ppm in F. G) the shape of the MEGA pulse in the frequency domain. Note: these (Cho+Spm+Cr)/Cit ratios are determined with LCModel. In line with previously published metabolite ratios, the citrate intensity in LCModel was scaled to the number of protons in citrate, rather than to the magnitude integral at this TE, which is smaller due to cancellation of signal intensity by the strongly coupled pattern.*

good adjustment of the dual frequency pulses is essential for obtaining consistent results. Spectrally selective refocusing pulses may be used instead of signal suppression pulses, that prevent refocusing of lipids by simultaneous volume and frequency selection (32,33). Care should be taken that these pulses fully excite or refocus the citrate spins and leave the lipid signals untouched.

For proper selective suppression or spectral excitation, the homogeneity of the B_0 field is critical. Poor homogeneity will not only negatively affect spectral quality as it causes broadening of the spectral lines; it will also decrease the effectiveness of frequency selective pulses. Broadened or shifted fat and water signals can suffer from diminished suppression and components of these signals may overlap with the resonances of interest. In addition, in the case of shifted or broadened spectral lines of citrate, the metabolite can be influenced by the frequency selective pulses for lipid and water suppression leading to decreased citrate intensities, comparable to the effect shown in Figure 3.5.

The dependence of the citrate signals on inter-pulse timing can also be exploited for spectral editing. By varying this timing (at a constant TE) in such a way that citrate is inverted in one measurement and in phase in the next measurement, uncoupled resonances can be removed from the spectrum by subtraction (34,35). In this way, rapid citrate imaging without lipid suppression is possible.

Polyamines / Spermine

The tissue concentration of polyamines in the prostate is relatively high. As spermine is the dominant polyamine in the prostate, we will focus on this compound. Polyamines are stored, like citrate, in the luminal space and a very strong correlation between the citrate and spermine concentration is reported for prostatic fluid specimens (36). A hypothesis for the strong correlation (r=0.94) is the formation of complexes between citrate and spermine since citrate is negatively charged, while spermine is positively charged. In this way ionic neutrality can be achieved (36). Polyamines play a role in prostatic growth and differentiation (37). A decrease in spermine has been suggested as a marker for prostatic malignancy (37,38). In prostate cancer a decrease in spermine or polyamine levels is observed compared to benign tissue using MR spectroscopy (38) and high resolution magic angle spinning experiments (14). The incorporation of polyamine levels measured with MR spectroscopy to improve detection of prostate cancer has been proposed and yielded an increased sensitivity at the same specificity (39).

Spermine is a coupled spin system and contains, besides its amine groups, ten methylene groups. These methylene protons consist of symmetrical pairs giving a total of four protons that resonate approximately at 1.81 ppm with further groups of four at 2.11 ppm, 3.13 ppm, 3.12 ppm and 3.18 ppm (40). These chemical shifts are pH dependent (41) and these quoted chemical shifts were measured at pH 7 (40). At a higher pH the amine groups are more protonated and therefore the chemical shifts are more downfield (41). Protons near a nitrogen atom show the largest pH-dependence. Spermine proton chemical shifts are also sensitive to temperature differences. We did temperature measurements at 500 MHz with a spermine compound dissolved in water. These measurements showed that protons near a nitrogen atom had the highest temperature dependence (unpublished data). For that reason, when one wants to perform a phantom measurement to determine the shape of spermine (with a certain sequence), the phantom should be measured at body temperature and have a pH in the physiological range. Local chemical shift correction to improve the separation between choline and spermine is hindered by the dependence of the chemical shift of spermine on the environment. Also, usually no water reference measurement is done that could be used for this purpose. The metabolites in the prostate spectrum are unsuitable for this purpose, as the chemical shift of citrate is environment-dependent and choline is not always well separable from spermine.

As with citrate, TE and inter-pulse timing influence the spectral shape of spermine and leading to dispersive components in the resonances. If dispersive parts are present in the 3.1-ppm region, this can negatively affect the apparent intensity of choline and/or creatine resonances. Furthermore, BASING and MEGA pulses that are used for simultaneous water and lipid suppression, invert the 2.1- and 1.8-ppm resonances of spermine (42). Without these pulses and crushers, the 2.1- and 1.8-ppm resonances could be helpful for decomposition of spermine from the 3.1-ppm region. Figure 3.6 shows the influence of the MEGA pulses on the spectral shape of spermine. As expected, the resonances at 1.8 and 2.1 ppm are (almost) completely crushed by the combination of MEGA pulses and crushing gradients. The resonances at 1.8 and 2.1 ppm are scalar coupled to the resonances in the

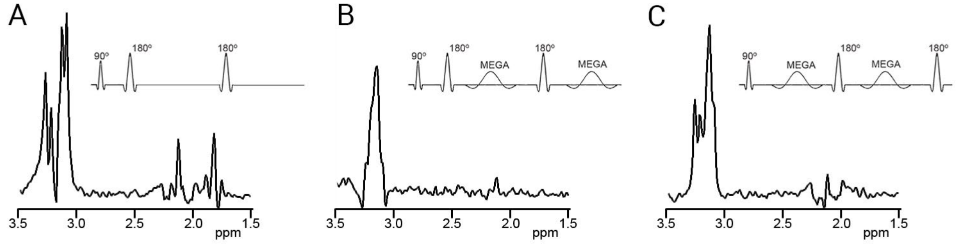

Figure 3.6. *The spectral shape of spermine measured in a phantom at 3T using PRESS with a TE of 145 ms (90˚ – 25ms – 180˚ – 72.5 ms – 180˚ - 45.5 ms – echo). The phantom contained 18 mM spermine, 9 mM ZnCl, 15 mM MgCl2, 18 mM CaCl2, and 60 mM of KCl (41,71). The pH was adjusted to 6.8 and the temperature was 310 K. A) The spermine spectral shape without the use of MEGA pulses. B) The spermine spectral shape when two MEGA pulses for combined water and lipid suppression are used surrounding the second refocusing pulse and in C) the spectral shape when two MEGA pulses are used surrounding the first refocusing pulse.*

3.1 ppm region; therefore, the selective refocusing of these upfield groups refocuses also the J-evolution of the downfield protons. This is evident from the difference in spectral shape and intensity of spermine in Figure 3.6B and 3.6C, where a different timing for the MEGA pulses is used. These measured spermine shapes can be used as prior knowledge for spectral fitting of the metabolites (42). Figure 3.7 demonstrates how the spermine shape can affect the choline and creatine region, showing two spectra from the same location in one volunteer that are measured with a different MEGA pulse timing, resulting in different (Cho+(Spm+)Cr)/Cit ratios.

T1 and T2 values of spermine reported in the literature are obtained *in vitro* and the T2 values were rather short and dependent on the presence of ions and proteins (41). No *in vivo* data of relaxation times of spermine spins is available yet.

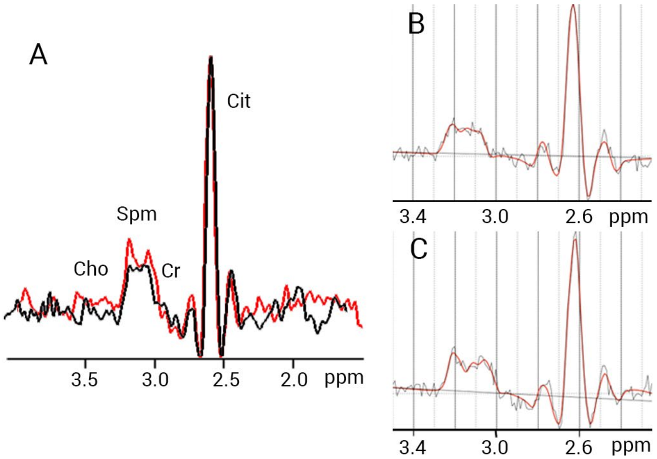

Figure 3.7. *A) Spectra of a healthy volunteer of the same voxel in two measurements, containing resonances of choline (Cho), spermine (Spm), creatine (Cr) and citrate (Cit). The difference between the measurements is the timing of the MEGA pulses. In the black spectrum, the MEGA pulses surround the second refocusing pulse (as in Fig. 3.5B) and in the red spectrum the MEGA pulses surround the first refocusing pulse (as in Fig. 3.5C). Two different LCModel basis sets were used for the fitting (to take the differences in spermine shapes into account) and the (Cho+Spm+Cr)/Cit amplitude ratios were: 0.35 (black and fit displayed in B) and 0.46 (red and fit displayed in C). This demonstrates the influence of spectral spermine shape on the (Cho+Spm+Cr)/Cit ratio.*

Evaluation of the metabolite ratio

Prostate ^{1}H MRSI spectra can be evaluated qualitatively or (semi-)quantitatively. Qualitative guidelines are based on visual inspection of the height of choline compared to the citrate height (43,44). When using this qualitative approach of comparing peak heights in a prospective multi-centre setting, no additional value for ^{1}H MRSI was found compared to the use of MRI alone for the localization of prostate cancer in the peripheral zone (45). In this study, data homogeneity across different centers was not validated with e.g. mean values of non-cancer tissue across centers. This, together with the lack of a clear definition of tumor focus size that needed to be localized, could explain the disappointing results.

A more quantitative aproach is determination of metabolite concentrations in prostate spectra with the help of a reference compound. If the tissue water concentration is known in the volume of interest and the individual metabolites are fitted reliably, water can be used as an internal reference to obtain absolute prostate metabolite concentrations (e.g. (6,46)). This requires additional time for a water reference measurement, which is often not available. More practical, and sufficient for diagnostic purposes, is the use of the (Cho+Cr)/Cit ratio for classification. The usability of this ratio for prostate cancer localization was demonstrated in a prospective multi-centre study, where an area under the receiver operating characteristic curve of 0.88 was obtained for discriminating normal peripheral zone tissue from cancer (47). Classification thresholds for the (Cho+Cr)/Cit ratio are needed to apply MR spectroscopy for prostate disease in clinical routine.

Establishing the ratio of choline (plus spermine) plus creatine over citrate ratio

The simplest method of calculating the (Cho+Cr)/Cit ratio is to use integration techniques and calculate a ratio based on these values (integral values). This has been used by many researchers to calculate the ratio (Table 3.2). But as discussed above, strong coupling effects and a long echo time can produce a spectral shape of citrate that has an integral close to zero and small differences in citrate intensity will induce very variable ratios. One way to circumvent this problem is by fitting the metabolites to a model signal. Model signals can be measured with phantom solutions (e.g.(42)). Alternatively, they can be simulated, when the chemical shifts and J-coupling constants are known for the metabolites of interest (e.g.(42,48)). There are several software packages available that can be used to make model signals, e.g. NMRSIM (part of Topspin, Bruker BioSpin Corporation, Billerica, MA), GAMMA (49) and its successor VeSPA (http://scion.duhs.duke.edu/vespa/). The model signals can be used to obtain fits of the metabolites in the time (50,51) or frequency domain (52). The output is typically a relative metabolite concentration value incorporating the amount of protons of the metabolite. These relative concentrations depend on the goodness of the fit and correlation between fits; for overlapping metabolites overestimation of one metabolite at the cost of underestimation of another, will result in a ratio that is unrepresentative for the tissue if the metabolites have a different amount of protons. So if the metabolites are fitted individually with such a quantification algorithm, the concentrations must be reconverted to their relative spectral amplitude prior to summation and division in the ratio. This procedure removes individual information gained from each metabolite but improves the reliability of the ratio. For spectral patterns dominated by absorption components, this amplitude ratio will give comparable results as the integral ratio. But in contrast to the integral ratio, the amplitude ratio is less sensitive to the dispersive parts of citrate. The amplitude ratio gave good results for discrimination between different prostate tissues in a 3T study, where the spectral citrate shape had non-negligible dispersive parts (47).

The fit of the individual metabolites has been used to derive the choline over citrate plus spermine ratio [Cho/(Cit+Spm)], a ratio that takes the counteracting effects of the increase in choline and decrease in citrate and spermine in prostate cancer into account (42). However, due to the inherent uncertainty in individual metabolite quantification (53), we recommend to use a (Cho+Cr)/Cit ratio rather than a simpler choline/citrate (or Cho/(Cit+Spm)) ratio. In most studies, spermine is not fitted individually (e.g.(45,53-56)), and spermine resonances are included in the creatine and choline fits (39). The ratio should therefore be seen as the choline plus spermine plus creatine over citrate ratio.

Classification thresholds for choline (plus spermine) plus creatine over citrate ratio

In the previous sections, the acquisition parameters that influence the prostate metabolite signals, and thus consequently the (Cho+(Spm+)Cr)/Cit ratio, were discussed. In principle it is possible to correct for T1, T2 relaxation and J-modulations, and obtain a 'normalized' ratio that is acquisition independent. However, this requires knowledge of their precise values, which are not available (current reports show quite some variation in T1, T2), and these values may also vary for different tissue morphology (e.g. cancer, benign disease and normal prostate). Moreover, fitting of the individual metabolite signals is also necessary, which can be challenging because of overlap between choline, creatine and spermine signals. For that reason, we cannot work with a 'normalized' ratio and the (Cho+Cr)/Cit ratio thus has to be established per institution or per protocol.

The mean (Cho+Cr)/Cit plus two or three times the standard deviation of normal tissue was used as a cut off value to classify voxels as 'cancerous' (5,57-59). The use of a 5 point classification scale based on the mean and standard deviation of the (Cho+Cr)/Cit ratio of normal prostate tissue has been proposed (44). Because the (Cho+Cr)/Cit ratio is higher for normal transition zone tissue than for peripheral zone tissue, the cut off values vary for the two tissues. Table 3.2 and 3.3 provide an overview of reported mean (Cho+Cr)/Cit ratios for normal peripheral zone tissue at 1.5 and 3 T. For 1.5 T, the used TEs in these studies are quite similar (120 – 130 ms) and often the same platform and post processing methods are used, but still there is quite some variation in the reported (Cho+Cr)/Cit ratios. At 3 T, there are considerable differences between prostate spectroscopy packages of the vendors, with TEs varying from 85 to 145 ms and TRs from 750 to 1300 ms (27). At 7 T, optimal acquisition

	Average (Cho+Cr)/Cit ratio ± stand. dev.	**Vendor**	**Post processing method**	**TE/TR (ms)**
Kurhanewicz et al. 1996 (5)	*0.54 ± 0.11 (PZ)* *0.83 ± 0.34 (TZ)*	*GE*	*Integration of designated frequency ranges*	*130 / 1000*
Males et al. 2000 (30)	*0.22 ± 0.13 (PZ)** *0.31 ± 0.17 (PZ)*	*GE*	*Integration of designated frequency ranges*	*130 / 1000*
Mueller Lisse et al. 2001 (64)	*0.24 ± 0.13 (PZ)*	*GE*	*Integration of designated frequency ranges*	*130 / 1000*
Shukla-Dave et al. 2007 (39)	*0.59 ± 0.03 (PZ)*	*GE*	*Integration of designated frequency ranges*	*130/1000*
Mazaheri et al. 2008 (65)	*0.73 ± 0.18 (PZ)*	*GE*	*Integration of designated frequency ranges*	*130/1000*
García-Martín et al. 2011 (42)	*0.24 ± 0.06 (PZ)*	*GE*	*LCModel fitting (50)*	*130/1000*
Weis et al. 2009 (66)	*0.50 ± 0.16*	*Philips*	*AMARES fitting in the MRUI software package (48)*	*130/1200*
Kaji et al. 2002 (67)	*0.58 ± 0.38 (PZ)* *0.72 ± 0.51 (TZ)*	*Siemens*	*Integrals of Lorentzian lineshapes using Luise (67)*	*135/1500*
Dorsten et al. (68)	*0.38 ± 0.15 (PZ)* *0.43 ± 0.16 (TZ)*	*Siemens*	*AMARES fitting in the MRUI software package (48)*	*120/1200*
Scheenen et al. 2011 (51)	*0.28 (0.21–0.37) (PZ)*** *0.36 (0.28–0.44) (TZ)*	*Siemens*	*Model spectra time domain using PRISMA*	*120 / 650*

Table 3.2. *Average (Cho+Cr)/Cit ratios for benign tissue (either in the peripheral zone (PZ), transition zone (TZ) or combined) at 1.5 T from different studies using different post processing methods.*

** Two techniques for water suppression were used. No statistical difference in the (Cho+Cr)/Cit ratio was found.*

*** No average and standard deviation were provided, but the median and 25th and 75th percentile.*

	Average (Cho+Cr)/Cit ratio ± stand. dev.	**Vendor**	**Post processing method**	**TE/TR (ms)**
Weis et al. 2011 (72)	*0.40 ± 0.09 (PZ)** *0.53 ± 0.12 (TZ)**	*Philips*	*LCModel fitting*	*140 / 1500*
Scheenen et al 2007 (54)	*0.22 ± 0.12 (PZ)* *0.34 ± 0.14 (TZ)*	*Siemens*	*Model spectra time domain using PRISMA*	*145 / 750*
Selnaes et al 2012 (48)	*0.38 (0.35-0.42)** (PZ)*	*Siemens*	*Model spectra time domain using PRISMA*	*145 / 750*

Table 3.3. *Average (Cho+Cr)/Cit ratios for peripheral zone (PZ) and transition zone (TZ) tissue at 3 T from three studies using different post processing methods*

** Measured in males older than 51 years of age*

*** In brackets the confidence interval is given.*

protocols still need to be established (60). The studies reporting (Cho+Cr)/Cit values for 3T-spectra are still limited (Table 3.3), but it can be expected that the metabolite ratios for normal tissue at 3 T will be more variable among studies and quite different (Cho+Cr)/Cit values would be obtained for the same patient measured on systems of different vendors. The dependency on acquisition and post-processing protocols asks for assessment of the mean and standard deviation of normal tissue per institution or per used protocol.

The derived classification thresholds are not necessarily institution-dependent. If the same acquisition protocol and post-processing method are used at different institutions, the (Cho+(Spm+)Cr)/Cit ratio can be compared between these institutions. Previously, no significant differences in the (Cho+Cr)/Cit amplitude ratio were found of any of the benign prostate tissues between patients among different institutions (47). Furthermore, the amplitude ratio gave good reproducibility in repeated measurements of the same subjects (61).

Standardized threshold approach

A more advanced classification strategy is the use of the standardized threshold approach, which was introduced by Jung et al (62) to give more weight to the increase in choline and decrease in polyamines observed in prostate cancer. The standardized threshold approach was developed for use in the peripheral zone (62), but later expanded for the transition zone (63). In this approach, an initial score (from 1 to 5) is given to each spectrum (Table 3.4 and 3.5) based on the mean (Cho+Cr)/Cit ratio of normal tissue and its standard deviation. . The initial score is adapted for certain choline over creatine (Cho/Cr) values. The fit for the Cho/Cr ratio is simplified in cancer tissue, due to the decrease of polyamine resonances, and might therefore be more reliable in tumor voxels than in normal voxels. For voxels with an initial score of 2 or 3, the initial score is increased to 4 if the Cho/Cr ratio is larger than or equal to 2. An initial score of 4 or 5 is decreased to 3 or 4, respectively, if the Cho/Cr ratio is smaller than 2 (Table 3.4 and 3.5). With this reproducible approach (61), good accuracy (72-87 %) for the differentiation of benign and malignant voxels was obtained in the peripheral zone (62) and transition zone (63). The cut off value for the Cho/Cr ratio was optimized to develop the standardized threshold approach as an aggressiveness assessment (55). Using this assessment it was found that only 10% of the highly aggressive tumors would be misclassified as less aggressive (55). The cut off values provided in Table 3.4 and 3.5 can only be used for spectra acquired with the same sequence, at the same field strength and similar post-processing (Note: no fitting of separate polyamines). If one wants to use the standardized threshold approach with other settings, one should first establish the correct cut off values.

Five-point standardized scoring system			
Score and Score definition	*Peripheral Zone (Cho+Cr)/Cit ratio*	*Central Gland (Cho+Cr)/Cit ratio*	*Cho/Cr ratio adjustment*
1: Definitely benign tissue	*≤0.44*	*≤0.52*	*- If Cho/Cr ratio ≥2, then: adjust 3 and 2 into 4. - If Cho/Cr ratio < 2, then: adjust 5 into 4 and 4 into 3.*
2: Probably benign tissue	*0.44<CC/C≤0.58*	*0.52<CC/C≤0.66*	
3: Possibly malignant tissue	*0.58<CC/C≤0.72*	*0.66<CC/C≤0.80*	
4: Probably malignant tissue	*0.72<CC/C≤0.86*	*0.80<CC/C≤0.94*	
5: Definitely malignant tissue	*>0.86*	*>0.94*	
CC/C = choline plus creatine to citrate			

Table 3.4. Example of cut off values of the standardized threshold approach used at 1.5 T (73) (TE/TR 120/650 ms). The ratio is obtained from integrals of Gaussian lineshapes.

Five-point standardized scoring system			
Score and Score definition	*Peripheral Zone (Cho+Cr)/Cit ratio*	*Central Gland (Cho+Cr)/Cit ratio*	*Cho/Cr ratio adjustment*
1: Definitely benign tissue	*≤0.34*	*≤0.48*	*- If Cho/Cr ratio ≥2, then: adjust 3 and 2 into 4. - If Cho/Cr ratio < 2, then: adjust 5 into 4 and 4 into 3.*
2: Probably benign tissue	*0.34<CC/C≤0.46*	*0.48<CC/C≤0.62*	
3: Possibly malignant tissue	*0.46<CC/C≤0.58*	*0.62<CC/C≤0.76*	
4: Probably malignant tissue	*0.58<CC/C≤0.70*	*0.76<CC/C≤0.90*	
5: Definitely malignant tissue	*>0.70*	*>0.90*	
CC/C = choline plus creatine to citrate			

Table 3.5. Example of cut off values of the standardized threshold approach used at 3 T (55). The Cho+Cr/Cit cut off values are based on the mean and standard deviation of normal tissue values published in (54).

Concluding remarks

We have discussed different aspects of the acquisition and post-processing that influence the (Cho+Cr)/Cit ratio. In principle this ratio could be vendor-independent with similar acquisition protocols and post processing, which would be convenient for the common use of classification thresholds of the ratio for disease features. Although this may be the case for 1.5 T to some extent, it is not for 3T systems. Thus in all clinical applications, institution or protocol dependent thresholds have to be established. To promote clinical usability of prostate MR spectroscopic imaging it would be desirable if consensus could be reached on field strength dependent common acquisition and postprocessing protocols.

References

1. Siegel R, Naishadham D, Jemal A. Cancer statistics, 2012. CA Cancer J Clin 2012;62(1):10-29.
2. Hoeks CMA, Barentsz JO, Hambrock T and others. Prostate cancer: Multiparametric MR imaging for detection, localization, and staging. Radiology 2011;261(1):46-66.
3. Thomas MA, Narayan P, Kurhanewicz J, Jajodia P, Weiner MW. 1H MR spectroscopy of normal and malignant human prostates in Vivo. J Magn Reson B 1990;87(3):610-619.
4. Kurhanewicz J, Vigneron DB, Nelson SJ, Hricak H, MacDonald JM, Konety B, Narayan P. Citrate as an in vivo marker to discriminate prostate cancer from benign prostatic hyperplasia and normal prostate peripheral zone: detection via localized proton spectroscopy. Urology 1995;45(3):459-466.
5. Kurhanewicz J, Vigneron DB, Hricak H, Narayan P, Carroll P, Nelson SJ. Three-dimensional H-1 MR spectroscopic imaging of the in situ human prostate with high (0.24-0.7-cm3) spatial resolution. Radiology 1996;198(3):795-805.
6. Heerschap A, Jager GJ, Van Der Graaf M, Barentsz JO, Ruijs SHJ. Proton MR spectroscopy of the normal human prostate with an endorectal coil and a double spin-echo pulse sequence. Magn Reson Med 1997;37(2):204-213.
7. Kobus T, Wright AJ, Scheenen TW, Heerschap A. Mapping of prostate cancer by 1H MRSI. NMR in Biomed 2013.DOI: 10.1002/nbm.2973
8. Swanson MG, Keshari KR, Tabatabai ZL, Simko JP, Shinohara K, Carroll PR, Zektzer AS, Kurhanewicz J. Quantification of choline- and ethanolamine-containing metabolites in human prostate tissues using 1H HR-MAS total correlation spectroscopy. Magn Reson Med 2008;60(1):33-40.
9. Glunde K, Bhujwalla ZM. Metabolic Tumor Imaging Using Magnetic Resonance Spectroscopy. Semin Oncol 2011;38(1):26-41.
10. Ackerstaff E, Pflug BR, Nelson JB, Bhujwalla ZM. Detection of increased choline compounds with proton nuclear magnetic resonance spectroscopy subsequent to malignant transformation of human prostatic epithelial cells. Cancer Res 2001;61(9):3599-3603.
11. Govindaraju V, Young K, Maudsley AA. Proton NMR chemical shifts and coupling constants for brain metabolites. NMR in Biomed 2000;13(3):129-153.
12. Wallimann T, Wyss M, Brdiczka D, Nicolay K, Eppenberger HM. Intracellular compartmentation, structure and function of creatine kinase isoenzymes in tissues with high and fluctuating energy demands: The ‘phosphocreatine circuit’ for cellular energy homeostasis. Biochem J 1992;281(1):21-40.
13. Kassen A, Sutkowski DM, Ahn H, Sensibar JA, Kozlowski JM, Lee C. Stromal cells of the human prostate: initial isolation and characterization. Prostate 1998;28(2):89-97.
14. Swanson MG, Zektzer AS, Tabatabai ZL and others. Quantitative analysis of prostate metabolites using 1H HR-MAS spectroscopy. Magn Reson Med 2006;55(6):1257-1264.
15. Lynch MJ, Masters J, Pryor JP, Lindon JC, Spraul M, Foxall PJ, Nicholson JK. Ultra high field NMR spectroscopic studies on human seminal fluid, seminal vesicle and prostatic secretions. J Pharm Biomed 1994;12(1):5-19.
16. Costello LC, Franklin RB. Citrate metabolism of normal and malignant prostate epithelial cells. Urology 1997;50(1):3-12.
17. Moore GJ, Sillerud LO. The pH Dependence of Chemical Shift and Spin-Spin Coupling for Citrate. J Magn Reson B 1994;103(1):87-88.
18. Van der Graaf M, Heerschap A. Effect of Cation Binding on the Proton Chemical Shifts and the Spin-Spin Coupling Constant of Citrate. J Magn Reson B 1996;112(1):58-62.
19. Trabesinger AH, Meier D, Dydak U, Lamerichs R, Boesiger P. Optimizing PRESS localized citrate detection at 3 Tesla. Magn Reson Med 2005;54(1):51-58.
20. Mulkern RV, Bowers JL, Peled S, Williamson DS. Density-matrix calculations of the

1.5 T citrate signal acquired with volume-localized STEAM sequences. J Magn Reson B 1996;110(3):255-266.

21. Wilman AH, Allen PS. The response of the strongly coupled AB system of citrate to typical 1H MRS localization sequences. J Magn Reson B 1995;107(1):25-33.
22. Scheenen TWJ, Gambarota G, Weiland E, Klomp DWJ, Fütterer JJ, Barentsz JO, Heerschap A. Optimal timing for in vivo 1H-MR spectroscopic imaging of the human prostate at 3T. Magn Reson Med 2005;53(6):1268-1274.
23. Van der Graaf M, Jager GJ, Heerschap A. Removal of the outer lines of the citrate multiplet in proton magnetic resonance spectra of the prostatic gland by accurate timing of a point- resolved spectroscopy pulse sequence. Magn Reson Mater Phy 1997;5(1):65-69.
24. Schick F, Bongers H, Kurz S, Jung WI, Pfeffer M, Lutz O. Localized proton MR spectroscopy of citrate in vitro and of the human prostate in vivo at 1.5 T. Magn Reson Med 1993;29(1):38-43.
25. Van der Graaf M, Van den Boogert HJ, Jager GJ, Barentsz JO, Heerschap A. Human prostate: multisection proton MR spectroscopic imaging with a single spin-echo sequence--preliminary experience. Radiology 1999;213(3):919-925.
26. Cunningham CH, Vigneron DB, Marjanska M, Chen AP, Xu D, Hurd RE, Kurhanewicz J, Garwood M, Pauly JM. Sequence design for magnetic resonance spectroscopic imaging of prostate cancer at 3 T. Magn Reson Med 2005;53(5):1033-1039.
27. Verma S, Rajesh A, Fütterer JJ, Turkbey B, Scheenen TWJ, Pang Y, Choyke PL, Kurhanewicz J. Prostate MRI and 3D MR spectroscopy: How we do it. AJR Am J Roentgenol 2010;194(6):1414-1426.
28. Kobus T, Wright AJ, Asten JJ, Heerschap A, Scheenen TW. In vivo 1H MR spectroscopic imaging of aggressive prostate cancer: Can we detect lactate? Magn Reson Med 2013;DOI: 10.1002/mrm.24635.
29. Mescher M, Tannus A, Johnson MO, Garwood M. Solvent suppression using selective echo dephasing. J Magn reson A 1996;123(2):226-229.
30. Males RG, Vigneron DB, Star Lack O, Falbo SC, Nelson SJ, Hricak H, Kurhanewicz J. Clinical application of BASING and spectral/spatial water and lipid suppression pulses for prostate cancer staging and localization by in vivo 3D H-1 magnetic resonance spectroscopic imaging. Magn Reson Med 2000;43(1):17-22.
31. Star-Lack J, Nelson SJ, Kurhanewicz J, Huang LR, Vigneron DB. Improved water and lipid suppression for 3D PRESS CSI using RF band selective inversion with gradient dephasing (BASING). Magn Reson Med 1997;38(2):311-321.
32. Schricker AA, Pauly JM, Kurhanewicz J, Swanson MG, Vigneron DB. Dualband spectral-spatial RF pulses for prostate MR spectroscopic imaging. Magn Reson Med 2001;46(6):1079-1087.
33. Cunningham CH, Vigneron DB, Chen AP, Xu D, Hurd RE, Sailasuta N, Pauly JM. Design of symmetric-sweep spectral-spatial RF pulses for spectral editing. Magn Reson Med 2004;52(1):147-153.
34. Gambarota G, Van Der Graaf M, Klomp D, Mulkern RV, Heerschap A. Echo-time independent signal modulations using PRESS sequences: A new approach to spectral editing of strongly coupled AB spin systems. J Magn Reson 2005;177(2):299-306.
35. Kickler N, Gambarota G, Mekle R, Gruetter R, Mulkern R. Echo-time independent signal modulations for strongly coupled systems in triple echo localization schemes: An extension of S-PRESS editing. J Magn Reson 2010;203(1):108-112.
36. Lynch MJ, Nicholson JK. Proton MRS of human prostatic fluid: Correlations between citrate, spermine, and myo-inositol levels and changes with disease. Prostate 1997;30(4):248-255.
37. Schipper RG, Romijn JC, Cuijpers VMJI, Verhofstad AAJ. Polyamines and prostatic cancer. Biochem Soc T 2003;31(2):375-380.
38. Van der Graaf M, Schipper RG, Oosterhof GO,

Schalken JA, Verhofstad AA, Heerschap A. Proton MR spectroscopy of prostatic tissue focused on the detection of spermine, a possible biomarker of malignant behavior in prostate cancer. Magma 2000;10(3):153-159.

39. Shukla-Dave A, Hricak H, Moskowitz C and others. Detection of prostate cancer with MR spectroscopic imaging: An expanded paradigm incorporating polyamines. Radiology 2007;245(2):499-506.
40. Willker W, Flögel U, Leibfritz D. A 1H/13C inverse 2D method for the analysis of the polyamines putrescine, spermidine and spermine in cell extracts and biofluids. NMR in Biomed 1998;11(2):47-54.
41. Spencer NG, Eykyn TR, DeSouza NM, Payne GS. The effect of experimental conditions on the detection of spermine in cell extracts and tissues. NMR in Biomed 2010;23(2):163-169.
42. García-Martín ML, Adrados M, Ortega MP, Fernández González I, Lõpez-Larrubia P, Viaño J, García-Segura JM. Quantitative 1H MR spectroscopic imaging of the prostate gland using LCModel and a dedicated basis-set: Correlation with histologic findings. Magn Reson Med 2011;65(2):329-339.
43. Yuen JS, Thng CH, Tan PH, Khin LW, Phee SJ, Xiao D, Lau WK, Ng WS, Cheng CW. Endorectal magnetic resonance imaging and spectroscopy for the detection of tumor foci in men with prior negative transrectal ultrasound prostate biopsy. J Urol 2004;171(4):1482-1486.
44. Barentsz JO, Richenberg J, Clements R, Choyke P, Verma S, Villeirs G, Rouviere O, Logager V, Fütterer JJ. ESUR prostate MR guidelines 2012. Eur Radiol 2012;22(4):746-757.
45. Lowry M, Liney GP, Turnbull LW, Manton DJ, Blackband SJ, Horsman A. Quantification of citrate concentration in the prostate by proton magnetic resonance spectroscopy: zonal and age-related differences. Magn Reson Med 1996;36(3):352-358.
46. Selnæs KM, Heerschap A, Jensen LR, Tessem MB, Schweder GJV, Goa PE, Viset T, Angelsen A, Gribbestad IS. Peripheral zone prostate cancer localization by multiparametric magnetic resonance at 3 T: Unbiased Cancer identification by matching to histopathology. Invest Radiol 2012;47(11):624-633.
47. Smith S, Levante T, Meier BH, Ernst RR. Computer simulations in magnetic resonance. An object-oriented programming approach. J Magn Reson A 1994;106(1):75-105.
48. Naressi A, Couturier C, Devos J, Janssen M, Mangeat C, De Beer R, Graveron-Demilly D. Java-based graphical user interface for the MRUI quantitation package. Magma 2001;12(2-3):141-152.
49. Vanhamme L, van den Boogaart A, Van Huffel S. Improved method for accurate and efficient quantification of MRS data with use of prior knowledge. J Magn Reson 1997;129(1):35-43.
50. Provencher SW. Estimation of metabolite concentrations from localized in vivo proton NMR spectra. Magn Reson Med 1993;30(6):672-679.
51. Scheenen TWJ, Fütterer J, Weiland E and others. Discriminating cancer from noncancer tissue in the prostate by 3-dimensional proton magnetic resonance spectroscopic imaging: A prospective multicenter validation study. Invest Radiol 2011;46(1):25-33.
52. Pels P, Osturk-Isik E, Swanson MG, Vanhamme L, Kurhanewicz J, Nelson SJ, Van Huffel S. Quantification of prostate MRSI data by model-based time domain fitting and frequency domain analysis. NMR in Biomed 2006;19(2):188-197.
53. Scheenen TW, Heijmink SW, Roell SA, Hulsbergen-Van de Kaa CA, Knipscheer BC, Witjes JA, Barentsz JO, Heerschap A. Three-dimensional proton MR spectroscopy of human prostate at 3 T without endorectal coil: feasibility. Radiology 2007;245(2):507-516.
54. Kobus T, Hambrock T, Hulsbergen-Van De Kaa CA, Wright AJ, Barentsz JO, Heerschap A, Scheenen TWJ. In vivo assessment of prostate cancer aggressiveness using magnetic resonance spectroscopic imaging at 3 T with an endorectal coil. Eur Urol 2011;60(5):1074-1080.
55. Zakian KL, Sircar K, Hricak H and others.

Correlation of proton MR spectroscopic imaging with gleason score based on step-section pathologic analysis after radical prostatectomy. Radiology 2005;234(3):804-814.

56. Weinreb JC, Blume JD, Coakley FV and others. Prostate cancer: Sextant localization at MR imaging and MR spectroscopic imaging before prostatectomy - Results of ACRIN prospective multi-institutional clinicopathologic study. Radiology 2009;251(1):122-133.
57. Sciarra A, Panebianco V, Ciccariello M, Salciccia S, Cattarino S, Lisi D, Gentilucci A, Alfarone A, Bernardo S, Passariello R. Value of magnetic resonance spectroscopy imaging and dynamic contrast-enhanced imaging for detecting prostate cancer foci in men with prior negative biopsy. Clin Cancer Res 2010;16(6):1875-1883.
58. Lagemaat MW, Scheenen TW. Role of high-field MR in studies of localized prostate cancer. NMR in Biomed 2013. DOI: 10.1002/nbm.2967
59. Lagemaat MW, Zechmann CM, Fütterer JJ and others. Reproducibility of 3D 1H MR spectroscopic imaging of the prostate at 1.5T. J Magn Reson Imaging 2012;35(1):166-173.
60. Jung JA, Coakley FV, Vigneron DB, Swanson MG, Qayyum A, Weinberg V, Jones KD, Carroll PR, Kurhanewicz J. Prostate depiction at endorectal MR spectroscopic imaging: investigation of a standardized evaluation system. Radiology 2004;233(3):701-708.
61. Fütterer JJ, Scheenen TWJ, Heijmink SWTPJ, Huisman HJ, Hulsbergen-Van De Kaa CA, Witjes JA, Heerschap A, Barentsz JO. Standardized threshold approach using three-dimensional proton magnetic resonance spectroscopic imaging in prostate cancer localization of the entire prostate. Invest Radiol 2007;42(2):116-122.
62. Heerschap A, De Jager G, De Koster A, Barentsz J, De la Rosette J, Debruyne F, Ruijs J. 1H MRS of prostate pathology. Proc Int Soc Magn Reson Med. Volume S1. New York, New York, USA; 1993.
63. Chen AP, Cunningham CH, Kurhanewicz J, Xu D, Hurd RE, Pauly JM, Carvajal L, Karpodinis K, Vigneron DB. High-resolution 3D MR spectroscopic imaging of the prostate at 3 T with the MLEV-PRESS sequence. Magn Reson Imaging 2006;24(7):825-832.
64. Mueller Lisse UG, Vigneron DB, Hricak H and others. Localized prostate cancer: Effect of hormone deprivation therapy measured by using combined three-dimensional H-1 MR spectroscopy and MR imaging: Clinicopathologic case-controlled study. Radiology 2001;221(2):380-390.
65. Mazaheri Y, Shukla-Dave A, Hricak H and others. Prostate cancer: Identification with combined diffusion-weighted MR imaging and 3D1H MR spectroscopic imaging - Correlation with pathologic findings. Radiology 2008;246(2):480-488.
66. Weis J, Ahlström H, Hlavcak P, Häggman M, Ortiz-Nieto F, Bergman A. Two-dimensional spectroscopic imaging for pretreatment evaluation of prostate cancer: comparison with the step-section histology after radical prostatectomy. Magn Reson Imaging 2009;27(1):87-93.
67. Kaji Y, Wada A, Imaoka I, Matsuo M, Terachi T, Kobashi Y, Sugimura K, Fujii M, Maruyama K, Takizawa O. Proton two-dimensional chemical shift imaging for evaluation of prostate cancer: external surface coil vs. endorectal surface coil. J Magn Reson Imaging 2002;16(6):697-706.
68. van Dorsten FA, van der Graaf M, Engelbrecht MR, van Leenders GJ, Verhofstad A, Rijpkema M, de la Rosette JJ, Barentsz JO, Heerschap A. Combined quantitative dynamic contrast-enhanced MR imaging and 1H MR spectroscopic imaging of human prostate cancer. J Magn Reson Imaging 2004;20(2):279-287.
69. Futterer JJ, Scheenen TW, Huisman HJ, Klomp DW, van Dorsten FA, Hulsbergen-van de Kaa CA, Witjes JA, Heerschap A, Barentsz JO. Initial Experience of 3 Tesla Endorectal Coil Magnetic Resonance Imaging and 1H-Spectroscopic Imaging of the Prostate. Invest Radiol 2004;39(11):671-680.

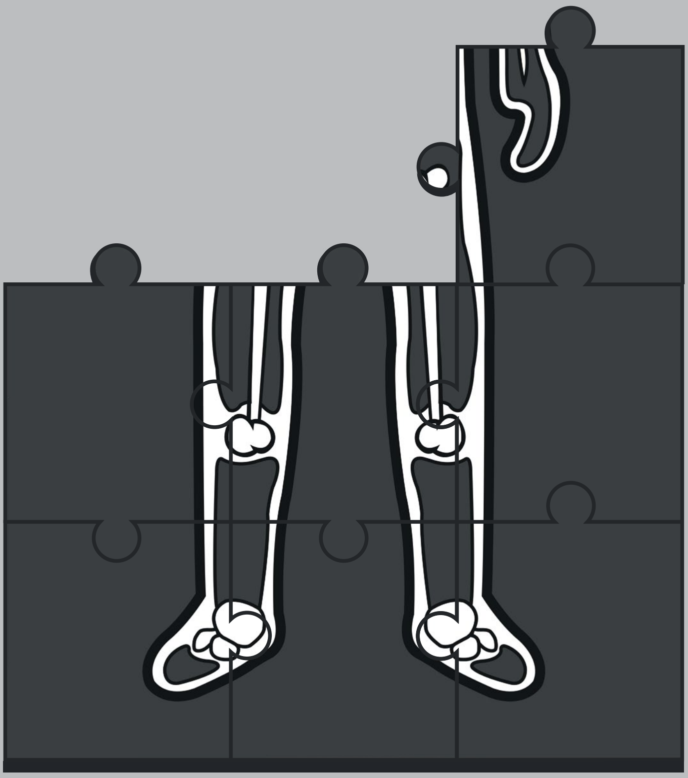

4

CHAPTER FOUR

In Vivo Assessment of Prostate Cancer Aggressiveness Using Magnetic Resonance Spectroscopic Imaging at 3T with an Endorectal Coil

This chapter is based on the publication:
In vivo assessment of prostate cancer aggressiveness using magnetic resonance spectroscopic imaging at 3T with an endorectal coil
T. Kobus, T. Hambrock, C.A. Hulsbergen-van de Kaa, A.J. Wright, J.O. Barentsz, A. Heerschap and T.W.J. Scheenen
European Urology, 2011 Nov;60(5):1074-80.

Introduction

Prostate cancer is the most frequently diagnosed non-cutaneous cancer in European men and accounted for 9.3% of cancer-related deaths in men in 2008 (1). A large European study (2) showed that screening for prostate cancer by means of prostate-specific antigen (PSA) levels will result in a mortality reduction of 20% at the cost of overdiagnosis of many indolent cancers. If unnecessary side-effects due to overtreatment of indolent tumors are to be prevented, while at the same time all aggressive tumors are to be treated, accurate discrimination between indolent and life-threatening cancers is essential.

Generally, transrectal ultrasound (TRUS)-guided biopsies are performed to confirm the presence of prostate cancer and to determine the Gleason score of the tumor. However, the multifocal nature and heterogeneity of these tumors cause sampling errors and may lead to underestimation of their aggressiveness. Several studies demonstrate discrepancies between the Gleason score identified in biopsies and the subsequent radical prostatectomy specimens (3,4). For optimal diagnosis the most aggressive tumor focus should be identified.

Proton magnetic resonance (MR) spectroscopic imaging (^{1}H MRSI) provides spatial mapping of the tissue levels of the metabolites citrate (Cit), choline (Cho) and creatine (Cr) in the whole prostate gland (5,6). Prostate cancer tissue is characterized by lower Cit levels and/or higher Cho levels compared to normal tissue (7), resulting in the ratio of choline plus creatine to citrate [(Cho+Cr)/Cit] as a marker for prostate cancer (7,8). MR imaging (MRI) and ^{1}H MRSI have detected high grade tumors in patients with elevated PSA with high sensitivity (9). Other studies found a correlation (10) and a trend (11) between the Gleason score and the (Cho+Cr)/Cit ratio at 1.5 T with the use of an endorectal coil. No relation with aggressiveness was found at 1.5 T without the use of an endorectal coil (12). At 3 T, no relation was found using just body-array coils (6). The use of an endorectal coil increases the signal-to-noise ratio and might provide enough sensitivity at 3 T to classify tumor aggressiveness.

Incorporation of the ratio of choline to creatine (Cho/Cr) is interesting since Cho supposedly increases in malignant tissue due to altered phospholipid metabolism (13) and increased Cho/Cr ratios have been used in standardized scoring systems for ^{1}H MRSI of the prostate (14,15). High-resolution *ex vivo* magic angle spinning nuclear MR of prostate biopsies showed a significant correlation of the Gleason score to the Cho/Cr ratio, among other ratios (16). These studies suggest that the Cho/Cr ratio has additional potential to classify tumor aggressiveness *in vivo*.

The purpose of this study was to validate the performance of ^{1}H MRSI of the prostate at 3 T with an endorectal coil in assessing tumor aggressiveness based on the (Cho+Cr)/Cit and Cho/Cr ratios, using the Gleason score from histopathology of the radical prostatectomy specimen as the gold standard.

Materials and methods

Subjects

This study was approved by the institutional ethics review board, and the need for informed consent was waived for the retrospective study. One hundred eight consecutive patients with biopsy-proven prostate cancer had a 3-T MR exam between October 2006 and February 2009 as well as a radical prostatectomy between October 2006 and April 2009. Of these patients, 72 had a ^{1}H MRSI exam and were retrospectively selected for this study. Patients were excluded if they were not examined with an endorectal coil (n=4), had prior neoadjuvant therapy (n=9), had no tumor foci with a volume of at least 0.5 cm^3 according to the histopathologic analysis (n=14), or had no reliable histopathology (n=2).

Magnetic resonance data acquisition

All MR exams were performed on a 3T MR system (Magnetom Trio, Siemens, Erlangen, Germany). An endorectal surface coil (Medrad, Pittsburgh, PA, USA) was combined with body array coils for signal reception. In all patients, an intramuscular injection of 1 mg glucagon (GlucaGen, Novo Nordisk, Gentofte, Denmark) and an injection of 20 mg butylscopolamine bromide (Buscopan, Boehringer Ingelheim, Ingelheim, Germany) were used to suppress peristalsis.

Fast-gradient echo sequences were used to check the position of the coils. High-spatial resolution T2-weighted images were made in three directions. A prostate specific MRSI sequence was used (17), including suppression of water and fat signals and an adapted sampling scheme (5,18). The actual volume of the spherical voxels was 0.37 or 0.64 cm^3 (5).

Histopathologic analysis

All radical prostatectomy specimens were uniformly processed and completely embedded according to a clinical protocol (19). After formalin fixation and inking of the surface, the prostate specimen was serially sectioned at 4 mm intervals, perpendicular to the dorsal-rectal surface, and all slices were macroscopically photographed. One urological pathologist (C.A.H.K.) evaluated all radical prostatectomy specimens and outlined for each slice the location of the tumor(s) on the photographs. Each tumor focus was graded according to the 2005 International Society of Urological Pathology Modified Gleason Grading System (20), and each patient was staged following the 2002 TNM classification (21).

The primary, secondary and tertiary Gleason grades were used for a qualitative grading of the tumor aggressiveness. Tumors were classified as low grade if they consisted only of

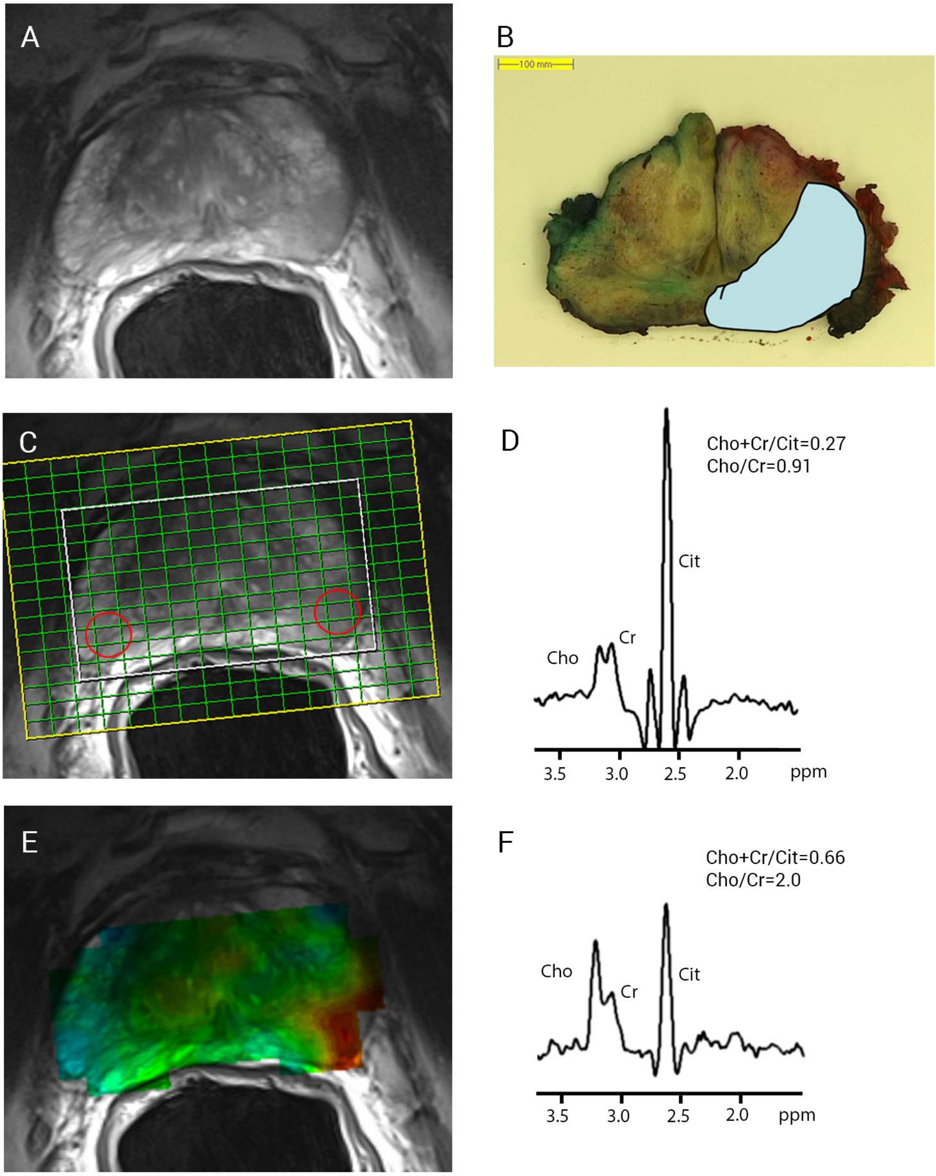

Figure 4.1. *MRI and MRSI of a 65-year-old patient with prostate cancer (PSA level 5.3 ng/ml, Gleason Score 4+5) A) T2-weighted MR image of the prostate with a tumor in the left peripheral zone. For tumor localization the histopathology (B) is used as the gold standard. The spectroscopy grid is displayed on top of the T2-weighted image in C. In the right and left peripheral zone a non-cancer voxel and cancer voxel, respectively, are indicated, obtained with a echo time of 145ms and a repetition time of 750ms. D shows a spectrum of non cancer tissue, while in F the spectrum of a cancer voxel is shown with deviating signal intensities for the different metabolites. The calculated (Cho+Cr)/Cit ratio and the Cho/Cr ratio are indicated in the spectra of both tissues. The metabolite map in E shows the (Cho+Cr)/Cit distribution over the prostate.*

grades 2 and/or 3; as intermediate grade, with a secondary or tertiary grade of 4 but no 5 component; or as high grade with 4 as primary and/or 5 as a primary/secondary or tertiary grade (Table 4.1).

No of patients		*43*
PSA level, mean, ng/ml (range)		*8.33 (2.08 - 40.96)*
Age, mean, yr (range)		*61 (42-70)*
Clinical stage		
T2		*19*
T3		*23*
T4		*1*
***Gleason score** - Peripheral zone:*		*No of tumors:*
3+2	*low*	*2*
3+3	*low*	*10*
3+3+4	*intermediate*	*1*
3+4	*intermediate*	*10*
3+4+5	*high*	*3*
4+3	*high*	*9*
4+3+5	*high*	*2*
4+4	*high*	*1*
4+5	*high*	*2*
Gleason Score - Central gland:		
2+3	*low*	*2*
3+2	*low*	*3*
3+2+4	*intermediate*	*1*
2+4+5	*high*	*1*
4+3	*high*	*1*
4+3+5	*high*	*3*
Gleason score - Both zones:		
4+3	*high*	*1*
4+4	*high*	*1*

Table 4.1: *Patient and tumor characteristics.*
**The tumors are classified according to their aggressiveness*
There were 17 low grade, 12 intermediate grade and 24 high grade tumors.

Voxel selection and statistical analysis

One radiologist (T.H.), blinded to the spectra, used the results of the histopathologic analysis to assign all spectroscopic voxels containing tumor tissue on high-resolution T2-weighted images with the voxel matrix of the spectroscopic exam projected over these images

(Figure 4.1C). Only clinically significant tumors with a minimal size of 0.5 cm^3 (22,23) on the histopathologic analysis were included. Figure 4.1 shows an example of a T2-weighted image and corresponding histopathology.

The signals of interest were fitted with a prototype software package (metabolite report, Siemens), and the (Cho+Cr)/Cit and Cho/Cr ratios were calculated automatically. Two spectroscopists independently (T.K. and T.W.J.S.) inspected the quality of the automated fit for sufficient signal-to-noise ratio, the absence of lipid signals, and the absence of baseline distortions. Only voxels that were approved by both spectroscopists were included in the remainder of the study.

For every tumor, the voxel with the highest (Cho+Cr)/Cit ratio and the voxel with the highest Cho/Cr ratio were determined. The highest (Cho+Cr)/Cit and Cho/Cr values of all data from each aggressiveness class were checked for normality and compared with each other using a Kruskal-Wallis test. The Pearson correlation coefficient was used to determine the correlation between the two ratios. To test the correlation between the ratios and the different aggressiveness classes the Kendall τ rank correlation coefficient was determined.

To enable incorporation of both metabolite ratios in discrimination of aggressiveness classes, the standardized threshold approach (14,15) was used. The conventional standardized threshold approach uses an initial malignancy rating (ranging from 1 [definitely benign] to 5 [definitely malignant]) based upon the mean and standard deviation (SD) of the (Cho+Cr)/Cit ratio of noncancereous tissue (distinction is made between peripheral zone (PZ) and central gland (CG)) with an adjustment to the initial rating based upon the Cho/Cr ratio (Table 4.2) (15).

This malignancy rating was determined for all accepted voxels in each tumor using the mean (Cho+Cr)/Cit ratios and SDs of noncancereous tissue described earlier (6). To optimize the

Five-point standardized scoring system			
Score and Score definition	*Peripheral Zone (Cho+Cr)/Cit ratio*	*Central Gland (Cho+Cr)/ Cit ratio*	*Cho/Cr ratio adjustment*
1: Definitely benign tissue	*≤0.34*	*≤0.48*	*- If Cho/Cr ratio ≥2.3, then: adjust 3 and 2 into 4.* *- If Cho/Cr ratio < 2.3, then: adjust 5 into 4 and 4 into 3.*
2: Probably benign tissue	*0.34<CC/C≤0.46*	*0.48<CC/C≤0.62*	
3: Possibly malignant tissue	*0.46<CC/C≤0.58*	*0.62<CC/C≤0.76*	
4: Probably malignant tissue	*0.58<CC/C≤0.70*	*0.76<CC/C≤0.90*	
5: Definitely malignant tissue	*>0.70*	*>0.90*	
CC/C = choline plus creatine to citrate			

Table 4.2. Conventional standardized threshold approach definitions

standardized scoring system for aggressiveness assessment with 3T data, the Cho/Cr cut off level, which adjusts the initial malignancy rating, was varied between 1 and 4 with 0.1 intervals. For all 31 of these Cho/Cr “adaptation levels” the highest malignancy rating per tumor was calculated and used to obtain receiver operating characteristic (ROC) curves to determine the accuracy.

The area under the curve (AUC) of the ROC curves were determined to study the performance of discrimination of low-grade from higher-grade tumors and high-grade from lower-grade tumors using the maximum (Cho+Cr)/Cit, maximum Cho/Cr and the five-point scale of the standardized threshold approach. All AUCs were compared for statistical differences (24).

Statistical analyses were performed with GraphPad Prism software (GraphPad Software Inc, La Jolla, CA, USA) and MATLAB (Mathworks, Natick, MA, USA). For all statistical tests a p value of 0.05 was used to show significance.

Results

Of the 108 patients, 43 passed the inclusion criteria. A summary of patient and tumor characteristics is provided in Table 4.1. The mean time between the MR exam and radical prostatectomy was 6 weeks (range: 0-21). The MR exam (example in Figure 4.1) was performed on average 46 days after TRUS-guided biopsy (range: 19-107). The total number of clinically significant tumors was 53 in 43 patients. Forty tumors were located in the PZ, 11 in the CG and 2 tumors covered both zones (assigned as PZ tumor for analysis). The average tumor size on histopathology was 6.3 cm^3 (range: 0.52-33.5). The patient Gleason scores of the tumors that were excluded because the volume was smaller than 0.5 cm^3 were 2+3 (n=2), 3+3 (n=9), 3+4 (n=2) and no malignancy detected (n=1).

In total, the radiologist selected 1892 tumor voxels. Of these voxels, 77% (1463 of 1892) passed the quality inspection of both spectroscopists. Three patients - and therefore 5 tumors - had to be excluded from the analysis, because none of the spectra of the selected voxels were usable.

A small, but significant correlation was found between the maximum (Cho+Cr)/Cit ratio and the aggressiveness classes (p=0.02, r=0.27; Figure 4.2A). The comparison of the medians of the three aggressiveness classes revealed a significant difference between the low and high grade tumors. The maximum Cho/Cr ratio also correlated significantly with the aggressiveness classes (p<0.01, r=0.31; Figure 4.2B). The median Cho/Cr of the low grade tumors was significantly different from the high grade tumors. Table 4.3 shows the AUCs representing the performance of the aggressiveness assessments.

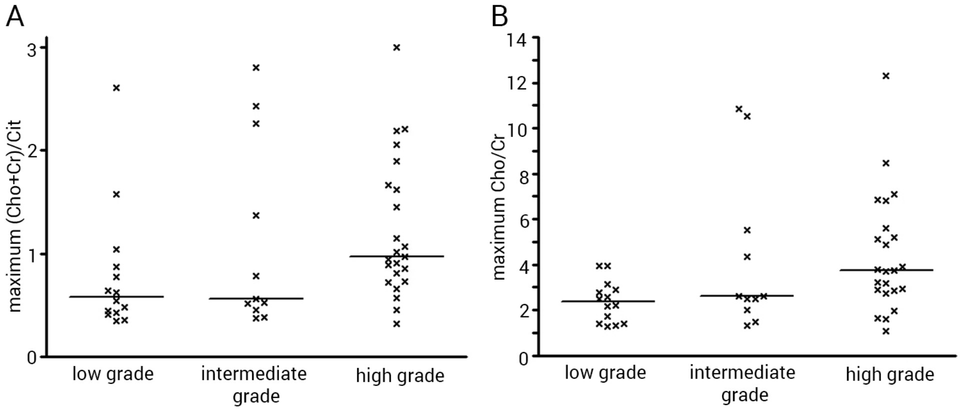

Figure 4.2. *A) The distribution of the maximum (Cho+Cr)/Cit ratio per tumor aggressiveness class. The horizontal bars indicate the median. One high grade tumor had a maximum (Cho+Cr)/Cit ratio of 58 which has been plotted at a (Cho+Cr)/Cit ratio of 3 for displaying purposes. B) Distribution of the maximum Cho/Cr ratio per aggressiveness class. The horizontal bars indicate the median.*

The correlation between the maximum (Cho+Cr)/Cit ratio and the maximum Cho/Cr ratio was 0.51 ($p<0.001$). For each tumor, the maximum (Cho+Cr)/Cit was plotted against the maximum Cho/Cr value (Figure 4.3).

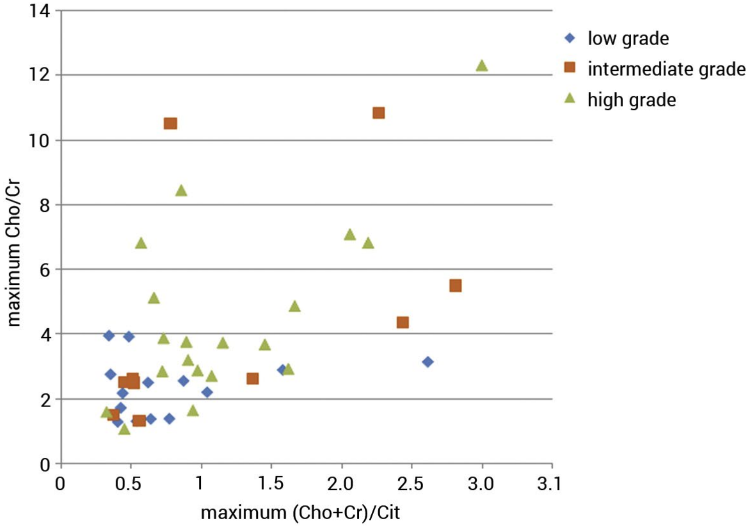

Figure 4.3. *The maximum (Cho+Cr)/Cit ratio for each tumor focus plotted against the maximum Cho/Cr ratio of that focus. The tumors are divided by aggressiveness class. The (Cho+Cr)/Cit ratio of one high grade tumor was cut off at 3 for displaying purposes*

	Low-grade vs high- & intermediate-grade tumors	***High-grade vs low- & intermediate-grade tumors***
Maximum (Cho+Cr)/Cit	*0.70*	*0.69*
Maximum Cho/Cr	*0.74*	*0.71*
Standardized threshold approach	*0.78*	*0.73*

Table 4.3. *The areas under the ROC curves for the discrimination among different aggressiveness classes using the maximum (Cho+Cr)/Cit ratio Cho/Cr and the standardized threshold approach. For the standardized threshold approach an optimized Cho/Cr rating adaptation level of 2.3 was used.*

A Cho/Cr adaptation level of 2.3 for the standardized threshold approach gave the highest AUCs when discriminating high-grade from low- and intermediate-grade tumors (AUC=0.73) and low- from the combined high- and intermediate-grade tumors (AUC=0.78). The malignancy ratings, using an adaptation level of 2.3, are shown in Figure 4.4, and the median malignancy rating of the high (median=5) and low (median=3) grade tumors was significantly different.

In all discriminations between aggressiveness classes (Table 4.3), the AUCs of the standardized threshold method with an adaptation level of 2.3 were higher than the AUCs for the maximum (Cho+Cr)/Cit or Cho/Cr ratio alone, but these differences were not significant.

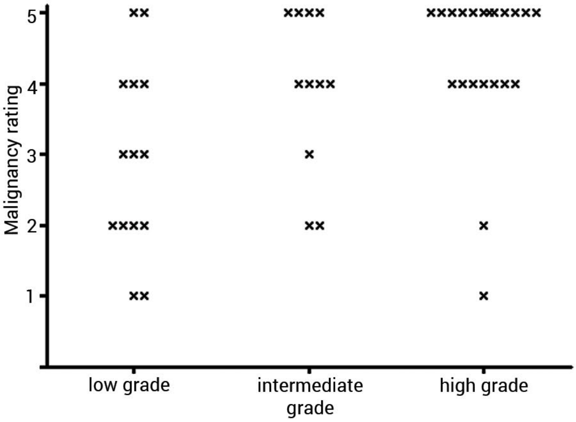

Figure 4.4. *The highest malignancy ratings according to the standardized threshold approach for each tumor in the aggressiveness classes. A Cho/Cr adaptation level of 2.3 was used.*

Discussion

With an increasing number of reports on overdiagnosis (2,25), an individualized prostate cancer aggressiveness assessment is essential. Currently the pretreatment aggressiveness is determined with biopsies, but often the Gleason score is underestimated (3,4). MRI/MRSI could be a prognostic noninvasive approach to differentiate among patients as suitable candidates for active surveillance and patients that need immediate treatment. Moreover, it would enable targeted therapy, such as intensity-modulated radiotherapy or high-intensity focused ultrasound, to be applied to the most aggressive part of the tumor. In a detection setting, MRI/MRSI could guide a biopsy so that it could be taken from the most aggressive part of a tumor. Validation is the first step in the development of such a prognostic MRSI approach. We assessed the tumor aggressiveness differentiation by the AUC of the ROC curves and this method produced similar results when using either the (Cho+Cr)/Cit ratio (0.70) or the Cho/Cr raio (0.74). The performance of combining both ratios was better (0.78), although this difference was not statistically significant, because of a relative small sample size. The AUCs reflect considerable overlap between the ratios in the different aggressiveness classes, similar to what has been reported in other studies concerning the relationship between the (Cho+Cr)/Cit ratio and Gleason score (10,11).

We investigated whether a combination of both ratios would increase the performance of separating low-grade from higher-grade tumors. The original standardized threshold approach was developed to improve tumor localization at 1.5 T with a Cho/Cr level of 2 to adjust the initial malignancy rating (14,15). As the timing of the MRSI pulse sequence at 3 T is different (17) from the timing at 1.5T, we optimized the Cho/Cr adaptation level of the standardized threshold approach for tumor aggressiveness classification at 3 T, retaining the original concept of defining the thresholds based on the mean and SDs of noncancereous PZ and CG tissues. When all tumors with a malignancy rating of 4 or 5 would be classified as high grade, only 10% of the high-grade tumors would be misclassified as a lower grade. Fifty-two percent of the intermediate- and low-grade tumors would be misclassified as high grade, which is better than previous results (68%) using MRI and ^{1}H MRSI in patients with an elevated PSA level (9).

As in current clinical practice, MR examinations of the prostate are often multiparametric; the standardized threshold approach could be extended to include more predictive variables for the assessment of aggressiveness. Features such as the apparent diffusion coefficient or pharmacokinetic parameters of dynamic contrast-enhanced MRI could be included to improve the performance (26).

The tumors of the patients in this study were divided into three clinically useful classes of aggressiveness: low, intermediate and high. The nature of the Gleason score does not lend itself to a linear relationship with an aggressiveness marker. Using three aggressiveness classes, the tertiary Gleason scores could be taken into account and Gleason 7 tumors could be divided into primary grade 3 and primary grade 4 tumors. The primary grade 4 tumors are more aggressive and have an increased risk for progression (27,28). Tumors with a tertiary Gleason score of 5 have a higher risk of extraprostatic extension (29) and PSA recurrence

(28,30) than tumors with the same score without a tertiary pattern. For these reasons, three classes of aggressiveness were used, which still enabled us to answer clinically relevant questions on aggressiveness.

Our study had several limitations. First, it was a retrospective single-institution study with a limited number of patients; therefore, our results may not be extrapolated to the general patient population. The data can be considered as promising but preliminary, and our conclusions need confirmation by a prospective, multicentre trial, which is currently underway. We did not correct for possible correlation between multiple tumors in a single patient (6 cases of two clinically significant tumors within one prostate). Although we distinguished between tumors in the PZ and those in the CG, we did not do a separate aggressiveness analysis for the two regions because of the limited number of CG tumors(n=11). We excluded 14 patients from our initial patient cohort because of tumor size on histopathology of less than 0.5 cm^3. Next to the fact that these small tumors are clinically insignificant (no high grade cancer present), the actual volume of the voxels of our MRSI examinations was too large to represent tumor foci of these sizes without too much surrounding noncancereous tissue within the voxel of interest. Metabolite ratios of these voxels would represent a mixture between cancer and noncancereous tissue.

Conclusion

This study showed that proton MR spectroscopic imaging offers potential for *in vivo* noninvasive assessment of prostate cancer aggressiveness, which has important implications. We have modified the existing standardized threshold approach to assess tumor aggressiveness at 3 T. The initial results of combining the (Cho+Cr)/Cit and Cho/Cr ratio were promising for the discrimination among different aggressiveness classes.

References

1. Ferlay J, Parkin DM, Steliarova-Foucher E. Estimates of cancer incidence and mortality in Europe in 2008. Eur J Cancer 2010;46(4):765-781.
2. Schroder FH, Hugosson J, Roobol MJ and others. Screening and prostate-cancer mortality in a randomized European study. N Engl J Med 2009;360(13):1320-1328.
3. Tomioka S, Nakatsu H, Suzuki N, Murakami S, Matsuzaki O, Shimazaki J. Comparison of Gleason grade and score between preoperative biopsy and prostatectomy specimens in prostate cancer. Int J Urol 2006;13(5):555-559.
4. Rajinikanth A, Manoharan M, Soloway CT, Civantos FJ, Soloway MS. Trends in Gleason Score: Concordance Between Biopsy and Prostatectomy over 15 Years. Urology 2008;72(1):177-182.
5. Scheenen TW, Klomp DW, Roll SA, Futterer JJ, Barentsz JO, Heerschap A. Fast acquisition-weighted three-dimensional proton MR spectroscopic imaging of the human prostate. Magn Reson Med 2004;52(1):80-88.
6. Scheenen TW, Heijmink SW, Roell SA, Hulsbergen-Van de Kaa CA, Knipscheer BC, Witjes JA, Barentsz JO, Heerschap A. Three-dimensional proton MR spectroscopy of human prostate at 3 T without endorectal coil: feasibility. Radiology 2007;245(2):507-516.
7. Kurhanewicz J, Vigneron DB, Hricak H, Narayan P, Carroll P, Nelson SJ. Three-dimensional H-1 MR spectroscopic imaging of the in situ human prostate with high (0.24-0.7-cm3) spatial resolution. Radiology 1996;198(3):795-805.
8. Heerschap A, Jager GJ, Van Der Graaf M, Barentsz JO, De La Rosette JJMCH, Oosterhof GON, Ruijter ETG, Ruijs SHJ. In vivo proton MR spectroscopy reveals altered metabolite content in malignant prostate tissue. Anticancer Res 1997;17(3 A):1455-1460.
9. Villeirs GM, De Meerleer GO, De Visschere PJ, Fonteyne VH, Verbaeys AC, Oosterlinck W. Combined magnetic resonance imaging and spectroscopy in the assessment of high grade prostate carcinoma in patients with elevated PSA: A single-institution experience of 356 patients. European journal of radiology 2009;Epub ahead of print.
10. Kurhanewicz J, Vigneron DB, Males RG, Swanson MG, Yu KK, Hricak H. The prostate: MR imaging and spectroscopy: Present and future. Radiol Clin North Am 2000;38(1):115-138.
11. Zakian KL, Sircar K, Hricak H and others. Correlation of proton MR spectroscopic imaging with gleason score based on step-section pathologic analysis after radical prostatectomy. Radiology 2005;234(3):804-814.
12. Jambor I, Borra R, Kemppainen J and others. Functional imaging of localized prostate cancer aggressiveness using 11C-acetate PET/CT and 1H-MR spectroscopy. J Nucl Med 2010;51(11):1676-1683.
13. Ackerstaff E, Pflug BR, Nelson JB, Bhujwalla ZM. Detection of increased choline compounds with proton nuclear magnetic resonance spectroscopy subsequent to malignant transformation of human prostatic epithelial cells. Cancer Res 2001;61(9):3599-3603.
14. Jung JA, Coakley FV, Vigneron DB, Swanson MG, Qayyum A, Weinberg V, Jones KD, Carroll PR, Kurhanewicz J. Prostate depiction at endorectal MR spectroscopic imaging: investigation of a standardized evaluation system. Radiology 2004;233(3):701-708.
15. Fütterer JJ, Scheenen TWJ, Heijmink SWTPJ, Huisman HJ, Hulsbergen-Van De Kaa CA, Witjes JA, Heerschap A, Barentsz JO. Standardized threshold approach using three-dimensional proton magnetic resonance spectroscopic imaging in prostate cancer localization of the entire prostate. Invest Radiol 2007;42(2):116-122.
16. Van Asten JJA, Cuijpers V, Hulsbergen-Van De Kaa C, Soede-Huijbregts C, Witjes JA, Verhofstad A, Heerschap A. High resolution

magic angle spinning NMR spectroscopy for metabolic assessment of cancer presence and Gleason score in human prostate needle biopsies. Magma (New York, NY 2008;21(6):435-442.

17. Scheenen TWJ, Gambarota G, Weiland E, Klomp DWJ, Fütterer JJ, Barentsz JO, Heerschap A. Optimal timing for in vivo 1H-MR spectroscopic imaging of the human prostate at 3T. Magn Reson Med 2005;53(6):1268-1274.
18. Pohmann R, von Kienlin M. Accurate phosphorus metabolite images of the human heart by 3D acquisition-weighted CSI. Magn Reson Med 2001;45(5):817-826.
19. Van Oort IM, Bruins HM, Kiemeney LALM, Knipscheer BC, Witjes JA, Hulsbergen-Van De Kaa CA. The length of positive surgical margins correlates with biochemical recurrence after radical prostatectomy. Histopathology 2010;56(4):464-471.
20. Epstein JI, Allsbrook Jr WC, Amin MB and others. The 2005 International Society of Urological Pathology (ISUP) consensus conference on Gleason grading of prostatic carcinoma. Am J Surg Pathol 2005;29(9):1228-1242.
21. Greene FL, Page DL, Flemming ID, Fritz AG, Balch CM, Haller DG, Morrow M. AJCC Cancer Staging Manual. 6th edition New York: Springer-Verlag; 2002.
22. Augustin H, Hammerer PG, Graefen M, Erbersdobler A, Blonski J, Palisaar J, Daghofer F, Huland H. Insignificant prostate cancer in radical prostatectomy specimen: time trends and preoperative prediction. Eur Urol 2003;43(5):455-460.
23. Stamey TA, Freiha FS, McNeal JE, Redwine EA, Whittemore AS, Schmid HP. Localized prostate cancer. Relationship of tumor volume to clinical significance for treatment of prostate cancer. Cancer 1993;71(3 Suppl):933-938.
24. Metz CE, Herman BA, Roe CA. Statistical comparison of two ROC-curve estimates obtained from partially-paired datasets. Med Decis Making 1998;18(1):110-121.
25. Andriole GL, Crawford ED, Grubb RL, 3rd and others. Mortality results from a randomized prostate-cancer screening trial. N Engl J Med 2009;360(13):1310-1319.
26. Seitz M, Shukla-Dave A, Bjartell A, Touijer K, Sciarra A, Bastian PJ, Stief C, Hricak H, Graser A. Functional Magnetic Resonance Imaging in Prostate Cancer. Eur Urol 2009;55(4):801-814.
27. Chan TY, Partin AW, Walsh PC, Epstein JI. Prognostic significance of Gleason score 3+4 versus Gleason score 4+3 tumor at radical prostatectomy. Urology 2000;56(5):823-827.
28. Hattab EM, Koch MO, Eble JN, Lin H, Cheng L. Tertiary Gleason Pattern 5 is a Powerful Predictor of Biochemical Relapse in Patients With Gleason Score 7 Prostatic Adenocarcinoma. J Urol 2006;175(5):1695-1699.
29. Mosse CA, Magi-Galluzzi C, Tsuzuki T, Epstein JI. The Prognostic Significance of Tertiary Gleason Pattern 5 in Radical Prostatectomy Specimens. Am J Surg Pathol 2004;28(3):394-398.
30. Pan CC, Potter SR, Partin AW, Epstein JI. The prognostic significance of tertiary Gleason patterns of higher grade in radical prostatectomy specimens: A proposal to modify the Gleason grading system. Am J Surg Pathol 2000;24(4):563-569.

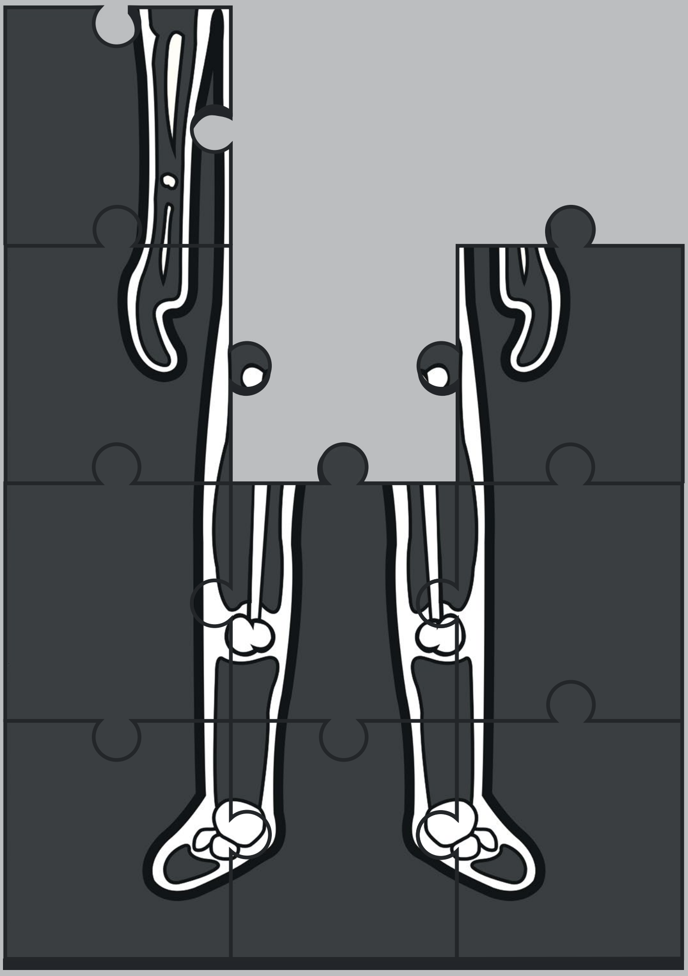

5

CHAPTER FIVE

Prostate Cancer Aggressiveness: *In Vivo* Assessment of MR Spectroscopy and Diffusion-weighted Imaging at 3 T

This chapter is based on the publication:

Prostate cancer aggressiveness: *in vivo* assessment of MR spectroscopy and diffusion-weighted imaging at 3 T
T. Kobus, P.C. Vos, T. Hambrock, M. De Rooij, C.A. Hulsbergen-Van de Kaa, J.O. Barentsz, A. Heerschap, T.W.J. Scheenen
Radiology, 2012 Nov;265(2):457-467

Introduction

Prostate cancer is the most common cancer in American men, with approximately 217 730 new cases reported in 2010 (1). In 30%–50% of the men in whom prostate cancer is diagnosed, the disease is indolent and not life threatening (2). However, in some patients, the tumor is aggressive and will lead to death if it is not treated. Screening for prostate cancer by measuring prostate-specific antigen (PSA) levels will lead to a 20% reduction in the number of deaths from prostate cancer after 9 years (3). Estimates show that 50% of the men in whom prostate cancer is diagnosed on the basis of screening findings would not have had any clinical symptoms for the rest of their lives (4). Autopsy studies showed that high-grade prostatic intraepithelial neoplasia, a precursor of prostate cancer, is present in up to 86% of the men aged 80 years or older (5). To prevent overtreatment in patients with an indolent tumor, one must account for life expectancy and clinical features, such as clinical stage, PSA level, and biopsy Gleason score (2). Currently, the Gleason score is determined by histopathologic analysis of transrectal ultrasound (TRUS)-guided biopsies; this leads to underestimation of the Gleason score in 26%–41% of biopsy specimens when compared with prostatectomy specimens (6-9). Thus, a reliable and preferably noninvasive measure of prostate cancer aggressiveness is needed.

For several years, a number of groups have investigated whether magnetic resonance (MR) techniques can yield information about tumor aggressiveness. One of these techniques is diffusion-weighted imaging (DWI), which measures the mobility of water molecules due to Brownian motion. The apparent diffusion coefficient (ADC) is a quantitative measure that reflects the compartmentalization of water in tissues. In malignant prostate tissue, the cellular density is increased, resulting in increased restriction of free water diffusion represented by a decreased ADC value (10,11). Several studies have been performed to investigate the correlation between the Gleason score and the ADC value of the tumor, with conflicting results. Contrary to earlier findings lacking a significant correlation (12-14), more recent articles have reported on the existence of a correlation between the ADC value and the Gleason score (15-19) or the level of differentiation of the tumor (20). Three-dimensional (3D) proton MR spectroscopic imaging (^{1}H MRSI) enables detection of the metabolites choline (Cho), polyamines (mainly spermine), creatine (Cr), and citrate (Cit). The (Cho+Cr)/Cit ratio has been suggested as a marker for prostate cancer, since a decrease in the Cit level and an increase in the Cho level is observed in malignant prostate tissue (21,22). When the (Cho+Cr)/Cit ratio was related to the Gleason score, a significant correlation (23,24), a trend (25), or no correlation (26) were reported. Although these results are promising, both modalities show substantial overlap between the different Gleason scores and the metabolic ratio or ADC values.

The ADC value was combined with the Cho/Cit ratio (27,28) or the Cho plus polyamines plus Cr to Cit ratio (29) to improve the localization of prostate cancer. The combination was significantly better than use of either the metabolic ratio (27,29) or the ADC value (27,28) alone. However, to our knowledge, no study has been performed in which the researchers attempted to combine both modalities to assess prostate cancer aggressiveness.

The improved tumor localization with both modalities and the correlation between the Gleason score and the ADC value and that between the Gleason score and the metabolic ratio are an indication that the combination of DWI and ^{1}H MRSI might enable noninvasive assessment of prostate cancer aggressiveness. The aim of this study was to determine the individual and combined performance of MRSI and DWI at 3 T in the *in vivo* assessment of prostate cancer aggressiveness by using histopathologically defined regions of interest (ROIs) on radical prostatectomy specimens to define the prostate cancer regions to be investigated.

Materials and methods

Subjects

The institutional ethics review board of the Radboud University Nijmegen Medical Centre approved this retrospective study and waived the requirement for informed consent. A total of 122 consecutive patients with biopsy-proven prostate cancer underwent a clinical MR examination performed with a 3T system and radical prostatectomy between October 2006 and December 2009. The following inclusion criteria were used: (a) ^{1}H MRSI and DWI performed during the same examination, (b) use of an endorectal coil for signal reception, (c) performance of detailed histopathology where at least one tumor focus with a volume of 0.5 cm^3 or more was detected, and (d) no neoadjuvant therapy. A total of 54 patients met all inclusion criteria and were retrospectively included in this study. The other patients were excluded because MRSI was not performed (n = 41), an endorectal coil was not used (n = 4), the tumor was too small (n = 14), or neoadjuvant therapy was administered (n = 9).

MR Examination

A whole-body 3T system (Magnetom Trio; Siemens Healthcare, Erlangen, Germany) was used for the MR examinations. For signal reception, an endorectal coil (Medrad, Pittsburgh, PA, USA) and an eight-element phased-array coil (Siemens Healthcare) were used. The balloon of the endorectal coil was filled with inert perfluoropolyether liquid (Fomblin; Solvay Solexis, Bollate, Italy) to minimize susceptibility differences between the endorectal coil and the tissue. To suppress peristalsis, the patients received intramuscular injections of 1 mg glucagon (GlucaGen; Novo Nordisk, Gentofte, Denmark) and 20 mg of butylscopolamine bromide (Buscopan; Boehringer Ingelheim, Ingelheim, Germany).

First, the relative positions of the patient and endorectal coil were checked with fast gradient-echo images. Next, high-spatial-resolution T2-weighted images (Table 5.1) were obtained. DWI was performed with a singleshot echo-planar imaging sequence with diffusion-encoding gradients in three directions (Table 5.1). The section thickness was 3 mm, and an in-plane resolution of 1.5 x 1.5 mm was used. The imager software automatically calculated the ADC maps from the images with b values of 0, 50, 500, and 800 sec/mm^2 by fitting signal attenuation as a function of the b value to mono-exponential decay.

For 3D ^{1}H MRSI, a point-resolved spectroscopic sequence was used with outer volume suppression and Mescher-Garwood dual-frequency water and lipid suppression (30) (Table 5.1). Weighted elliptical sampling of the k-space, zero filling, and Hanning filters were used to shorten acquisition time and minimize signal contamination from adjacent voxels. The nominal voxel size before apodization with the Hanning function was either 5 x 5 x 5 mm or 6 x 6 x 6 mm; after apodization, voxel size was best approximated by a sphere with a volume of 0.37 or 0.64 cm^3, respectively (3

	Echo time (ms)	***Repetition time (ms)***	***Matrix size***	***Field of View (mm)***	***Slice thick-ness (mm)***
T2-weighted transversal image	*84-116*	*3030-5460*	*222 x 448*	*89 x 180*	*3*
T2-weighted sagittal image	*98-125*	*3360-5710*	*268 x 384*	*134 x 192*	*3*
T2-weighted coronal image	*98-127*	*2400-4290*	*192 x 384*	*96 x 192*	*3*
Diffusion weighted imaging	*81-96*	*2300-4100*	*136 x 136*	*204 x 204*	*3*
Spectroscopic imaging	*145*	*750*	*Resolution: 5 x 5 x 5 or 6 x 6 x 6 mm*		

Table 5.1. Parameters of the MR exam

Histopathologic Evaluation

Immediately after surgery, the prostatectomy specimens were injected with formalin and fixed overnight in 10% neutral buffered formaldehyde. After ink was applied to the surface, the prostate was cut into 4-mm-thick transverse slices perpendicular to the dorsal rectal surface, and each slice was photographed. After routine hematoxylineosin staining, a urologic pathologist (C.A.H.) with 20 years of experience evaluated all prostatic specimens and outlined the location of the tumor or tumors on the photographs for each slice (32). Each tumor was graded according to the 2005 International Society of Urological Pathology Modified Gleason Grading System (33), and lesions in each patient were staged by following the 2002 TNM classification (34).

Tumors were classified into aggressiveness classes on the basis of the primary, secondary, and tertiary Gleason grade, provided at least 5% of a third pattern was present. The subdivision was as follows: low-grade tumors were those that consisted of only Gleason grade 2 and/or 3 components. Intermediate-grade tumors were those that had a secondary or tertiary Gleason grade 4 component but no grade 5 component. High-grade tumors were those with a primary grade 4 component and/or a grade 5 component present (primary, secondary, or tertiary grade).

ROI Selection

3D ^{1}H MRSI resulted in voxels with the lowest spatial resolution of the two functional imaging modalities; therefore, we based the choice of ROIs on the size and location of spectroscopic imaging voxels. The voxel matrix of the spectroscopic examination, which did not contain the spectra, was placed over the T2-weighted images. A radiologist (T.H.) used the photographs of the specimen sections with the tumors outlined to assign all MRSI voxels representing tumor tissue. To obtain unbiased measures, the radiologist was blinded to the spectra and ADC maps. Only clinically important tumors with a volume of at least 0.5 cm^3 were included (35,36). Voxels that had more than 50% of their volume outside the prostate were not included. Metabolite Report (Siemens Healthcare) was used for automated fitting of the spectra of the selected tumor voxels and calculation of the (Cho+Cr)/Cit and Cho/Cr ratios (Figure 5.1C,E). The software plots the original signal, the fit, and the residuals; these were inspected by two spectroscopists (T.K., T.W.J.S; 3 and 10 years of experience, respectively) working independently. The spectroscopists were asked to accept only spectra with correct positions of the resonances, sufficient signal-to-noise ratio, adequate phasing, absence of baseline distortions, and absence of lipid signals. Only voxels that passed the inspection of both spectroscopists were included in the MRSI analysis. The percentage of voxels that was accepted was determined.

To combine the ADC values with the spectroscopy voxels, home-built software (37) was used to plot a semitransparent ADC map over the T2-weighted images. If the patient had moved between the two recordings, a manual rigid translation of the ADC maps compared with the T2-weighted image was performed by a spectroscopist (T.K., 3 years experience) in consensus with a radiologist (T.H., 6 years experience) to overlay the prostate on both images. The outline of the prostate, bladder, seminal vesicles, and endorectal coil was used as a reference. The radiologist checked the ADC map for good quality. The MRSI matrix was then placed over the ADC map. Around each selected MRSI voxel (also around the voxels rejected by the spectroscopists), a spherical ROI of the true size of that voxel was drawn (Figure 5.1F), and the 25th percentile ADC value of all ADC pixels in that ROI was determined. The 25th percentile was chosen to take into account tumor heterogeneity and to capture focal regions of higher cellularity. This is in accordance with several other studies involving dynamic contrast-enhanced imaging that used a percentile of pharmacokinetic values to obtain information about the so-called hot spots, which are regions with the greatest microvessel density (37-39). The most aberrant part (ie, the highest grade or cellularity) of the tumor on the ADC map (ADC hot spot) could be smaller than the spectroscopic imaging voxels. For this reason, the 25th percentile, a measure for the lowest ADC values in a ROI, was chosen. If the ROI was partly outside the prostate, the ADC values of this region were not representative of the tumor. Thus, the ROI was readjusted so it contained only intraprostatic tissue.

Data Analysis

The data were analyzed by one spectroscopist (T.K., 3 years experience). The analysis was performed at the tumor level, and multiple tumors in one patient were treated as independent tumors. The volume of each tumor was calculated based on dimensions reported by the pathologist, and the average tumor volume of all tumors was determined. In all patients, the average time between the MR examination and biopsy and between the MR examination and prostatectomy were calculated.

For each tumor, the following three variables were computed to perform the analysis:
(a) the maximum (Cho+Cr)/Cit ratio of all approved spectroscopy voxels;
(b) the maximum Cho/Cr ratio of all approved spectroscopy voxels;
(c) the minimum of all 25th percentile ADC values of the ROIs.

The maximum metabolic ratios were used (24), as it was expected that the highest ratios represented the most aberrant part of the tumor. For the ADC values, the opposite relationship was expected; therefore, the minimum 25th percentile ADC value was chosen. Analysis of tumors originating in the peripheral zone (PZ) and those originating in the transition zone (TZ) was performed separately. Tumors that covered both zones were considered TZ tumors when the tumor covered at least 70% of the TZ (40); otherwise, they were considered PZ tumors. The three variables were related to the aggressiveness classes. The correlation between the aggressiveness classes and the (Cho+Cr)/Cit ratio, Cho/Cr ratio, and ADC variables was determined with the Spearman rank correlation coefficient. All aggressiveness classes were tested for normality with a Kolmogorov-Smirnov test, which was performed for all three variables. The medians of the non-normally distributed aggressiveness classes were determined and compared with a Kruskal-Wallis test with a Dunn post hoc test to account for multiple comparisons.

The performance of all individual measures in the discrimination of low-grade tumors from the combined intermediate- and high-grade tumors was evaluated with receiver operating characteristic (ROC) curves. The area under the ROC curve (AUC) was calculated as a measure of performance. All confidence intervals of the AUC were calculated as described by Hanley and McNeil (41).

The standardized-threshold approach (STA) was presented previously to combine the (Cho+Cr)/Cit ratio and the Cho/Cr ratio into one measure for malignancy probability and aggressiveness assessment (24,42,43). In the STA, the (Cho+Cr)/Cit ratio is used to obtain an initial rating of the malignancy, which is adapted for deviating Cho/Cr ratios. The initial rating (range, 1–5) is based on the mean and standard deviation of the (Cho+Cr)/Cit ratio of noncancerous tissue (26), and distinction is made between PZ and TZ (40) (Table 5.2). The

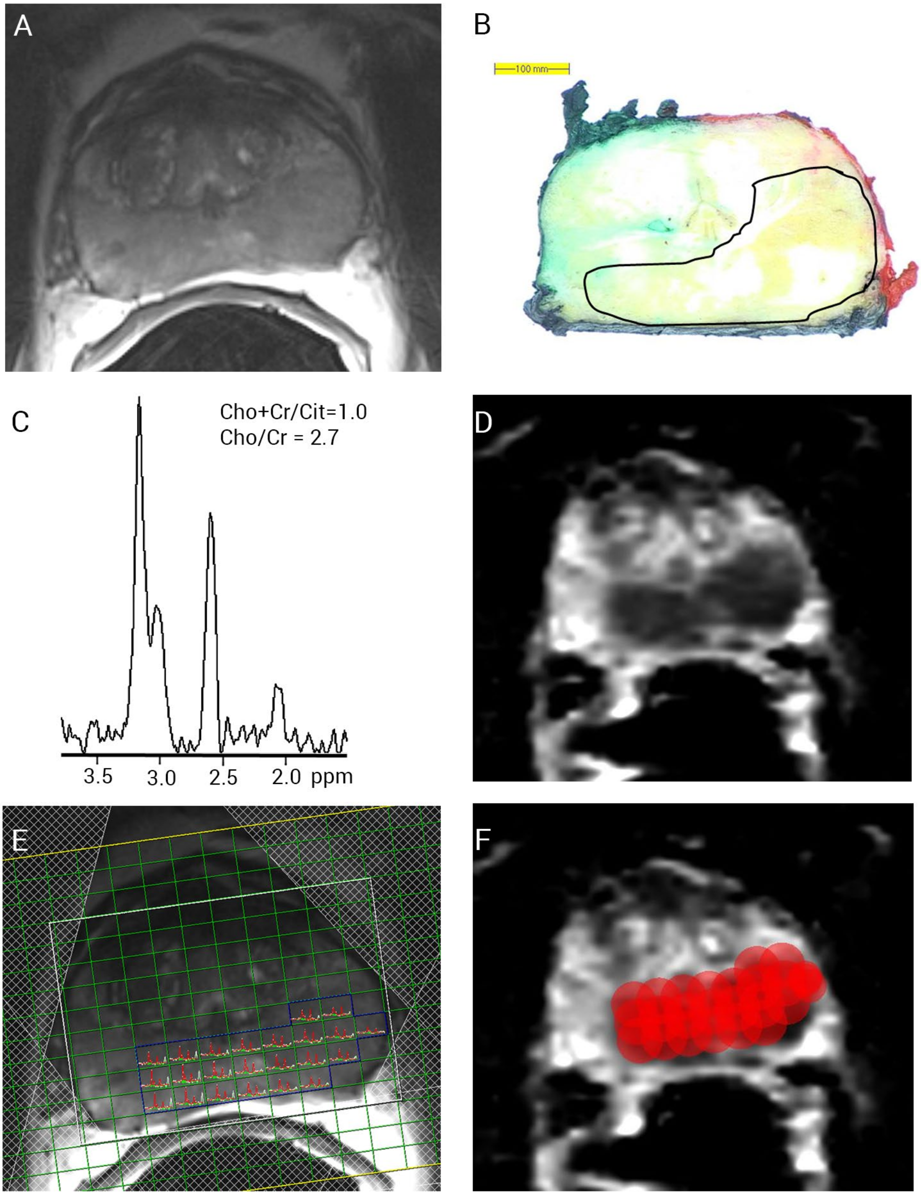

Figure 5.1. *Transverse T2-weighted image (A) and ADC map (D) of the prostate with a tumor (Gleason score, 3+4) in the peripheral zone, as shown at histopathologic examination (B). E) Spectroscopy matrix with plots of the spectra of the voxels that are completely in the tumor and one spectrum in more detail (C). F) ADC image shows corresponding local regions of interest (red spheres). Spheres represent the true size of a spectroscopy voxel.*

optimal Cho/Cr adaptation level of 2.3 for aggressiveness assessment (24) is used in this study to adapt the initial rating. When Cho/Cr ratio is at least 2.3, an initial score of 3 or 2 is increased to 4. When Cho/Cr ratio is less than 2.3, an initial score of 5 is adapted to 4, and a score of 4 is adapted to 3 (Table 5.2). For all MRSI voxels, the malignancy rating of the STA was determined, and the maximum malignancy rating of all voxels within one tumor was used to differentiate tumor aggressiveness classes.

Five-point standardized scoring system			
Score and Score definition	*Peripheral Zone (Cho+Cr)/Cit ratio*	*Central Gland (Cho+Cr)/ Cit ratio*	*Cho/Cr ratio adjustment*
1: Definitely benign tissue	*≤0.34*	*≤0.48*	*- If Cho/Cr ratio ≥2.3, then: adjust 3 and 2 into 4.* *- If Cho/Cr ratio < 2.3, then: adjust 5 into 4 and 4 into 3.*
2: Probably benign tissue	*0.34<CC/C≤0.46*	*0.48<CC/C≤0.62*	
3: Possibly malignant tissue	*0.46<CC/C≤0.58*	*0.62<CC/C≤0.76*	
4: Probably malignant tissue	*0.58<CC/C≤0.70*	*0.76<CC/C≤0.90*	
5: Definitely malignant tissue	*>0.70*	*>0.90*	
CC/C = choline plus creatine to citrate			

Table 5.2. Standardized threshold approach definitions

To combine all three variables, a logistic regression model (LRM) was used to classify the PZ and TZ tumors into either low- or higher-grade tumors. The higher-grade category comprised intermediate- and high-grade tumors. The output of the LRM is an aggressiveness likelihood, with a score of 0–1 representing the probability that a tumor belonged to the higher-grade class. ROC curves were used to determine the accuracy of the aggressiveness likelihoods. To compensate for testing these models with the same data used to build the model, a bias-corrected AUC was determined. To this end, 1000 random bootstrap samples with replacement were drawn from the original data. Each bootstrap sample was used to train an LRM without variable selection, the original data set was tested with this model, and an ROC curve was constructed. Next, the average difference of the bootstrapped AUCs and the initial AUC, which was obtained earlier by training and testing with the original data, was determined. By subtracting the average difference from the initial AUC, a bias-corrected measure was obtained (25,44). The bias-corrected AUC and standard error were calculated and compared with the AUC of the individual ADC value, (Cho+Cr)/Cit ratio, Cho/Cr ratio, and STA (45). Since data were obtained in the same patients, the correlation between the AUCs had to be taken into account (45). To be able to do this for the LRM, the aggressiveness likelihoods of the original data set were used to determine the correlation. Bonferroni correction was used to compensate for the multiple comparisons.

Finally, the correlation between the variables was investigated. By determining the correlation between the values of the different variables derived from the same location, an impression of their complementary value was obtained. To this end, the spectroscopy voxel with the highest (Cho+Cr)/Cit ratio was selected, and the Cho/Cr ratio of this voxel and the 25th percentile ADC value of the corresponding ROI were determined. The Spearman correlation coefficient between the (Cho+Cr)/Cit ratio and each of the two corresponding variables was determined. The same procedure was followed to determine the correlation between the voxel with the highest Cho/Cr ratio and the two other variables that belong to that voxel. Finally, this was performed for the ROI with the lowest 25th percentile ADC value and the two corresponding ratios. In 14 tumors, the quality of the corresponding spectrum was not accepted, and the values of these tumors could not be included in the correlation analysis. The Spearman correlation coefficients were also determined for all voxels that were accepted based on the quality of the spectra. Matlab (version 7.7.0.471; Mathworks, Natick, MA, USA) was used for statistical analysis. For all statistical tests, a P value of .05 or less indicated a significant difference.

Results

On the basis of the selection criteria, 70 clinically important tumors were identified in 54 patients. However, the data of six patients had to be excluded: Two patients had moved between the ^{1}H MRSI examination and the DWI examination, and the diffusion weighted images could not be accurately placed over the T2-weighted images. Three patients had no usable spectra. One patient had a distorted ADC map. The patient and tumor characteristics of the remaining 48 patients (61 tumors) are shown in Table 5.3. The average tumor volume at histopathology was 6.7 cm^3 (range, 0.5–33.5 cm^3). The average time between the MR examination and prostatectomy was 8 weeks (range, 0–21 weeks). The MR examination was performed on average 60 days (range, 19–337 days) after TRUS-guided biopsy. A total of 42 tumors originated in the PZ, and 19 originated in the TZ. A total of 1920 ROIs were identified in these tumors, of which 1556 (81%) passed the MRSI quality control by both spectroscopists.

For each aggressiveness class, the medians of the three variables of ROIs are given in Table 5.4. In the PZ, the medians of the low-grade ($1.13 \cdot 10^{-3}$ mm^2/sec) and intermediate-grade ($1.04 \cdot 10^{-3}$ mm^2/sec) tumors were significantly different from the medians of the high grade tumors ($0.76 \cdot 10^{-3}$ mm^2/sec) for the minimum 25th percentile ADC values ($P < .05$) (Figure 5.2). In the TZ, this difference was lacking for the ADC values. On the other hand, in the TZ, the medians of both metabolite ratios (Table 5.4) were significantly different between low- and high-grade tumors ($P < .05$) (Figure 5.2). In the PZ, the metabolite ratios were not significantly different for any of the aggressiveness classes.

For the PZ tumors, significant correlations were observed between the aggressiveness classes and the maximum (Cho+Cr)/Cit ratio ($\rho = 0.36$, $P < 0.02$), maximum Cho/Cr ratio ($\rho = 0.35$, $P < 0.03$), and minimum 25th percentile ADC value ($\rho = -0.63$, $P < 0.001$). In the TZ, the (Cho+Cr)/Cit ratio (ρ = 0.58, P <0.01) and Cho/Cr ratio (ρ = 0.60, P <0.01) correlated significantly with tumor aggressiveness; the correlation with ADC values was not significant (ρ = -0.43, P = 0.06).

The AUCs for the different aggressiveness assessments are given in Table 5.5. To differentiate low-grade tumors from higher-grade tumors, the ADC value had the highest AUC (0.81) in the PZ, and the Cho/Cr ratio had the highest AUC (0.90) in the TZ. After Bonferroni

No of patients		*48*
PSA level, mean, ng/ml (range)		*9.9 (2.1 - 41.0)*
Age, mean, yr (range)		*63 (42-70)*
Clinical stage		
T2		*24*
T3		*23*
T4		*1*
Gleason score - Peripheral zone:		*No of tumors:*
3+2	*low*	*1*
3+3	*low*	*12*
3+3+4	*intermediate*	*1*
3+4	*intermediate*	*11*
3+4+5	*high*	*2*
4+3	*high*	*10*
4+3+5	*high*	*2*
4+4	*high*	*1*
4+5	*high*	*2*
5+3	*high*	*1*
Gleason score - Central gland:		
2+3	*low*	*2*
3+2	*low*	*5*
3+3	*low*	*1*
3+2+4	*intermediate*	*1*
3+4	*intermediate*	*1*
2+4+5	*high*	*1*
4+2+3	*high*	*1*
4+3+5	*high*	*4*
4+4	*high*	*1*
4+5+2	*high*	*1*

Table 5.3. *Patient and tumor characteristics*
**The tumors are classified according to their aggressiveness*
There were 21 low grade, 14 intermediate grade and 26 high grade tumors.

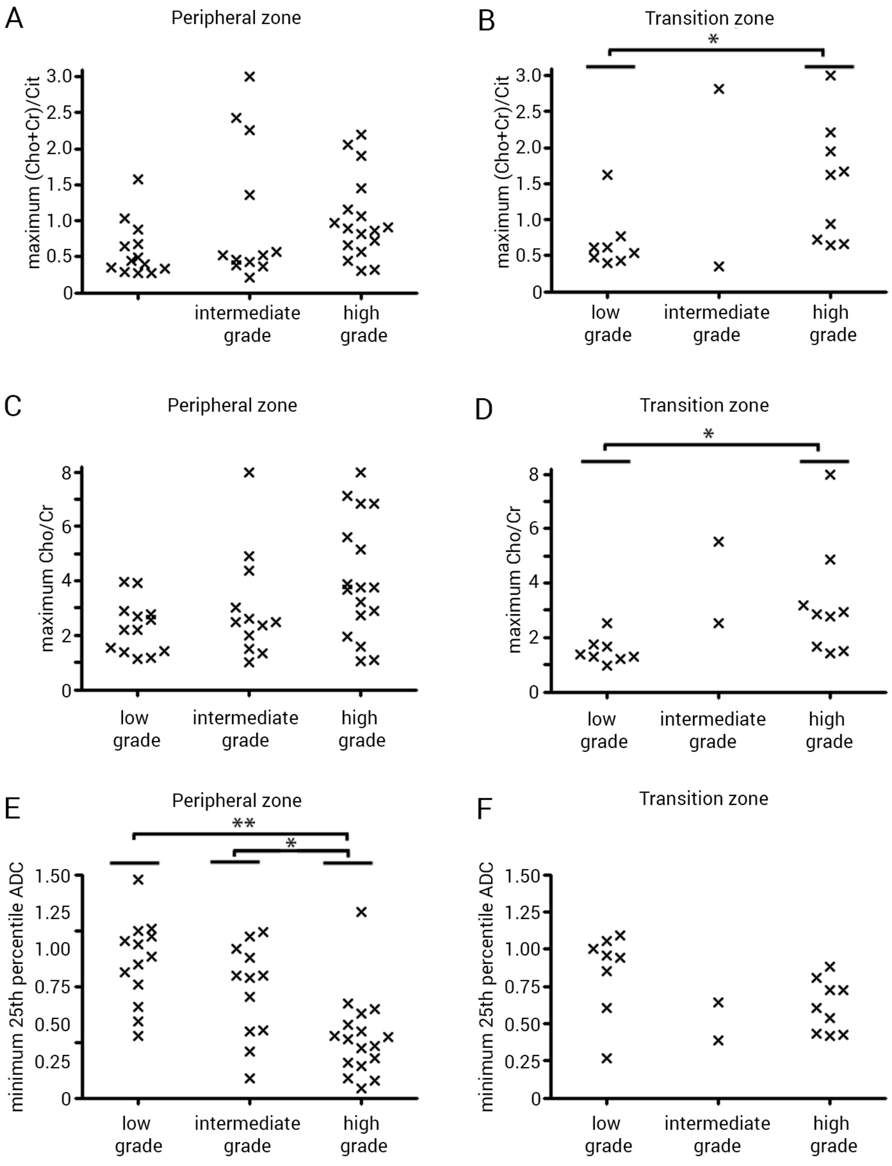

Figure 5.2. *Maximum (Cho+Cr)/Cit ratios of tumors in the peripheral zone (A) and the transition zone (B), maximum Cho/Cr ratio of tumors in the peripheral zone (C) and the transition zone (D), and the minimum 25th percentile ADC values in the peripheral zone (E) and the transition zone (F). The (Cho+Cr)/Cit ratio of two tumors were cut off at 3 (original values: 16.7 and 58.4) and the Cho/Cr ratio of three tumors were cut off at 8 (original values 10.8, 8.5 and 12.3) for display purposes. Significant differences P<0.05 (*) and P<0.001 (**) were noted between the medians of the aggressiveness classes.*

		Low grade	**Intermediate grade**	**High grade**
(Cho+Cr)/Cit	Peripheral zone	0.44	0.52	0.89
	Transition zone	0.58	1.58	1.62
Cho/Cr	Peripheral zone	2.21	2.50	3.75
	Transition zone	1.36	4.01	2.86
ADC	Peripheral zone	$1.13 \cdot 10^{-3}$ mm^2/s	$1.04 \cdot 10^{-3}$ mm^2/s	$0.76 \cdot 10^{-3}$ mm^2/s
	Transition zone	$0.95 \cdot 10^{-3}$ mm^2/s	$0.51 \cdot 10^{-3}$ mm^2/s	$0.61 \cdot 10^{-3}$ mm^2/s
STA	Peripheral zone	2	4	5
	Tranzition zone	2	3	4

Table 5.4 *Median of the maximum (Cho+Cr)/Cit ratio, the maximum Cho/Cr, minimum 25th percentile of the ADC values, and maximum STA for the different aggressiveness classes.*

correction, none of the AUCs of the individual modalities were significantly different for any of the comparisons between aggressiveness classes. In Table 5.5, the AUCs are given for the STA, and the bias-corrected AUCs are given for the LRM. The AUC obtained with the LRM and that obtained with the STA were not significantly different from the other variables. In the PZ, the STA resulted in a higher AUC than did the individual metabolite ratios. In both the PZ and the TZ, there was a significant difference between the median malignancy rating of the low-grade tumors and that of the high-grade tumors.

In Table 5.6, the Spearman correlation coefficients are given for the correlation between the voxels with the highest (Cho+Cr)/Cit ratio, the highest Cho/Cr ratio, and the minimum 25th percentile ADC value corresponding to these voxels. Also, correlations of the highest Cho/Cr ratio and the lowest 25th percentile ADC value and their corresponding variables are given. All correlations were significant, except for the minimum 25th percentile ADC value and the corresponding Cho/Cr ratio.

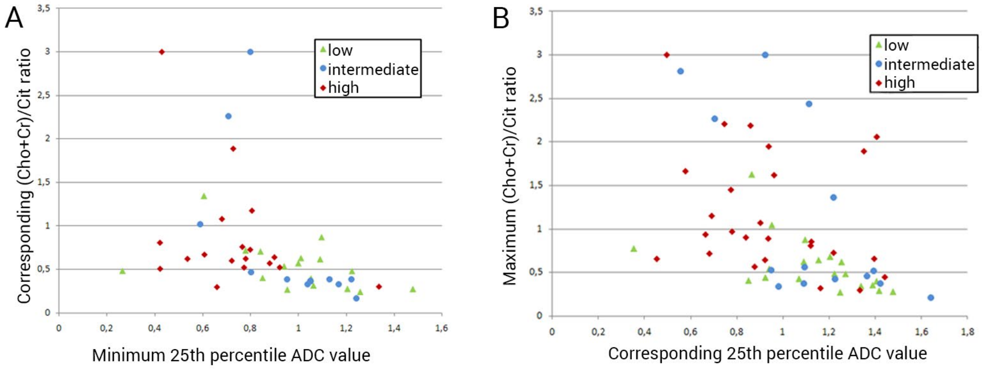

Figure 5.3. *A) The minimum 25th percentile ADC plotted against the (Cho+Cr)/Cit ratio of the corresponding voxel (ρ= -0.64, p<0.01 B) The maximum (Cho+Cr)/Cit ratios plotted against the corresponding 25th percentile ADC value. (ρ= -0.59, p<0.01). For display purposes (Cho+Cr)/Cit ratios higher than 3 were cut off at 3.*

		Low grade versus high and intermediate grade
(Cho+Cr)/Cit	*Peripheral zone*	*0.71 (0.54 - 0.87)*
	Transition zone	*0.82 (0.63 - 1)*
Cho/Cr	*Peripheral zone*	*0.67 (0.50 - 0.84)*
	Transition zone	*0.90 (0.75 - 1)*
STA	*Peripheral zone*	*0.77 (0.63 - 0.92)*
	Transition zone	*0.86 (0.70 - 1)*
ADC	*PZ*	*0.81 (0.69 - 0.94)*
	Transition zone	*0.80 (0.59 - 1)*
LRM	*PZ*	*0.78 (0.64 - 0.92)*
	TZ	*0.87 (0.70 – 1)*

Table 5.5. *Area under the ROC curves for discrimination between different aggressiveness classes using the maximum (Cho+Cr)/Cit ratio, maximum Cho/C ratio and minimum of the 25th percentile ADC. Also the AUCs for STA and LRM, which combine two and three variables respectively, are given. Distinction is made between PZ and TZ tumors.*

The variables that showed the highest correlation, that is, the maximum (Cho+Cr)/Cit ratio plotted against the corresponding 25th percentile ADC value of that voxel (ρ = -0.59) and the minimum 25th percentile ADC with the corresponding (Cho+Cr)/Cit ratio (ρ = -0.64), are plotted in Figure 5.3. The correlation coefficients when all accepted voxels and local ROIs were included were 0.64 between both metabolite ratios, -0.47 between the (Cho+Cr)/Cit ratio and the ADC value, and -0.2 between the ADC value and the Cho/Cr ratio. All correlations were significant (P <0.001).

	Corresponding (Cho+Cr)/Cit	***Corresponding Cho/Cr***	***Corresponding 25th percentile ADC***
Maximum (Cho+Cr)/Cit		*0.44**	*-0.59**
Maximum Cho/Cr	*0.43 **		*-0.31**
Minimum 25th percentile ADC	*-0.64**	*-0.24*	

Table 5.6. *The Spearman correlation coefficients between the metabolite ratio or 25th percentile ADC value of the most deviating ROI and the two variables corresponding to that ROI. (*) p<.01*

Discussion

In this study, the potential of the individual and combined use of metabolite ratios and ADC values to discriminate between different prostate cancer aggressiveness classes was investigated. A significant correlation was found between the aggressiveness classes and the maximum (Cho+Cr)/Cit ratio, maximum Cho/Cr ratio, and minimum ADC values. For differentiation between aggressiveness classes, the combination of the three variables by means of LRM did not result in better differentiation than that with any of the individual variables.

The performance of ADC values alone in the assessment of aggressiveness was comparable with that of previous studies. Although some researchers found no significant correlation between the ADC value and the Gleason score (12-14), studies performed more recently have shown a significant correlation (15-18,20). Three studies used TRUS-guided biopsy to assess the Gleason score (13-15), which might have led to underestimation of the true aggressiveness. Thus, in our study, the whole-mount histopathologic slice obtained at radical prostatectomy was used as the reference standard, and it enabled us to confirm the existence of a significant negative correlation in the PZ between ADC values and tumor aggressiveness. In the TZ, this correlation was not significant. In two other separate studies, researchers evaluated ADC values in the PZ and TZ and found as we did, that there was a significant correlation for the PZ but not the TZ at 1.5 T (15,18). In the other studies in which researchers found a significant correlation, only the PZ was evaluated (17) or the tumors from both zones were combined in their correlation assessment (16,20). A direct comparison with previous studies might not be valid for several reasons. In these studies, the choice of ROIs was performed differently. Either the mean or the median ADC value of an ROI was used, and other b values for DWI were often used. Although we had a limited number of TZ tumors, we chose to analyze both regions separately, as the tissue composition is different in these regions.

When separating these regions, both metabolic ratios—the maximum (Cho+Cr)/Cit ratio and the maximum Cho/Cr ratio— correlated significantly with aggressiveness class in the PZ and TZ. A relationship between the (Cho+Cr)/Cit ratio and the Gleason grade was demonstrated previously in the PZ (23,25) and in both regions combined (24). Despite the low number of TZ tumors, both metabolite ratios showed a significant correlation in the TZ in our study.

The overall performance of the individual variables in the discrimination between low- and higher-grade tumors, which was assessed with the AUC, was comparable. However, although the difference was not significant, in the PZ, the ADC values yielded higher AUCs than did the metabolite ratios, while in the TZ, the metabolite ratios performed better than the ADC. Combining both modalities by means of LRM did not result in a higher AUC. The STA, combining both metabolic ratios, yielded better results in the PZ than the individual metabolite ratios; however, like the LRM, the differences lacked significance. The large overlap between the variables and the relative small patient numbers led to large confidence intervals of the AUCs.

The lack of significantly improved performance of the LRM compared with that of the individual modalities raises the question of whether ADC values and metabolic ratios provide complementary information for cancer characterization. The validity of this question is strengthened by the strong correlations between the 25th percentile ADC values and the (Cho+Cr)/Cit ratio. Both variables might be influenced by the same morphologic change. A positive correlation between the decrease in ADC value and the reduction of luminal space was found earlier (46). This luminal space of normal prostate tissue contains high amounts of Cit secreted by healthy prostate cells, which have a high level of Cit production (47,48). The decrease in Cit signal intensity in malignant tissue can reflect a reduction of luminal space, as well as an altered metabolism (oxidization of Cit due to the lack of zinc (49)). The absence or decrease in luminal space in patients with prostate cancer results in a simultaneous decrease of apparent water mobility and Cit levels. One could argue against performing the spectroscopic portion of an integrated MR examination for prostate cancer characterization to save time. However, in the TZ, the LRM performed better than ADC alone. Moreover, in the TZ, the metabolic ratios significantly correlated to aggressiveness, while this relationship was lacking for the ADC. Another aspect to take into account is the dynamic range of both techniques. For DWI, the range of ADC values that can be measured is restricted by the gradient strength and diffusion time. The length of diffusion time is limited by T2 relaxation. By its nature, a metabolite ratio demands a denominator that has a sufficient signal-to-noise ratio. However, there is no upper limit of the ratio, which implies a larger possible range in metabolite ratios compared with ADC values.

The histopathologic analysis of the prostatectomy specimen was used as the reference standard. By blinding the radiologist who performed ROI selection for the ADC maps and spectra, we tried to make the ROI selection as objective as possible. Exact matching of step-section histopathologic findings to MR imaging findings is considered difficult. As the focus was not on assessing values from the whole tumor but on assessing values from the most aberrant part, exact matching is less critical. We assumed that the most deviating voxels (ROIs) represented the most aggressive part of the tumor. The division of the tumors in three clinically relevant aggressiveness classes enabled us to take the tertiary Gleason grade into account. With these three classes, we could also divide Gleason 7 tumors into primary grade 3 and primary grade 4 tumors. The primary grade 4 tumors are more aggressive (50,51), and a difference in ADC values between the two Gleason 7 tumors has been reported (16,18). The number of patients with a clinical stage T3 lesion who underwent prostatectomy in this study might seem high. However, the clinical stage was determined on the basis of histopathologic findings, which means that small amounts of tumor beyond the capsule will be detected. In several patients with T3 lesions, the extraprostatic extension was so minimal that there were no positive resection margins.

Although we defined three aggressiveness classes to study correlations, the important clinical question is how well one can discriminate low-grade tumors from higher-grade tumors. Thus, for most of the analyses, two groups were used: low-grade tumors and combined intermediate- and high-grade tumors. The ability to select with a high degree of certainty patients who do not need treatment is very relevant and important in this time of increased PSA testing. A recent study showed that to prevent one prostate cancer death with PSA screening, 48 patients need to undergo treatment (3). It is essential to decrease the number of patients who undergo unnecessary treatment, and this study is a step in this direction.

Our study had a number of limitations. The results of this study might not apply to the general patient population, as this was a single-institution validation study with a limited number of patients. The true clinical value of the two modalities in assessing aggressiveness needs to be studied in a prospective study. We did not correct for possible correlation between multiple tumors in one patient. (Seven patients had two clinically important tumors within the prostate, and one patient had three tumors within his prostate.) Four of the seven patients had both tumors in the PZ, and the other three patients had tumors in both regions; therefore, these tumors were not included in the same analysis, as we separated PZ and TZ tumors. It is necessary to divide the tumors into two regions because it is known that the ADC values and (Cho+Cr)/Cit ratios of the normal PZ and TZ are different (15,26,52). A consequence of separating the two regions is the limited number of TZ tumors to perform the analysis (19 of 61 tumors), with only two TZ tumor foci in the intermediate aggressiveness class. A bias in this study was created by limiting inclusion to patients who underwent prostatectomy. Patients with very aggressive tumors usually do not undergo prostatectomy, and the aberrant values of the metabolite ratios and ADC values, which these patients might have, are not included in the analysis. Inclusion of these patients could have led to a clearer discrimination between the aggressiveness classes. A final limitation was the assumption that patient-related movement and therefore discrepancy between the T2-weighted sequence and the spectroscopic examination was minimal. If necessary, the ADC map was translated to overlap well with the T2-weighted image, but this procedure could not be performed for the spectroscopic grid, as there were no landmarks.

In conclusion, this study enabled us to confirm that ^{1}H MRSI and DWI offer potential for *in vivo* noninvasive assessment of prostate cancer aggressiveness, and both MR methods have comparable performance. However, there is still considerable overlap between the aggressiveness classes and the ADC values or metabolic ratios, possibly caused by tumor heterogeneity. The combination of both modalities did not result in a better performance for aggressiveness assessment; nonetheless, the better performance of the metabolite ratios in the TZ and of the ADC values in the PZ indicates that both modalities might have complementary value. More research is necessary to study how and to what extent these two functional imaging modalities can provide additional information.

References

1. Jemal A, Siegel R, Xu J, Ward E. Cancer statistics, 2010. CA Cancer J Clin 2010;60(5):277-300.
2. Walsh PC, DeWeese TL, Eisenberger MA. Localized prostate cancer. New Engl J Med 2007;357(26):2696-2705.
3. Schroder FH, Hugosson J, Roobol MJ and others. Screening and prostate-cancer mortality in a randomized European study. N Engl J Med 2009;360(13):1320-1328.
4. Draisma G, Boer R, Otto SJ, van der Cruijsen IW, Damhuis RAM, Schröder FH, de Koning HJ. Lead times and overdetection due to prostate-specific antigen screening: Estimates from the European randomized study of screening for prostate cancer. J Natl Cancer I 2003;95(12):868-878.
5. Sakr WA, Grignon DJ, Haas GP, Schomer KL, Heilbrun LK, Cassin BJ, Powell IJ, Montie JA, Pontes JE, Crissman JD. Epidemology of high grade prostatic intraepithelial neoplasia. Pathol Res Pract 1995;191(9):838-841.
6. Kvåle R, Möller B, Wahlqvist R, Fosså SD, Berner A, Busch C, Kyrdalen AE, Svindland A, Viset T, Halvorsen OJ. Concordance between Gleason scores of needle biopsies and radical prostatectomy specimens: A population-based study. BJU Int 2009;103(12):1647-1654.
7. Divrik RT, Eroglu A, Åžahin A, Zorlu F, Ozen H. Increasing the number of biopsies increases the concordance of Gleason scores of needle biopsies and prostatectomy specimens. Urol Oncol-Semin Ori 2007;25(5):376-382.
8. Tomioka S, Nakatsu H, Suzuki N, Murakami S, Matsuzaki O, Shimazaki J. Comparison of Gleason grade and score between preoperative biopsy and prostatectomy specimens in prostate cancer. Int J Urol 2006;13(5):555-559.
9. Rajinikanth A, Manoharan M, Soloway CT, Civantos FJ, Soloway MS. Trends in Gleason Score: Concordance Between Biopsy and Prostatectomy over 15 Years. Urology 2008;72(1):177-182.
10. Sato C, Naganawa S, Nakamura T, Kumada H, Miura S, Takizawa O, Ishigaki T. Differentiation of noncancerous tissue and cancer lesion by apparent diffusion coefficient values in transition and peripheral zones of the prostate. J Magn Res Imaging 2005;21(3):258-262.
11. Issa B. In vivo measurement of the apparent diffusion coefficient in normal and malignant prostatic tissues using echo-planar imaging. J Magn Reson Imaging 2002;16(2):196-200.
12. Kim CK, Park BK, Han JJ, Kang TW, Lee HM. Diffusion-weighted imaging of the prostate at 3 T for differentiation of malignant and benign tissue in transition and peripheral zones: Preliminary results. J Comput Assist Tomogr 2007;31(3):449-454.
13. Gibbs P, Pickles MD, Turnbull LW. Diffusion imaging of the prostate at 3.0 tesla. Invest Radiol 2006;41(2):185-188.
14. Pickles MD, Gibbs P, Sreenivas M, Turnbull LW. Diffusion-weighted imaging of normal and malignant prostate tissue at 3.0T. J Magn Reson Imaging 2006;23(2):130-134.
15. Tamada T, Sone T, Jo Y, Toshimitsu S, Yamashita T, Yamamoto A, Tanimoto D, Ito K. Apparent diffusion coefficient values in peripheral and transition zones of the prostate: Comparison between normal and malignant prostatic tissues and correlation with histologic grade. J Magn Reson Imaging 2008;28(3):720-726.
16. Itou Y, Nakanishi K, Narumi Y, Nishizawa Y, Tsukuma H. Clinical utility of apparent diffusion coefficient (ADC) values in patients with prostate cancer: Can ADC values contribute to assess the aggressiveness of prostate cancer? J Magn Reson Imaging 2011;33(1):167-172.
17. Hambrock T, Somford DM, Huisman HJ, van Oort IM, Witjes JA, Hulsbergen-van de Kaa CA, Scheenen TJW, Barentsz JO. Relationship between Apparent Diffusion Coefficients at 3.0-T MR Imaging and Gleason Grade in Peripheral Zone Prostate Cancer. Radiology 2011;259(2):459-461.

18. Verma S, Rajesh A, Morales H, Lemen L, Bills G, Delworth M, Gaitonde K, Ying J, Samartunga R, Lamba M. Assessment of aggressiveness of prostate cancer: Correlation of apparent diffusion coefficient with histologic grade after radical prostatectomy. AJR Am J Roentgenol 2011;196(2):374-381.
19. Turkbey B, Shah VP, Pang Y and others. Is apparent diffusion coefficient associated with clinical risk scores for prostate cancers that are visible on 3-T MR images? Radiology 2011;258(2):488-495.
20. Yoshimitsu K, Kiyoshima K, Irie H, Tajima T, Asayama Y, Hirakawa M, Ishigami K, Naito S, Honda H. Usefulness of apparent diffusion coefficient map in diagnosing prostate carcinoma: Correlation with stepwise histopathology. J Magn Reson Imaging 2008;27(1):132-139.
21. Kurhanewicz J, Vigneron DB, Hricak H, Narayan P, Carroll P, Nelson SJ. Three-dimensional H-1 MR spectroscopic imaging of the in situ human prostate with high (0.24-0.7-cm3) spatial resolution. Radiology 1996;198(3):795-805.
22. Heerschap A, Jager GJ, Van Der Graaf M, Barentsz JO, De La Rosette JJMCH, Oosterhof GON, Ruijter ETG, Ruijs SHJ. In vivo proton MR spectroscopy reveals altered metabolite content in malignant prostate tissue. Anticancer Res 1997;17(3 A):1455-1460.
23. Kurhanewicz J, Vigneron DB, Males RG, Swanson MG, Yu KK, Hricak H. The prostate: MR imaging and spectroscopy: Present and future. Radiol Clin North Am 2000;38(1):115-138.
24. Kobus T, Hambrock T, Hulsbergen-Van De Kaa CA, Wright AJ, Barentsz JO, Heerschap A, Scheenen TWJ. In vivo assessment of prostate cancer aggressiveness using magnetic resonance spectroscopic imaging at 3 T with an endorectal coil. Eur Urol 2011;60(5):1074-1080.
25. Zakian KL, Sircar K, Hricak H and others. Correlation of proton MR spectroscopic imaging with gleason score based on step-section pathologic analysis after radical prostatectomy. Radiology 2005;234(3):804-814.
26. Scheenen TW, Heijmink SW, Roell SA, Hulsbergen-Van de Kaa CA, Knipscheer BC, Witjes JA, Barentsz JO, Heerschap A. Three-dimensional proton MR spectroscopy of human prostate at 3 T without endorectal coil: feasibility. Radiology 2007;245(2):507-516.
27. Reinsberg SA, Payne GS, Riches SF, Ashley S, Brewster JM, Morgan VA, deSouza NM. Combined use of diffusion-weighted MRI and 1H MR spectroscopy to increase accuracy in prostate cancer detection. AJR Am J Roentgenol 2007;188(1):91-98.
28. Riches SF, Payne GS, Morgan VA, Sandhu S, Fisher C, Germuska M, Collins DJ, Thompson A, Desouza NM. MRI in the detection of prostate cancer: Combined apparent diffusion coefficient, metabolite ratio, and vascular parameters. AJR Am J Roentgenol 2009;193(6):1583-1591.
29. Mazaheri Y, Shukla-Dave A, Hricak H and others. Prostate cancer: Identification with combined diffusion-weighted MR imaging and 3D1H MR spectroscopic imaging - Correlation with pathologic findings. Radiology 2008;246(2):480-488.
30. Scheenen TWJ, Gambarota G, Weiland E, Klomp DWJ, Fütterer JJ, Barentsz JO, Heerschap A. Optimal timing for in vivo 1H-MR spectroscopic imaging of the human prostate at 3T. Magn Reson Med 2005;53(6):1268-1274.
31. Scheenen TW, Klomp DW, Roll SA, Futterer JJ, Barentsz JO, Heerschap A. Fast acquisition-weighted three-dimensional proton MR spectroscopic imaging of the human prostate. Magn Reson Med 2004;52(1):80-88.
32. Van Oort IM, Bruins HM, Kiemeney LALM, Knipscheer BC, Witjes JA, Hulsbergen-Van De Kaa CA. The length of positive surgical margins correlates with biochemical recurrence after radical prostatectomy. Histopathology 2010;56(4):464-471.
33. Epstein JI, Allsbrook Jr WC, Amin MB and others. The 2005 International Society of Urological Pathology (ISUP) consensus

conference on Gleason grading of prostatic carcinoma. Am J Surg Pathol 2005;29(9):1228-1242.

34. Greene FL, Page DL, Flemming ID, Fritz AG, Balch CM, Haller DG, Morrow M. AJCC Cancer Staging Manual. 6th edition New York: Springer-Verlag; 2002.
35. Augustin H, Hammerer PG, Graefen M, Erbersdobler A, Blonski J, Palisaar J, Daghofer F, Huland H. Insignificant prostate cancer in radical prostatectomy specimen: time trends and preoperative prediction. Eur Urol 2003;43(5):455-460.
36. Stamey TA, Freiha FS, McNeal JE, Redwine EA, Whittemore AS, Schmid HP. Localized prostate cancer. Relationship of tumor volume to clinical significance for treatment of prostate cancer. Cancer 1993;71(3 Suppl):933-938.
37. Vos PC, Hambrock T, Hulsbergen - Van De Kaa CA, Fütterer JJ, Barentsz JO, Huisman HJ. Computerized analysis of prostate lesions in the peripheral zone using dynamic contrast enhanced MRI. Med Phys 2008;35(3):888-899.
38. Mayr NA, Yuh WTC, Arnholt JC and others. Pixel analysis of MR perfusion imaging in predicting radiation therapy outcome in cervical cancer. J Magn Reson Imaging 2000;12(6):1027-1033.
39. Hayes C, Padhani AR, Leach MO. Assessing changes in tumour vascular function using dynamic contrast-enhanced magnetic resonance imaging. NMR in Biomed 2002;15(2):154-163.
40. McNeal JE, Redwine EA, Freiha FS, Stamey TA. Zonal distribution of prostatic adenocarcinoma. Correlation with histologic pattern and direction of spread. Am J Surg Pathol 1988;12(12):897-906.
41. Hanley JA, McNeil BJ. The meaning and use of the area under a receiver operating characteristic (ROC) curve. Radiology 1982;143(1):29-36.
42. Fütterer JJ, Scheenen TWJ, Heijmink SWTPJ, Huisman HJ, Hulsbergen-Van De Kaa CA, Witjes JA, Heerschap A, Barentsz JO. Standardized threshold approach using three-dimensional proton magnetic resonance spectroscopic imaging in prostate cancer localization of the entire prostate. Invest Radiol 2007;42(2):116-122.
43. Jung JA, Coakley FV, Vigneron DB, Swanson MG, Qayyum A, Weinberg V, Jones KD, Carroll PR, Kurhanewicz J. Prostate depiction at endorectal MR spectroscopic imaging: investigation of a standardized evaluation system. Radiology 2004;233(3):701-708.
44. Efron B, Tibshirani RJ. An Introduction to the Bootstrap. New York: NY: Chapman & Hall; 1993.
45. Hanley JA, McNeil BJ. A method of comparing the areas under receiver operating characteristic curves derived from the same cases. Radiology 1983;148(3):839-843.
46. Langer DL, Van Der Kwast TH, Evans AJ, Plotkin A, Trachtenberg J, Wilson BC, Haider MA. Prostate tissue composition and MR measurements: Investigating the relationships between ADC, T2, Ktrans, Ve, and corresponding histologic features. Radiology 2010;255(2):485-494.
47. Costello LC, Franklin RB. Concepts of citrate production and secretion by prostate. 1. Metabolic relationships. Prostate 1991;18(1):25-46.
48. Costello LC, Franklin RB. Citrate metabolism of normal and malignant prostate epithelial cells. Urology 1997;50(1):3-12.
49. Costello LC, Franklin RB. Novel role of zinc in the regulation of prostate citrate metabolism and its implications in prostate cancer. Prostate 1998;35(4):285-296.
50. Chan TY, Partin AW, Walsh PC, Epstein JI. Prognostic significance of Gleason score 3+4 versus Gleason score 4+3 tumor at radical prostatectomy. Urology 2000;56(5):823-827.
51. Hattab EM, Koch MO, Eble JN, Lin H, Cheng L. Tertiary Gleason Pattern 5 is a Powerful Predictor of Biochemical Relapse in Patients With Gleason Score 7 Prostatic Adenocarcinoma. J Urol 2006;175(5):1695-1699.
52. Scheenen TWJ, Fütterer J, Weiland E and others. Discriminating cancer from noncancer

tissue in the prostate by 3-dimensional proton magnetic resonance spectroscopic imaging: A prospective multicenter validation study. Invest Radiol 2011;46(1):25-33.

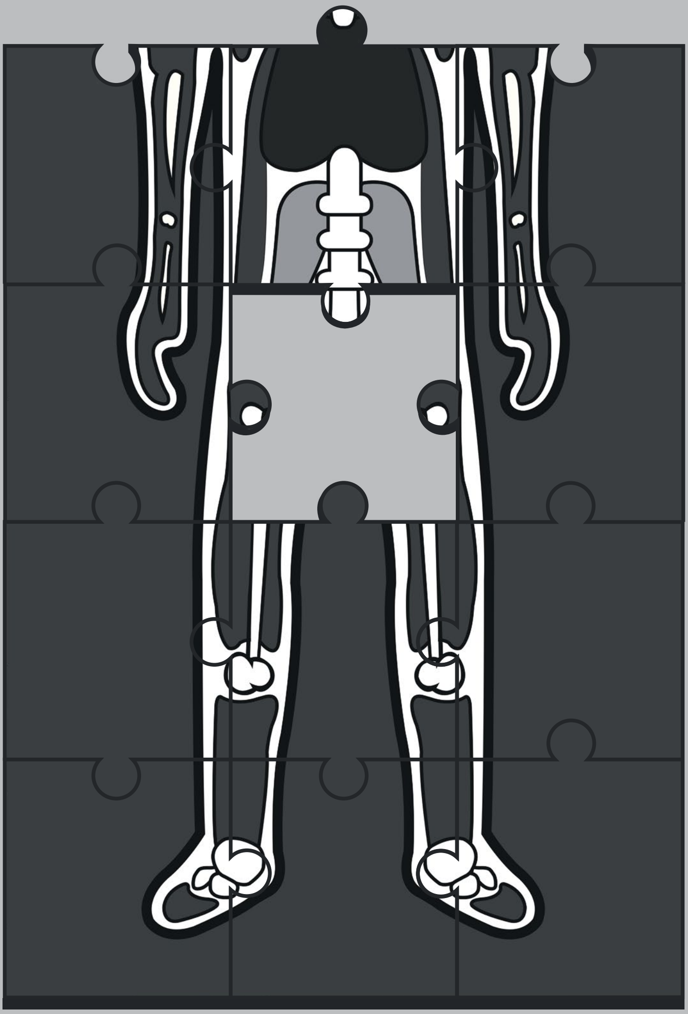

6

CHAPTER SIX

The Contribution of Morphological Features to Parameter Values in MR Spectroscopic and Diffusion-weighted Imaging of the Human Prostate

This chapter is based on:

The contribution of morphological features to parameter values in MR spectroscopic and diffusion-weighted imaging of the human prostate

T. Kobus, J.A.W.M. van der Laak, M.C. Maas, T. Hambrock, C.C. Bruggink, C.A. Hulsbergen-Van de Kaa, T.W.J. Scheenen and A. Heerschap

In preparation

Introduction

Magnetic resonance imaging (MRI) is increasingly being used for the detection, staging and characterization of prostate cancer. Multi-parametric MRI is often used for this purpose (1), preferably consisting of high-resolution T2-weighted images for anatomy, in combination with at least two functional MRI techniques (2). The functional techniques used most for prostate MR are diffusion-weighted imaging (DWI), dynamic contrast enhanced (DCE) MRI and ^{1}H MR spectroscopic imaging (^{1}H MRSI). Several studies have indicated that a combination of T2w-imaging with two functional techniques provides a better tumor characterization than with just one functional technique (3-6). This increased performance suggests that the functional MR images contain complementary information about morphologic and physiologic changes in prostate cancer.

On cellular level, prostate tissue can be divided into two main components: stromal tissue (mainly connective and smooth muscle tissue) and glandular or epithelial tissue. Glandular tissue consists of epithelial cells surrounding the luminal space. Approximately 30% normal peripheral zone prostate tissue consists of luminal space (7). In contrast, in cancer the volume percentage of luminal space is decreased, while simultaneously the volume percentages of epithelial nuclei and cytoplasm increase (7). The relation between the morphology of prostatic tissue and MR imaging has been studied for T2w imaging, DWI and DCE-MRI (7-9). Parameter values of DCE-MRI correlated with microvessel density (8, 9), and with the volume of luminal space, epithelial cytoplasm and nuclei (7). The T2 relaxation time and apparent diffusion coefficient (ADC) of DWI correlated inversely with the relative volume of nuclei and cytoplasm, and positively with amount of luminal space (7). Tissues with a lot of extracellular free water have a long T2 relaxation time, while the T2 is shorter in cell dense tissue (10). It is hypothesized that the decrease in T2 relaxation time in prostate cancer comes from the replacement of the luminal space by epithelial cancer cells (7). This structural alteration in prostate cancer tissue could also explain the decrease in ADC value, which is sensitive to the free water diffusivity in the luminal space.

With ^{1}H MRSI, the spatial distribution of the metabolites citrate (Cit), choline (Cho), spermine (Spm) as the main polyamine, and creatine (Cr) can be studied within the prostate gland. The ratio of (Cho(+Spm)+Cr)/Cit increases in tumor tissue compared to healthy tissue (11, 12), because the intensity of Cit decreases while the intensity of Cho often increases in spectra of prostate cancer tissue. Cit is an intermediate in the citric acid cycle and in most tissues Cit is immediately converted into isocitrate and further metabolized. The prostate, on the contrary, is the only organ with high Cit levels: production and storage of Cit in the luminal space is one of the main functions of the prostate (13). Metabolism of Cit is prevented in healthy prostate epithelial cells by high zinc concentrations, which inhibit mitochondrial (m-) aconitase activity, the enzyme that catalyzes Cit to isocitrate in the citric acid cycle (13-15).

However, in cancer tissue the zinc build up is lacking and Cit is oxidized. Prostatic fluids contain between 50-180 mM of Cit (15-17) and epithelial cells presumably only a few mM (based on measurements in epithelial cells of the rat prostate (13)). As the luminal space, where prostatic fluid with Cit comes from, occupies about 30% of the volume of the prostate in the healthy peripheral zone, it is expected that proportionally lower tissue levels of Cit are measured by ^{1}H MRSI. This is indeed the case: these tissue levels have been estimated to be about 40 mM in the peripheral zone (18-21). As prostate cancer is characterized by dedifferentiation of epithelial cells and filling of prostate lumen with these cells, it is likely that the reduction in luminal space will have a substantial contribution to the decrease of Cit content in prostate cancer tissue as measured by ^{1}H MRSI.

Therefore, we hypothesize that the low Cit signal observed in prostate cancer spectra reflects in the first place these morphological alterations, rather than changes in metabolism. These morphological transformations are also suggested as the cause of chances in the ADC value in prostate cancer (7). The present study aims to establish a relation between the parameter values of MRSI and DWI and tissue morphology assessed using digital image analysis of scanned histological sections. Better understanding of the biological mechanisms causing the detected MR signal changes can help to further understand the disease and improve the use of MR in prostate cancer management.

Methods

Subjects

The institutional ethics review board approved this retrospective study and waived the need for informed consent. For this study 57 patients were included who had a clinical multi-parametric MR examination involving both MRSI and DWI, followed by a radical prostatectomy. The MR investigations were performed between January 2009 and July 2012, as requested by a urologist, and aimed to examine the local extent of the tumor.

MR protocol and processing

All MR examinations were performed on a whole-body 3T-system (Magnetom Trio; Siemens Healthcare, Erlangen, Germany). For signal reception, either an eight-element external phased-array coil (Siemens Healthcare) was used (n=21) or this coil was combined with an endorectal coil (Medrad, Pittsburgh, PA) (n=36). The balloon surrounding the endorectal coil was filled with perfluoropolyether liquid (Fomblin, Solvay Solexis, Bollate, Italy) to limit susceptibility differences between the tissue and the coil. To minimize peristaltic movement of the bowels, patients received intramuscular injections of 1 mg glucagon (Glucagen, Nordisk, Genlofte, Denmark) and 20 mg butylscopolaminebromide (Buscopan, Boehringer-Ingelheim, Ingelheim, Germany).

Median patient age (years)		*64, range: 48 – 70*	
Median PSA level (ng/ml)		*7.95, range: 2.9-76*	
Tumor stage**			
T2		*21*	
T3		*30*	
T4		*3*	
Gleason score in selected slice*			
2+2	*1*	*3+4+5*	*4*
2+3	*2*	*3+5+4*	*2*
3+2	*3*	*4+3*	*4*
3+3	*9*	*4+3+5*	*4*
3+2+4	*3*	*4+4*	*2*
2+3+4	*1*	*4+5*	*1*
3+3+4	*2*	*4+5+3*	*3*
3+4	*12*	*5+4+3*	*1*
3+4+2	*1*		

Table 6.1. *Patient characteristics. PSA= Prostate Specific Antigen*
** Data are given in number of tumors with that Gleason score that are included in this study.*
*** Data are given in number of patients.*

The MR examination started with localizers (fast gradient-echo images) to check the position of the coils. Next, high-resolution T2-weighted images were made in three orthogonal directions. The transversal slices were aligned perpendicular to the rectal wall. A single shot echo-planar imaging sequence was used for DWI with diffusion encoding gradients in three directions. The DWI images had the same orientation as the transverse T2-weighted images. B-values of 50, 500 and 800 s/mm^2 or 100, 400 and 800 s/mm^2 were used. ADC maps were calculated from all b-images by fitting a mono-exponential decay to the signal attenuation as a function of the b-value. For ^{1}H MRSI a point resolved spectroscopy sequence (PRESS) was used with an echo time of 145 ms and a TR of 750 ms (22). Lipid and water suppression was applied using dual frequency-selective MEGA pulses and crusher gradients (23). Weighted acquisition of k-space was combined with a Hanning filter and zero-filling to minimize signal contamination from non-neighboring voxels. As a consequence, the true size of the spectroscopy voxels can best be approximated by spheres with a volume of 0.37, 0.64 or 1.01 ml (24). The chosen voxel size depended on whether or not the endorectal coil was used and the size of the prostate.

Histopathology and processing

After surgery, the prostates were injected with formalin and fixed overnight in 10% neutral buffered formaldehyde. Three different ink colors were applied to the surface of the prostate for orientation purposes and evaluation of surgical resection margins. Each prostate was cut in 4-mm thick transverse slices, perpendicular to the rectal wall. The slices were photographed. Of each slice, a thin section was cut, and stained with hematoxylin and eosin (HE). The prostate slices of patients operated before 2012 were divided in halves, quarters, or in rare cases in sextants. Of the other patients' slices whole mount sections were cut. For each patient one slice, preferably containing a large amount of tumor tissue was selected for the matching. A uro-pathologist [CAHK] marked all tumor regions in this slice (Figure 6.1A) and determined per tumor the percentage area of each Gleason growth pattern according to published guidelines (25). Furthermore, regions that contained inflammation, necrosis or granuloma were indicated.

The section(s) of the chosen slice and of one adjacent slice were digitally scanned with 10x magnification using a slide scanner (DotSlide system, Olympus, Tokyo, Japan). For slices consisting of multiple sections, the digital sections were copied to Adobe Photoshop (Adobe Systems, San Jose, CA) and combined to reconstruct one whole slice (Figure 6.1B) to enable matching with MR at a later stage.

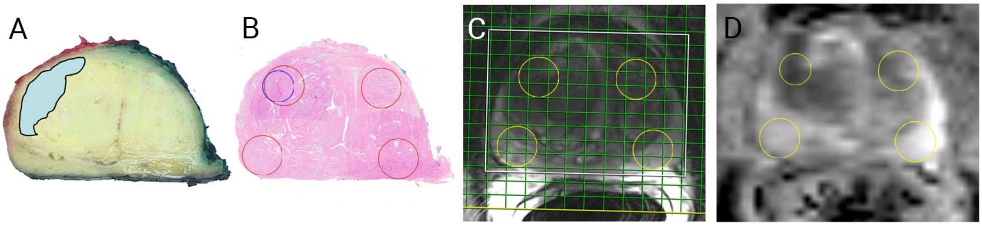

Figure 6.1. *Matching example of the data of a 53-year old patient with a Gleason score 2+3 tumor. A) Photograph of one of the prostate slices with the location of the tumor indicated in blue. B) The four digitized sections stained with hematoxylin and eosin are combined to form one slice. The regions of interest (ROIs) corresponding to the spectroscopy voxels are indicated with red circles. For the correlation with the apparent diffusion coefficient (ADC), one ROI was adjusted so it contained only tumor tissue (blue circle) C) The T2-weighted image with the spectroscopy grid. The selected spectroscopy voxels are encircled. D) The corresponding ADC map with in yellow the ROIs.*

The digitized sections were segmented into lumen, nuclei and stroma & epithelial cytoplasm based on color deconvolution as described by Ruifrok et al (26) using Matlab (version 7.14; Mathworks, Natick, MA). The difference in staining of stroma and epithelial cytoplasm was too small to differentiate between these two and these were therefore combined into one feature. For the segmentation, optical density maps were generated for each color channel of the image (red, green and blue [RGB]). For each pixel, the difference between the minimum and maximum channel density was compared to a threshold to detect areas not covered with tissue. By grouping pixels with values below the threshold, individual lumens were defined. Detected lumens having an area smaller than a disk with a radius of 7 pixels (=

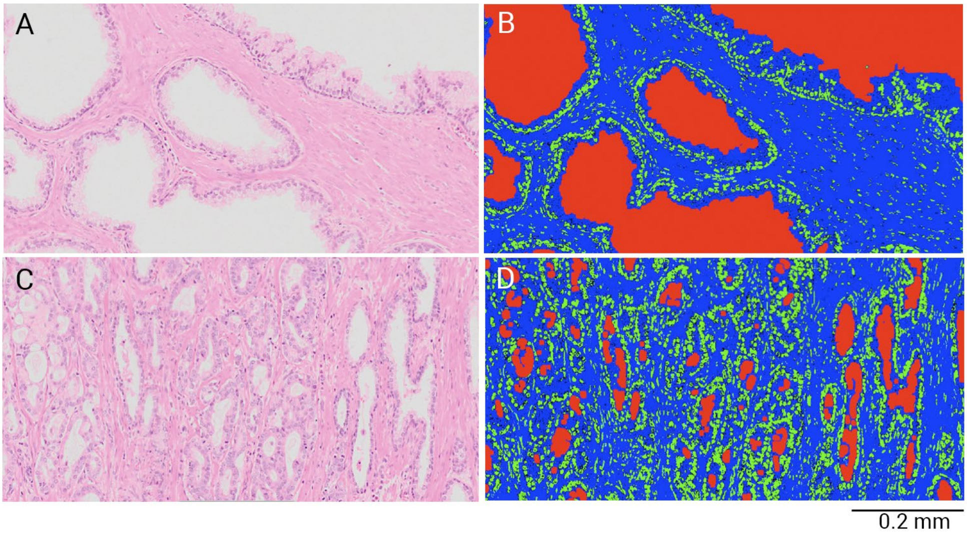

Figure 6.2. *Hematoxylin and eosin stained sections and corresponding segmentation in lumen (red), nuclei (green) and stroma & cytoplasm (blue) of a 64-year old patient with a Gleason score 4+3 tumor. A, B) Normal transition zone tissue. C, D) Tumor tissue.*

$1.6\cdot10^{-3}$ mm^{2}) were considered to represent vascular lumens and were therefore excluded. Two datasets with training pixels representing nuclei and stroma & cytoplasm were compiled. The inverse matrix of their averaged optical RGB densities was determined. For each pixel the contribution to nuclei and stroma & cytoplasm was determined by multiplying the optical densities of the original image by these inverse matrices. For both nuclei and stroma & cytoplasm a cut off value was chosen, which allowed assignment of each pixel to the corresponding morphological component (Figure 6.2). As there was variation in the HE staining of the sections, it was not possible to use the same cut off values for all slices. Therefore, [TK] determined the three cut off values for each slice on a small sample. After segmentation, the results were inspected and if necessary, the cut off values were adjusted.

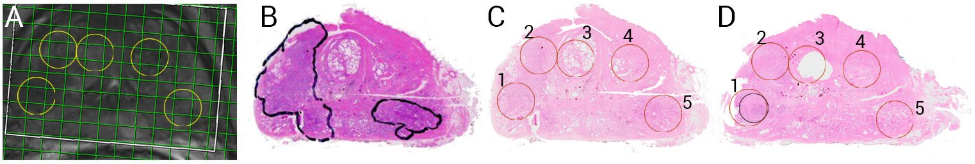

Figure 6.3. *Adjustment of regions of interest (ROIs) in adjacent slices. A) T2-weighted image with spectroscopy grid of a 68 year-old man with a 3+4+5 tumor. The yellow circles indicate the true size of the selected voxels. B) Hematoxylin and eosin (H&E) slice indicating the tumor regions. C) The ROIs corresponding to the voxels selected in A. D) The adjacent H&E slice was used to average the histopathological parameters as the volume of the MRSI voxels is substantially larger than the H&E slices. For ROIs 2, 4 and 5 the average parameters of the two ROIs in the adjacent slices were determined. For ROI 1 a small adjustment was made (black circle) and the average of the two ROIs was obtained. ROI 3 in slice D was not used and only the histopathological parameters of ROI 3 in slice C were used.*

To study the intra-observer variability, the cut off values of four slices were determined three times in separate sessions at least 10 days apart.

Matching MR(S)I and histopathology

Two readers experienced in reading prostate MRI [AH and TK] matched independently the stained section with a T2w imaging slice and reached consensus for the cases of disagreement. Next, one of the readers [TK] checked this matching with a uro-radiologist who also had experience with prostate histopathology [TH] and adjustments were made where necessary. In cases of doubt, a uro-pathologist [CAHK] was consulted. When no matching was possible, e.g. due to misalignment of the prostate before slicing, the patient was excluded from the analysis. [TH] and [TK] matched the T2w imaging slice including MRSI grid, the corresponding DWI slice (using anatomical landmarks), and the HE-section in Adobe Photoshop as separate layers (Figure 6.1). For this manual in-plane registration, only proportional scaling was used to overlay the slices correctly; care was taken not to deform the slices. Per patient 1 to 8 non-overlapping circular regions of interest (ROIs) could be selected that matched MRSI voxels and had the size of the true radius of these voxels (Figure 6.1). Blinded from the segmentation of pathology, the ROIs were placed in regions containing mainly peripheral zone (PZ), transition zone (TZ) or tumor tissue. As the ROIs had to be entirely within one section, the placement of the ROIs was somewhat restricted. Care was taken not to place these ROIs in fragmented parts of the section or in regions that contained inflammation, granuloma or necrosis. The spectroscopy matrix grid was shifted in the cases where this improved the placement of ROIs and a new transformation of k-space was calculated by the MR system. As the spectroscopy voxels are relatively large (0.36 – 1.01 cm^3) and the histopathologic sections only a few micrometer thick, the ROIs were copied to an adjacent section (4 mm apart), so the average histopathologic features of the two sections could be determined (Figure 6.3). When the ROI was partly outside the adjacent section or in fragmented tissue, the ROI was altered for the cases where small adjustments were sufficient. In the cases where no ROI on the adjacent section could be chosen, only the original ROIs were used and no average was obtained (Figure 6.3).

On the ADC maps, ROIs were drawn on exactly the same regions and locations as the MRSI ROIs. The mean ADC value of the pixels in that ROI was determined (Figure 6.1D). The ADC ROIs were not necessarily restricted to the size of the spectroscopy voxels. To minimize partial volume effects, if necessary, new smaller tumor ROIs were drawn for the ADC analysis (Figure 6.1B & D). This was done while blinded for the ADC map. Furthermore, a new adjusted ROI was drawn if the ROIs included non-prostatic tissue on the ADC map. All ROIs had to consist of at least 20 ADC pixels to ensure a representative ADC value. The ROIs with inadequate histopathological segmentation were excluded from the analysis. For the ADC maps, the adjacent pathology slice was not used. The percentage areas of nuclei, lumen and stroma & cytoplasm were determined for all ROIs.

Spectroscopic data analysis

The ratio of choline plus creatine to citrate [(Cho+Cr)/Cit] or including spermine the ratio of [(Cho+Spm+Cr)/Cit], are frequently used as quantitative measures in prostate MRSI. To determine the (Cho+Spm+Cr)/Cit ratios, the corresponding signals in MR spectra were fitted with LCModel (27) using a basis-set with simulated signals for Cho, Spm, Cr and Cit. Fitting was performed with a first order phase of 0. As there is a strong overlap between Cho, Spm and Cr, their individual fits are not always reliable. To make the ratio less sensitive to the individual fits, the concentrations given by LCModel are converted to a pseudo-integral (the intensity in relation to the integral of a singlet of one resonating proton in absorption mode). Only spectra were accepted of which the Cramér-Rao lower bounds (CRLB) of the Cit fit and the CRLB for the combination of Cho, Spm and Cr were 30% or smaller. Furthermore, the signal-to-noise ratio (SNR) determined by LCModel had to be at least 3, the full width at half maximum had to be smaller than 11 Hz, and the absolute zero order phase smaller than 85°.

Previously, we have used the Cho/Cr ratio as biomarker for the Cho increase in prostate cancer, for which we did not include a separate Spm fit (28, 29). As overlap between Spm and Cr signals can lead to inconsistent results for each of the compounds separately, we included, for this study, Spm in the denominator to obtain the Cho/(Cr+Spm) ratio. The fits are probably most reliable in cancer tissue, where the absence of polyamines and increase in Cho makes the fitting easier. Only spectra were accepted of which the CRLB of the Cho fit and the CRLB of either Cr or Spm were 30% or smaller and of which the correlation coefficient between Cho and Spm, as determined by LCModel, was smaller than -0.5. The SNR, full width at half maximum and zero order phase requirements were the same as described above.

Statistical analysis

The MR parameters were plotted against each of the quantitative features of histopathology, which were percentage areas of lumen, nuclei and stroma & cytoplasm, and the ratio of percentage areas of nuclei to lumen. As Cit is the denominator of the (Cho+Spm+Cr)/Cit ratio, we plotted the inverse of this ratio [Cit/(Cho+Spm+Cr)] against the percentage area of lumen. Furthermore, a decrease of Cit has been observed in prostatic fluids of cancer patients (30), so a different relationship between tissue levels of Cit in cancer tissue and benign tissue as measured by ^{1}H MRSI and histopathological parameters is anticipated. Therefore, two separate plots were made in which the Cit/(Cho+Spm+Cr) ratio was plotted against lumen using either tumor or benign data points. The relationship between each pair of parameters was determined using linear mixed effect models. The mixed effect model accounts for multiple ROIs per patient and patient IDs were included as random-effect on the intercept. The slopes were tested against a zero slope with a t-test and Bonferroni correction was applied to compensate for multiple comparisons. As part of the data were non-parametric, the data could not be normalized, which would facilitate comparison of the slopes of the different MR parameters. Therefore, the upper 95%-confidence interval of the

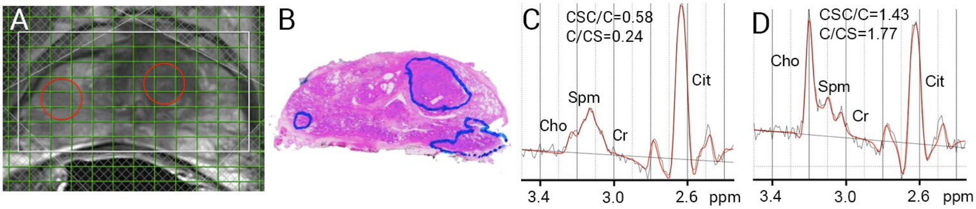

Figure 6.4. *A) T2 weighted image with spectroscopy grid of the prostate of a 58 year-old man with Gleason 3+3 tumors. The yellow circles indicate the true voxel size of the spectra in C (right peripheral zone) and D (tumor in the left transition zone). B) Corresponding hematoxylin and eosin stained slice with the outline of the tumors. C-D) LCModel fits of normal peripheral zone tissue (C) and tumor tissue (D).*

slope was divided by the slope (95%-CI/slope) to obtain an impression in the goodness of the fits of the linear mixed models.

All data were tested for normality using a Lilliefors test. For each tissue type, the mean and standard deviation of the normally distributed parameters were determined and compared with ANOVA and a Tukeys post-test. The median, 25th and 75th percentiles were calculated for non-parametric data and compared with a Kruskal-Wallis test with a Dunn's post-test. The statistical analysis was performed using Matlab 7.14 and Prism 4 (GraphPath Software, La Jolla, CA).

Results

Of the fifty-seven patients that met the inclusion criteria, the examination of three patients had to be excluded because in one patient the sections could not be segmented reliably and for two patients no good match between the MRI and histopathology was possible. In the prostates of the remaining 54 patients (see Table 6.1 for relevant patient details) 191 ROIs could be selected. For the ADC analysis, 184 of 191 ROIs could be included, of which 46 contained predominantly PZ tissue, 66 predominantly TZ tissue and 72 predominantly tumor tissue. For the spectroscopy analysis, 165 of 191 ROIs passed quality control for the (Cho+Spm+Cr)/Cit ratio. An example of a good fit is shown in Figure 6.4. There were 40 voxels containing mainly PZ tissue, 63 containing mainly TZ tissue and 62 voxels with mainly tumor tissue. 128 voxels could be used for the analysis of the Cho/(Cr+Spm) ratio, of which 30 were predominantly PZ voxels, 46 predominantly TZ voxels and 50 predominantly tumor voxels.

An example of the segmentation of TZ and tumor tissue is shown in Figure 6.2. The median percentage areas of the morphological components for benign and tumor PZ and TZ tissue are given in Table 6.2 and shown in Figure 6.5. For this, the ROIs drawn for the ADC analysis

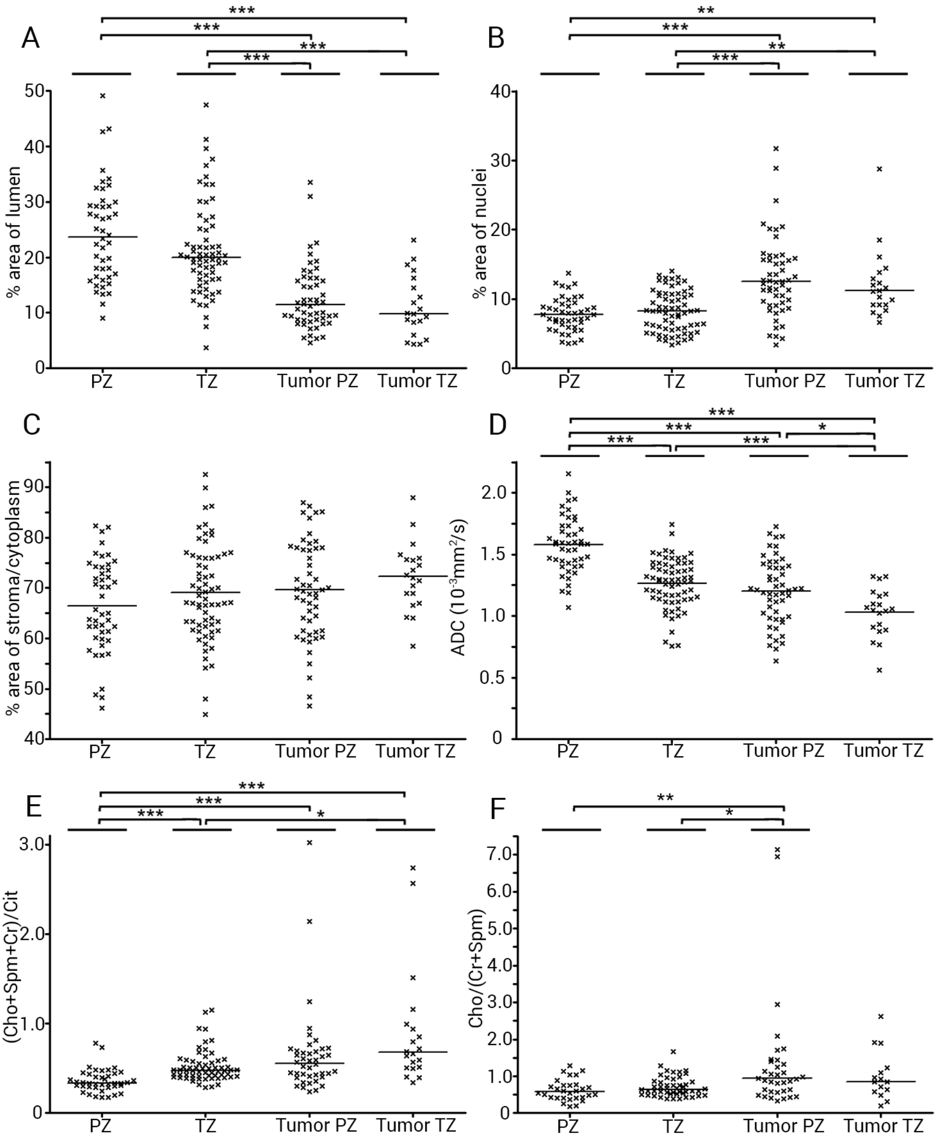

Figure 6.5. *Distributions of the percentage areas of lumen (A), nuclei (B) and stroma & cytoplasm (C) for peripheral zone (PZ), transition zone (TZ) and tumor tissue. Distributions of the apparent diffusion coefficient (ADC), the choline plus spermine plus creatine to citrate [(Cho+Spm+Cr)/Cit] and Cho/(Spm+Cr) ratio are shown in D, E and F. The horizontal bars indicate the median (A, B, E and F) or mean (C, D). * p<0.05, ** p< 0.01***p < 0.001*

were used. While no statistical differences were found between the means of the percentage areas of stroma & cytoplasm for PZ, TZ and tumor ROIs, the medians of the percentage areas of lumen and nuclei for tumor ROIs in the PZ and TZ were significantly different from benign

	Lumen	*Nuclei*	*Stroma & Cytoplasm*
Normal peripheral zone	*23.7 (16.6-29.3)*	*7.7 (6.0-9.3)*	*66.5 ± 9.2*
Normal transition zone	*20.0 (16.1-25.2)*	*8.2 (5.7-10.7)*	*69.0 ± 9.5*
Tumor	*10.7 (8.5-16.0)*	*12.0 (9.2-15.6)*	*70.4 ± 9.1*
Peripheral zone tumor	*11.4 (8.7-16.0)*	*12.5 (9.3-15.8)*	*69.6 ± 9.8*
Transition zone tumor	*9.8 (7.1-15.4)*	*11.2 (9.2-13.4)*	*72.3 ± 6.8*

Table 6.2. Quantitative data of morphological components of normal peripheral zone, normal transition zone and tumor tissue. Data are given in median percentage areas with the 25th and 75th percentiles or as mean with standard deviation. The prostate zonal tissue indicated in the left column, is the dominating component in the region of interest, but other zonal tissue components can be present. A very small part of the tissue could not be classified.

PZ and TZ tissue (Figure 6.5). No significant differences in the fraction of histopathological components were found between PZ and TZ tumors. Furthermore, there was good intra-observer-variability: the mean difference between three repeated measurements of the same slices was 3.0% for lumen, 7.0% for the nuclei, and 1.3% for stroma & cytoplasm.

The mean ADC values of the two zonal tissues ($p<0.001$) and between tumors in these zones ($p<0.05$) were significantly different. For tumor tissue in each zone these values also differed with respect to normal tissue (Table 6.3, Figure 6.5). The median (Cho+Spm+Cr)/Cit ratio was significantly different between normal PZ tissue and tumor tissue (in PZ and TZ) ($p<0.001$) and between normal TZ tissue and TZ tumors ($p<0.05$) (Figure 6.5).

	ADC (x 10^{-3} mm^2/s)	*(Cho+Spm+Cr)/Cit*	*Cho/(Cr+Spm)*
Normal peripheral zone	*1.58±0.23*	*0.33 (0.29-0.42)*	*0.58 (0.42-0.75)*
Normal transition zone	*1.26±0.20*	*0.48 (0.41-0.58)*	*0.65 (0.52-0.86)*
Tumor	*1.15±0.26*	*0.59 (0.43-0.72)*	*0.90 (0.59-1.32)*
Peripheral zone tumor	*1.20±0.27*	*0.56 (0.41-0.70)*	*0.92 (0.59-1.38)*
Transition zone tumor	*1.03±0.20*	*0.68 (0.51-0.97)*	*0.85 (0.60-1.20)*

Table 6.3. The apparent diffusion coefficient (ADC), (Cho+Spm+Cr)/Cit ratio and Cho/(Cr+Spm) ratio for normal peripheral zone, normal transition zone and tumor tissue. ADC data are given as the mean with standard deviation and spectroscopy data as mean with the 25th and 75th percentiles. The tissue type indicated is the main component in the region of interest/voxel, but other tissue components can be present.

The ADC value had a significant positive relation with the percentage area of lumen (Figure 6.6A, $p<0.001$). Negative relations were found between the ADC value and the percentage areas of nuclei ($p<0.001$), stroma & cytoplasm ($p<0.01$) and the ratio of nuclei/lumen ($p<0.001$) (Table 6.4, Figure 6.6E). The 95%-CI/slope ratio for the relations with lumen, nuclei and nuclei/lumen were in the same range (Table 6.4), but for stroma & cytoplasm the 95%-CI/slope ratio was 1.74, which indicates a substantial spread on the data, which is also evident from the larger p-value.

The (Cho+Spm+Cr)/Cit ratio correlated positively with the percentage areas of nuclei ($p<0.001$), stroma & cytoplasm ($p<0.01$) and the ratio of nuclei/lumen ($p<0.001$) (Table 6.4, Figure 6.6F). The inverse of this ratio, the Cit/(Cho+Spm+Cr) ratio, related positively with the percentage area of lumen ($p<0.001$) (Figure 6.6B). These data were then separated in benign and cancer data points, as a decrease of Cit has been observed in prostatic fluids of cancer patients (30). Based on that study, a lower intercept for tumor voxels might be expected, which was the case (0.85 for tumor and 2.09 for benign voxels (Figure 6.6C & D)). There was also a large difference in the slopes of the two data sets. The fit for the benign data points was not significantly different from a zero-slope ($p=0.05$), while for the cancer voxels a steeper slope was found ($p<0.001$) compared to all data points (Table 6.4).

For the Cho/(Cr+Spm) ratio no significance was found with the percentage area of stroma & cytoplasm, but with the other histopathological parameters significant relations were found (Table 6.4). For some of the slopes relating ^{1}H MRSI parameters to histopathology, there was quite some spread on the data, indicated by larger 95%-CI/slope values (Table 6.4).

	Lumen	**Nuclei**	**Stroma & Cytoplasm**	**Nuclei/Lumen**
ADC value	*13.1*** *(1.30)*	*-20.0*** *(1.39)*	*-6.0*** *(1.74)*	*-141.9*** *(1.33)*
(Cho+Spm+Cr)/Cit		*0.023*** *(1.58)*	*0.009*** *(1.75)*	*0.229*** *(1.33)*
Cit/(Cho+Spm+Cr)	*0.043** (1.36) all data* *0.018 (2.02) benign* *0.074** (1.42) tumor*			
Cho/(Cr+Spm)	*-0.015** *(1.73)*	*0.053*** *(1.40)*	*-0.003* *(5.16)*	*0.324*** *(1.52)*

Table 6.4: Slopes for the MR parameters versus the fraction of morphological components
*Data are tested for significance against zero slope. **p<0.001, *p<0.01*
In brackets the ratio of the upper 95% confidence interval divided by the slope.

Discussion

In this study, the relations between the quantitative histopathological morphology of prostate tissue and the MR parameters of DWI and ^{1}H MRSI were investigated. The fraction of morphological components derived from a histopathological analysis of prostate specimens showed significant relations with values for the ADC and metabolite signal ratios

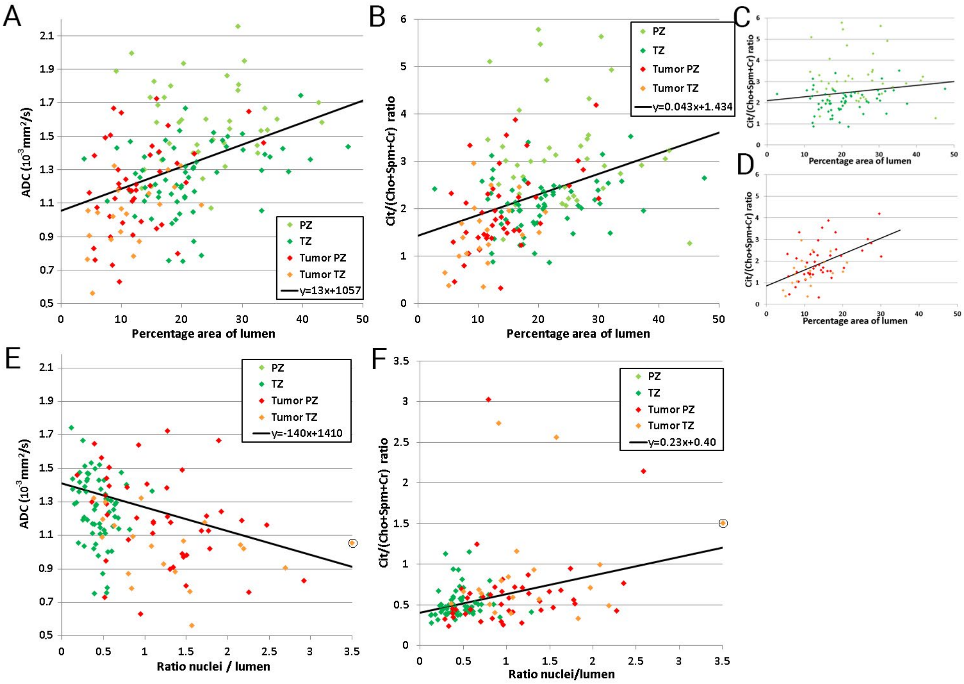

Figure 6.6. *A) ADC value of all ROIs plotted against the corresponding percentage area of lumen and in E) against the ratio of the percentage areas of nuclei and lumen. B) Cit/(Cho+Spm+Cr) ratio of all ROIs plotted against the corresponding percentage area of lumen. These data point were separated in benign voxels (C) and tumor voxels (D). F) (Cho+Spm+Cr)/Cit ratio plotted against the ratio of the percentage areas of nuclei and lumen. All data were fitted with a linear mixed effect model and slopes deviated significantly from zero (p<0.001), except the slope between the Cit/(Cho+Spm+Cr) ratio and the percentage are lumen (p=0.05). For displaying purposes, the encircled data points in E and F are moved along the x-axis from 6.5 to 3.5.*

(Cho+Spm+Cr)/Cit and Cho/(Cr+Spm). These results suggest that the differences in these values are at least in part due to morphological changes of prostate tissue.

Previously, ADC values have been correlated to the percentage area of nuclei, lumen, epithelial cytoplasm and stroma (7). Although the researchers applied z-score normalization on their data and used different b-values, the results are comparable to what we obtained in this study. They found a significant positive slope for the normalized ADC value plotted against the normalized percentage area of lumen and a negative slope against the normalized percentage area of nuclei, which corresponds to our findings. In that study also a negative slope with the percentage area of cytoplasm was found, while a relation with stroma was lacking (7). Due to the small intensity difference in HE-staining in our study, we did not distinguish between epithelial cytoplasm and stromal tissue, but these results suggest that the negative slope found between the ADC value and the combined percentage area of stroma & cytoplasm is driven by the cytoplasmic component. The relations between the ADC value and the amount of lumen, cytoplasm and nuclei have been explained to be dominated by the luminal space (7). In this view, a decrease in the ADC value is caused by a smaller luminal space, which is accompanied by a fractional increase in cytoplasm and nuclei (31). DWI of *ex vivo* prostate tissue at very high resolution (40 μm) also suggests that the ADC difference in tumor tissue depends on a change of the partial volumes of the stromal, epithelial and luminal space, which were estimated from three diffusion components derived from a tri-exponential fit (32).

Significant relations were also found between the ^{1}H MRSI derived metabolite ratios and fractional morphological components of the prostate analyzed by histology. The relation between tissue concentration of Cit and gland to stroma ratio has been studied previously in prostate tissue samples using high resolution MRS (33). In that study, more Cit was found for a higher amount of glands in benign prostatic hyperplasia (BPH) tissue. However, no significant relation between Cit and glands was found for cancer tissue (33). In our study, we did find a significant slope between Cit/(Cho+Spm+Cr) and the relative amount of lumen for tumor tissue, while this relation lacked significance for benign tissue. We combined both PZ and TZ benign tissue, did not study BPH separately and used a metabolite ratio. Also the fact that our method to quantify the morphological compounds was more accurate, can explain these differences.

Costello and Franklin attributed the decrease of Cit in prostate cancer to the lack of zinc leading to the activation of m-aconitase and consequently the oxidation of Cit (13-15). They hypothesized that the transformation of normal prostate cells to citrate-oxidizing cells occurs before a histopathological change can be observed (34). Another theory for the decrease in Cit in prostate cancers is an increase in the enzyme ATP-citrate lyase in malignant tissue, which would result in conversion of Cit to fatty acids, necessary for cell membrane synthesis (35). For m-aconitase and ATP-citrate lyase a relationship between their expression and prostate Cit levels has been observed (36). Both enzymes influence the Cit level in epithelial cells (which is estimated as low as 1-2 mM in epithelial cells of the rat ventral prostate (13)), while the majority of Cit is excreted into the luminal space. The tissue levels of Cit in the PZ as estimated by MRS are approximated at 31-42 μmol/g wet weight (20, 37) and 48 mM (38). So the effects of m-aconitase and ATP-citrate lyase can only be detected with ^{1}H MRSI if they not only affect Cit levels in the epithelial cells, but also disrupt the deposition of Cit to the luminal space. Although we cannot rule out with our data that these enzymes influence the Cit levels we observe with ^{1}H MRSI, it is likely that these contributions are much smaller than the morphological change.

We used the Cho/(Cr+Spm) ratio as biomarker for the Cho increase in prostate cancer. We expected a relation between Cho and the cell density (percentage area nuclei), as Cho is a precursor and breakdown product of phosphatidylcholine, a major cell membrane compound. Indeed, a significant relation was found. However, also metabolic processes (increased expression and activity of choline-kinase, a higher rate of choline transport and an increased phospholipase C and D activity) play a role in the Cho increase in cancer (39). The amount of Cho can thus be directly related to the cell density as well as to Cho metabolism and we cannot distinguish between these effects.

Our results indicate that the ADC value and (Cho+Spm+Cr)/Cit ratio might reflect the same underlying morphologic basis in the prostate. Both parameters are for an important part determined by the amount of luminal space. However, it is likely that other independent factors also contribute to their values. Based on high resolution *ex vivo* prostate DWI measurements three different diffusion components have been proposed, conveniently assigned to epithelial cells, stroma and the luminal space (32, 40), which all influence the ADC value. Furthermore, the Cit/(Cho+Spm+Cr) ratio depends also on Cho and Spm changes. However, the reported differences of Cho concentrations between tumor (7.1 mM (38)) and normal PZ tissue (4.3 mM (38)) are much smaller than the differences in Cit concentrations between tumor tissue (3.7 and 5.9 μmol/g wet weight (20, 37) or 12.5 mM (38)) and normal PZ (30.9 and 42.4 μmol/g wet weight (20, 37) or 48 mM (38)) or normal TZ tissue (46.3 and 64.5 μmol/g wet weight (20, 37)). Also reductions up to 75% of the Spm concentration have been observed in J-resolved MR spectroscopy experiments at high field in prostate cancer biopsy samples (41). Furthermore, complexation of Cit, Zn^{2+} and Spm (16, 42, 43) and interactions of these with proteins such as prostate specific antigen (44) might occur in prostatic fluid. In the case of tumor tissue the composition of prostatic fluid will change (42, 45) which may have an effect on T2 values of Cit and Spm (46). Next to this, in prostatic fluids of cancer patients, a decrease in Cit levels has been observed (30). Therefore, we did a separate analysis for benign and tumor voxels. In the case of a lower Cit concentration in tumor tissue, a lower intercept is expected, which we observed. Interestingly, we also found a large difference in the slopes of the two benign and tumor data sets. The slope for the tumor data points was steeper compared to all data points, while for the benign voxels the slope was not significantly different from a zero-slope. The lack of significance might be explained by the spread on the data: figure 6.6B & C show relative high Cit levels in ROIs with a relative small percentage area of lumen in the PZ, while in the TZ there are some outliers with low Cit levels and relatively high percentage areas of lumen. These might be the consequence of large lumen with low Cit concentrations or opposite. This demonstrates that other factors play a role. The Cit concentration in the prostatic fluid might for example drop in dilated lumen. Another aspect to consider is the fact that we used a linear model, although there is not necessarily a linear relation between the parameters, especially the validity of this model for a metabolite ratio might not be appropriate. In our study also a relation was made between the ADC value and (Cho+Spm+Cr)/Cit ratio with the fraction of nuclei to lumen ratio (Figure 6.6 C&D). This ratio incorporates some of the above-mentioned factors.

Although in this study significant relations were found, there was still substantial spread on the data. This overlap can partly be explained by the limitations of our study. The matching between histopathology and MR imaging is a difficult task. To minimize the error, the matching was done in consensus, and in doubt a pathologist was consulted. Both the T2w image and pathology slices were made perpendicular to the rectal wall; however, there might still be an angulation difference. Furthermore, discrepancies in the shape of the in and *ex vivo* prostate were present in some cases. Therefore, ROIs were placed only in locations with a good matching. This problem could have been diminished by using a mold, based on the prostate shape on the MR images, to cut the slices in the same orientation and preserve the *in vivo* shape (47). The ROI corresponding to a voxel had to be completely within the section of the pathology. As each prostate slice consisted in most cases of several sections, the ROI/voxels could not always consist of solely tumor tissue, leading to the introduction of partial volume effects. However, as these were also present in the MRSI and DWI data, these do not affect the relation between the MR parameters and histopathologic features. Since there is a volume difference between the MR(S)I slices and the thin (4 µm) histopathology sections, we have to assume that the HE-sections are representative for all tissue in the slice. For the spectroscopy voxels (volume between 0.37 and 1.0 cm^3), the average parameters of two adjacent histopathology slices (if possible) were used to reduce the dependence on one thin slice.

Although small, there were some variations between the repeated segmentations, especially for the smallest component: the nuclei. In some patients, the nuclei of the tumor cells were largely increased and the staining of these large nuclei was not homogenous and the true amount of nuclei might have been slightly underestimated. Due to the minimal differences in staining between epithelial cytoplasm and stromal tissue, no distinction could be made between these two, which limits the conclusions that can be drawn from this study. Although regions with artifacts (e.g. regions with many corpora amylacea) were not included, other artifacts might be present in the segmentation. For example, in some patients proteinaceous secretions were present in the luminal space. When these secretions were strongly stained, they have been erroneously classified as stromal tissue.

The use of a pulse sequence with a long echo time and short repetition time, and inhomogeneous coil profiles forced us to revert to ratios for the ^{1}H MRSI data. Therefore, it was not possible to directly relate Cit concentrations to the percentage area of lumen or Cho to the area of nuclei (or epithelial cytoplasm). To accomplish this, the water signal should be measured to enable absolute quantification of the metabolites. Such a measurement would be challenging and time-consuming. Assumptions regarding T1 and T2 of metabolites and water content are required for absolute quantification and the overlap between Cho, Spm and Cr would still be present. However, it would allow studying the relation of the metabolites with morphology more directly.

In conclusion, significant relations between the histological morphology of prostate tissue and the MR parameters of DWI and MRSI were found. These results suggest that the differences in ADC values and ^{1}H MRSI ratios between normal prostate and cancer tissue are largely determined by similar morphological changes, in particular the luminal space. Although we cannot rule out that biochemical processes (like m-aconitase or ATP-citrate lyase) and interactions in prostatic fluid also influence the Cit and Spm signals in ^{1}H MRSI of the prostate tissue, it is likely that these contributions are smaller than the morphological changes.

References

1. Hoeks CMA, Barentsz JO, Hambrock T, et al. Prostate cancer: Multiparametric MR imaging for detection, localization, and staging. Radiology. 2011;261(1):46-66.
2. Barentsz JO, Richenberg J, Clements R, et al. ESUR prostate MR guidelines 2012. Eur Radiol. 2012;22(4):746-57.
3. Franiel T, Stephan C, Erbersdobler A, et al. Areas Suspicious for Prostate Cancer: MR–guided Biopsy in Patients with at Least One Transrectal US-guided Biopsy with a Negative Finding—Multiparametric MR Imaging for Detection and Biopsy Planning. Radiology. 2011;259(1):162-72.
4. Kitajima K, Kaji Y, Fukabori Y, Yoshida K, Suganuma N, Sugimura K. Prostate cancer detection with 3 T MRI: Comparison of diffusion weighted imaging and dynamic contrast enhanced MRI in combination with T2 weighted imaging. J Magn Reson Imaging. 2010;31(3):625-31.
5. Fütterer JJ, Heijmink SWTPJ, Scheenen TWJ, et al. Prostate cancer localization with dynamic contrast-enhanced MR imaging and proton MR spectroscopic imaging. Radiology. 2006;241(2):449-58.
6. Tanimoto A, Nakashima J, Kohno H, Shinmoto H, Kuribayashi S. Prostate cancer screening: The clinical value of diffusion weighted imaging and dynamic MR imaging in combination with T2 weighted imaging. J Magn Reson Imaging. 2006;25(1):146-52.
7. Langer DL, Van Der Kwast TH, Evans AJ, et al. Prostate tissue composition and MR measurements: Investigating the relationships between ADC, T2, Ktrans, Ve, and corresponding histologic features. Radiology. 2010;255(2):485-94.
8. Schlemmer H-P, Merkle J, Grobholz R, et al. Can pre-operative contrast-enhanced dynamic MR imaging for prostate cancer predict microvessel density in prostatectomy specimens? Eur Radiol. 2004;14(2):309-17.
9. Ren J, Huan Y, Wang H, et al. Dynamic contrast-enhanced MRI of benign prostatic hyperplasia and prostatic carcinoma: correlation with angiogenesis. Clin Radiol. 2008;63(2):153-9.
10. Mitchell D, Burk Jr D, Vinitski S, Rifkin M. The biophysical basis of tissue contrast in extracranial MR imaging. American Journal of Roentgenology. 1987;149(4):831-7.
11. Kurhanewicz J, Vigneron DB, Hricak H, Narayan P, Carroll P, Nelson SJ. Three-dimensional H-1 MR spectroscopic imaging of the in situ human prostate with high (0.24-0.7-cm3) spatial resolution. Radiology. 1996;198(3):795-805.
12. Heerschap A, Jager GJ, Van Der Graaf M, et al. In vivo proton MR spectroscopy reveals altered metabolite content in malignant prostate tissue. Anticancer Res 1997;17(3 A):1455-60.
13. Costello LC, Franklin RB. Concepts of citrate production and secretion by prostate. 1. Metabolic relationships. Prostate. 1991;18(1):25-46.
14. Costello LC, Franklin RB. Citrate metabolism of normal and malignant prostate epithelial cells. Urology. 1997;50(1):3-12.
15. Costello LC, Franklin RB. Novel role of zinc in the regulation of prostate citrate metabolism and its implications in prostate cancer. Prostate. 1998;35(4):285-96.
16. Kavanagh JP. Sodium, potassium, calcium, magnesium, zinc, citrate and chloride content of human prostatic and seminal fluid. J Reprod Fertil. 1985;75(1):35-41.
17. Kavanagh J. Isocitric and citric acid in human prostatic and seminal fluid: implications for prostatic metabolism and secretion. The Prostate. 1994;24(3):139-42.
18. Kobus T, Wright AJ, Scheenen TW, Heerschap A. Mapping of prostate cancer by 1H MRSI. NMR in Biomed. 2013.
19. Lowry M, Liney GP, Turnbull LW, Manton DJ, Blackband SJ, Horsman A. Quantification of citrate concentration in the prostate by proton magnetic resonance spectroscopy: zonal and age-related differences. Magn Reson Med. 1996;36(3):352-8.

20. Liney GP, Turnbull LW, Lowry M, Turnbull LS, Knowles AJ, Horsman A. In vivo quantification of citrate concentration and water T2 relaxation time of the pathologic prostate gland using 1H MRS and MRI. Magn Reson Imaging. 1997;15(10):1177-86.
21. Swanson MG, Zektzer AS, Tabatabai ZL, et al. Quantitative analysis of prostate metabolites using 1H HR-MAS spectroscopy. Magn Reson Med. 2006;55(6):1257-64.
22. Scheenen TWJ, Gambarota G, Weiland E, et al. Optimal timing for in vivo 1H-MR spectroscopic imaging of the human prostate at 3T. Magn Reson Med. 2005;53(6):1268-74.
23. Mescher M, Tannus A, Johnson MO, Garwood M. Solvent suppression using selective echo dephasing. J Magn reson A. 1996;123(2):226-9.
24. Scheenen TW, Klomp DW, Roll SA, Futterer JJ, Barentsz JO, Heerschap A. Fast acquisition-weighted three-dimensional proton MR spectroscopic imaging of the human prostate. Magn Reson Med. 2004;52(1):80-8.
25. Epstein JI, Allsbrook Jr WC, Amin MB, et al. The 2005 International Society of Urological Pathology (ISUP) consensus conference on Gleason grading of prostatic carcinoma. Am J Surg Pathol. 2005;29(9):1228-42.
26. Ruifrok AC, Johnston DA. Quantification of histochemical staining by color deconvolution. Anal Quant Cytol. 2001;23(4):291.
27. Provencher SW. Estimation of metabolite concentrations from localized in vivo proton NMR spectra. Magn Reson Med. 1993;30(6):672-9.
28. Kobus T, Vos PC, Hambrock T, et al. Prostate cancer aggressiveness: In vivo assessment of MR spectroscopy and diffusion-weighted imaging at 3 T. Radiology. 2012;265(2):457-67.
29. Kobus T, Hambrock T, Hulsbergen-Van De Kaa CA, et al. In vivo assessment of prostate cancer aggressiveness using magnetic resonance spectroscopic imaging at 3 T with an endorectal coil. Eur Urol. 2011;60(5):1074-80.
30. Kline EE, Treat EG, Averna TA, Davis MS, Smith AY, Sillerud LO. Citrate Concentrations in Human Seminal Fluid and Expressed Prostatic Fluid Determined via< sup> 1</sup> H Nuclear Magnetic Resonance Spectroscopy Outperform Prostate Specific Antigen in Prostate Cancer Detection. J Urology. 2006;176(5):2274-9.
31. Sato C, Naganawa S, Nakamura T, et al. Differentiation of noncancerous tissue and cancer lesion by apparent diffusion coefficient values in transition and peripheral zones of the prostate. J Magn Res Imaging. 2005;21(3):258-62.
32. Bourne RM, Kurniawan N, Cowin G, et al. Microscopic diffusivity compartmentation in formalin-fixed prostate tissue. Magn Reson Med. 2012;68(2):614-20.
33. Schiebler ML, Miyamoto KK, White M, Maygarden SJ, Mohler JL. In vitro high resolution 1H-spectroscopy of the human prostate: Benign prostatic hyperplasia, normal peripheral zone and adenocarcinoma. Magn Reson Med. 1993;29(3):285-91.
34. Costello LC, Franklin RB, Narayan P. Citrate in the diagnosis of prostate cancer. Prostate. 1999;38(3):237-45.
35. Halliday KR, Fenoglio Preiser C, Sillerud LO. Differentiation of human tumors from nonmalignant tissue by natural abundance 13C NMR spectroscopy. Magn Reson Med. 1988;7(4):384-411.
36. Bertilsson H, Tessem MB, Flatberg A, et al. Changes in gene transcription underlying the aberrant citrate and choline metabolism in human prostate cancer samples. Clinical Cancer Research. 2012;18(12):3261-9.
37. Kurhanewicz J, Vigneron DB, Nelson SJ, et al. Citrate as an in vivo marker to discriminate prostate cancer from benign prostatic hyperplasia and normal prostate peripheral zone: detection via localized proton spectroscopy. Urology. 1995;45(3):459-66.
38. McLean MA, Barrett T, Gnanapragasam VJ, et al. Prostate cancer metabolite quantification relative to water in 1H MRSI in vivo at 3 Tesla. Magn Reson Med. 2011;65(4):914-9.
39. Ackerstaff E, Pflug BR, Nelson JB, Bhujwalla

ZM. Detection of increased choline compounds with proton nuclear magnetic resonance spectroscopy subsequent to malignant transformation of human prostatic epithelial cells. Cancer Res. 2001;61(9):3599-603.

40. Bourne R, Kurniawan N, Cowin G, Sved P, Watson G. 16 T Diffusion microimaging of fixed prostate tissue: Preliminary findings. Magn Reson Med. 2011;66(1):244-7.
41. Van der Graaf M, Schipper RG, Oosterhof GO, Schalken JA, Verhofstad AA, Heerschap A. Proton MR spectroscopy of prostatic tissue focused on the detection of spermine, a possible biomarker of malignant behavior in prostate cancer. Magma (New York, NY. 2000;10(3):153-9.
42. Lynch MJ, Nicholson JK. Proton MRS of human prostatic fluid: Correlations between citrate, spermine, and myo-inositol levels and changes with disease. Prostate. 1997;30(4):248-55.
43. Arver S. Zinc and zinc ligands in human seminal plasma. III. The principal low molecular weight zinc ligand in prostatic secretion and seminal plasma. Acta Physiol Scand. 1982;116(1):67-73.
44. Huang X, Knoell CT, Frey G, et al. Modulation of Recombinant Human Prostate-Specific Antigen: Activation by Hofmeister Salts and Inhibition by Azapeptides Appendix: Thermodynamic Interpretation of the Activation by Concentrated Salts. Biochemistry. 2001;40(39):11734-41.
45. Grover PK, Resnick MI. Analysis of prostatic fluid: evidence for the presence of a prospective marker for prostatic cancer. Prostate. 1995;26(1):12-8.
46. Spencer NG, Eykyn TR, DeSouza NM, Payne GS. The effect of experimental conditions on the detection of spermine in cell extracts and tissues. NMR in Biomed. 2010;23(2):163-9.
47. Shah V, Pohida T, Turkbey B, et al. A method for correlating in vivo prostate magnetic resonance imaging and histopathology using individualized magnetic resonance-based molds. Rev Sci Instrum. 2009;80:104301.

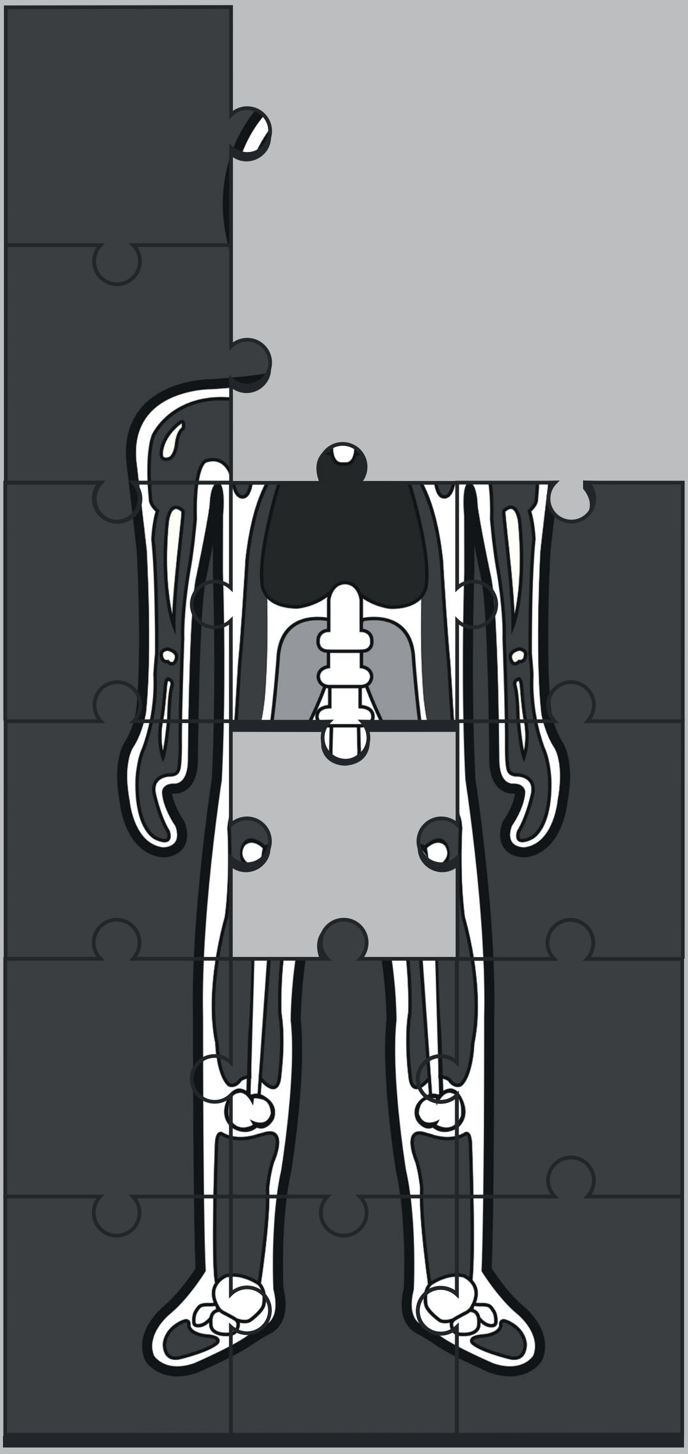

7

CHAPTER SEVEN

In vivo ^{1}H MR Spectroscopic Imaging of Aggressive Prostate Cancer: Can we detect lactate?

This chapter is based on the publication:
In vivo ^{1}H MR spectroscopic imaging of aggressive prostate cancer: can we detect lactate?
T. Kobus, A.J. Wright, J.J.A. Van Asten, A. Heerschap and T.W.J. Scheenen
Magnetic Resonance in Medicine, 2013, Jan;71(1):26-34

Introduction:

The estimated number of prostate cancer deaths in the United States was 32,050 in 2010, making the disease the second leading cause of cancer-related death (1). However, prostate cancer is often non-aggressive and it was shown that to prevent one prostate cancer death over 11 years by means of prostate-specific antigen (PSA) screening, 37 men need to be treated (2). It is estimated that half of these treated men would not have presented any clinical symptoms during the rest of their life if no screening had been performed (3). To prevent overtreatment, an accurate assessment of prostate cancer aggressiveness is indispensable.

Several MR techniques have shown promising results for a noninvasive assessment of cancer aggressiveness. One of these techniques is ^{1}H MR spectroscopic imaging (^{1}H MRSI), which can measure the distribution of choline (Cho) and creatine (Cr) compounds, citrate (Cit) and polyamines, mainly spermine (Spm), in the prostate. From these metabolites, the (Cho+Cr)/Cit ratio and the Cho/Cr are often used to detect prostate cancer (4-6) and to characterize cancer aggressiveness (7,8).

Another metabolite that is of strong interest for cancer characterization is lactate (Lac), which is an end-product of glycolysis. Lac may occur in tumors because of hypoxia and even under aerobic conditions as a result of high glycolytic rates, which is known as the Warburg effect. Increased Lac levels are linked to increased aggressiveness and distant metastasis (9-11). Previous attempts to measure hypoxia in the prostate were performed by blood oxygenation level-dependent MR imaging (12). A correlation with whole mount sections of the excised prostate, stained for hypoxia by pimonidazole indicated high sensitivity (88%) for detecting hypoxia, but limited specificity (36%) (12). Another important aspect of tumor hypoxia is that it reduces the effectiveness of chemotherapy and radiotherapy (9), which makes Lac an interesting potential marker to predict treatment outcome.

Using high resolution magic angle spinning (HR-MAS) spectroscopy, average Lac levels of 1.6 mmol/kg were reported in snap-frozen prostate cancer biopsy samples (compared to 0.6 mmol/kg in benign biopsy samples)(13). However, only 6 out of 16 tumor biopsy samples had a Gleason score of 7 or higher and the biopsy cores consisted mainly of benign tissue (only 27% of cancer tissue on average). From these HR-MAS studies we cannot derive whether Lac levels in high grade prostate cancer are high enough to be detected with *in vivo* ^{1}H MRSI.

Generally point-resolved spectroscopy (PRESS) volume localization is used in ^{1}H MRSI of the prostate, in combination with frequency-selective refocusing pulses and crushing gradients to suppress lipid and water signals (14). Since the chemical shifts of Lac and lipids overlap at 1.3 ppm, the Lac resonance is also affected and crushed by the frequency-selective refocusing pulses and gradients of conventional prostate MRSI. When a sequence without frequency-selective suppression is used to study Lac, periprostatic lipid contamination can only be prevented by accurate volume selection within the prostate and spatial saturation slabs positioned on periprostatic fat. Another issue that complicates the detection of Lac with the conventional PRESS sequence at higher field (≥ 3 T) is the chemical shift displacement artifact. The limited excitation and refocusing bandwidth of the pulses of conventional PRESS and the large chemical shift difference between the two Lac resonances at 1.3 ppm and 4.1 ppm means that the two resonances are excited at partially different locations in the prostate, which will lead to partial scalar evolution and as a consequence signal loss (15,16). A solution that overcomes both problems is the use of adiabatic pulses. Localization by adiabatic selective refocusing (LASER) uses three pairs of adiabatic full passage (AFP) pulses that result in a near-perfect volume excitation (17). To make this sequence less specific absorption rate (SAR) intense, we replaced two adiabatic pulses by one nonadiabatic slice-selective excitation pulse (semi-LASER) (18,19).

The aim of this study was to evaluate the presence of Lac in patients with highly aggressive prostate cancer. For this purpose the semi-LASER sequence was optimized for *in vivo* Lac detection. To quantify the amount of Lac in the prostate, an LCModel basis set was developed. As Lac could reveal the presence of hypoxia, which induces resistance to both radiotherapy and chemotherapy, Lac might be a valuable biomarker in ^{1}H MRSI for prostate cancer management. In MR spectra of patients without a detectable Lac resonance, we assessed a threshold value for Lac levels.

Methods:

MR Hardware, Pulse Sequence, and Timing

For all measurements a Siemens Trio 3T system (Siemens Healthcare, Erlangen, Germany) was used. The semi-LASER sequence for MRSI is shown in Figure 7.1 and consists of a 4 ms Shinnar-Le-Roux 90˚ excitation pulse and four adiabatic 2nd order hyperbolic secant pulses (20) of 8 ms duration. A γB_1 of 718 Hz was used for the adiabatic pulses, resulting in a bandwidth of 3 kHz. As there are four adiabatic full passage (AFP) pulses, there are four inter-pulse durations, τ1, τ2, τ3 and τ4, and a delay before acquisition, τ5, that can be varied at a given echo time (TE) (Figure 7.1).

For scalar coupled spin systems, like Lac and Cit, the echo time, inter-pulse timing and the type of pulses influence the spectral modulations. Lac consists of four nonexchangeable protons, of which the three protons in the methyl group resonate at 1.3 ppm and the other proton resonates at 4.1 ppm. The scalar coupling in Lac is 6.93 Hz and it is a weakly coupled spin-system (21). The use of an echo time (TE) of 144 ms will lead to a doublet of Lac at 1.3 ppm and a quartet at 4.1 ppm, both 180˚ out of phase.

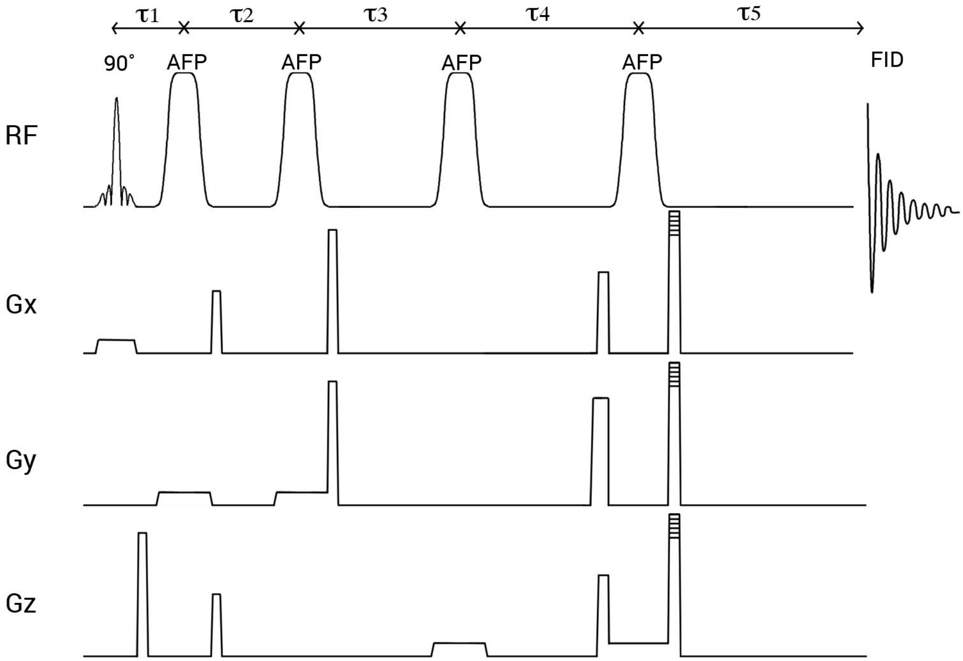

Figure 7.1. *In the semi-LASER sequence, the delays τ1 to τ4 between slice-selection and AFP pulses were varied to obtain an optimal shape of the citrate resonance at an echo time TE = 144 ms. From top to bottom, RF and the gradients in three directions (Gx, Gy and Gz) are indicated.*

Cit consists of two magnetically equivalent methylene groups, in which the protons in each methylene group are magnetically inequivalent, making it strongly coupled. The exact chemical shifts and scalar coupling of Cit depend on the pH (22) and cation concentration (23), but are ~2.57 ppm, 2.72 ppm and 15.5 Hz respectively (16). The spectral shape of Cit strongly depends on the TE, but also on the timing of the refocusing pulses (24,25). As Cit is important for prostate cancer detection and characterization with MRSI, a spectral shape that leads to a high signal intensity is preferable.

In this study a TE of 144 ms was chosen, as an inverted Lac signal is desired for better distinction between Lac and residual lipid signals. The timing of the four AFP pulses at this TE influences the shape of Cit and therefore simulations were performed to obtain the best pulse timing for an optimal Cit shape.

Simulation study:

The sequence and pulses were simulated using NMR-SIM software (part of Topspin, Bruker BioSpin Corporation, Billerica, MA, USA). The timing between the AFP pulses was varied and the corresponding simulated Cit and Lac signals were studied using the Topspin software. An optimal timing was obtained that resulted in a spectral Cit shape with a high signal intensity.

Phantom study:

After optimization of the interpulse timing, the sequence was tested on two phantoms. Phantom 1 contained Cit, Cho, and Cr, and phantom 2 held Lac and Cr. After localization and B_0 shimming the optimized semi-LASER sequence was tested on both phantoms.

Patients:

The institutional ethics review board waived the need for informed consent as the study was a short extension of a clinical MR exam. Seventeen patients with biopsy-proven prostate cancer were measured between December 2009 and September 2011. The patients were referred to the department of radiology by a urologist for an MRI exam to examine the local extent of the tumor. Only patients with aggressive prostate cancer were included, which was defined as either a Gleason score of 7 or higher at biopsy or a PSA level higher than 20 ng/ml. For signal reception an endorectal coil was combined with a body-array matrix. To suppress peristalsis the patients were injected intramuscularly with 1 mg glucagon (Glucagen, Nordisk, Gentofte, Denmark) and 20 mg of butylscopolaminebromide (Buscopan, Boehringer-Ingelheim, Ingelheim, Germany). The clinical exam consisted of high resolution T2-weighted imaging in three directions, diffusion weighted imaging, conventional PRESS based MRSI and dynamic contrast enhanced imaging. Before MRSI B_0 shimming was performed to optimize field homogeneity. PRESS spectroscopy was acquired in 16 of the 17 patients. For the PRESS based MRSI elliptical weighted k-space sampling and Hanning filtering was applied. The number of averages varied between 3 and 6, and between 10 and 14 phase encoding steps were used in each direction. Depending on the size of the prostate an effective voxel volume between 0.37 and 1.01 cm^3 was chosen. A TE of 145 ms and a TR of 750 ms were used (24).

In addition to the clinical exam, 17 patients were measured with the 3D MRSI semi-LASER sequence. For the 3D MRSI semi-LASER sequence an effective voxel volume, after Hanning filtering and elliptical weighted sampling, of 1.5 cm^3 was chosen. The number of phase encoding steps were either 8 or 10 in all directions and the number of averages varied between 1 and 4. Based on the T2-weighted images, the volume of interest was placed completely inside the prostate. To minimize lipid contamination, spatial lipid saturation slabs were placed around the volume of interest. The posture of the patient influences the amount of RF power needed for the adiabatic pulses. For each patient, the minimal TR for the semi-LASER sequence (and thus lowest acquisition time) was chosen that led to compliance with the SAR limit of that patient.

Data analysis:

A spectroscopist (TK), blinded for the spectra, selected all tumor-containing voxels in the PRESS and semi-LASER datasets based on the clinical reading of a radiologist of T2-weighted images and diffusion weighted images. Metabolite Report (Siemens Healthcare, Erlangen, Germany) was used for analysis of MR spectra acquired with the PRESS sequence. This prototype software package fits Cho, Cr and Cit signals in the time domain and was used to determine the (Cho+Cr)/Cit and Cho/Cr ratios (26). All fits were visually inspected by a spectroscopist (TK) and only the voxels that passed the quality check for sufficient SNR, appropriate fit and absence of baseline distortions were included. For each patient, the maximum (Cho+Cr)/Cit and Cho/Cr ratio of all accepted tumor voxels were determined. Furthermore, for all tumor voxels the malignancy rating by the standardized threshold approach (7,27,28) was determined. The standardized threshold approach is a method to combine both metabolite ratios into one score. The initial rating is based on the (Cho+Cr)/Cit ratio and ranges from 1 to 5, in which 5 indicates the highest malignancy probability. The cut off values for the (Cho+Cr)/Cit ratio are based on the values described in (26). The initial rating is adjusted for deviating Cho/Cr ratios and here a cut off of 2.3 is used (7). For each patient, the maximum malignancy rating was determined.

To analyze the semi-LASER spectra, an LCModel (29) basis set was developed for fitting Cho, Cr, Spm, Cit, Lac and a singlet at 2.05 ppm. The spectral shapes of Cho, Cr, Cit, Lac and the 2.05 singlet were simulated. For Cr, Cho and Lac only the methyl resonances at 3.0, 3.2 and 1.3 ppm, respectively, were included. The more downfield resonances around 4 ppm might be influenced by the water suppression, which could affect quantification. To obtain the spectral shape of Spm, a phantom containing Spm and trimethylsilyl propionic acid (as reference) at pH 6.8 and 310°K was measured in the MR-scanner using the semi-LASER sequence.

All spectra were analyzed twice. First it was determined whether a spectrum was contaminated with lipids by using the LCModel option to fit several lipid signals. For this fit, the Lac signal was excluded from the basis set, since the presence of Lac in the basis set could affect fitting of lipids. The output of these analyses was only used to determine whether a spectrum contained lipid signals. Next, the data were fit with Lac in the basis set, but without lipid fitting. The output of this fit was used to determine the Lac concentration in the prostate. All processing was performed without restricting the zero-order phase of the spectrum, a first-order phase of 0 and limited baseline flexibility. In the output, the integral values of the resonances with the corresponding Cramér-Rao lower bound (CRLB) were given. In this study, metabolite fits with a CRLB smaller than 20% were accepted. A CRLB of ≈ 20% indicates that signal changes of approximately 40% can be detected reliably, and is therefore often used as cut off for reliability (30).

Spectra were analyzed for the presence of Lac if the line-width was appropriate for small molecule metabolites (FWHM ≤0.1 ppm), there was no or limited lipid signal present in the spectra fitted for the presence of fat (CRLB of lipid fits ≥ 20%), and the SNR of the spectrum was sufficient (SNR ≥3). The SNR in LCModel is defined as the maximum in the spectrum (minus baseline) divided by two times the root-mean-square of the residuals (30). If in none of the tumor voxels of a patient a Lac fit was accepted, the hypothetical minimal Lac concentration was determined with the use of Cr as an internal reference. A simulated Lac signal was added to all spectra in a dataset. As the zero-order phase varies over the spectra, the simulated Lac signal of each spectrum was added with the phase of the spectrum determined by LCModel on the original dataset. Furthermore, the estimated full width at half-maximum of the fits of the accepted tumor voxels was used to determine the appropriate line-width of the added Lac signal for each patient. For all tumor voxels with a CRLB of the Lac fit smaller than 20%, the Lac concentration was determined as described in (31). The adapted formula for our purposes is:

$$[Lac] = [Cr]\left(\frac{I}{f_{T1}f_{T2}}\right)_{Lac}\left(\frac{f_{T1}f_{T2}}{I}\right)_{Cr} \qquad (7.1)$$

In which [Lac] is the Lac concentration, [Cr] the Cr concentration, I the integral of the fit and f_{T1} and f_{T2} the correction factors for relaxation effects. Since Cr and Lac both have one methyl-group contributing to their resonances at 3.0 and 1.3 ppm, no correction for a difference in number of protons is needed.

The correction factors for relaxation effects are:

$$f_{T1} \approx 1 - \exp(-TR/T_1) \qquad (7.2)$$

$$f_{T2} \approx \exp(-TE/T_2) \qquad (7.3)$$

For Cr the T1 and T2 of prostate measurements at 1.5 T were used, and these were 864 and 209 ms, respectively (32). As the relaxation times of Lac in the prostate are unknown, relaxation times obtained in brain measurements at 1.5 T were used. The shortest T2 for Lac found in literature was 225 ms (33). For Cho and Cr in the brain relative long T1 values of 1.39 s and 1.54 s (34) were reported compared to the prostate (837 ms and 864 ms, respectively). For brain only one T1 value for Lac was found at 1.55 s (35). Assuming a comparable difference between brain and prostate T1 values for Lac as observed for Cr and Cho, we estimated a T1-value of 0.9 s for Lac in the prostate. A Cr concentration of 4.4 mM, obtained from an *in vivo* MR measurement in the prostate, was used as the standard for all voxels (32). The amplitude of the simulated Lac signal was iteratively lowered by 10% until in none of the tumor voxels Lac was detected. The lowest minimal detectable Lac concentration was calculated for all tumor voxels that had sufficient SNR, an appropriate line-width, no lipids and an accepted Cr fit. For each patient this Lac detection limit was determined.

Results

At a TE of 144 ms, simulations showed an in-phase Cit spectrum with an interpulse timing τ1= 11 ms, τ2= 21 ms, τ3= 29 ms, τ4= 51 ms and τ5= 32 ms. This pulse timing led to a nearly fully absorptive Cit shape (Figure 7.2A) and an inverted Lac doublet (Figure 7.3A).

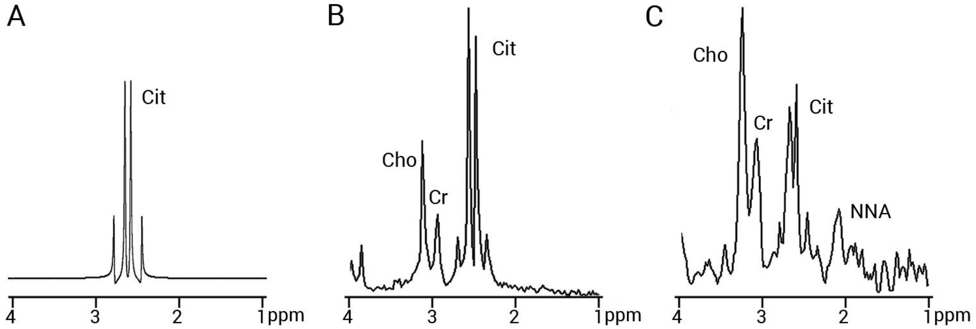

Figure 7.2. *Simulated and measured spectral shapes of Cit. An echo time of 144 ms with τ1= 11 ms, τ2= 21 ms, τ3= 29 ms, τ4= 51 ms and τ5= 32 ms is used for the simulated spectrum in A, the phantom measurement in B and the in vivo measurement in C (central gland tissue). The phantom contained Cho (9 mM), Cr (12 mM) and Cit (90 mM). In vivo also a signal likely representing an acetyl group, possibly N-acetyl neuraminic acid (NNA), was observed.*

The sequence was tested on two phantoms. The spectral shape of Cit, obtained from a phantom containing Cit, Cho, and Cit closely resembled that of the simulated Cit shape (Figures 7.2A,B). An inverted Lac signal was obtained in the second phantom which held Lac and Cr (Figure 7.3B).

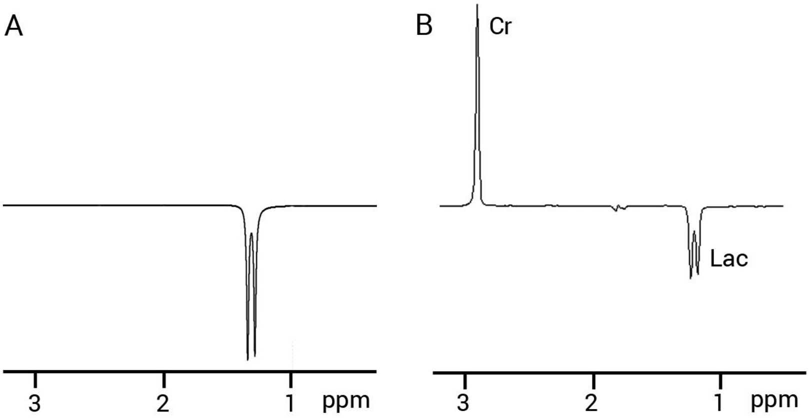

Figure 7.3. *A) Simulated spectral shape of Lac using the semi-LASER sequence with an echo time of 144 ms. B) The measured spectrum in a phantom containing Cr (100 mM) and Lac (100 mM).*

The 17 patients had an average PSA level of 20.2 ng/ml (3.7 – 79 ng/ml) and the following Gleason scores on biopsy: 6 (n=1), 7 (n=4), 8 (n=4), 9 (n=7) and 10 (n=1). Depending on patient body weight and body coil load, the TR for the semi-LASER sequence ranged from 1400 ms to 2280 ms, and the total acquisition time between 4:26 and 11:42 minutes.
The average of the maximum (Cho+Cr)/Cit ratio, obtained from the PRESS data, found in each patient was 12.6 (range 1.6 -105.3) and the average maximum Cho/Cr ratio was 12.2 (range 3.7 - 34.3). The maximum malignancy rating of the standardized threshold approach was in all patients 5, which is the highest value that can be obtained.

In the 17 patients measured with the 3D semi-LASER sequence, 897 (partially overlapping) tumor voxels could be selected. An effective voxel volume of 1.5 cm^3 was used in a field of view of 64 x 64 x 64 mm or 80 x 80 x 80 mm. Of these, 302 voxels (37%) met all criteria of sufficient SNR, an appropriate line-width and no lipid contamination. In three patients, none of the voxels met the criteria and these had to be excluded from the analysis. Only in two spectra of one patient, Lac was fitted with a CRLB smaller than 20%. However, in both spectra there was a large lipid resonance present, which was too broad to be recognized by LCModel as lipid. Therefore, the fitted Lac signal was not reliable.

Excluding this patient, in 11 of the remaining patients the minimum detectable Lac level could be determined and was 1.5 mM on average (range 0.9 - 3.5 mM) (Figure 7.4). In one patient the minimal detectable limit could not be determined due to technical failure and in one other there was a lack of a reliable Cr fit. In Figure 7.5 an original spectrum and the same spectrum with Lac added at the detection limit is shown for one voxel of the data set of one of the patients.

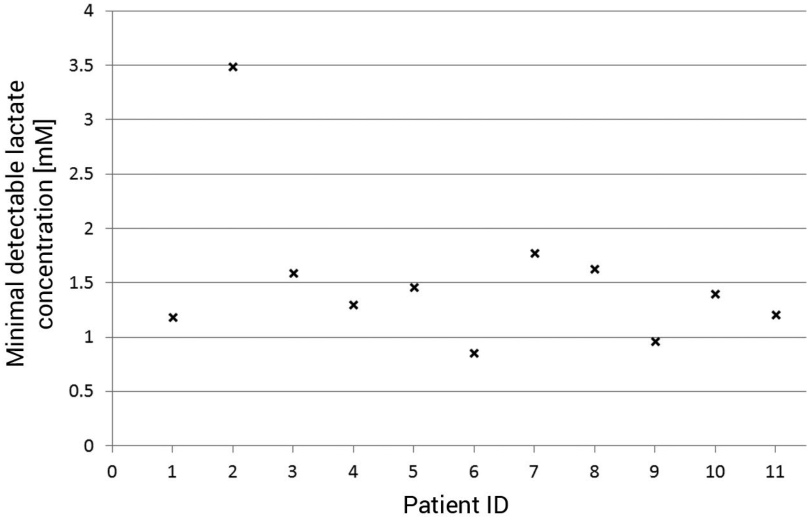

Figure 7.4. *The minimal detectable lactate concentration per patient. The mean detection limit for the MR spectroscopic imaging data was 1.5 mM.*

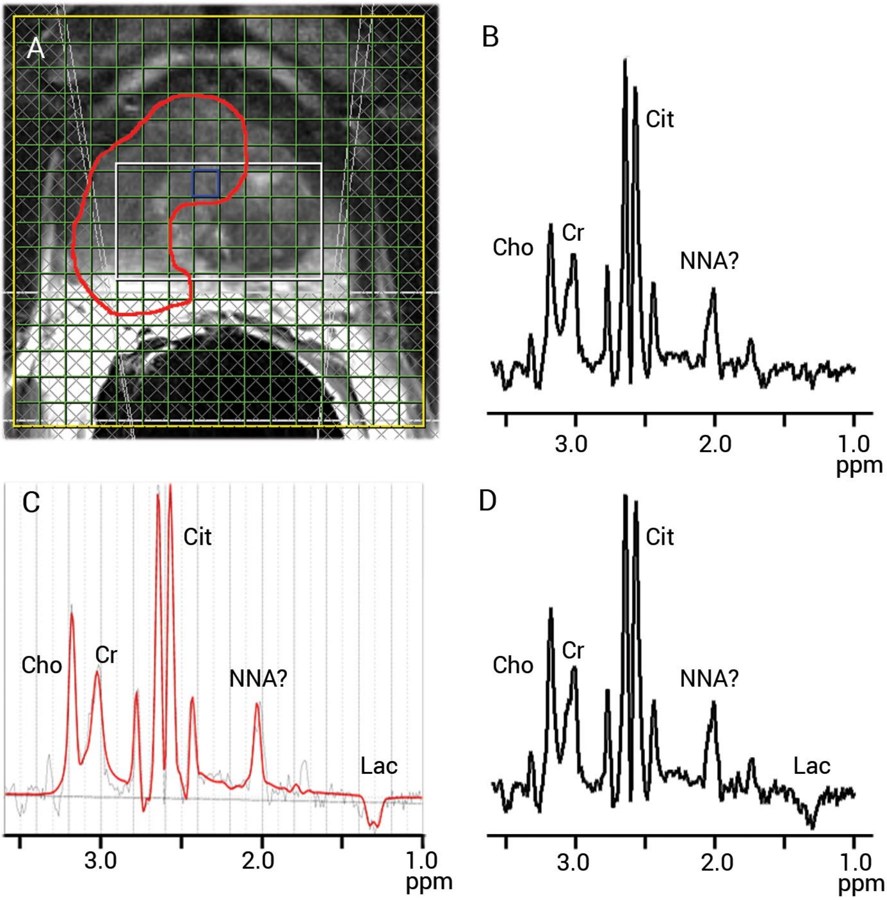

Figure 7.5. *A) T2-weighted image of the prostate of a 72-year-old male with a tumor in the right peripheral and transition zone (indicated in red) with a Gleason score of 9 and a PSA level of 16.3 ng/ml. In B the original spectrum of the blue voxel in A. Lac is added at the detection limit in D and C (LCModel fit), leading to a minimal detectable Lac concentration of 1.4 mM. The other detectable metabolites are Cho, Cr, Cit and possibly N-acetyl neuraminic acid (NNA). Not indicated are the signals of spermine, of which resonances can be found close to creatine.*

Although the spectra of several patients were contaminated with periprostatic lipid signals, in one patient the origin of the lipid signals was from the tumor. The biopsy samples of this patient had a Gleason score of 5+5 and extensive necrosis was present. The T2-weighted image shows areas of higher signal intensity in the tumor, which could be caused by lipids (Figure 7.6). More convincingly are the spectral maps (Figure 7.6), which show the highest intensity of lipid signals in the center of the tumor and small lipid signals on the edge of the volume of interest, illustrating accurate selection of the volume of interest with the semi-

LASER localization. If originating from periprostatic fat, the lipid signals would be largest in the edge of the volume of interest and lower in the center. Interestingly, the apparent diffusion coefficient (ADC) map has areas of low signal intensity on the rim of the tumor and high signal intensity in the center of the tumor (Figure 7.6).

Discussion

In this work we investigated the presence of Lac in patients with highly aggressive prostate cancer using *in vivo* ^{1}H MRS. For this purpose the semi-LASER sequence was optimized to obtain an inverted Lac signal and a maximized in-phase Cit shape. In total 17 prostate cancer patients were measured, but in none of the identified tumors was a Lac signal detected convincingly.

The lack of a Lac signal in our spectra does not imply that there is no Lac produced by these highly aggressive prostate tumors. It means that if these tumors produce Lac, that either Lac is rapidly cleared from the prostate, or that they produce it in small amounts. For that reason, the minimal detectable Lac concentration was determined. Some patients had to be excluded as lipid contamination could not be prevented, but in 11 patients the minimal detectable Lac concentration was determined. From the minimal detectable Lac concentrations, we estimate that Lac levels stay below 1.5 mM in cancer tissue of the prostate. In contrast, in brain tumors increased Lac signals are observed, ranging from 1.5±1.0 mM for astrocytoma grade 2 to 14.2±7.1 mM for brain metastases (36).

In astrocytomas a correlation between necrosis and lipid levels is observed, as well as an increase in lipid and Lac with tumor grade (36,37). In our study, all voxels with lipid signals were eliminated from the analysis. However, these might be the voxels of interest as the lipids can indicate necrosis, a consequence of hypoxia. Necrosis is not common in prostate cancer (38); though, in one of the patients, extensive necrosis was found in the biopsy tissue. The T2-weighted images of this patient showed areas in the tumor of high signal intensity, indicative of fat, and the spectra of tumor tissue showed large lipid resonances in the center of the tumor (Figure 7.6). As the lipid signals decreased to the edge of the volume of interest, these lipid signals did not arise from periprostatic fat. The accurate volume selection of the semi-LASER enabled the removal of frequency-selective lipid suppression and in combination with elliptical weighted sampling and Hanning filtering, intra-prostatic lipid signals could be detected reliably. Furthermore, the rim of the tumor had low ADC values, while the core of the tumor had high ADC values. It is hypothesized that these areas of high ADC represent necrosis (39).

In HR-MAS spectroscopy data of human prostate biopsies, a significant increase in the Lac over alanine ratio was observed in malignant compared to benign samples (40). However, Lac levels in *ex vivo* samples should be assessed with caution, as anaerobic energy metabolism of substrates could quickly produce Lac. This is confirmed by Swanson et al. (41) who performed HRMAS spectroscopy with postsurgical prostate tissues. They reported high Lac concentrations (~45 mmol/kg in benign and ~70 mmol/kg in malignant tissue), but hardly detected a glucose resonance, and did not find appreciably changes over time in the Lac concentration. This suggests that there was complete anaerobic conversion of glucose to Lac during the period of the surgery and tissue harvesting. Rather than a tumor marker by itself, the Lac concentration difference between benign and malignant tissue mainly suggests here a higher glucose level in tumor tissue (41), which can have several causes like a higher glycolytic activity and better/more perfusion. Tessem et al. (13) were able to freeze the prostatic tissue within 15 s after a biopsy. They reported Lac concentrations for malignant prostate tissue (mean 26% tumor in core) of 1.6 mmol/kg and 0.61 mmol/kg for benign tissue samples. As their Lac levels in malignant samples, which were mainly low grade and contained predominantly normal tissue, are higher than our detection limit in high grade tumors, probably still glucose was converted to Lac in the 15 s time-window. Nonetheless, this study ties in with our results of low Lac levels in the prostate.

An observation that supports these findings of low Lac levels in prostate cancer is the fact that glucose transporter 1 (GLUT1) is immunohistochemically undetectable in most prostate cancers, although overexpression was observed in a small number of highly proliferative cancers (42). GLUT1 is a marker for increased glucose metabolism and is suggested as a marker for hypoxia. The lack of GLUT1 expression might also explain the limited clinical usability for fluorodeoxyglucose positron emission tomography in prostate cancer evaluation (42). However, when the prostate was stained for hypoxia with pimonidazole, staining was seen in 70% of areas containing predominantly tumor, and in 33% of nontumor areas(12). This suggests the presence of hypoxia throughout the prostate, which is difficult to explain in such a well-perfused organ.

Mice studies using hyperpolarized ^{13}C labeled pyruvate showed an increase in Lac with prostate cancer development and progression (43). Also in the first human *in vivo* studies using hyperpolarized ^{13}C labeled pyruvate, Lac formation was observed and in cancer tissue a higher lactate/pyruvate ratio was detected (44). Hyperpolarization enables one to study very small concentrations of Lac, converted from pyruvate, but accurate quantification of Lac levels is difficult.

We calculated a minimal detectable Lac concentration of 1.5 mM in high grade prostate cancer. Some aspects of our analysis should be kept in mind regarding this detection limit. First of all, some assumptions about the relaxation times had to be made. All used relaxation times were obtained from 1.5 T data, and for Lac we assumed similar effects on the relaxation times when going to a field strength of 3 T as for Cr. As there are no T1 and T2

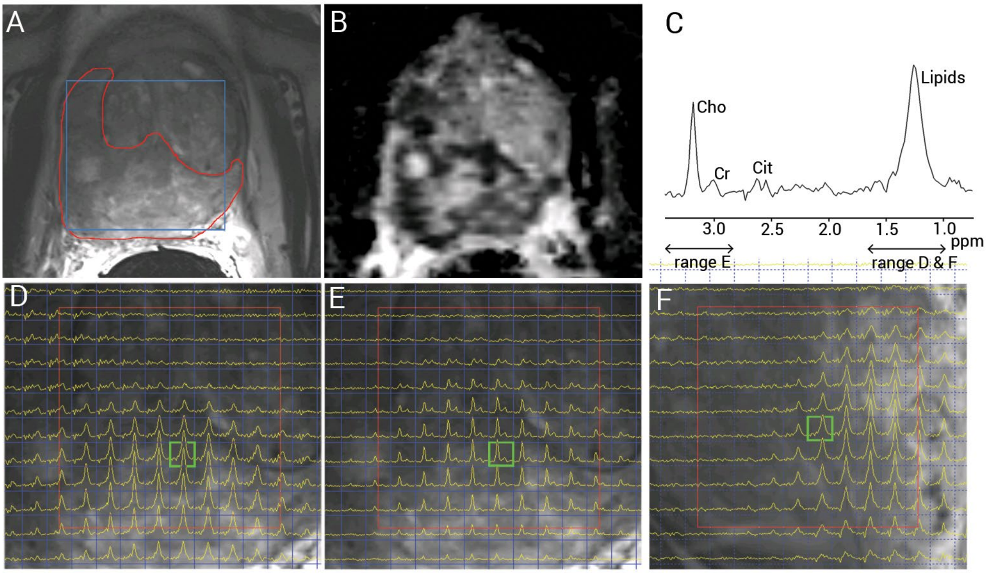

Figure 7.6. A) T2-weighted image of the prostate of an 80-year-old male with a tumor in the entire peripheral zone (indicated in red) with a Gleason score of 5+5 and a PSA level of 6.1 ng/ml. The outline of the tumor is guided by the T2-weighted and ADC images. The blue box indicates the area displayed in D-E. In B the ADC map which shows areas of low signal intensity at the rim of the tumor and high signal intensity in the center of the tumor. The spectrum of the semi-LASER sequence in C (green voxel in D-F) contains resonances of Cho, Cr, Cit and lipids. The frequency ranges of the spectral maps in (D-F) are indicated (range E and range D&F). The spectral map in D and F focus on the lipid resonance at 1.3 ppm in a transversal and saggittal view. There is no wraparound of lipid signals in any direction, and the highest lipid resonances are observed in the center of the tumor. The spectral map in D shows the Cho and Cr distribution over the prostate, with high Cho signals in the tumor and low Cho signals in the transition zone.

values available for Lac in the prostate, relaxation times from the brain were used. To prevent overestimation of the detection limit, the shortest T2 found in literature for Lac was chosen, as this leads to a higher minimal detectable Lac concentration then longer T2 values. For the Lac T1 value we took a value of 900 ms, assuming comparable differences between brain and prostate T1 values for Lac as observed for Cr and Cho. Next, for the calculation a constant Cr concentration was assumed of 4.4 mM. If the Cr concentration were lower in tumor tissue, the minimal detectable Lac concentration would be higher.

The removal of the frequency-selective refocusing pulses for lipid and water suppression, also enabled detection of other metabolites. In the spectra of most patients a resonance at 2.05 ppm was observed. It probably belongs to an acetyl group because of its chemical shift and persistence at longer TE. By means of simulations and phantom measurements (data not shown), we ruled out that this resonance belonged to Spm, glutamate or glutamine. A possible candidate is the sialic acid N-acetyl neuraminic acid, which has previously been observed in in vitro studies of human prostate specimens (45). Several researchers have studied the use of serum N-acetyl neuraminic acid levels as marker for prostate cancer (46,47). Significant differences between serum levels of healthy and prostate cancer patients were found, but these increases were also found for other cancers and N-acetyl neuraminic acid was therefore not specific enough for screening (46,47).

The deletion of the frequency selective refocusing pulses has the disadvantage of a higher chance for lipid contamination. This is evident from the relatively low number of voxels of acceptable quality without lipid contamination (595 voxels rejected out of 897). A comment needs to be made that 292 of the rejected voxels were from the patient who had extensive necrosis and lipid signals in the tumor. Although the chemical shift displacement error is only 4% for the adiabatic pulses, there is room for improvement to further eliminate lipid contamination.

All tumors showed highly abnormal spectra in the PRESS spectroscopy datasets. All tumors had the maximum malignancy rating of 5 and very deviating metabolite ratios. Because the tumors in these patients were so aggressive, these patients usually do not receive a prostatectomy and are therefore not included in validation studies based on histopathology. Our results reinforce the clinical usability of the (Cho+Cr)/Cit and Cho/Cr ratios for prostate cancer characterization. Furthermore, our method enabled detection of lipid resonances that originated almost certainly from the tumor, in a patient with extensive necrosis in the tumor biopsy samples (Gleason score 5+5). However, the lack of Lac signals in 17 patients with highly aggressive prostate cancer, makes Lac measured with ^{1}H MRS unsuitable as biomarker for prostate cancer characterization or as a method for treatment planning. Our detection limit shows that if Lac is present in highly aggressive prostate cancers, it is in low concentrations.

References

1. Jemal A, Siegel R, Xu J, Ward E. Cancer statistics, 2010. CA Cancer J Clin 2010;60(5):277-300.
2. Schröder FH, Hugosson J, Roobol MJ and others. Prostate-cancer mortality at 11 years of follow-up. New Engl J Med 2012;366(11):981-990.
3. Draisma G, Boer R, Otto SJ, van der Cruijsen IW, Damhuis RAM, Schröder FH, de Koning HJ. Lead times and overdetection due to prostate-specific antigen screening: Estimates from the European randomized study of screening for prostate cancer. J Natl Cancer I 2003;95(12):868-878.
4. Heerschap A, Jager GJ, Van Der Graaf M, Barentsz JO, De La Rosette JJMCH, Oosterhof GON, Ruijter ETG, Ruijs SHJ. In vivo proton MR spectroscopy reveals altered metabolite content in malignant prostate tissue. Anticancer Res 1997;17(3 A):1455-1460.
5. Kurhanewicz J, Vigneron DB, Nelson SJ, Hricak H, MacDonald JM, Konety B, Narayan P. Citrate as an in vivo marker to discriminate prostate cancer from benign prostatic hyperplasia and normal prostate peripheral zone: detection via localized proton spectroscopy. Urology 1995;45(3):459-466.
6. Kurhanewicz J, Vigneron DB, Hricak H, Narayan P, Carroll P, Nelson SJ. Three-dimensional H-1 MR spectroscopic imaging of the in situ human prostate with high (0.24-0.7-cm3) spatial resolution. Radiology 1996;198(3):795-805.
7. Kobus T, Hambrock T, Hulsbergen-Van De Kaa CA, Wright AJ, Barentsz JO, Heerschap A, Scheenen TWJ. In vivo assessment of prostate cancer aggressiveness using magnetic resonance spectroscopic imaging at 3 T with an endorectal coil. Eur Urol 2011;60(5):1074-1080.
8. Zakian KL, Sircar K, Hricak H and others. Correlation of proton MR spectroscopic imaging with gleason score based on step-section pathologic analysis after radical prostatectomy. Radiology 2005;234(3):804-814.
9. Wilson WR, Hay MP. Targeting hypoxia in cancer therapy. Nat Rev Cancer 2011;11(6):393-410.
10. Hirschhaeuser F, Sattler UGA, Mueller-Klieser W. Lactate: A metabolic key player in cancer. Cancer Res 2011;71(22):6921-6925.
11. Walenta S, Mueller-Klieser WF. Lactate: Mirror and motor of tumor malignancy. Semin Radiat Oncol 2004;14(3):267-274.
12. Hoskin PJ, Carnell DM, Taylor NJ and others. Hypoxia in Prostate Cancer: Correlation of BOLD-MRI With Pimonidazole Immunohistochemistry-Initial Observations. Int J Radiat Oncol Biol Phys 2007;68(4):1065-1071.
13. Tessem MB, Swanson MG, Keshari KR and others. Evaluation of lactate and alanine as metabolic biomarkers of prostate cancer using 1H HR-MAS spectroscopy of biopsy tissues. Magn Reson Med 2008;60(3):510-516.
14. Verma S, Rajesh A, Fütterer JJ, Turkbey B, Scheenen TWJ, Pang Y, Choyke PL, Kurhanewicz J. Prostate MRI and 3D MR spectroscopy: How we do it. AJR Am J Roentgenol 2010;194(6):1414-1426.
15. Lange T, Dydak U, Roberts TPL, Rowley HA, Bjeljac M, Boesiger P. Pitfalls in lactate measurements at 3T. AJNR Neuroradiol 2006;27(4):895-901.
16. De Graaf RA. In Vivo NMR Spectroscopy - 2nd Edition Principles and Techniques: John Wiley & Sons Ltd; 2007.
17. Slotboom J, Bovee W. Adiabatic Slice-Selective Rf Pulses and a Single-Shot Adiabatic Localization Pulse Sequence. Concepts Magn Resonance 1995;7(3):193-217.
18. Scheenen TWJ, Klomp DWJ, Wijnen JP, Heerschap A. Short echo time 1H-MRSI of the human brain at 3T with minimal chemical shift displacement errors using adiabatic refocusing pulses. Magn Reson Med 2008;59(1):1-6.
19. Scheenen TWJ, Heerschap A, Klomp DWJ.

Towards 1H-MRSI of the human brain at 7T with slice-selective adiabatic refocusing pulses. Magn Reson Mater Phy 2008;21(1-2):95-101.

20. Tannus A, Garwood M. Improved performance of frequency-swept pulses using offset-independent adiabaticity. J Magn Reson Ser A 1996;120(1):133-137.
21. Govindaraju V, Young K, Maudsley AA. Proton NMR chemical shifts and coupling constants for brain metabolites. NMR in Biomed 2000;13(3):129-153.
22. Moore GJ, Sillerud LO. The pH Dependence of Chemical Shift and Spin-Spin Coupling for Citrate. J Magn Reson B 1994;103(1):87-88.
23. Van der Graaf M, Heerschap A. Effect of Cation Binding on the Proton Chemical Shifts and the Spin-Spin Coupling Constant of Citrate. J Magn Reson B 1996;112(1):58-62.
24. Scheenen TWJ, Gambarota G, Weiland E, Klomp DWJ, Fütterer JJ, Barentsz JO, Heerschap A. Optimal timing for in vivo 1H-MR spectroscopic imaging of the human prostate at 3T. Magn Reson Med 2005;53(6):1268-1274.
25. Van der Graaf M, Jager GJ, Heerschap A. Removal of the outer lines of the citrate multiplet in proton magnetic resonance spectra of the prostatic gland by accurate timing of a point- resolved spectroscopy pulse sequence. Magn Reson Mater Phy 1997;5(1):65-69.
26. Scheenen TW, Heijmink SW, Roell SA, Hulsbergen-Van de Kaa CA, Knipscheer BC, Witjes JA, Barentsz JO, Heerschap A. Three-dimensional proton MR spectroscopy of human prostate at 3 T without endorectal coil: feasibility. Radiology 2007;245(2):507-516.
27. Jung JA, Coakley FV, Vigneron DB, Swanson MG, Qayyum A, Weinberg V, Jones KD, Carroll PR, Kurhanewicz J. Prostate depiction at endorectal MR spectroscopic imaging: investigation of a standardized evaluation system. Radiology 2004;233(3):701-708.
28. Fütterer JJ, Scheenen TWJ, Heijmink SWTPJ, Huisman HJ, Hulsbergen-Van De Kaa CA, Witjes JA, Heerschap A, Barentsz JO. Standardized threshold approach using three-dimensional proton magnetic resonance spectroscopic imaging in prostate cancer localization of the entire prostate. Invest Radiol 2007;42(2):116-122.
29. Provencher SW. Estimation of metabolite concentrations from localized in vivo proton NMR spectra. Magn Reson Med 1993;30(6):672-679.
30. Provencher SW. LCModel & LCMgui User's Manual 2009.
31. Bolan PJ, Meisamy S, Baker EH, Lin J, Emory T, Nelson M, Everson LI, Yee D, Garwood M. In vivo quantification of choline compounds in the breast with 1H MR spectroscopy. Magn Reson Med 2003;50(6):1134-1143.
32. Heerschap A, Jager GJ, Van Der Graaf M, Barentsz JO, Ruijs SHJ. Proton MR spectroscopy of the normal human prostate with an endorectal coil and a double spin-echo pulse sequence. Magn Reson Med 1997;37(2):204-213.
33. Sappey-Marinier D, Calabrese G, Hetherington HP, Fisher SNG, Deicken R, Van Dyke C, Fein G, Weiner MW. Proton magnetic resonance spectroscopy of human brain: Applications to normal white matter, chronic infarction, and MRI white matter signal hyperintensities. Magn Reson Med 1992;26(2):313-327.
34. Kreis R, Ernst T, Ross BD. Development of the human brain: In vivo quantification of metabolite and water content with proton magnetic resonance spectroscopy. Magn Reson Med 1993;30(4):424-437.
35. Frahm J, Bruhn H, Gyngell ML, Merboldt KD, Hanicke W, Sauter R. Localized proton NMR spectroscopy in different regions of the human brain in vivo. Relaxation times and concentrations of cerebral metabolites. Magn Reson Med 1989;11(1):47-63.
36. Howe FA, Barton SJ, Cudlip SA and others. Metabolic profiles of human brain tumors using quantitative in vivo 1H magnetic resonance spectroscopy. Magn Reson Med 2003;49(2):223-232.
37. Kuesel AC, Sutherland GR, Halliday W, Smith ICP. 1H MRS of high grade astrocytomas:

Mobile lipid accumulation in necrotic tissue. NMR in Biomed 1994;7(3):149-155.

38. Fajardo DA, Miyamoto H, Miller JS, Lee TK, Epstein JI. Identification of gleason pattern 5 on prostatic needle core biopsy: Frequency of underdiagnosis and relation to morphology. Am J Surg Pathol 2011;35(11):1706-1711.
39. Padhani AR, Liu G, Mu-Koh D and others. Diffusion-weighted magnetic resonance imaging as a cancer biomarker: Consensus and recommendations. Neoplasia 2009;11(2):102-125.
40. Van Asten JJA, Cuijpers V, Hulsbergen-Van De Kaa C, Soede-Huijbregts C, Witjes JA, Verhofstad A, Heerschap A. High resolution magic angle spinning NMR spectroscopy for metabolic assessment of cancer presence and Gleason score in human prostate needle biopsies. Magn Reson Mater Phy 2008;21(6):435-442.
41. Swanson MG, Zektzer AS, Tabatabai ZL and others. Quantitative analysis of prostate metabolites using 1H HR-MAS spectroscopy. Magn Reson Med 2006;55(6):1257-1264.
42. Reinicke K, Sotomayor P, Cisterna P, Delgado C, Nualart F, Godoy A. Cellular distribution of glut-1 and glut-5 in benign and malignant human prostate tissue. J Cell Biochem 2012;113(2):553-562.
43. Albers MJ, Bok R, Chen AP and others. Hyperpolarized 13C lactate, pyruvate, and alanine: Noninvasive biomarkers for prostate cancer detection and grading. Cancer Research 2008;68(20):8607-8615.
44. Nelson SJ, Kurhanewicz J, Vigneron D and others. Proof of Concept Clinical Trial of Hyperpolarized C-13 Pyruvate in Patients with Prostate Cancer. 2012; Melbourne, Australia.
45. Schiebler ML, Miyamoto KK, White M, Maygarden SJ, Mohler JL. In vitro high resolution 1H-spectroscopy of the human prostate: Benign prostatic hyperplasia, normal peripheral zone and adenocarcinoma. Magn Reson Med 1993;29(3):285-291.
46. Hobarth K, Hofbauer J, Fang-Kircher S. Plasma sialic acid in patients with prostate cancer. Brit J Urol 1993;72(5 I):621-624.
47. Lagana A, Pardo-Martinez B, Marino A, Fago G, Bizzarri M. Determination of serum total lipid and free N-acetylneuraminic acid in genitourinary malignancies by fluorimetric high performance liquid chromatography. Relevance of free N-acetylneuraminic acid as tumour marker. Clin Chim Acta 1995;243(2):165-179.

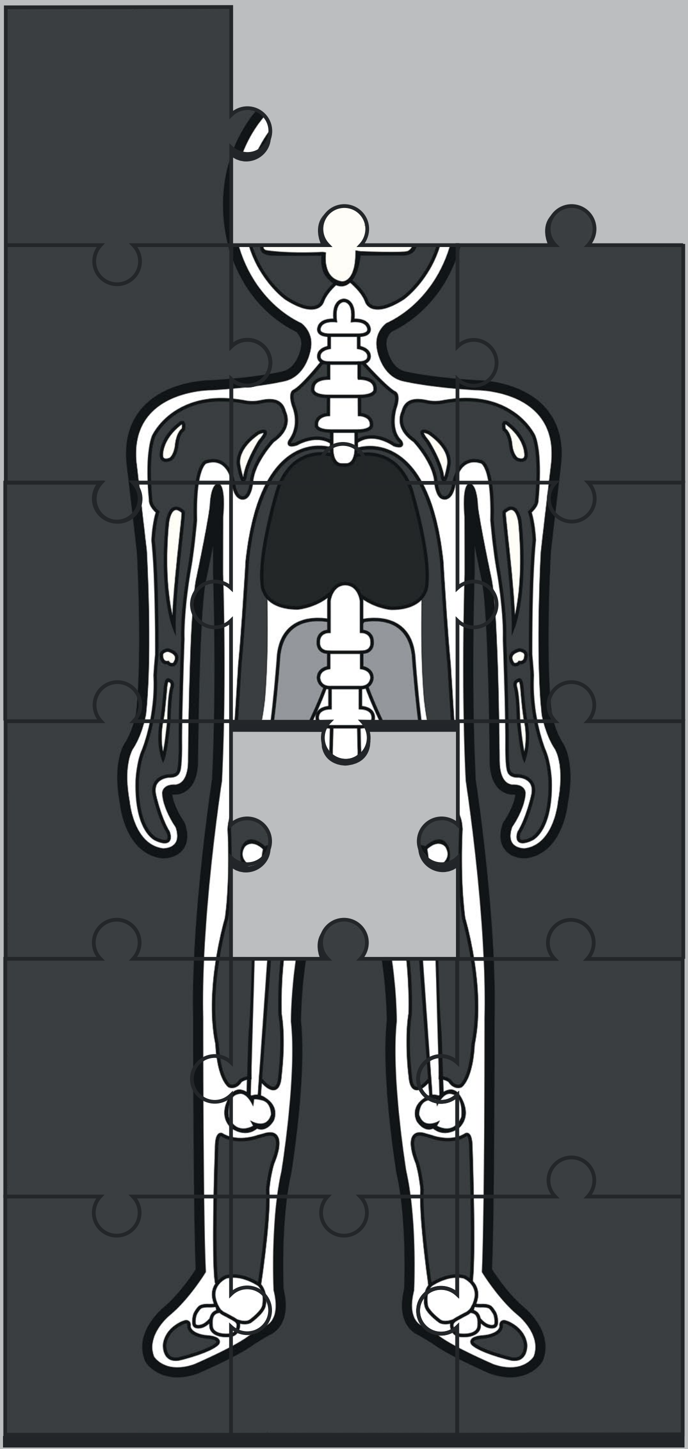

8

CHAPTER EIGHT

In vivo ^{31}P MR Spectroscopic Imaging of the Human Prostate at 7 T: Safety and Feasibility

This chapter is based on the publication:

In vivo ^{31}P MR spectroscopic imaging of the human prostate at 7 T: safety and feasibility
T. Kobus, A.K. Bitz, M.J. van Uden, M.W. Lagemaat, E. Rothgang, S. Orzada, A. Heerschap and T.W.J. Scheenen
Magnetic Resonance in Medicine, 2013, Dec; 68 (6):1683-95

Introduction

Magnetic resonance (MR) is increasingly being used in the diagnosis, localization and staging of prostate cancer. Prostate cancer is characterized by a hypointense signal on T2-weighted images. Unfortunately, more benign pathologies like benign prostatic hyperplasia and prostatitis also show this decreased signal intensity. Higher specificities for detection (1) and localization (2,3) of prostate cancer were obtained when proton MR spectroscopic imaging (^{1}H MRSI) was added to the reading of T2-weighted images. The use of MRSI enables the detection of biochemical changes that are characteristic for certain diseases. ^{1}H MRSI has been used to discriminate noncancer tissue from cancer tissue in the prostate using the choline plus creatine to citrate ratio. In cancer tissue an increase in this ratio is observed compared to normal tissue in single institution studies (4-6) as well as in a multicenter setting (7).

Phosphorus spectroscopy enables detection of metabolites with phosphorus atoms, e.g. phosphocreatine (PCr), inorganic phosphate (Pi), the three phosphate groups of adenosine triphosphate (ATP), phosphomonoesters (PME), and phosphodiesters (PDE). In the early nineties, *in vivo* phosphorus spectroscopy of the human prostate was pioneered with measurements that used an endorectal coil (8-11). Using merely the coil reception profile for localization, differences in the PME to PCr ratio, the PME to β-ATP ratio and PCr to β-ATP ratio were observed between normal and cancer tissue (9,10). These studies were performed on a 2-T system and in 10 to 30 min one spectrum of a volume between 1.5 and 3 cm^3 could be acquired. To obtain information from different parts of the prostate, the endorectal coil was repositioned between different acquisitions (9).

At a magnetic field strength of 7 T, the increased chemical shift difference between signals might enable detection of the individual resonances of PME, i.e. phosphoethanolamine (PE) and phosphocholine (PC), and PDE, i.e. glycerophosphoethanolamine and glycerophosphocholine. Detection of these individual resonances could improve prostate cancer characterization, e.g. in the assessment of aggressiveness. A significant correlation between the Gleason score, the histopathological measure for aggressiveness, and the GPC/PC ratio has been reported in prostate cancer samples (12). The increased magnetic field strength also results in a higher signal-to-noise ratio (13), which makes it possible to perform localized three dimensional (3D) ^{31}P MR spectroscopic imaging at a relevant spatial resolution in a clinically acceptable measurement time with a ^{31}P endorectal loop coil. In order to do so, ^{1}H MR imaging is necessary to relate the metabolic information to anatomy. When obtaining anatomical, T2-weighted images of the abdomen at a field strength of 7 T severe inhomogeneities in the radiofrequency (RF) transmit field need to be overcome. Reaching refocusing flip angles in the center of the body at 7 T requires a significant amount of RF power, whereas the specific absorption rate (SAR) scales approximately with the square of the field strength. So the increased RF power demand and RF transmit inhomogeneity is opposed by restrictions in RF power deposition with SAR limits, requiring the development of new coils and methods that enable a more efficient RF excitation.

Previously, Metzger et al. described a method to image the prostate at 7 T using multi transmit coils and RF shimming (14). The phase of the different coil elements was adjusted to obtain maximal B_1^+ coherence at the location of the prostate. When combining an eight-channel ^1H transmit/receive (TxRx) coil setup with a ^{31}P endorectal TxRx loop coil, RF coupling between the eight-channel coil elements and the ^{31}P endorectal coil needs to be investigated. The RF wavelength of the ^1H frequency in biological tissues at 7 T is ~12 cm. With these wavelengths, the ^{31}P prostate coil and cables might interfere with the eight-channel ^1H coil. This coupling could lead to inhomogeneous flip angle distributions and increased local SAR levels. If coupling exists between the coils or cables, this should be prevented or at least it should be ensured that the SAR stays within safe limits and that the images are not affected by an unpredictable B_1^+ distribution.

In this feasibility study, we dealt with all prerequisites for a setup that combines an eight-channel TxRx ^1H coil with a ^{31}P TxRx endorectal coil to study phosphorus metabolites in the prostate. The safety limits at our institution are based on the International Electrotechnical Commission (IEC) 60601-2-33 (Edition 3.0) safety guidelines (15). These state, as limits for local coils at normal operating level, a maximum time-averaged SAR of 10 W/kg or a maximum local tissue temperature of 39 °C. Since the body temperature of volunteers and patients in general is not measured before an MR exam, an input power leading to a maximum local increase of 1 °C was used in this study as a safety limit. To assess compliance with these limits, Finite Integration Technique (FIT) simulations of both coils as well as their combination were performed to study the RF, SAR and temperature distribution. From the simulations the locations of the highest SAR deposition and temperature increase could be obtained and these were validated by phantom measurements providing B_1^+ and temperature maps. Finally, *in vivo* temperature measurements were performed, by placing temperature probes on the ^{31}P endorectal coil at the positions with the highest determined power losses. From the simulations, phantom studies and *in vivo* measurements, the maximum input power to comply with the safety guidelines for transmitting with the ^{31}P endorectal coil and eight-channel ^1H array coil could be derived. *In vivo* measurements in compliance with the safety limits were performed using adiabatic excitation and phosphorus spectra were obtained from the entire prostate and surrounding tissue with high spatial resolution (4 cm^3) in a single measurement.

Methods

Hardware

^{31}P TxRx endorectal coil and interface

The mechanical housing and conductors of an inflatable ^{1}H receive endorectal coil for use at 3 T (Medrad, Pittsburgh, PA, USA) was used for the design of the ^{31}P TxRx endorectal coil. The coil was tuned and matched to 50 Ω at 120.3 MHz using small ceramic capacitors (American Technical Ceramics, Huntington Station, NY, USA) capable of handling a voltage up to 500 V. The tuning and matching can, to some extent, be adapted by inflating or deflating the balloon of the endorectal coil. A coaxial cable connected the RF-coil to a home-built TxRx switch with an integrated small band low noise preamplifier (Advanced Receiver Research, Burlington, CT, USA). The TxRx switch was used to interface the coil to a 7-T whole-body MR system (Magnetom, Siemens Healthcare, Erlangen, Germany). Figure 8.1A shows the electronics circuit of the ^{31}P RF-coil.

The forward and reflected power in the ^{31}P transmit channel are monitored by the RF supervision provided by the manufacturer of the MR system. To determine the reference voltage of the coil, the endorectal coil was placed on a phantom containing Pi. A ^{31}P MRSI pulse-acquire sequence with a 1-ms block pulse was played out at different power levels to estimate the reference power for a flip angle of 180° (γB_1 = 500 Hz) at a distance of 2.5 cm of the center of the coil, which is the distance between the coil and the center of the prostate *in vivo*. The resulting spectra were analyzed for a dip in the intensity of Pi at this distance.

Eight-channel ^{1}H TxRx array coil

The eight-channel ^{1}H TxRx coil for imaging (16) consists of two arrays with four microstrip line elements, each with meanders (17). Each element has a length of 25 cm, a width of 10 cm and a thickness of 2 cm. The arrays are placed dorsally and ventrally to the body. The elements of the dorsal array are arranged on a planar sliding frame inside a polymethylmethacrylate housing. The sliding frame is used to place the array at the desired position along the longitudinal axis of the patient. Including a thin cushion for patient comfort, the distance from the elements to the body surface is 25 mm. The elements of the ventral array are enclosed in individual modules made of polycarbonate. The modules are interconnected with a neoprene sheet making the ventral array flexible so that it can be accommodated to the patient's contour. The distance between the elements and the body is 30 mm, as determined by the module dimensions. Low input impedance preamplifiers and TxRx switches are placed in a separate multipurpose box at the head of the patient table, and the cable length was chosen accordingly to achieve preamp decoupling during reception.

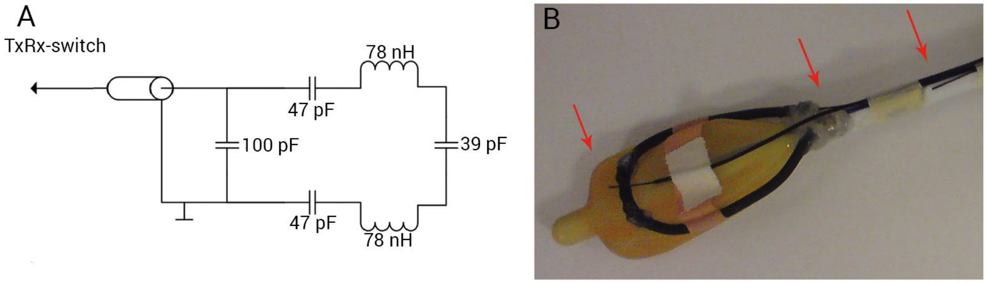

Figure 8.1. *A) Schematics of the electronic circuit of the ^{31}P TxRx endorectal coil. B) The ^{31}P TxRx endorectal coil without the outer balloon. The arrows indicate the location of the three fiber optic temperature sensors at the top of the coil, feed point and coil wire to study the temperature increase in the phantom study. The coil loop has a length of 7.0 cm and a width of 3.7 cm.*

RF shimming system

^{1}H MR imaging was performed with an add-on system for RF shimming (18) which was integrated into the 7-T MR system and the flexible eight-channel array coil. The RF amplifier of the standard system consists of eight individual modules providing a maximum peak power of 1 kW each (LPPA 13080W, Dressler, Germany) with which the eight-channel RF shimming setup was realized. Computer-controlled attenuators and phase shifters were inserted into the low-power RF chain directly at the input ports of the amplifier. The eight-channel mode is activated by coaxial relays (CX600N, Tohtsu, Japan) connected to the output ports of the RF amplifiers which bypass the power combiner and power monitor of the standard system and make the eight individual channels available at the patient table.

Unlike the ^{31}P transmit channel, the monitoring of the eight ^{1}H transmit channels cannot be performed by the single channel manufacturer's supervision system. Therefore, a custom-built on-line RF supervision was realized by the use of three logarithmic root-mean-square power meters (TALES, Siemens Healthcare, Erlangen, Germany) which monitor forward and reflected power in the eight transmit channels via directional couplers (19). A real-time field programmable gate array (NI PXI 7852 R, National Instruments, Austin, TX, USA) with corresponding software performed time-averaging of the transmitted RF power over intervals of 10 s and 6 min according to the IEC safety guidelines (15). The correlation between transmit power and localized SAR was determined by RF simulations which are described below. If the maximum permissible input power was exceeded, the software immediately blanked the RF power by emergency relays located in the vector modulator circuit. The monitoring software further included test loops for malfunction detection of the attenuators and phase shifters, and thus correct adjustment of the target RF shim was checked.

In vivo B_1^+ mapping was performed with a protocol based on a presaturation single-shot turboFLASH sequence provided by the vendor of the MR system (20). Relative B_1^+ magnitude

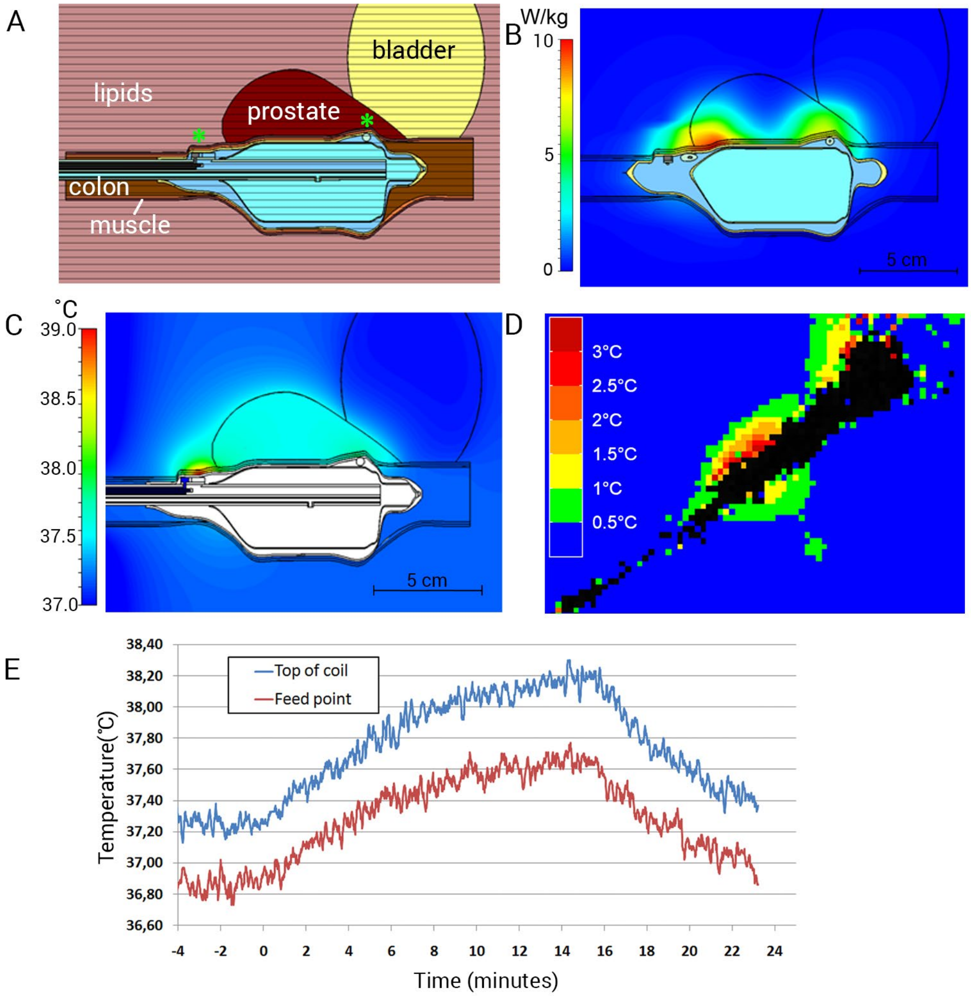

Figure 8.2. *Safety validation of the ^{31}P endorectal coil. A) FIT simulation model of the endorectal ^{31}P coil, rectum, bladder and prostate. Not shown are two muscles each lateral of the prostate B) Calculated SAR$_{10g}$ using the model in A at an RF input power of the ^{31}P endorectal coil of 0.95W leading to a maximum 10 W/kg assuming a worst case approximation of close contact of tissue and RF-feed without any gap. C) Transient thermal simulations after a scan duration of 15 min at a time-averaged input power of 1.3 W leading to a maximum temper ature of 39°C. D) Image of the temperature increase measured by MR-thermometry after 2 min of 9.1 W of time-averaged input power with the ^{31}P endorectal coil in a phantom. The endorectal coil is rotated 45° counterclockwise in plane compared to the orientation in A-C. E) The temperature measured in vivo with fiber optic temperature sensors at the top of the coil and at the feed point during a 15 min ^{31}P MR spectroscopy measurement with the endorectal coil at an input power of 1.9 W. The temperature offset of the two sensors is due to small calibration differences. The location of the fiber optic sensors is shown in A with 2 green asterisks (left: feed point, right: top of the coil).*

and relative phase maps of a single slice were acquired *in vivo* by low flip angle (estimated below 10°) imaging with an echo time (TE) of 5 ms and a repetition time (TR) of 1 s from each coil without presaturation (field of view (FOV) 300x300 mm, in plane resolution 4.7 x 4.7 mm, slice thickness 8 mm). The total acquisition time was 8 s. For the phase maps, the first channel was taken as reference. Thus, the argument of the complex signal ratio between an individual channel and the first channel gives the relative phase. To obtain relative B_1^+ magnitude maps, the individual maps are normalized to the square root of the sum of squares of all individual maps. The relative B_1^+ maps were imported into a graphical user interface which allows the selection of a region of interest (ROI) in the prostate. A RF shimming algorithm was applied which maximizes the magnitude of the B_1^+ distribution inside the ROI by optimizing the transmit phase of the channels while maintaining equal amplitudes. After the desired shim is determined, the vector modulators are automatically programmed with the corresponding phase settings by the control computer. The whole RF shimming procedure including data acquisition, ROI selection, and calculation of the optimal phases takes ~3 min. The flip angle map of the prostate-optimized RF shim was obtained by two images acquired with and without a saturation pulse before the turboFLASH sequence. The cosine of the flip angle produced by the saturation pulse can be approximated by the signal ratio of the pre-saturated image and the reference image without saturation with the same TE, TR, acquisition time, FOV and resolution as for the relative maps. The flip angle map of the prostate-optimized RF shim was used for transmitter adjustment.

Safety of the coil setups

Safety validation of the ^{31}P endorectal coil

FIT simulations, phantom studies and *in vivo* measurements were performed to test the safety of the use of the ^{31}P endorectal coil. Numerical computations (CST Studio Suite 2011, Darmstadt, Germany) of the RF field distribution and the corresponding SAR produced by the ^{31}P endorectal coil were performed according to previously presented safety tests for a ^{1}H TxRx endorectal coil (21,22). For the simulation, a detailed computer-aided design model of the coil and the surrounding tissues (prostate, bladder, muscles and lipids) was derived (Figure 8.2A). The dimensions of the prostate were determined from high-resolution MR images of the human prostate obtained at 3T. Permittivity and electric conductivity of the tissues at 120.3 MHz were taken from literature (23) and the transverse electromagnetic wave of the coaxial cable was used for RF field excitation at the connector of the cable. The feed point of the loop coil consisting of a small printed circuit board with three capacitors and the connections to the inner and outer conductor of the coaxial cable was modeled as exactly as possible, because it is expected that a high local SAR will be generated in the region of the feed point. With the simulation, we determined the maximum input power to comply with the maximum 10g-averaged SAR (SAR_{10g}) of 10W/kg. The input power is defined in this study as the difference between forward and reflected power at the table plug. As the simulations provide the input power at the excitation port of the model, we assumed a loss of 1 dB between the table plug to the connecter at the cable of the coil in the simulations to be able to compare results.

To validate that the SAR_{10g} does not underestimate the RF exposure, transient thermal simulations were also performed. For this, the well-known bioheat-transfer equation by Pennes (24), implemented in the simulation software, was utilized. The thermal parameters (heat capacity, thermal conductivity, metabolism, blood perfusion) of the tissues in the model were taken from parameter sets provided with available heterogeneous body models (25). The heat source for the temperature simulation is given by the power losses in the tissue calculated previously in the RF field simulation. By use of the simulation the time-averaged input power was determined at which a maximum local temperature of 39°C, specified in the guidelines, was reached after a scan duration of 15 min.

The location of the highest power deposition obtained by the RF simulations was verified in a phantom by MR temperature mapping. A phantom was used as *in vivo* MR temperature mapping is difficult to perform in the pelvis. A gel phantom was designed with approximately the same dielectric properties as abdominal human tissue (23). A 2% cellulose phantom gel was made using a mixture of isopropanol (52%) and water (48%) (26). Before dissolving the cellulose, the liquid mixture was buffered with Na_2HPO_4 and NaH_2PO_4 to pH=7. Sodium chloride (335mM) was added to obtain a representative conductivity, taking into account the decreasing effect on the conductivity of cellulose and a phantom temperature of 5°C for a high viscosity of the gel (27). The phantom had the following dimensions: 22.5 x 15 x 11.5 cm. The relative permittivity and conductivity of the phantom were measured and were 45 and 0.8 S/m respectively. The ^{31}P endorectal coil was placed in the phantom and the eight-channel array coil was positioned around it. RF shimming was performed to minimize the effect of B_1 inhomogeneities on the temperature measurements.

To measure the temperature increase with MR thermometry, phase images, acquired with a standard gradient echo sequence, were obtained with the eight-channel array coil before and after transmitting excessive RF power at 120.3 MHz for 2 min with the ^{31}P endorectal coil. Due to the limited sensitivity of the MR thermometry method an arbitrary high time-averaged input power of 9.1 W was used to acquire adequate phase images. Using the phase images, the temperature change in three slices of 2 mm perpendicular to the coil was calculated (28). The center slice was placed through the feeding point and top of the coil, at the location with the highest predicted SAR deposition according to the simulations. A TE of 17 ms was used and the in-plane resolution was 2 x 2 mm. For MR temperature map validation, three fiber optic temperature sensors of the Luxtron FOT Lab Kit (LumaSense Technologies, Santa Clara, CA, USA) were fixed on the ^{31}P endorectal coil. The sensors were placed close to the feed point, the top of the coil, and on the coil wire as indicated in Figure 8.1B, measuring the temperature before, during and after RF transmission.

The fiber optic temperature sensors were also used for *in vivo* temperature measurements at the previously determined locations of the highest temperature increase. Thus, the influence of the active thermal regulatory system (e.g. increasing blood perfusion with temperature) on the RF induced temperature elevation could be taken into account. The thermal regulatory system cannot be modeled by simulation. The outer balloon with two temperature sensors was enveloped in a thin condom. It was expected that the insulating effects of the thin latex layer were minimal, and therefore, these were neglected. Next, measurements with increasing power settings were performed to determine the input power that resulted in maximal 1˚C temperature increase during a 15-min ^{31}P MRSI measurement. This limit was chosen in order to assure that a maximum absolute temperature of 39°C is not exceeded *in vivo*, independent of the state of health of the individual volunteer.

Safety validation of the combined setup of the ^{31}P endorectal coil and eight-channel ^{1}H array coil

The coupling of the eight-channel ^{1}H array coil with the ^{31}P endorectal coil was assessed by simulations and verified in phantom measurements. The simulations were performed with a heterogeneous body model of a 70-kg male (25) in which the prostate, rectum, muscles, fat, and bones of the lower abdomen were modeled with a spatial resolution of 2 mm. The simulations were performed with and without the previously described model of the endorectal coil at a realistic position aligned to the prostate in the heterogeneous body model. For the eight-channel array coil, a computer-aided design-based model was derived from the exact geometries of the implemented coil design. Further, the MR environment with gradient shield, bore cover, and patient table was considered in the model. Dielectric losses from all materials were taken into account. Using a network cosimulation the matching and tuning network, the feed cables, as well as the balanced-unbalanced transformer realized by a coax cable of a half wavelength, inserted at the feed point of every coil element, were considered including losses in the network components. At both transmit frequencies, 120.3 MHz for the ^{31}P endorectal coil and 297.2 MHz for the eight-channel ^{1}H array coil, the coupling of the coil ports was monitored and a possible perturbation of the transmit fields due to the presence of the coil for the other nucleus was analyzed. Furthermore, it was evaluated whether relevant elevations of the local B_1^+ field and SAR distribution generated by the eight-channel array coil occurred close to the ^{31}P endorectal coil which would indicate RF coupling between the different coils. For the calculation of the power-loss density produced by the ^{1}H array coil inside the body the phase settings for the applied RF shim in the volunteer were used and the corresponding SAR could be evaluated. Here, the RF shim for the healthy volunteer enrolled in the *in vivo* ^{31}P MRSI measurement was utilized. The volunteer's body physique agreed well with the body model. The SAR findings were additionally confirmed by transient thermal simulations in the human body model.

The ^{31}P endorectal coil was placed in the above-mentioned gel phantom. On both sides of the phantom, a bottle with the same conductivity and relative permittivity was placed to approximate the loading of a human body in the eight-channel array coil, which was placed around the three phantoms. Using the eight-channel array coil B_0 and RF shimming of a prostate-sized volume in the phantom gel were performed. Next, a B_1^+ map was acquired using an Actual Flip Angle Imaging sequence (29,30). This gradient echo sequence makes use of two TRs (20 and 100 ms) and one TE of 2.04 ms and produces a 3D B_1^+ map of the transmitted RF power in the phantom. The resolution was 5 x 3 x 3 mm. Since the B_1^+ map does not provide information about the electric fields, which can induce heating of the patient, the spatial distribution of the local temperature increase was measured as well. To

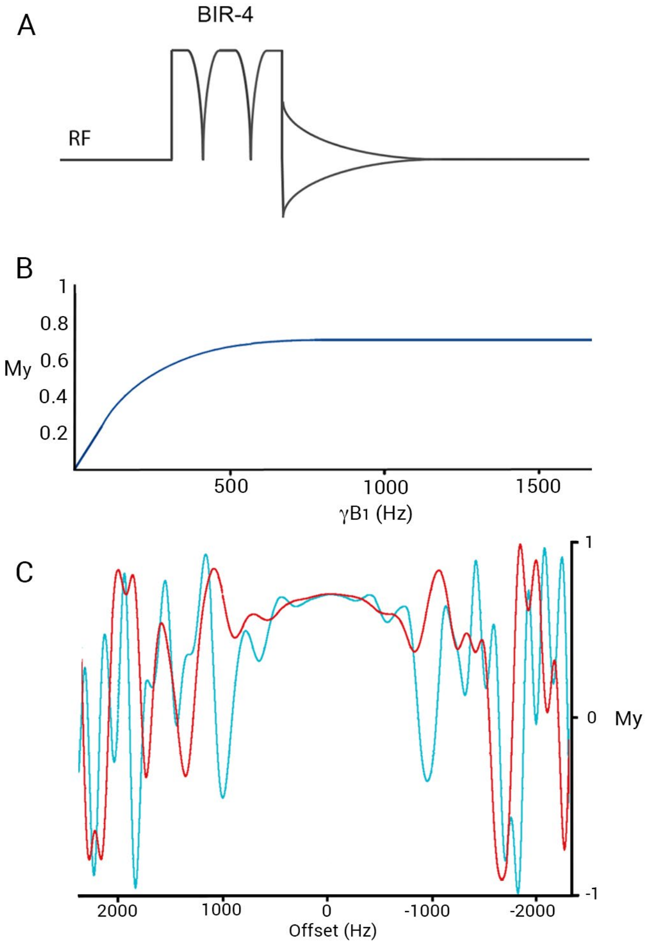

Figure 8.2. *A) Pulse acquire sequence with a BIR-4 pulse for excitation of the free induction decay. A delay of 0.42 ms between the end of the BIR-4 pulse and start of data acquisition accommodates phase encode gradients in three directions (not shown) B) The RF field profile illustrates that the adiabatic condition is met at a* γB_1 *of 700 Hz and higher. The on-resonance transverse magnetization is 0.71, corresponding to a flip angle of 45°. C) Excitation profile at a* γB_1 *of 933 Hz (red) and 700 Hz (blue) resulting in an excitation bandwidth of approximately 1.5 kHz and 1 kHz respectively.*

this end, a relatively high time-averaged RF power of 58 W (intentionally inducing heating in the phantom) was transmitted with the eight-channel array coil for 2 min. Temperature difference maps were calculated as described in the previous section. The temperature was simultaneously measured with the fiber optic temperature sensors (Figure 8.1B).

Measurement protocol

^{31}P RF excitation pulse

For 3D ^{31}P MRSI, a pulse-acquire sequence was used with an 8 ms adiabatic excitation BIR-4 pulse with a flip angle of 45° (Figure 8.2A). The phase roll, induced by the small delay (0.42 ms) between excitation and start of signal reception to accommodate the phase encode gradients, was removed by 1st order phase correction. The adiabatic condition and bandwidth of the RF pulse (Figure 8.2B,C) were calculated using the Bloch equations in NMRSIMTM (part of Topspin, Bruker BioSpin Corporation, Billerica, MA, USA).

In vivo ^{31}P MRSI measurement

The institutional review board gave approval to perform the *in vivo* measurements on a volunteer and signed informed consent was obtained. The ^{31}P endorectal coil was positioned close to the prostate in the rectum of a healthy volunteer. To inflate the inner balloon of the coil, inert perfluoro-polyether liquid (Fomblin, Solvay Solexis, Bollate, Italy) was used. The use of perfluoro-polyether minimizes susceptibility differences between the endorectal coil and the tissue, which is a prerequisite for adequate B_0 shimming. The volunteer was placed in supine position on the dorsal array of the eight-channel array coil. The ventral array was fixed over the lower abdomen. To check the matching and loading of the ^{31}P coil and the individual elements of the ^{1}H array coil, power reflection measurements (S_{11}) were performed. The coupling between the coils was assessed by determining the decoupling between the endorectal coil and each element of the array coil at the frequencies of 120.25 and 297.05 MHz. An intramuscular injection of Butylscopolaminebromide (Buscopan, Boehringer-Ingelheim, Ingelheim, Germany) was used to suppress peristalsis.

Fast gradient echo MR sequences were used to check the position of both the ^{31}P endorectal coil and the eight-channel array coil. RF shimming was performed to obtain maximal B_1^+ coherence at the position of the prostate. For anatomical information, six transversal T2-weighted images of the prostate were acquired using a TE of 71 ms and a TR of 3 s. 3D phasemap shimming was applied to optimize the B_0 homogeneity at the prostate's position. For ^{31}P MRSI, the full FOV of the endorectal coil was spatially encoded (FOV 100 x 100 x 100 mm, matrix of 8 x 8 x 8, 15 averages). The acquisition bandwidth was set to 5000 Hz. The nominal voxel size was 12.5 x 12.5 x 12.5 mm, which resulted in an effective voxel volume of 5.8 cm^3 after apodization of the k-space weighted sampling (TR 1.5 s, acquisition time 11 min). In a second measurement, the nominal voxel size was decreased to 11 x 11 x 11 mm (FOV 110 x 110 x 110 mm, matrix of 10 x 10 x 10, 10 averages), representing an effective voxel volume of 4.0 cm^3 (acquisition time 18 min).

With the combination of a TR of 1.5 s and an excitation angle of 45° we expected limited saturation of the phosphorus metabolites, as estimated T1 relaxation times at 2 T ranged from 1.1s (PCr) to 2.6 s (PME) (9), which are not reported to increase when moving to 7 T (no clear field strength dependence has been established (31)).

Results

When validating compliance of a coil setup with either SAR guidelines or temperature limits with different models and measurements, quite a few different input powers need to be reported in this section. Therefore, an overview of the different input powers for three coil setups is given in Table 8.1 along with a short reason why this input power is reported later.

Coil setup:	*Input power*	*- Reason* *- Method*
^{31}P TxRx endorectal coil	*0.95 W*	*- Power leading to a maximum 10g averaged SAR of 10W/kg* *- Derived from RF (SAR) simulations*
	1.3 W	*- Power leading to a maximum local temperature of 39˚C* *- Derived from thermal simulations*
	9.1 W	*- Arbitrary high power for sufficient temperature increase* *- Phantom temperature mapping for SAR simulation validation*
	1.9 W	*- Power leading to a temperature increase in vivo of 1˚C* *- In vivo measurement with temperature probes*
^{1}H TxRx 8-channel array coil	*33W*	*- Power leading to a maximum 10g averaged SAR of 10W/kg* *- Derived from RF (SAR) simulations*
Combined ^{31}P TxRx endorectal coil and ^{1}H TxRx 8-channel array coil	*33W*	*- Power leading to a maximum 10g averaged SAR of 10W/kg* *- Derived from RF (SAR) simulations*
	58 W	*- Arbitrary high power for sufficient temperature increase* *- Phantom temperature mapping for SAR simulation validation*

Table 8.1. The different input powers for the three coil setups and the reason for their use.

^{31}P endorectal coil and eight-channel ^{1}H array coil

The reflection coefficient (S_{11}) of the ^{31}P TxRx endorectal coil was -9 dB during use in the phantom and -16 dB during *in vivo* use at the ^{31}P operating frequency of 120.25 MHz. The unloaded Q-factor of the endorectal coil was 316 and the loaded Q-factor during *in vivo* use was 34. The reference voltage of the ^{31}P coil at a distance of 2.5 cm of the center of the coil to attain γB_1 = 500 Hz (29 μT) was 75V. The average S_{11} of the eight elements of the eight-channel array coil was -14.8 dB (range -9 to -22 dB).

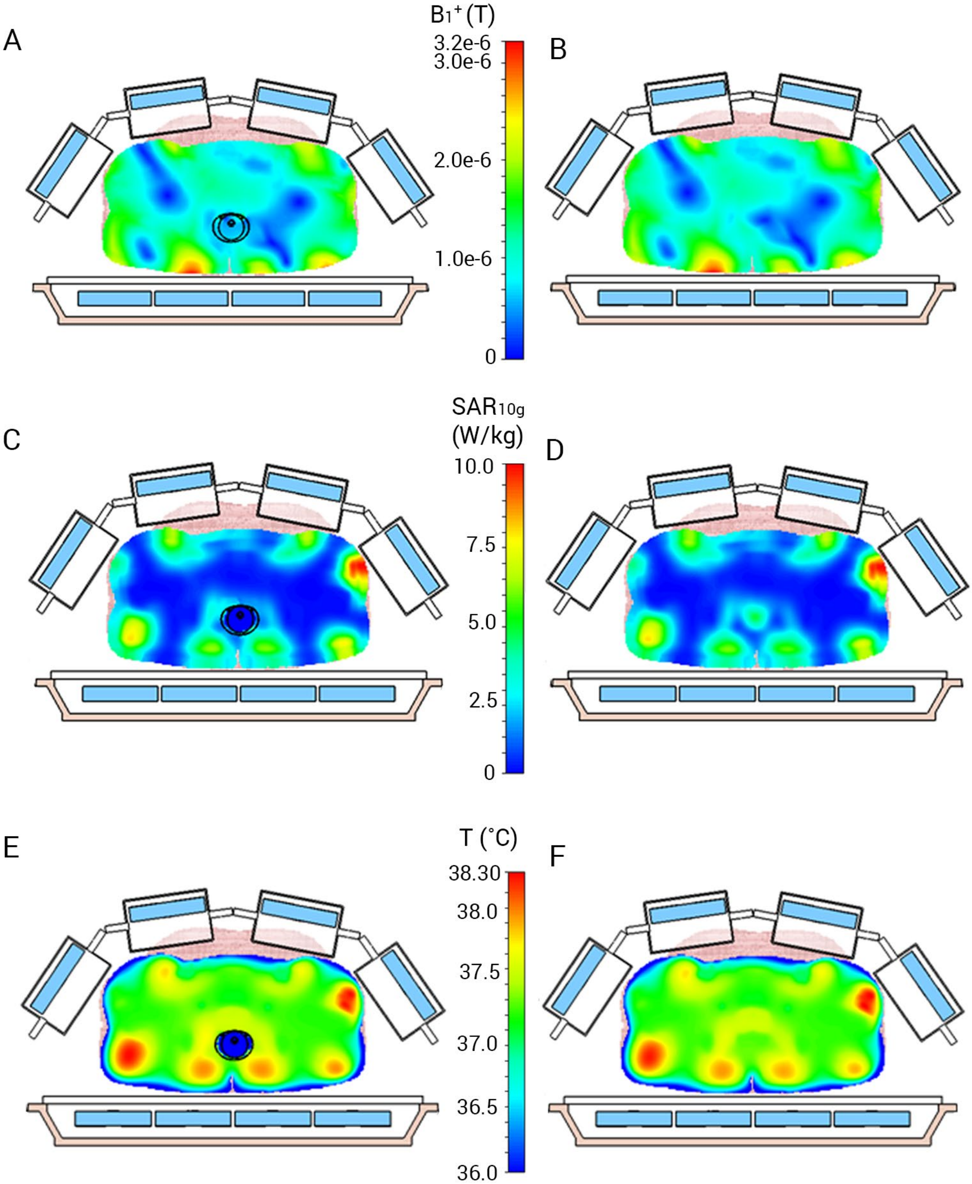

Figure 8.4. *FIT simulations of the lower abdomen surrounded by the eight elements of the ^{1}H array coil. For the simulations a RF shim maximizing the B_1^+ coherence in the prostate is used. A) B_1^+ distribution at an input power of 33 W of the ^{1}H array coil with the endorectal coil present. B) B_1^+ distribution as in A but without the endorectal coil. C) SAR_{10g} distribution at an input power of 33 W of the ^{1}H array coil with the endorectal coil present. D) SAR_{10g} as in C but without the endorectal coil. E) Temperature distribution after a scan duration of 15 min at a time-averaged input power of 33 W of the ^{1}H array coil with the endorectal coil present. F) Temperature distribution as in E but without the endorectal coil. The location of the prostate is just above the endorectal coil.*

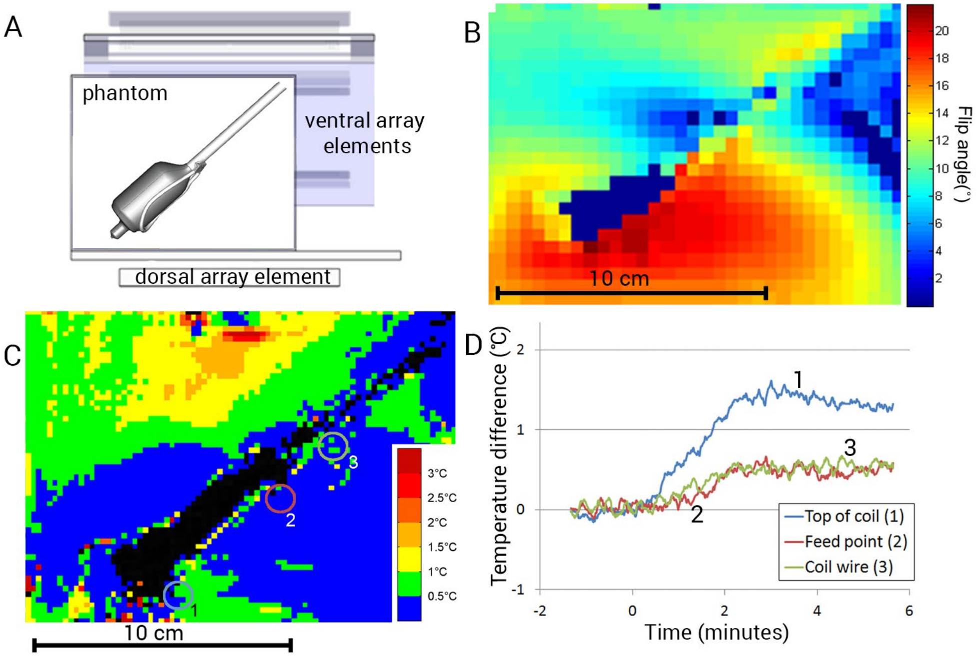

Figure 8.5. *Phantom study to investigate the presence of coupling between ^{31}P endorectal coil and eight-channel ^{1}H array coil. A) Sagittal 3D orientation of the coils and the phantom. The 2D planes in B and C are of this sagittal plane. B) Absolute B_1^+ map using the eight-channel array coil showing the flip angle distribution. RF shimming was used to obtain maximal B_1^+ coherence in the area representing the location of the prostate, below the endorectal coil-loop. C) Temperature map after 2 min of RF power transmission of 58 W with the eight-channel array coil. D) The temperature increase measured with the fiber optic temperature sensors placed at the top of the coil (1 in C), feed point (2 in C) and coil wire (3 in C).*

Safety validation of the ^{31}P endorectal coil

The RF simulations showed that a time-averaged input power of 0.95 W led to a maximum SAR_{10g} of 10 W/kg (Figure 8.3B, Table 8.1). The transient thermal simulations showed that a time-averaged input power of 1.3 W led to a maximum local temperature of 39°C after a scan duration of 15 min (Figure 8.3C, E). The calculated S_{11} in the model was -8.7 dB at the frequency of 120.3 MHz.

Figure 8.3D illustrates the temperature increase in the phantom after 2 min exposure to 9.1 W time-averaged input power with the ^{31}P endorectal coil. There was good agreement between the SAR profile of the simulations (Figure 8.3B) and the temperature profile around the coil loop (Figure 8.3D). A maximum temperature increase of 3˚C was observed near the top and feed point of the coil.

In the *in vivo* temperature measurements, a time-averaged input power of 1.9 W for the duration of 15 min resulted in a temperature increase of just below 1°C, well below the IEC limit of 39°C during the entire examination (Figure 8.3E).

Safety validation of the combined setup of the ^{31}P endorectal coil and eight-channel ^{1}H array coil

The FIT simulations predicted that both coils at both operating frequencies were well decoupled by at least -50 dB. The influence of the endorectal coil on the B_1^+ distribution of the eight-channel array coil was negligible (Figure 8.4A,B). Furthermore, the simulation showed that the RF shim concentrated the B_1^+ in the region of the prostate. The highest SAR was located close to the individual elements, and the maximum $SAR_{10g,}$ using *in vivo* prostate RF shim settings, was close to the upper left coil element of the ^{1}H array coil (Figure 8.4C,D). The maximum permissible time-averaged input power of the eight-channel array coil at which the safety limit for the localized SAR_{10g} of 10 W/kg was not exceeded was 33W (Figure 8.4C,D). There was no relevant SAR elevation close to the endorectal coil, which indicates that the combination of both coils could be operated under safe conditions. This was further supported by the temperature simulations (Figure 8.4E,F), which also showed no difference in temperature distribution with and without the endorectal coil after a 15-min experiment for an input power of 33 W.

The absolute B_1^+ map (Figure 8.5B) showed the flip angle distribution over the phantom. The RF shimming method worked well and resulted in maximized B_1^+ at the desired location (Figure 8.5B). No B_1^+ elevation was visible near the coil wire. The MR temperature map after 2 min of excessive RF power transmission of 58W with the eight-channel ^{1}H array coil showed an increase at the top and bottom of the phantom, near the elements of the eight-channel coil but not close to the endorectal coil-loop or the coil-wire (Figure 8.5C). The temperature increase measured with the fiber optic temperature sensors was 1.3, 0.5 and 0.5°C at the top, feed point and wire of the endorectal coil, respectively (Figure 8.5D). The sensor at the top of the coil was closest to the dorsal elements of the ^{1}H array coil.

The decoupling between the ^{31}P endorectal coil and each individual element of the 8-channel ^{1}H array coil during *in vivo* use was on average -71 dB (range -60 to -80 dB) at 120.25 MHz and -70 dB (range -64 to -80 dB) at 297.05 MHz, demonstrating excellent decoupling.

RF shimming

We reconstructed relative maps of the B_1^+ magnitude for the individual transmit channels of the eight-channel array coil with the endorectal coil inserted into the rectum (Figure 8.6A). Though all elements contributed to the central region where the prostate was located, the individual maps were well separated in the outer region. No significant B_1^+ distortions due the ^{31}P endorectal coil located in the rectum were visible. RF shimming resulted in quite a homogeneous flip angle distribution for the optimized RF shim (Figure 8.6B). The achieved standard deviation of the flip angle inside the prostate was +/- 10 %.

^{31}P RF excitation pulse

The calculations from the Bloch equations showed that the adiabatic condition for the BIR-4 pulse of 8ms was met at a γB_1 of 700 Hz and higher (Figure 8.2B). The larger γB_1, the larger the excitation bandwidth (Figure 8.2C). The maximum permissible time-averaged power of 1.9W was reached with the 8 ms pulse with a γB_1 of 933 Hz at 2.5 cm of the coil at a TR of 1.5 s, resulting in a homogeneous excitation bandwidth of 1.5 kHz or more within 2.5 cm of the coil conductors (Figure 8.2C). This led to an excitation range of 12 ppm at the ^{31}P frequency at 7 T, indicating good excitation in the posterior and middle part of the prostate. The excitation bandwidth in the anterior part was less. The *in vivo* ^{31}P MRSI experiments were performed with these experimental settings.

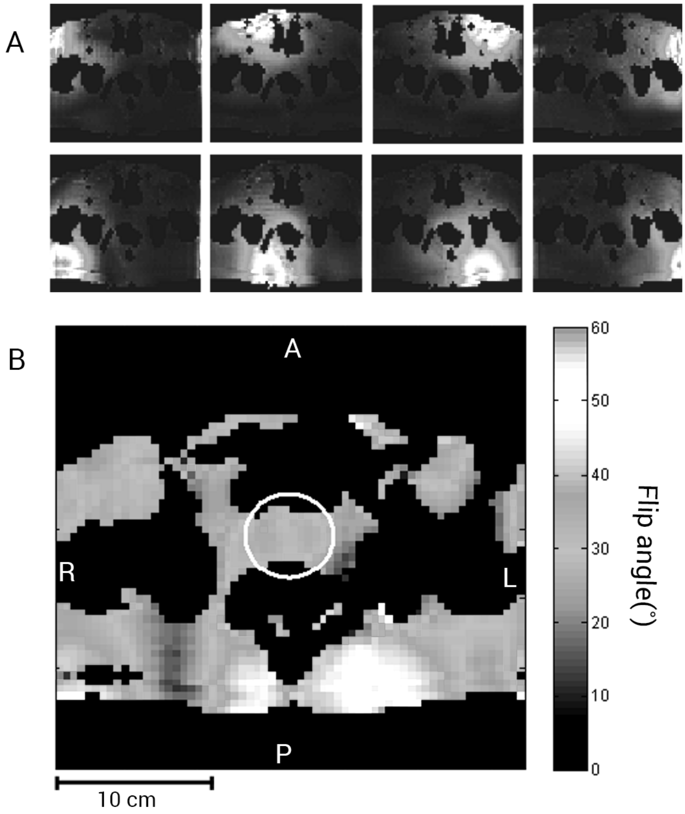

Figure 8.6. A) In vivo relative maps of the B_1^+ magnitude for the individual transmit channels of the array coil with the endorectal coil inserted into the rectum. B) Flip angle distribution for the optimized phase setting of the array coil. Transmit phases were adjusted in order to obtain maximum B_1^+ inside the prostate (ROI: white circle). The achieved standard deviation of the flip angle inside the ROI is +/- 10 %.

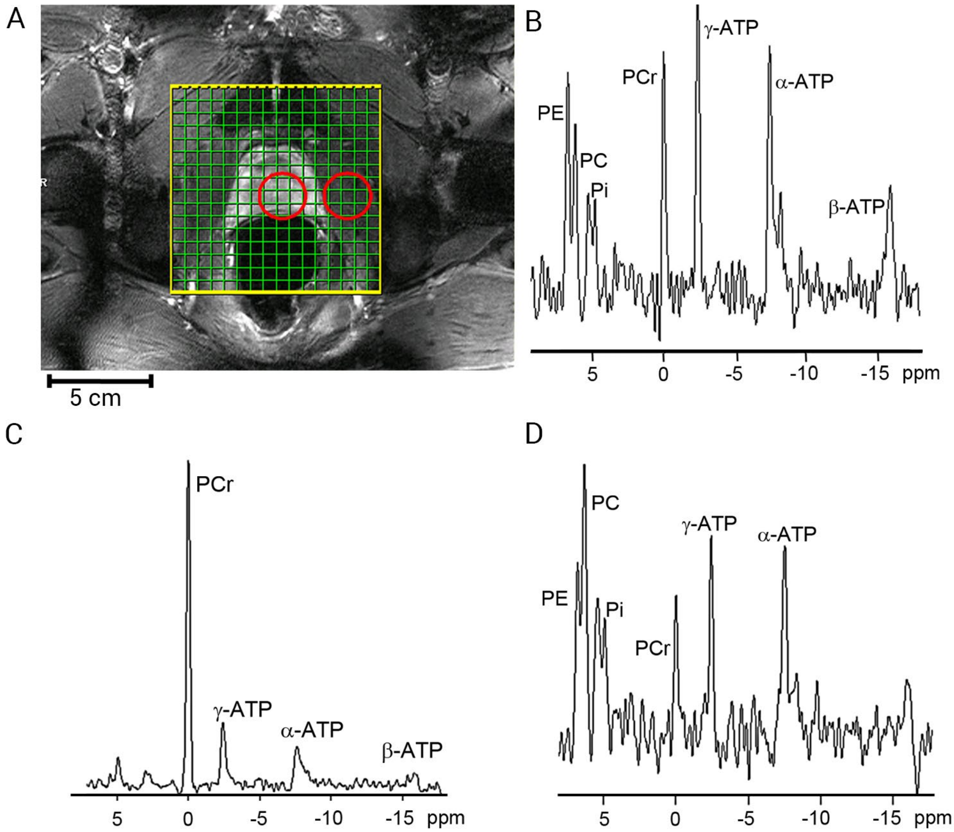

Figure 8.7. *In vivo ^{31}P MRSI of the prostate at 7T. A) T2-weighted image of the prostate with one slice of the 3D ^{31}P MR spectroscopy grid. The ^{31}P spectra of 5.8 cm^3 voxels of the prostate (B), muscle (C) and seminal vesicles (D) contain the following metabolites: phoshocreatine (PCr), inorganic phosphate (Pi), adenosine triphosphate (ATP), phosphoetanolamine (PE) and phosphocholine (PC). The red circles represent the perimeter at 64% of the maximum signal intensity of the spatial response function: best approximation of the true voxel size.*

In vivo measurement

Using the RF shimming algorithm, good image quality in the base, middle and apex of the prostate was obtained. B_0 shimming of a ROI over the whole prostate resulted in a water line-width at half maximum of 50 Hz (magnitude). The 3D ^{31}P MRSI grid was aligned using fast gradient echo and T2-weighted images (Figure 8.7A). In the prostate, the resonances of PC, PE, Pi, PCr and γ-, α- and β-ATP were detectable (Figure 8.7B). The intensity of β-ATP was attenuated due to the limited bandwidth of the BIR-4 pulse. From the seminal vesicles, which are at larger distance from the center of the coil, good quality spectra were obtained showing an increase in the PC signal (Figure 8.7D & 8.8B). In the surrounding muscles, a high PCr intensity compared to γ- and α-ATP was observed, while in the prostate the intensity of

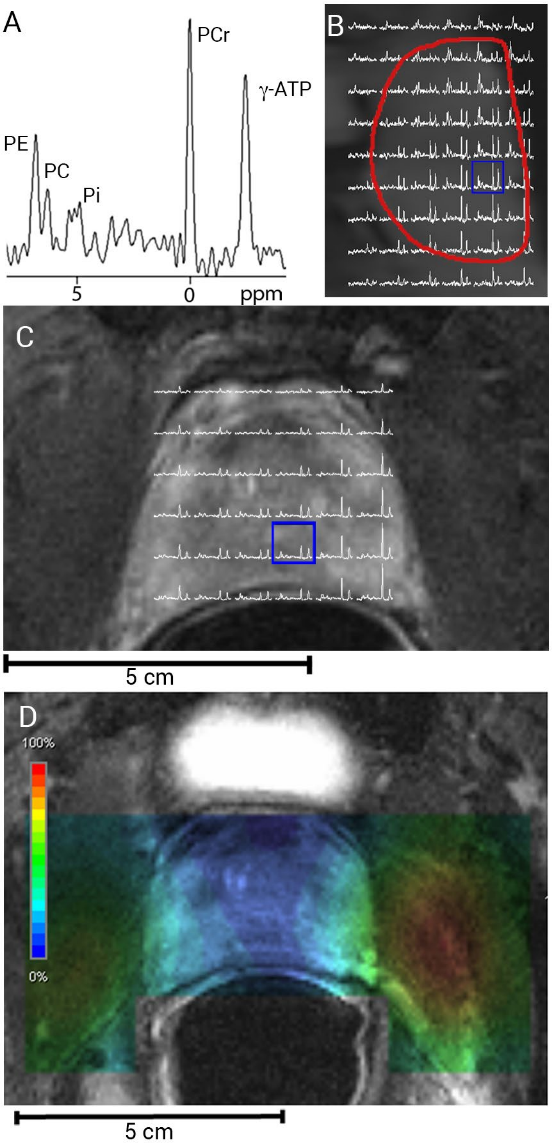

Figure 8.8. *Spatial maps of the ^{31}P spectra (voxels 5.8 cm^3). A) The enlarged spectrum demonstrates the frequency range of the spectra in the transverse (C) and saggital (B) planes. The shown metabolites are phosphoethanolamine (PE), phosphocholine (PC), inorganic phosphate (Pi), phosphocreatine (PCr) and γ- adenosine triphosphate (γ-ATP). The map in the saggital plane demonstrates the increase in PC signal near the seminal vesicles (upper right region). The signal-to-noise ratio (ratio of the signal integral and standard deviation of the noise) after apodization (20 Hz) of PCr and PE in this spectrum were 163 and 98 respectively. D) Metabolite map of the PCr integral of ^{31}P MR spectroscopic imaging (4 cm^3 voxels) placed over a T2-weighted image of the prostate. The low PCr signals in the prostate are minimally contaminated with the high PCr signals of the surrounding muscle.*

PCr was almost equal to the ATP's (Figure 8.7B,C). This could also be demonstrated with a metabolite map of the fitted integral of the PCr signal of the second *in vivo* measurement obtained with 4 cm^3 voxels (Figure 8.8D) and a spatial map of the metabolites in the transversal plane (Figure 8.8C). The extent of the transmit field can also be appreciated in this figure.

Discussion

We have demonstrated that our setup for *in vivo* 3D ^{31}P MRSI of the human prostate at 7 T is feasible for acquisition of this data. For this setup, we combined an eight-channel ^{1}H TxRx array coil and a ^{31}P TxRx endorectal coil to obtain both anatomical information and signals from the phosphorus metabolites. For both coils, the maximum input powers were determined to comply with the IEC 60601-2-33 (Edition 3.0) guidelines, which were a maximum of 10W/kg for the SAR_{10g} or a maximum local tissue temperature of 39 °C.

To ensure that no coupling occurred between the ^{31}P endorectal coil and the eight-channel ^{1}H array coil, simulations and phantom measurements were performed. The FIT simulations showed that the highest SAR_{10g} of the array coil was observed near the ^{1}H elements, with as well as without the endorectal coil present. It was verified by temperature simulations, that the temperature elevation close to the elements of the body coil also exceeded the temperature increase near the endorectal coil. Similar to the SAR evaluation, the temperature distribution was equal with and without the endorectal coil. This was further confirmed by phantom studies showing neither elevated B_1^+ fields nor a temperature increase near the endorectal coil-loop or its wire. In addition, the *in vivo* coupling between the endorectal coil and each of the ^{1}H elements was below -60dB, demonstrating excellent decoupling between the coils. With the absence of coupling with the ^{31}P TxRx coil and the local SAR_{10g} hot-spot close to one of the array elements, we concluded that the presence of the ^{31}P coil does not influence the SAR limitations of use of the ^{1}H body-array coil.

The location of the prostate in the center of the trunk, B_1^+ inhomogeneities, and destructive B_1^+ interferences make it difficult to get enough absolute B_1^+ in the prostate. Therefore, phase modulation of the individual elements is necessary to obtain maximal B_1^+ coherence in the prostate. RF shimming theoretically also enables that a possible perturbation of the B_1^+ distribution of the eight-channel array coil by the endorectal coil can be taken into account during the RF optimization in the prostate. However, no additional B_1^+ perturbations by the endorectal coil were observed in the simulations and phantom studies. Combining the eight-channel array coil and RF shimming system resulted in high-quality anatomical information over the whole prostate and no influence on the image quality in the presence of the coil was seen *in vivo*.

The maximum permitted RF deposition with the ^{31}P endorectal coil followed from the safety validation. To stay within the SAR_{10g} safety limits, the maximum permitted input power was 0.95 W according to the FIT model simulations of the prostate. The thermal simulations showed that a higher input power of 1.3W could be used to stay below a local temperature of 39˚C. *In vivo* an even higher power level was possible because heat can be dissipated by blood flow through the tissue. Limiting the *in vivo* temperature increase at the hot-spot of the endorectal coil to 1˚C during a measurement of 15 min allowed a maximum time-averaged RF power of 1.9 W.

The differences in reported power limits for the ^{31}P endorectal coil can be explained after having a detailed look at the results. The difference in maximum power based on the SAR simulations (0.95 W) and thermal simulations (1.3W), confirms that the safety limits based on the SAR calculations are conservative and ensure that the temperature limits will not be exceeded. The difference in the SAR and temperature distribution in Figure 8.3(B,C) demonstrates the influence of the heat capacity, thermal conductivity, metabolism and blood perfusion of the tissue on the temperature. When the feed point is close to badly perfused fat tissue, a SAR hot spot results in a larger local temperature increase than the hot spot at the top of the coil inside well-perfused prostate tissue (Figure 8.3C): the highest predicted temperature increase is not located within the prostate. Next, there is a difference between the simulations and the power limit determined *in vivo* (1.9 W). The simulations represent a worst case approximation that the tissue and RF-feed are only separated by the latex from the balloon, with no gaps from residual air or glue between the inner and outer balloon. Furthermore, the *in vivo* measurement also takes into account the active thermal regulatory system (e.g. increase of blood perfusion with temperature) which was not modeled by the bioheat transfer equation in the thermal simulations. Lastly, we cannot be completely sure that the location of the fiber optic temperature sensor is at the exact same location as the location of highest power deposition derived from the simulation. As shown in Figure 8.3C, also the position of the coil in the rectum is of importance. The possible differences in actual positioning of the coil and temperature sensors compared to the simulated positioning of these in the model invoked our conservative limit of a maximum 1˚C temperature increase during the *in vivo* measurement.

The SAR limit in our study is based on the normal operating mode of the IEC guideline. In the first level operation mode the maximum SAR_{10g} limit is 20 W/kg, which would result in an input power of 1.9W in the RF simulation (twice the simulated input power of 0.95W compliant with normal operating mode), which incidentally is the same as the power determined with the *in vivo* temperature measurement.

Following an extensive safety validation, an *in vivo* experiment was performed. While in previous studies at 1.5 and 2 T in 7-30 min, one single unlocalized spectrum was obtained

(8-11), we were able to acquire a complete 3D MRSI dataset in the same time (11-18 min) with accurate localization and relatively high spatial resolution (effective voxel volume down to 4 cm^3). A metabolite map (Figure 8.8D) indicated minimal contamination of the low PCr signals in the prostate by the larger PCr signals of the surrounding smooth muscles. The spectra of the different regions in the prostate were of high spectral quality and had a good signal to noise ratio (Figure 8.7). Also at larger distances from the coil (e.g. in the seminal vesicles and anterior part of the prostate) the spectra contained usable information (Figure 8.7D & 8.8), demonstrating good performance of the coil. An effective voxel volume of 5.6 cm^3 makes it possible to study the different parts (base, midgland, apex) of the prostate (Figure 8.8). As the peripheral zone and central gland in prostate cancer patients have volumes in the order of 20 cm^3 and larger (32), this resolution also enables detection of metabolic differences between the zones.

Some differences were observed compared to the spectra obtained at 1.5 and 2 T (8-11). First of all, the increase in chemical shift dispersion enabled the separation of PE and PC signals at 7 T. At 1.5 and 2 T only one peak was visible for PME. In low field studies also a peak was assigned to PDE, while the spectra in the current study are lacking a clear peak for PDE (Figure 8.7B,D). Low glycerophosphoethanolamine and glycerophosphocholine levels are reported for prostate tissue *in vitro* (12,33). The signal-to-noise ratio might be insufficient to detect these peaks in our study. In the Pi region, two or three separate peaks were observed, compared to one peak at lower field strength. What these peaks represent, e.g. compartments with different pH, and how they can be of aid in unraveling metabolic pathways related to prostate cancer should be studied in more detail with more volunteers and patients.

Conclusion

This study demonstrated that it is safe to combine a ^{31}P TxRx endorectal coil with an eight-channel ^{1}H TxRx body-array coil for prostate imaging and ^{31}P 3D MRSI. The SAR levels of the eight-channel ^{1}H coil were not influenced by the presence of the ^{31}P endorectal coil as was validated by phantom studies, simulations and *in vivo* measurements. Furthermore, the maximum time-averaged input power of the ^{31}P endorectal coil was determined. The first *in vivo* results are promising as high-quality ^{31}P MR spectra were obtained from the whole prostate and surrounding tissues of a healthy volunteer using an effective voxel volume down to 4 cm^3 in an 18-min acquisition. To investigate the value of ^{31}P MRSI at 7 T for the characterization of prostate cancer, an extensive study with prostate cancer patients is required.

References

1. Villeirs GM, Oosterlinck W, Vanherreweghe E, De Meerleer GO. A qualitative approach to combined magnetic resonance imaging and spectroscopy in the diagnosis of prostate cancer. European journal of radiology 2010;73(2):352-356.
2. Scheidler J, Hricak H, Vigneron DB, Yu KK, Sokolov DL, Huang LR, Zaloudek CJ, Nelson SJ, Carroll PR, Kurhanewicz J. Prostate cancer: localization with three-dimensional proton MR spectroscopic imaging--clinicopathologic study. Radiology 1999;213(2):473-480.
3. Fütterer JJ, Heijmink SWTPJ, Scheenen TWJ and others. Prostate cancer localization with dynamic contrast-enhanced MR imaging and proton MR spectroscopic imaging. Radiology 2006;241(2):449-458.
4. Heerschap A, Jager GJ, Van Der Graaf M, Barentsz JO, De La Rosette JJMCH, Oosterhof GON, Ruijter ETG, Ruijs SHJ. In vivo proton MR spectroscopy reveals altered metabolite content in malignant prostate tissue. Anticancer Res 1997;17(3 A):1455-1460.
5. Kurhanewicz J, Vigneron DB, Hricak H, Narayan P, Carroll P, Nelson SJ. Three-dimensional H-1 MR spectroscopic imaging of the in situ human prostate with high (0.24-0.7-cm3) spatial resolution. Radiology 1996;198(3):795-805.
6. Scheenen TW, Heijmink SW, Roell SA, Hulsbergen-Van de Kaa CA, Knipscheer BC, Witjes JA, Barentsz JO, Heerschap A. Three-dimensional proton MR spectroscopy of human prostate at 3 T without endorectal coil: feasibility. Radiology 2007;245(2):507-516.
7. Scheenen TWJ, Fütterer J, Weiland E and others. Discriminating cancer from noncancer tissue in the prostate by 3-dimensional proton magnetic resonance spectroscopic imaging: A prospective multicenter validation study. Invest Radiol 2011;46(1):25-33.
8. Kurhanewicz J, Thomas A, Jajodia P, Weiner MW, James TL, Vigneron DB, Narayan P. 31P spectroscopy of the human prostate gland in vivo using a transrectal probe. Magn Reson Med 1991;22(2):404-413.
9. Thomas MA, Narayan P, Kurhanewicz J, Jajodia P, James TL, Weiner MW. Detection of phosphorus metabolites in human prostates with a transrectal 31P NMR probe. J Magn Reson 1992;99(2):377-386.
10. Narayan P, Jajodia P, Kurhanewicz J and others. Characterization of prostate cancer, benign prostatic hyperplasia and normal prostates using transrectal 31phosphorus magnetic resonance spectroscopy: A preliminary report. J Urol 1991;146(1):66-74.
11. Hering F, Muller S. 31P MR spectroscopy and 1H MR imaging of the human prostate using a transrectal probe. Urol Res 1991;19(6):349-352.
12. Komoroski RA, Holder JC, Pappas AA, Finkbeiner AE. 31P NMR of phospholipid metabolites in prostate cancer and benign prostatic hyperplasia. Magn Reson Med 2011;65(4):911-913.
13. Qiao H, Zhang X, Zhu XH, Du F, Chen W. In vivo 31P MRS of human brain at high/ultrahigh fields: a quantitative comparison of NMR detection sensitivity and spectral resolution between 4 T and 7 T. Magn Reson Med 2006;24(10):1281-1286.
14. Metzger GJ, Snyder C, Akgun C, Vaughan T, Ugurbil K, Van De Moortele PF. Local B1 + shimming for prostate imaging with transceiver arrays at 7T based on subject-dependent transmit phase measurements. Magn Reson Med 2008;59(2):396-409.
15. International Electrotechnical Commission -IEC60601-2-33, Edition 3.0, 2010-03: Medical electrical equipment – Part 2-33: Particular for the safety of magnetic resonance equipment for medical diagnosis.
16. Orzada S, Quick HH, Ladd ME, Bahr A, Bolz T, Yazdanbakhsh P, Solbach K, Bitz AK. A Flexible 8-channel Transmit/receive Body Coil for 7 T Human Imaging. Proceedings of the 17th Annual Meeting of ISMRM. Honolulu, Hawaii, USA; 2009. p 2999.
17. Orzada S, Bahr A, Bolz T. A Novel 7 T Microstrip

Element using Meanders to Enhance Decoupling. Proceedings of the 16th Annual Meeting of ISMRM. Toronto, Ontario, Canada; 2008. p 2979.

18. Bitz AK, Brote I, Orzada S and others. An 8-channel Add-on RF Shimming System for Whole-body 7 Tesla MRI Including Real-time SAR Monitoring. Proceedings of the 17th Annual Meeting of ISMRM. Honolulu, Hawaii, USA; 2009. p 4767.
19. Brote I, Orzada S, Kraff O and others. A Multi-channel SAR Prediction and Online Monitoring System at 7T. Proceedings of the 17th Annual Meeting of ISMRM. Honolulu, Hawaii, USA; 2009. p 4788.
20. Fautz HP, Vogel M, Gross P, Kerr A, Zhu Y. B1 Mapping of Coil Arrays for Parallel Transmission. Proceedings of the 16th Annual Meeting of ISMRM. Toronto, Ontario, Canada; 2008. p 1247.
21. Klomp DW, Bitz AK, Heerschap A, Scheenen TW. Proton spectroscopic imaging of the human prostate at 7 T. NMR Biomed 2009;22(5):495-501.
22. Bitz AK, Klomp DW, Ladd ME. Experimental and numerical determination of SAR and temperature distribution of a human endorectal coil for MR imaging of the prostate at 7T. Proceedings of the 16th Annual Meeting of ISMRM. Toronto, Ontario, Canada; 2008. p 903.
23. Gabriel C. Compilation of the dielectric properties of body tissues at RF and microwave frequencies: Brooks AFB, TX: Brooks AFB, Tech. Rep. ; 1996.
24. Pennes HH. Analysis of tissue and arterial blood temperatures in the resting human forearm. J Appl Physiol 1998;85(1):5-34.
25. Christ A, Kainz W, Hahn EG and others. The Virtual Family - Development of surface-based anatomical models of two adults and two children for dosimetric simulations. Phys Med Biol 2010;55(2):N23-N38.
26. Âkerlöf G. Dielectric constants of some organic solvent-water mixtures at various temperatures. J Am Chem Soc 1932;54(11):4125-4139.
27. Zhao GQ, Chen SB. Microviscosity of hydrophobically modified hydroxyethyl cellulose aqueous solutions. J Colloid Interf Sci 2008;322(2):678-680.
28. Ishihara Y, Calderon A, Watanabe H, Okamoto K, Suzuki Y, Kuroda K, Suzuki Y. A precise and fast temperature mapping using water proton chemical shift. Magn Reson Med 1995;34(6):814-823.
29. Yarnykh VL. Actual flip-angle imaging in the pulsed steady state: A method for rapid three-dimensional mapping of the transmitted radiofrequency field. Magn Reson Med 2007;57(1):192-200.
30. Amadon A, Boulant N. Simultaneous Measurement of B0- And B1-Maps with Modified Actual Flip Angle Imaging Sequence. Proceedings of the 16th Annual Meeting of ISMRM. Toronto, Ontario, Canada; 2008.
31. Lei H, Zhu XH, Zhang XL, Ugurbil K, Chen W. In vivo 31P magnetic resonance spectroscopy of human brain at 7 T: An initial experience. Magn Reson Med 2003;49(2):199-205.
32. Zechmann CM, Simpfendörfer T, Giesel FL, Zamecnik P, Thieke C, Hielscher T, Meinzer HP, Delorme S. Comparison of peripheral zone and central gland volume in patients undergoing intensity-modulated radiotherapy. J Comput Assist Tomogr 2010;34(5):739-745.
33. Swanson MG, Keshari KR, Tabatabai ZL, Simko JP, Shinohara K, Carroll PR, Zektzer AS, Kurhanewicz J. Quantification of choline- and ethanolamine-containing metabolites in human prostate tissues using 1H HR-MAS total correlation spectroscopy. Magn Reson Med 2008;60(1):33-

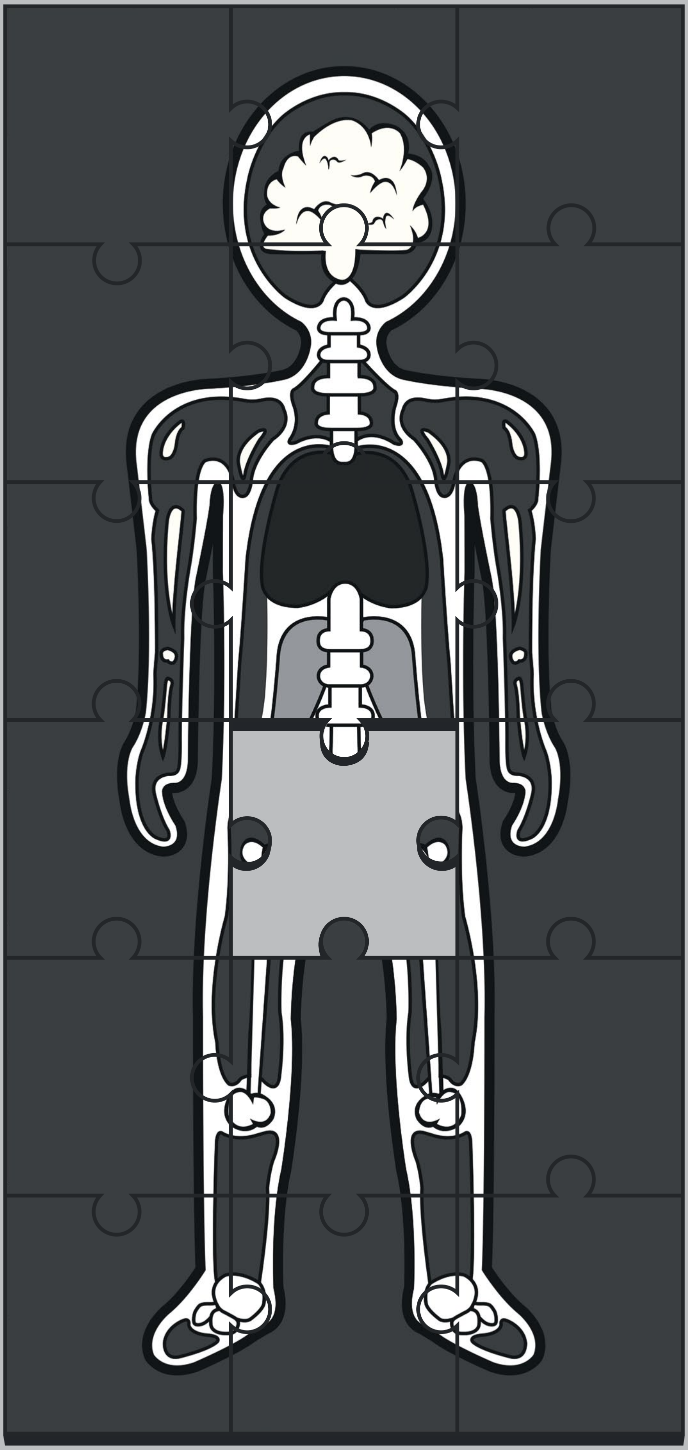

9

CHAPTER NINE

Summary and Future Perspectives

Summary and Future perspectives

In this thesis, the performance of two magnetic resonance (MR) techniques for *in vivo* noninvasive assessment of prostate cancer aggressiveness was studied. These techniques are: MR spectroscopic imaging (MRSI) and diffusion-weighted imaging (DWI).

Summary

With prostate ^{1}H MRSI, the spatial distribution of the metabolites choline, creatine, polyamines (spermine) and citrate can be studied. From these, the ratio of choline (plus spermine) plus creatine over citrate [(Cho+(Spm+)Cr)/Cit] can be derived and used as a marker of prostate cancer. The apparent diffusion coefficient (ADC) of DWI reflects the compartmentalization of the tissue, which is a useful measure for detection, localization and characterization of cancer foci (**chapter 2**).

Routine clinical use of prostate ^{1}H MRSI requires more automation of data-processing than currently available. In addition, for a more widespread use, a general classification scheme for prostate cancer management would be beneficial. The appearance of the metabolite signals (especially that of citrate) in the spectrum does not only depend on the underlying anatomy, metabolism and physiology of the tissue, but also on acquisition parameters (echo time, repetition time, pulse sequence timing and field strength). There are differences between the acquisition protocols of the major MR vendors for prostate MRSI, which lead to (Cho+Cr)/Cit values that are not directly comparable. Classification thresholds should be derived for each of the available protocols to increase the clinical usability of MRSI for the prostate (**chapter 3**).

In this thesis, it was demonstrated that the (Cho+Cr)/Cit ratio and the ratio of choline over creatine [Cho/Cr] offer possibilities for an *in vivo*, noninvasive assessment of prostate cancer aggressiveness. The maximum (Cho+Cr)/Cit and Cho/Cr showed a relation with cancer aggressiveness and gave good results for differentiation among tumor aggressiveness classes. The combination of the two metabolite ratios was used in a standardized threshold approach with promising results to discriminate between different aggressiveness classes (**chapter 4**).

For tumors in the peripheral zone, significant correlations were found between aggressiveness classes and the minimum 25th percentile ADC value, the maximum (Cho+Cr)/Cit ratio, and the maximum Cho/Cr ratio. For transition zone tumors, the correlation was significant only for the maximum (Cho+Cr)/Cit and Cho/Cr ratios. MRSI and DWI have comparable performance for assessment of prostate cancer aggressiveness. Combining standard versions of both modalities in one measure did not result in a better performance. Nonetheless, better performances using the metabolite ratios in the transition zone and the ADC value in the peripheral zone were observed, which suggest that they do have complementary value (**chapter 5**).

To get a better understanding of (Cho+Spm+Cr)/Cit ratio (or its inverse Cit/(Cho+Spm+Cr) ratio) and the ADC value, these parameters were related to the underlying prostate morphology. The ADC value related positively with the percentage area of lumen and negatively with the percentage area of nuclei. A positive relation was found between the Cit/(Cho+Spm+Cr) ratio and the percentage area of lumen. These similar relationships of the ADC and Cit/(Cho+Spm+Cr) ratio with the amount of luminal space indicate that this morphological feature is an important factor determining changes in both MR parameters. However, as the origin of the signals is different (water movement versus levels of metabolites and their environment) it is plausible that other factors will contribute as well (**chapter 6**).

^{1}H MRSI can also be used to observe lactate, an interesting marker for cancer as it is a reporter of the Warburg effect and a sign of hypoxia. However, in our study we found no convincing lactate signal in 17 patients with highly aggressive prostate cancer using a semi-LASER sequence optimized for *in vivo* lactate detection in the prostate. We estimated that on average the lactate levels in high-grade prostate cancer are below 1.5 mM, which indicates that if lactate is increased in prostate cancer, it remains at low concentrations, in agreement with the absence of substantial necrosis in prostate cancer. The absence of pulses and gradients for peri-prostatic lipid suppression made it possible to detect lipids in the prostate and possibly N-acetyl neuraminic acid (**chapter 7**).

Metabolites with a phosphorus-atom can be studied with ^{31}P MRSI and this could provide new information for prostate cancer characterization. An extensive safety validation of our newly developed set-up showed that we can safely use a ^{31}P endorectal coil in combination with an external eight-channel ^{1}H array coil to perform ^{31}P MRSI of the prostate at 7 T. We were able to obtain spectra from the entire prostate of a healthy volunteer with a spatial resolution of 4 cm^3. The spectral resolution enabled separate detection of phosphocholine, phosphoethanolamine, inorganic phosphate, and other metabolites that could play an important role in the characterization of prostate cancer (**chapter 8**).

Discussion and future perspectives

As multi-parametric MR imaging is nowadays believed to be the optimal way to diagnose prostate cancer by MR, the clinical value of MRSI and DWI of the prostate should also be evaluated in this context. General guidelines regarding how to perform and analyze a multi-parametric measurement of the prostate are provided by the European Society of Urogenital Radiology (1). For all modalities applies that the particular assessments are still largely qualitative. As discussed in chapter 3, the (Cho+Cr)/Cit ratio of MRSI depends not only on physiology and metabolism, but also on acquisition parameters. Since the different MR-vendors have different ^{1}H MRSI acquisition protocols, the ratio is vendor- and field dependent. In principle the (Cho+Cr)/Cit ratio could be vendor-independent with similar acquisition protocols and post processing. To promote clinical usability of prostate MRSI it would be desirable if consensus could be reached on field strength dependent common acquisition and post processing protocols. However, also for DWI and DCE-MRI no consistency in imaging parameters and post-processing is established. For DWI, it is recommended to use ADC maps for a quantitative assessment and add high b-value images for a qualitative approach (1). However, quantitative ADC values should be assessed with care as there is no uniformity in the measured b-values, mono- and bi-exponential fits are used, and there is also a dependence on the field-strength. At this moment, there are no general quantitative classification thresholds available for DWI.

In our studies, we have shown how ^{1}H MRSI can, and how it cannot, be used for *in vivo* noninvasive assessment of prostate cancer aggressiveness. Both the (Cho+Cr)/Cit and the Cho/Cr ratio, as well as their combination in the standardized threshold approach, gave good results for assessment of aggressiveness. Previously, the value of ^{1}H MRSI for detection and localization of prostate cancer has been demonstrated (e.g. (2-6)) and the technique has also been used to monitor treatment response (e.g. (7-13)). Still, the use of ^{1}H MRSI as a routine clinical tool occurred up till now only at (academic) sites dedicated to its application. The translation to a clinical routine application depends on several factors. Not only a robust and automated acquisition procedure, which is able to deal with movement and field inhomogeneities, is necessary, but also rapid and easy digestible display of the results and proper training of the clinical users are important. And above all it has to be clear that methods are generally applicable and produce reliable and significant clinical results, also compared to other MR approaches or modalities.

Especially the complementary value of ^{1}H MRSI and DWI needs more attention. We demonstrated that the two modalities have comparable performance for *in vivo* noninvasive assessment of prostate cancer aggressiveness and their combination did not lead to improved results. Furthermore, we saw that the ADC value and citrate signal in MRSI both depend on the amount of luminal space in the tissue. So one might suggest to skip one of the two modalities during a multi-parametric prostate MR exam. The higher resolution, shorter acquisition time, and availability of an intuitive display of results are all in favor for the use of DWI instead of ^{1}H MRSI. However, the (Cho+Cr)/Cit ratio has potentially a larger dynamic range (as it is not limited by gradient strength and diffusion time), had a slightly better performance for transition zone tumors, and might show a metabolic change in the tissue before a morphologic change occurs. These last two aspects need more investigation as no longitudinal studies were performed to investigate the changes in the (Cho+Cr)/Cit ratio over time and in our studies only a limited number of transition zone tumors were included. In the transition zone of elderly men benign prostatic hyperplasia (BPH) is often present. BPH appears very heterogeneous on T2-weighted images, with areas of low signal intensity that are similar to prostate cancer. No improvement for detection and localization of transition zone tumors was observed for a multi-parametric MRI, consisting of T2 weighted imaging, DCE-MRI and DWI, compared to T2-weighted imaging alone (14). But the role of MRSI was not assessed in this study. When the (Cho+Cr)/Cit and Cho/Cr ratios of benign and tumor tissue in the transition zone were compared, significant differences were found (15). However, there was also considerable overlap present, which is similar to our results. The role of MRSI for the transition zone should be further explored, preferably in a prospective and multi-parametric setting, to fully determine the added value of each modality.

With further improvement of MRSI acquisition technology and the use of higher fields, it is hoped that the set of (surrogate) prostate cancer biomarker signals can be expanded beyond those currently employed in MRSI to enhance the sensitivity of this technique. This was attempted in this thesis by optimizing a semi-LASER sequence to study a broader range of metabolites. In this way, we could rule out the use of lactate as *in vivo* prostate cancer biomarker, at least when obtained with ^{1}H MRSI. However, we were able to pick up another signal with this sequence, possibly of N-acetyl neuraminic acid. Significant differences between serum levels of N-acetyl neuraminic acid in healthy and prostate cancer patients were found (16, 17). However, the serum levels were not specific enough for screening. The diagnostic value of this metabolite detected with ^{1}H MRSI was not evaluated in our study and could be topic of future research. Moreover, we could confirm the presence of lipid signals in the prostate in one patient with highly aggressive prostate cancer (Gleason 5+5 and necrosis). The presence of lipids is a sign of necrosis and this could explain the hyper-intense regions in the center of this patient's tumor observed on the T2-weighted image and ADC map. This was a unique observation. However, the clinical usability will be limited as necrosis is rare in prostate cancer.

Because we used a semi-LASER sequence without lipid suppression techniques, we had to place the volume of interest completely inside the prostate to prevent peri-prostatic lipid contamination, which limits its clinical applicability. A semi-LASER sequence with the incorporation of lipid suppression pulses and gradients could be an alternative to the PRESS sequence, as our semi-LASER-spectra were of high quality. However, to reach adiabicity of the refocusing-pulses, high RF powers were needed, leading to long repetition times to comply with safety regulations. To limit the acquisition time, techniques could be incorporated that decrease the required RF power, for example by the implementation of gradient offset independent adiabatic pulses (GOIA) (18, 19). With adiabatic pulses less chemical shift displacement will occur and thus less lipid signal problems may be expected, which also could facilitate the use of shorter echo-times with signals of more metabolites than those observed currently. Thus progress in ^{1}H MRSI is expected to make it more robust, faster and with better spectral and spatial resolution and to provide more (potential) biomarkers.

The introduction of human 7T-systems enabled us to perform 3D ^{31}P MRSI of the prostate in a clinical acceptable measurement time. The safety and feasibility study of our setup for *in vivo* ^{31}P MRSI of the prostate at 7 T paved the way for a patient study to investigate its value for prostate cancer management. While the (Cho+Cr)/Cit ratio of ^{1}H MRSI largely depends on the intensity of citrate, no citrate is detected with ^{31}P MRSI, giving the technique potentially more value than ^{1}H MRSI when used in combination with DWI. With the increased spectral resolution at 7 T, more metabolites could be studied than in previous low field studies (20-22); for example, the metabolite phosphoethanolamine can now be distinguished from phosphocholine. Using ^{31}P NMR on prostate extracts, significantly lower levels of phosphoethanolamine were observed in prostate cancer compared to BPH tissue (23, 24), which could be an interesting biomarker for transition zone tumors. A patient study investigating the potential for ^{31}P MRSI for prostate cancer detection is ongoing at the moment of writing. With a spatial resolution of 4 cm^3, it will be challenging to demonstrate its value due to partial volume effects obscuring differences in the metabolites among different tissues. Currently, 7T-systems are mainly used in a research setting. While there has been a lot of effort to enable and optimize T2-weighted imaging at 7 T (25-27), the implementation of other functional techniques as DWI needs attention as well. When these issues are addressed and if we can demonstrate the value of ^{31}P MRSI for the management of prostate cancer, 7T-systems might be used for clinical prostate examinations.

Currently the use of prostate-specific antigen levels in the blood to screen for prostate cancer is under investigation (e.g. (28)). Screening will not only lead to a reduction in the mortality rate of prostate cancer (28), but also to substantial overdiagnosis. Fifty percent of the patients diagnosed with prostate cancer as a result of screening would not have presented any clinical symptoms during their lives without screening (29). This will consequently have an impact on the quality of life. When 1000 men between the ages of 55 and 69 are screened annually over their lifetime, the life-years gained by screening (73 years) will decrease to 56 years (23% decrease) when quality of life is taken into account (30). Reliable classification of tumors as indolent will prevent overtreatment in these patients and increase their quality of life. ^{1}H MRSI and DWI both have value for *in vivo* noninvasive assessment of prostate cancer aggressiveness. MRSI has been incorporated in nomograms to predict insignificant prostate cancer (31, 32). The ADC values and ^{1}H MRSI ratios both showed overlap between the aggressiveness classes; however, if we can use MR to prevent aggressive treatment even in a small portion of patients with an indolent cancer, this can increase the quality of life for these patients substantially.

Another setting that can benefit from the information of MRSI and DWI are the MR-guided prostate interventions. When performing MR-guided prostate biopsies, MRSI and DWI can be used to direct the needle to the part of the tumor that looks most malignant. This way, the pathologist can assess the Gleason score of, what is likely, the most aggressive part of the tumor. Also ultrasound-guided biopsies with MR images fused to the ultrasound imaging can be better targeted in this way. There is a growing interest in focal therapies for localized disease, where only the tumor itself is treated in a minimal invasive way, while the normal prostate and its function are preserved. MR imaging is used to guide focal therapies like cryotherapy, high intensity focused ultrasound, RF- and laser-techniques, which are used to ablate tumor tissue. Furthermore, DWI and ^{1}H MRSI can be used to improve the dose distribution for intensity modulated radiotherapy.

To conclude, DWI and ^{1}H MRSI can both be used for a noninvasive aggressiveness assessment. This assessment can be used to guide biopsies and to improve the choice and application of therapy: active surveillance, focal therapy, or a more aggressive treatment. However, for routine clinical use, both methods could benefit from standardization and general quantitative classification thresholds. These thresholds should be assessed in a multi-parametric MR setting and evaluated in a prospective multi-center study.

References

1. Barentsz JO, Richenberg J, Clements R, et al. ESUR prostate MR guidelines 2012. Eur Radiol. 2012;22(4):746-57.
2. Jung JA, Coakley FV, Vigneron DB, et al. Prostate depiction at endorectal MR spectroscopic imaging: investigation of a standardized evaluation system. Radiology. 2004;233(3):701-8.
3. Scheidler J, Hricak H, Vigneron DB, et al. Prostate cancer: Localization with three-dimensional proton MR spectroscopic imaging - Clinicopathologic study. Radiology. 1999;213(2):473-80.
4. Fütterer JJ, Heijmink SWTPJ, Scheenen TWJ, et al. Prostate cancer localization with dynamic contrast-enhanced MR imaging and proton MR spectroscopic imaging. Radiology. 2006;241(2):449-58.
5. Scheenen TWJ, Fütterer J, Weiland E, et al. Discriminating cancer from noncancer tissue in the prostate by 3-dimensional proton magnetic resonance spectroscopic imaging: A prospective multicenter validation study. Invest Radiol. 2011;46(1):25-33.
6. Villeirs GM, De Meerleer GO, De Visschere PJ, Fonteyne VH, Verbaeys AC, Oosterlinck W. Combined magnetic resonance imaging and spectroscopy in the assessment of high grade prostate carcinoma in patients with elevated PSA: a single-institution experience of 356 patients. European journal of radiology. 2011;77(2):340-5.
7. Kurhanewicz J, Vigneron DB, Hricak H, et al. Prostate cancer: metabolic response to cryosurgery as detected with 3D H-1 MR spectroscopic imaging. Radiology. 1996;200(2):489-96.
8. Parivar F, Hricak H, Shinohara K, et al. Detection of locally recurrent prostate cancer after cryosurgery: Evaluation by transrectal ultrasound, magnetic resonance imaging, and three- dimensional proton magnetic resonance spectroscopy. Urology. 1996;48(4):594-9.
9. Coakley FV, Hui ST, Qayyum A, et al. Endorectal MR imaging and MR spectroscopic imaging for locally recurrent prostate cancer after external beam radiation therapy: Preliminary experience. Radiology. 2004;233(2):441-8.
10. Pickett B, Kurhanewicz J, Coakley F, Shinohara K, Fein B, Roach M. Use of MRI and spectroscopy in evaluation of external beam radiotherapy for prostate cancer. Int J Radiat Oncol Biol Phys. 2004;60(4):1047-55.
11. Pucar D, Shukla-Dave A, Hricak H, et al. Prostate cancer: correlation of MR imaging and MR spectroscopy with pathologic findings after radiation therapy-initial experience. Radiology. 2005;236(2):545-53.
12. Zaider M, Zelefsky MJ, Lee EK, et al. Treatment planning for prostate implants using magnetic-resonance spectroscopy imaging. International Journal of Radiation Oncology Biology Physics. 2000;47(4):1085-96.
13. Mueller Lisse UG, Vigneron DB, Hricak H, et al. Localized prostate cancer: Effect of hormone deprivation therapy measured by using combined three-dimensional H-1 MR spectroscopy and MR imaging: Clinicopathologic case-controlled study. Radiology. 2001;221(2):380-90.
14. Hoeks CM, Hambrock T, Yakar D, et al. Transition Zone Prostate Cancer: Detection and Localization with 3-T Multiparametric MR Imaging. Radiology. 2013;266(1):207-17.
15. Zakian KL, Eberhardt S, Hricak H, et al. Transition zone prostate cancer: Metabolic characteristics at 1H MR spectroscopic imaging-initial results. Radiology. 2003;229(1):241-7.
16. Hobarth K, Hofbauer J, Fang-Kircher S. Plasma sialic acid in patients with prostate cancer. Brit J Urol. 1993;72(5 I):621-4.
17. Lagana A, Pardo-Martinez B, Marino A, Fago G, Bizzarri M. Determination of serum total lipid and free N-acetylneuraminic acid in genitourinary malignancies by fluorimetric high performance liquid chromatography. Relevance of free N-acetylneuraminic acid as tumour marker. Clin Chim Acta. 1995;243(2):165-79.

18. Tannús A, Garwood M. Adiabatic pulses. NMR in Biomed. 1997;10(8):423-34.
19. Near J, Romagnoli C, Curtis AT, et al. High field MRSI of the prostate using a transmit/receive endorectal coil and gradient modulated adiabatic localization. J Magn Reson Imaging. 2009;30(2):335-43.
20. Thomas MA, Narayan P, Kurhanewicz J, Jajodia P, James TL, Weiner MW. Detection of phosphorus metabolites in human prostates with a transrectal 31P NMR probe. J Magn Reson. 1992;99(2):377-86.
21. Hering F, Muller S. 31P MR spectroscopy and 1H MR imaging of the human prostate using a transrectal probe. Urol Res. 1991;19(6):349-52.
22. Narayan P, Jajodia P, Kurhanewicz J, et al. Characterization of prostate cancer, benign prostatic hyperplasia and normal prostates using transrectal 31phosphorus magnetic resonance spectroscopy: A preliminary report. J Urol. 1991;146(1):66-74.
23. Cornel E, Smits G, Oosterhof G, et al. Characterization of human prostate cancer, benign prostatic hyperplasia and normal prostate by in vitro 1H and 31P magnetic resonance spectroscopy. J Urology. 1993;150(6):2019.
24. Komoroski RA, Holder JC, Pappas AA, Finkbeiner AE. 31P NMR of phospholipid metabolites in prostate cancer and benign prostatic hyperplasia. Magn Reson Med. 2011;65(4):911-3.
25. Metzger GJ, Snyder C, Akgun C, Vaughan T, Ugurbil K, Van De Moortele PF. Local B1 + shimming for prostate imaging with transceiver arrays at 7T based on subject-dependent transmit phase measurements. Magn Reson Med. 2008;59(2):396-409.
26. Maas MC, Vos EK, Lagemaat MW, et al. Feasibility of T2-weighted turbo spin echo imaging of the human prostate at 7 tesla. Magn Reson Med. 2013.
27. Metzger GJ, van de Moortele PF, Akgun C, et al. Performance of external and internal coil configurations for prostate investigations at 7 T. Magn Reson Med. 2010;64(6):1625-39.
28. Schröder FH, Hugosson J, Roobol MJ, et al. Prostate-cancer mortality at 11 years of follow-up. New Engl J Med. 2012;366(11):981-90.
29. Draisma G, Boer R, Otto SJ, et al. Lead times and overdetection due to prostate-specific antigen screening: Estimates from the European randomized study of screening for prostate cancer. J Natl Cancer I. 2003;95(12):868-78.
30. Heijnsdijk EA, Wever EM, Auvinen A, et al. Quality-of-life effects of prostate-specific antigen screening. New Engl J Med. 2012;367(7):595-605.
31. Shukla-Dave A, Hricak H, Akin O, et al. Preoperative nomograms incorporating magnetic resonance imaging and spectroscopy for prediction of insignificant prostate cancer. BJU International. 2012;109(9):1315-22.
32. Shukla-Dave A, Hricak H, Kattan MW, et al. The utility of magnetic resonance imaging and spectroscopy for predicting insignificant prostate cancer: an initial analysis. BJU Int. 2007;99(4):786-93.

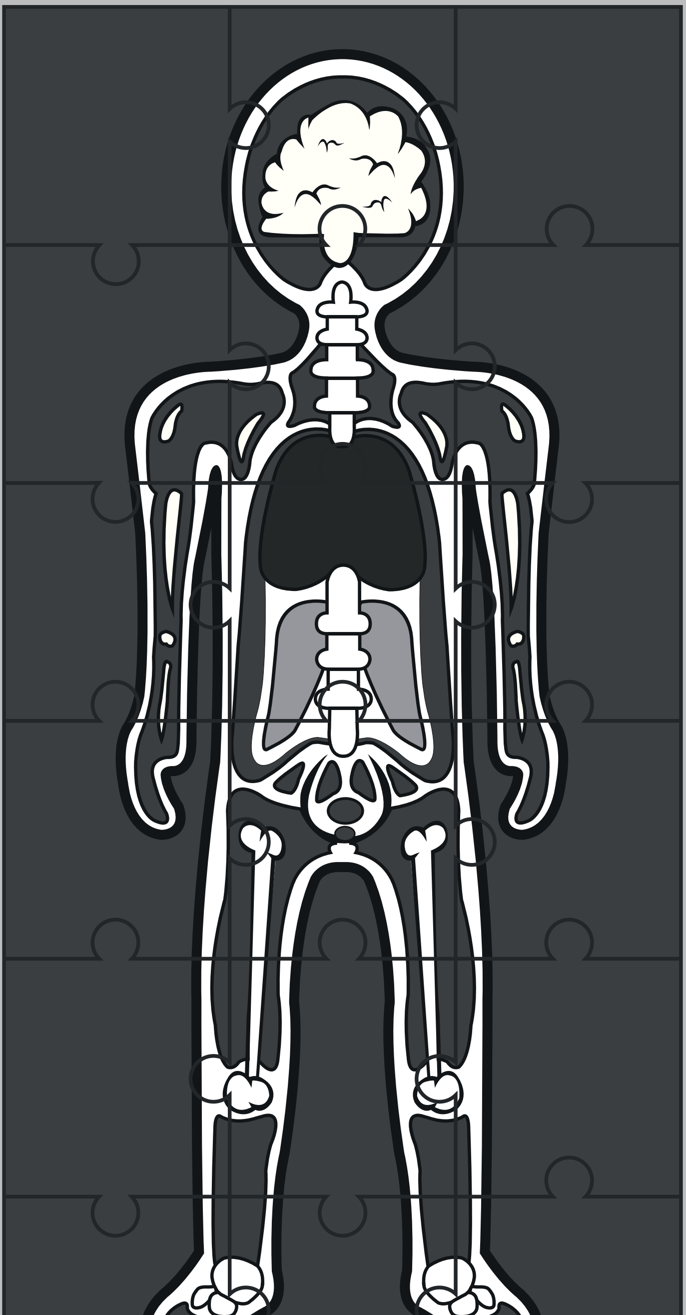

NEDERLANDSE SAMENVATTING
LIST OF ABBREVIATIONS
LIST OF PUBLICATIONS
DANKWOORD
CURRICULUM VITAE

Nederlandse Samenvatting

In dit proefschrift zijn twee technieken die gebruik maken van magnetische resonantie (MR) onderzocht voor een *in vivo*, niet-invasieve bepaling van de agressiviteit van prostaatkanker. Deze technieken zijn: MR spectrosopische imaging (MRSI) en diffusie gewogen imaging (DWI).

Met proton (^{1}H) MRSI kan de spatiële verdeling van de metabolieten choline, creatine, polyamines (vooral spermine) en citraat in de prostaat worden bestudeerd. Hiervan kan de ratio van choline (plus spermine) plus creatine over citraat [(Cho+(Spm+)Cr)/Cit] worden bepaald en deze kan gebruikt worden als marker voor prostaatkanker. De schijnbare diffusiecoëfficiënt (ADC) van DWI is afhankelijk van de structuur van het weefsel en is een goede maat voor detectie, lokalisatie en karakterisatie van prostaatkanker (**hoofdstuk 2**).

Voor routinematig gebruik van prostaat ^{1}H MRSI in de kliniek is meer automatisering van de dataverwerking nodig dan wat op dit moment voor handen is. Verder zou een algemeen classificatie schema voor de management van prostaatkanker bijdragen aan breder gebruik. De vorm en intensiteit van de metabolieten (vooral citraat en spermine) in het spectrum hangt niet alleen af van de onderliggende anatomie, stofwisseling en fysiologie van het weefsel, maar ook van de acquisitie parameters (echo tijd, repetitie tijd, puls timing in de sequentie en veld sterkte). Er zijn verschillen tussen de acquisitie protocollen van de MR vendors voor prostaat MRSI, wat leidt tot (Cho+Cr)/Cit waarden die niet direct vergelijkbaar zijn. Classificatie drempels zouden moeten worden bepaald voor alle beschikbare protocollen om MRSI van de prostaat meer bruikbaar te maken in de kliniek (**hoofdstuk 3**).

In dit proefschrift is bewezen dat de (Cho+Cr)/Cit ratio en de ratio van choline over creatine (Cho/Cr) mogelijkheden bieden voor een *in vivo*, niet-invasieve bepaling van de agressiviteit van prostaatkanker. De maxima van de (Cho+Cr)/Cit en Cho/Cr ratios in de tumor relateren met de agressiviteit van de tumor en goede resultaten zijn behaald voor de differentiatie tussen agressiviteitklassen. Het combineren van de twee metaboliet ratios leidde tot veelbelovende resultaten voor differentiatie tussen verschillende agressiviteitklassen (**hoofdstuk 4**).

Vervolgens is de agressiviteitsanalyse uitgebreid met DWI. Voor tumoren in de perifere zone werden significante correlaties gevonden tussen de agressiviteitklassen en het minimum 25ste percentiel van de ADC waarden, de maximum (Cho+Cr)/Cit ratio en de maximum Cho/Cr ratio. For tumoren in de transitie zone was de correlatie alleen significant voor de maximum (Cho+Cr)/Cit ratio en de Cho/Cr ratio. MRSI en DWI gaven vergelijkbare resultaten voor de bepaling van de agressiviteit van prostaatkanker. Het combineren van beide technieken leverde geen verbeterde resultaten op. Toch suggereren de betere resultaten voor de metaboliet ratios in the transitie zone en de ADC waarde in de perifere zone dat MRSI en DWI complementaire waarde hebben (**hoofdstuk 5**).

Om meer inzicht te krijgen in de complementaire waarde van beide technieken is de relatie tussen de onderliggende morfologie en de metaboliet ratios en de ADC waarde onderzocht. De ADC waarde liet een positieve relatie zien met het percentage oppervlak van de luminale ruimte en een negatieve relatie met het percentage oppervlak van de kernen. Er is ook een positieve relatie gevonden tussen de Cit/(Cho+Spm+Cr) ratio en het percentage oppervlak van de luminale ruimte. Deze significante relaties suggereren dat de verschillen in ADC waarde en Cit/(Cho+Spm+Cr) ratio die we zien tussen de normaal en tumor prostaat weefsel, morfologische variaties representeren in de prostaat weefsel, voornamelijk in de luminale ruimte. Hoewel we niet kunnen uitsluiten dat er ook biochemische processen (zoals m-aconitase or ATP-citraat lyase) en interacties in het prostaat vocht ook de citraat and spermine signalen beinvloeden, is het waarschijnlijk dat deze bijdragen kleiner zijn dat de morphologische veranderingen (**hoofdstuk 6**).

^{1}H MRSI kan ook worden gebruikt om lactaat te detecteren, wat een interessante marker is voor kanker omdat het een teken is van het Warburg effect en van hypoxia. In deze studie hebben we geen overtuigend lactaat signaal gevonden in 17 patiënten met zeer agressieve prostaatkanker. We hebben hiervoor gebruik gemaakt van een semi-LASER sequentie die geoptimaliseerd is voor *in vivo* lactaat detectie in de prostaat. We hebben een schatting gemaakt dat de gemiddelde lactaat concentratie in agressieve prostaatkankers en deze is lager dan 1.5 mM. Dit laat zien dat als lactaat verhoogd is in prostaatkanker, lactaat in lage concentratie blijft. De afwezigheid van pulsen en gradiënten voor onderdrukking van lipiden rond de prostaat heeft het mogelijk gemaakt om lipiden waar te nemen in de prostaat net als vermoedelijk N-acetyl neuraminic zuur (**hoofdstuk 7**).

Metabolieten met een fosforatoom kunnen worden bestudeerd met ^{31}P MRSI en dit kan nieuwe informatie opleveren voor de karakterisatie van prostaatkanker. Een uitgebreide validatie van de veiligheid van onze nieuwe set-up heeft laten zien dat we veilig een ^{31}P endorectale spoel kunnen gebruiken in combinatie met een externe achtkanaals $_1$H spoel om prostaat ^{31}P MRSI te verrichten op 7 T. In een gezonde vrijwilliger hebben we spectra van de hele prostaat kunnen meten met een spatiële resolutie van 4 cm^3. De spectrale resolutie maakte de detectie mogelijk van fosfocholine, fosfoethanolamine, anorganisch fosfaat en andere metabolieten die een belangrijke rol kunnen spelen voor de karakterisatie van prostaatkanker (**hoofdstuk 8**).

List of Abbreviations

3D	Three-dimensional
ADC	Apparent Diffusion Coefficient
AFP	Adiabatic Full Passage
ATP	Adenosine Triphosphate
AUC	Area under the Curve
B_0	External Magnetic Field
BASING	Band-Selective Inversion with Gradient Dephasing
BPH	Benign Prostatic Hyperplasia
CG	Central Gland
Cho	Choline
(Cho(+Spm)+Cr)/Cit	Choline (plus Spermine) plus Creatine to Citrate
Cit	Citrate
Cr	Creatine
CRLB	Cramér-Rao lower bound
δ	Chemical Shift / Duration of the Gradients
Δ	Time between the gradients / Difference in chemical shifts
D	Diffusion Coefficient
DCE-MRI	Dynamic Contrast Enhanced Magnetic Resonance Imaging
DWI	Diffusion-weighted Imaging
E	Magnetic Energy
ESUR	European Society of Urogenital Radiology
FOV	Field Of View
FIT	Finite Integration Technique
γ	Gyromagnetic Ratio
G	Gradient Strength
GPC	Glycerophosphocholine
GPE	Gycerophosphoethanolamine
h	Planck’s Constant
HE	Hematoxylin and Eosin
HR-MAS	High Resolution Magic Angle Spectroscopy
IEC	International Electrotechnical Commission
ISUP	International Society of Urological Pathology
J	Scalar Coupling Constant
k	Boltzmann constant
LASER	Localization by Selective Adiabatic Refocusing
LRM	Logistic Regression Model
μ	Magnetic Moment
M	Magnetization Vector

MEGA	Mescher-Garwood pulse
MR	Magnetic Resonance
MRI	Magnetic Resonance Imaging
MRS	Magnetic Resonance Spectroscopy
MRSI	Magnetic Resonance Spectroscopic Imaging
OVS	Outer Volume Saturation
PC	Phosphocholine
PE	Phosphoethanolamine
PCr	Phosphocreatine
PDE	Phosphodiesters
Pi	Inorganic Phosphate
PME	Phosphomonoesters
ppm	Parts per Million
PRESS	Point Resolved Spectroscopy
PSA	Prostate-Specific Antigen
PZ	Peripheral Zone
r	Displacement
RF	Radiofrequency
ROC	Receiver Operating Characteristic
ROI	Region of Interest
σ	Shielding Constant
S	Signal Intensity
SAR	Specific Absorption Rate
SAR_{10g}	10g-averaged Specific Absorption Rate
SD	Standard Deviation
SNR	Signal-to-Noise Ratio
Spm	Spermine
SRF	Spatial Response Function
STA	Standardized-Threshold Approach
STEAM	Stimulated Echo Acquisition Mode
T	Temperature
t	Time
TCA	Tricarboxylic Acid Cycle
TE	Echo Time
TR	Repetition Time
TRUS	Transrectal Ultrasound
TxRx	Transmit/Receive
TZ	Transition Zone
v	Frequency
VOI	Volume Of Interest

List of Publications

In vivo assessment of prostate cancer aggressiveness using magnetic resonance spectroscopic imaging at 3 T with an endorectal coil
T. Kobus, T. Hambrock, C.A. Hulsbergen-van de Kaa, A.J. Wright, J.O. Barentsz, A. Heerschap, T.W.J. Scheenen
European Urology, 2011 Nov;60(5):1074-1080.

Prostate cancer aggressiveness: in vivo assessment of MR spectroscopy and diffusion-weighted imaging at 3 T
T. Kobus, P.C. Vos, T. Hambrock, M. De Rooij, C.A. Hulsbergen-Van de Kaa, J.O. Barentsz, A. Heerschap, T.W.J. Scheenen
Radiology, 2012 Nov;265(2):457-467

In vivo ^{31}P MR spectroscopic imaging of the human prostate at 7T: safety and feasibility
T. Kobus, A.K. Bitz, M.J. van Uden, M.W. Lagemaat, E. Rothgang, S. Orzada, A. Heerschap and T. W.J. Scheenen
Magnetic Resonance in Medicine. 2012 Dec;68(6):1683-1695

Quality Control of Prostate ^{1}H MRSI Data
A.J. Wright, **T. Kobus**, K.M. Selnæs, T.W.J. Scheenen, and A. Heerschap.
NMR In Biomedicine, 2013 Feb;26(2):193-203

In vivo ^{1}H MR spectroscopic imaging of aggressive prostate cancer: can we detect lactate?
T. Kobus, A.J. Wright, J.J.A. Van Asten, A. Heerschap and T.W.J. Scheenen
Magnetic Resonance in Medicine, 2014, Jan;71(1):26-34

Mapping of prostate cancer by proton MR spectroscopic imaging
T. Kobus, A.J. Wright, T.W.J. Scheenen, A. Heerschap
NMR in Biomedicine, 2013; Jan;27(1):39-52

Feasibility of T2 -weighted turbo spin echo imaging of the human prostate at 7 tesla.
M.C. Maas, E.K. Vos, M.W. Lagemaat, A.K. Bitz, S. Orzada, **T. Kobus**, O. Kraff, S. Maderwald, M.E. Ladd, T.W.J. Scheenen.
Magnetic Resonance in Medecine. 2014; May;71(5):1711-9

Assessment of Prostate Cancer Aggressiveness Using Dynamic Contrast-enhanced Magnetic Resonance Imaging at 3 T.
E.K. Vos, G.J. Litjens, **T. Kobus**, T. Hambrock, C.A. Kaa, J.O. Barentsz, H.J. Huisman, T.W.J. Scheenen.
European Urology 2013; 2013 Sep;64(3):448-55

Phosphorus Magnetic Resonance Spectroscopic Imaging at 7 T in Patients With Prostate Cancer.
M.W. Lagemaat, E.K. Vos, M.C. Maas, A.K. Bitz, S. Orzada, M.J. van Uden, **T. Kobus**, A. Heerschap, T.W. Scheenen.
Investigative Radiology 2014; May;49(5):363-72

Metabolite ratios in ^{1}H MR spectroscopic imaging of the prostate
T. Kobus, A.J. Wright, A. Heerschap and T.W.J. Scheenen
Magnetic Resonance in Medicine, 2014; Epub ahead of print

^{31}P MR spectroscopic imaging of the human prostate at 7T: T1 relaxation times, nuclear Overhauser effect and spectral characterization
M.W. Lagemaat, M.C. Maas, E.K. Vos, A.K. Bitz, S. Orzada, E. Weiland, M.J. van Uden, **T. Kobus**, A. Heerschap, T.W.J. Scheenen
Magnetic Resonance in Medicine, 2014; Epub ahead of print

The contribution of morphological features to parameter values in MR spectroscopic and diffusion-weighted imaging of the human prostate.
T. Kobus, J.A.W.M. van der Laak, M.C. Maas, T. Hambrock, C.C. Bruggink, C.A. Hulsbergen-Van de Kaa, T.W.J. Scheenen and A. Heerschap, in preparation

Dankwoord

Dit zal waarschijnlijk het meest gelezen hoofdstuk van mijn proefschrift zijn en een van de leukste om te schrijven! Er zijn veel personen die aan dit boekje hebben bijgedragen en in allerlei vormen. Verschillende mensen hebben vooral inhoudelijk bijgedragen, velen hebben geholpen met de nodige ontspanning, van andere heb ik juist meer ondersteuning gekregen en dan zijn er natuurlijk ook degene die mij geïnspireerd hebben dit onderzoek te doen. Ik heb een hele leuke tijd gehad in Nijmegen en ik ga mijn best doen iedereen hiervoor te bedanken!

Dit proefschrift was zeker niet zo geweest zoals het nu is zonder de bijdrage van mijn copromotor, Tom Scheenen. Tom, heel erg bedankt voor je super goede begeleiding. Ik heb veel van je geleerd en dankzij jou is mijn promotie soepel verlopen. In de tijd dat ik in Nijmegen heb gewerkt, heb je je eigen onderzoeksgroep op weten te zetten. Hierdoor hadden we een goed team voor het pionierswerk op 7 T. Het bespreken van artikelen met ons groepje was zeer inzichtelijk en je hebt een duidelijke en goed gefundeerde mening waar we allemaal wat van kunnen leren. Dankzij jouw kritische blik zijn artikelen goed wanneer ze opgestuurd worden en dit heeft er voor gezorgd dat we in leuke bladen hebben kunnen publiceren! Je hebt me aangemoedigd door te gaan met onderzoek en een fellowship aan te vragen. Ik ben je daar erg dankbaar voor en ik hoop nog lang met je samen te mogen werken! Naast werk moet er natuurlijk ook tijd voor ontspanning zijn. Gezellig biertjes drinken, hiken in California of Utah, en jullie achtertuin is ideaal voor barbecues, feestjes en kamperen! Heel erg bedankt!

Daarnaast wil ik graag mijn promotor, Arend Heerschap, bedanken. Arend, dank je wel dat je me hebt aangenomen op het Koningin Wilhelmina Onderzoeksprijs project dat je samen met Jelle Barentsz toegewezen hebt gekregen. Het bepalen van de agressiviteit van prostaat kanker is een belangrijk onderwerp en ik heb hier met veel plezier aan gewerkt. Ik denk dat we hele interessante en relevante artikelen hebben weten te publiceren. Jouw feedback op mijn artikelen was altijd relevant, to-the-point en heeft tot betere artikelen geleid. Je hebt een hele fijne werksfeer weten creëren in de Biomedical MR groep en mede daardoor kijk ik ernaar uit om na mijn post-doc in Boston terug te keren naar Nijmegen om hier mijn onderzoek voort te zetten. Er is totaal geen barrière om bij langs te komen met vragen, je deur staat altijd open en de barbecues bij jou en Gonda thuis waren erg gezellig, net als de kerst/winterdiners!

Alan Wright, heel erg leuk dat je mijn paranimf wilt zijn! We hebben veel samengewerkt, maar ook ontzettend veel gelachen! Samen met Isa was je m’n roomie in de ‘onderwaterkamer’ en na de verhuizing konden we je niet missen, dus ben je ons komen vergezellen in de nieuwe kamer! Je hebt me veel geleerd over de post-processing van spectra en jouw kennis van statistiek heeft zeker aan de kwaliteit van onze artikelen bijgedragen. Ik wens je heel veel succes in Cambridge en ik hoop dat je daar goed onderzoek kan gaan doen en mooie artikelen mag publiceren!

Een groot deel van mijn proefschrift zou niet mogelijk geweest zijn zonder de hulp van Christina Hulsbergen - van de Kaa. Christina, je hebt veel tijd besteed aan het uitlijnen van tumoren op prostaat coupes zodat wij deze konden correleren aan de MR-beelden. Het was heel inzichtelijk om met jou naar de histopathologie van prostaten te kijken. Ik denk dat iedereen die met prostaat MRI werkt dit eens zou moeten doen. Het was heel verhelderend om te zien wat voor kleine details we soms op willen pikken met MRI en waarom dat soms dus niet lukt. Bedankt voor je geduld.

Thomas Hambrock, heel veel dank voor de uren dat je me hebt geholpen met het matchen van de pathologie met de MR beelden. Tijdens je opleiding tot radioloog heb je hier zelfs in je weekend tijd voor gemaakt! Je bent altijd super geïnteresseerd in onderzoek en vol goede ideeën over vervolg studies. Ik hoop dat je onderzoek en kliniek kan blijven combineren en dat je veel fantasierijke verhalen blijft vertellen!

Ook wil ik graag Jelle Barentsz bedanken. Dankzij jouw vooruitstrevende kijk op MR van de prostaat is het Radboud een van de meest vooraanstaande centra op dit gebied. Je hebt een goed team om je heen weten te verzamelen en ik ben blij dat ik in dit team heb mogen werken.

Er zijn nog veel meer mensen die bij hebben gedragen aan mijn publicaties en die ik graag wil bedanken. Sj@kie van Asten, je hebt me erg geholpen met jouw LCModel kennis, je linuxbakken en je mooie bash-scriptjes. Je bent altijd heel geïnteresseerd en meelevend en dat waardeer ik enorm! Miriam Lagemaat, we hebben vele ritjes samen naar Essen gemaakt, discussies gevoerd over sequenties en gebrainstormd over van alles. Daarnaast ben je ook altijd in voor gezelligheid, een lekker biertje, een afdaling op de ski, een etentje bij jou en Sten thuis of een spelletje! Veel succes met je de volgende stap in je carrière! Mark van Uden, jouw vakkundige soldeerkunsten hebben geleid tot de ^{31}P endorectale spoel voor 7 T. Je bent altijd bereid om nog een keer uit te leggen hoe een PIN-diode ook al weer werkt, wat de scattering parameters zijn of hoe je twee spoelen ontkoppeld. Gelukkig zijn onze gesprekken op Paaspop wat luchtiger ;-) MC Massive (aka Marnix Maas), dank je wel alle tijd die je hebt besteed aan LCModel en Metabolite Report. Je bent bezig het onderzoek voort te zetten naar het bepalen van de agressiviteit van prostaat kanker op 3 en 7 T. Succes! Al ons werk op 7 T was niet mogelijk zonder de goede samenwerking met het Erwin L. Hahn Instituut in Essen. Im Besonderen möchte ich Andreas Bitz und Stephan Orzada danken. Ihr wart während unserer Prostata-Messungen immer da. Andreas, du hast viele Stunden damit verbracht, Spulen, Prostatae und 'Duke' zu simulieren. Unser Artikel in MRM hat eine Menge deiner Zeit in Anspruch genommen! Stephan, du hast ein großes Wissen über Spulen und Gerätetechnik. Dank deinem Spulen-Design waren wir in der Lage großartige Bilder einer Prostata zu machen. Jeroen van de Laak, dankzij jou konden we de prostaat coupes digitaliseren en segmenteren. Dit was onmisbaar voor het laatste artikel en heeft ons hele interessante inzichten gegeven. I also would like to thank Eva Rothgang and Elisabeth Weiland from Siemens in Erlangen for their input to improve our articles.

Natuurlijk wil ik ook Caroline Bruggink en Maarten de Rooij niet overslaan. Ik vond het tof dat jullie je stage op onze afdeling hebben gevolgd en me hebben geholpen met het onderzoek. Dit heeft geleid tot twee mooie artikelen. Dank jullie wel!

Hetty, we hebben samen veel leuke dingen gedaan: stappen in Valkenswaard, zomerfeesten, op reis met ons Oeike in Australië, met Alan en Willemijn naar Mayrhofen, en met de Tien naar Tignes! En nu zijn we allebei het avontuur aangegaan in Amerika, leuk! Isa, je was vanaf het begin mijn roomie en dat is zo gebleven! We hebben samen heel veel kopjes thee, Wiener Melange, Blue Fantasy en biertjes gedronken! Gezellig! Eline, jij bent altijd in voor gezelligheid en draait er je hand niet voor om om daarvoor vanuit Wijchen te komen fietsen! Leuk dat je in het Radboud in opleiding bent gegaan, blijven we collega's! Andor, tof dat ook wij collega's blijven. Ik kijk er nu al naar uit om straks weer met een rood-wit-gele sjaal mee op stap te gaan in Oeteldonk!

Ook wil ik graag alle mannen van de Biomedical MR groep bedanken. Ik heb jullie bijna allemaal wel eens of meerdere keren in de MR scanner gelegd om spectra van jullie prostaat te verkrijgen! Thanks guys! Het leuke aan de Biomedical MR group is dat we ook buiten het werk veel gezellige dingen hebben gedaan. Helaas wordt dit dankwoord te lang als ik jullie daar allemaal persoonlijk voor ga bedanken. Dus iets minder persoonlijk, maar wel heel veel dank voor de samenwerking en gezelligheid aan alle andere promovendi, postdocs en collega's van de Biomedical MR groep: Anne, Barbara, Bart (Van de Bank en Siemens/Philips), Bob, Christine, Cindy, Devasish, Edwin, Fernando, Frits, Houshang, Jannie, Kim, Marc, Marinette, Morteza, Patricia, Rianne, Valerio, Vincent en Yi. Allemaal ook bedankt voor de heerlijke taarten die jullie hebben gemaakt (of soms gekocht) en het in de rij staan voor Bossche bollen van Jan de Groot!

Dank ook aan iedereen van de prostaat werkgroep die ik nog niet genoemd heb: Caroline, Derya, Esther, Henkjan, Joyce, Jurgen, Geert, Kristian, Martijn (Hoogenboom en Schouten), Martin, Oscar, Patrik, Pieter en Wendy.

Verder wil ik graag Marijke Hogenkamp bedanken voor het inplannen van mijn studies en Leonie Vos en Solange Estourgie voor het regelen van allerlei andere zaken. Vele MR-laboranten hebben me geholpen tijdens de studies, dank daarvoor!

Ik heb veel plezier beleefd aan het organiseren van het ISMRM Benelux congres in Hoeven. Naast mijn medeorganisatoren, wil ik ook mijn bestuursgenoten van de ISMRM Benelux bedanken voor de gezellige vergaderingen, die vaak gepaard gingen met een heerlijke maaltijd.

Naast werk is er natuurlijk ook tijd voor ontspanning. En een goede manier om te ontspannen is mountainbiken met Pieter en Eric! Maar niet alleen in de bossen zijn jullie goed gezelschap, het is ook altijd gezellig als we een biertje drinken in de Dollars of Aesculaaf, patatjes eten bij de Febo, de Kuukse kroegentocht lopen, of een filmpje pakken bij de Lux!

Verder wil ik Oeike (aka Marcel) bedanken voor alle gezelligheid in de Aesculaaf, in Australië, in Boston en in het kleine Nijmegen! Kim Sweers, hoewel de wijn heeft plaatsgemaakt voor thee, is het nog altijd super gezellig om weer met je bij te kletsen. Ook met InfusiX is het altijd als van ouds! Tripjes naar Ryan-air bestemmingen, carnavallen in Oeteldonk, lekker eten bij de klinker, (een etappe van) de vierdaagse lopen en uitjes in Maastricht en West-Friesland! En dan wil ik nog Sjors en Piet bedanken voor leuke avondjes gamen en praten over opstellingen voor gedragsstudies en zebravisjes!

Ik luister erg graag naar muziek en gelukkig heb ik een aantal mensen gevonden die wel dezelfde muzieksmaak hebben als ik, namelijk de muzikanten van Joekskapel Ald Ïezer. Dank jullie wel voor alle repetities en leuke optredens! Saxofoon spelen is echt ontspanning en ik kom over een tijdje graag weer met jullie meespelen.

Verder wil ik iedereen van de familie bedanken voor hun interesse en gezelligheid! Amber, Els, Fleur, Jochem, Loes en Mark, jullie zijn een super uitbreiding van de familie en ik ben blij met jullie als broertjes en zusjes! Oma Broos, je bent heel geïnteresseerd in hoe het met me gaat en het is altijd gezellig bij jou op de koffie, je hebt genoeg te vertellen! Oma Kobus, of ook wel cybergranny! Je bent helemaal bij de tijd met skypen, facebook en emailen. Zo kunnen we mooi contact houden nu de afstand tussen Winterswijk en mij steeds groter wordt! Ooms, tantes en neefjes, super leuk dat jullie altijd geïnteresseerd zijn in hoe het gaat!

Lieve opa’s, helaas zijn jullie er geen van alle meer om dit mee te mogen maken, maar jullie zijn voor mij een grote inspiratie en motivatie voor kanker onderzoek en jullie verdienen dan ook zeker een vermelding en grote dank! Lieve opa Baard, wat ik me vooral van je herinner zijn de kieteldood, water in de knieën, je kriebelbaard en hoe gemeen (prostaat)kanker kan zijn… Lieve opa Sjaak, hoewel ik je Limburgse accent niet altijd kon verstaan, konden we altijd met je lachen! Lieve opa van de Heuvel, helaas was jouw prostaatkanker agressief en hebben de uitzaaiingen je veel pijn bezorgd... Opa Sjaak en jij hebben ons als jullie eigen kleinkinderen beschouwd en dat was heel fijn! Dank! Lieve opa Broos, ons medisch wonder, enorme doorzetter en mijn grootste inspirator. Je had geen behoefte meer aan een behandeling voor prostaatkanker en wie kon je ongelijk geven gezien alle behandelingen die je al onderging. Ik weet zeker dat je dolgraag bij mijn promotie had willen zijn en dat je ontzettend trots zou zijn op dit boekje!

Lieve Ferry, Liset en Jelle, jullie zijn de beste broers en zus die je je maar kan wensen! Ik vind het super fijn dat we een hechte band hebben en dat jullie altijd voor me klaar staan. Weer eens verhuizen, in de tuin werken, blaren lopen tijdens de vierdaagse, een website bouwen, de kou in Boston trotseren, m'n reisgenootje zijn in Peru, Stockholm of Turkije, het maakt niet uit wat. Met z'n allen op wintersport, party-en op Paaspop of los gaan tijdens Ferrie's Herriehok, het is altijd gezellig! Jelle, ik vind het heel tof dat je mijn paranimf wilt zijn!! Je staat altijd voor iedereen klaar, je bent super geïnteresseerd in mijn werk en onze band is nog beter geworden in Nijmegen!

Mam en Jan, niet alleen hebben jullie me vaak mogen verhuizen, we hebben gelukkig ook veel leuke dingen gedaan. Gezellig elke week repeteren met de joekskapel en als ik mee at was er altijd een toetje in huis! Samen op vakantie naar Turkije en Barcelona of op sinterklaasweekend met enorme surprises en uitdagende quizzen. Pap en Marlies, het is een feest bij jullie te eten, er staat altijd wat lekkers op tafel met vaak een kaasplankje en af en toe zelfs soufflé toe! Ik hoop dat we onze jaarlijkse traditie om met kerst op wintersport te gaan er nog even inhouden: lekker après-ski-en, heerlijke Oostenrijkse maaltijden, lunches en schnaps en natuurlijk super mooie pistes! Lieve mam & Jan, lieve pap & Marlies! Dank jullie wel voor jullie support, interesse, gezelligheid, liefde, aandacht en dat jullie er altijd voor me zijn! Ik hou van jullie!

En het laatste plekje van het dankwoord is natuurlijk voor Maarten. Lieve Maarten, we hebben het super fijn samen, ik kan niet alleen geweldig met je lachen, je luistert ook altijd naar al m'n verhalen! Ik word altijd helemaal vrolijk van je, vooral als je weer heerlijke crème brûllée hebt gemaakt. Jummie! Ik ben heel erg blij dat we samen zijn en hoewel de afstand het nu natuurlijk niet makkelijk maakt, weet ik zeker dat we samen een hele mooie toekomst tegemoet gaan! Ik hou van je! Kus

Curriculum Vitae

Thiele Kobus was born in Veghel in 1983 and grew up in Erp, a small village in Brabant. She did her pre-university education at Zwijsen College in Veghel and specialized in ‘Nature and Science’ and ‘Nature and Health’. She continued her education at the University of Twente in Enschede, where she studied Biomedical Engineering. During her master, she spent time abroad in Sydney for her internship at the University of Technology and on the Canadian east coast for a study tour. She gained interest for research during her master assignment, which involved selective stimulation of the cardiac fibers in the vagal nerve. She graduated cum laude and decided to start an academic career as a PhD-researcher at Radboudumc in Nijmegen. Guided by her supervisors Arend Heerschap and Tom Scheenen, she investigated the assessment of prostate cancer aggressiveness using magnetic resonance techniques. The result of this research lies before you.

Thiele applied for a Marie Curie Fellowship and a fundamental cancer research fellowship of the Dutch Cancer Society, to continue her career in cancer research. These fellowships enabled her to work in Boston at the Brigham and Women’s Hospital / Harvard Medical School as a postdoctoral researcher to investigate the possibilities for opening the blood brain-barrier for localized treatment of tumors in the brain. After two years of experience as researcher in Boston, she will continue her research at the Radboudumc in Nijmegen.